UNIVERSITÉ DE STRASBOURG

École doctorale
Physique, chimie-physique
ED 182
Université de Strasbourg

ÉCOLE DOCTORALE 182

UMR-7550

THÈSE présentée par :

Rashi JAIN

soutenue le : **25 Novembre 2021**

pour obtenir le grade de : **Docteur de l'université de Strasbourg**

Discipline/ Spécialité : Astrophysique

Stellar populations in Globular Clusters

Constraints on stellar physics and Subtle Relationships between color and environment

THÈSE dirigée par :

Mme LANÇON Ariane	Professeur, Université de Strasbourg
M. PRUGNIEL Philippe	Astronome, Observatoire de Lyon

RAPPORTEURS :

M. LARSEN Søren S.	Professeur Associé, Radboud University, Pays-Bas
Mme. RECIO-BLANCO Alejandra	Astronome, Université Côte d'Azur

---

AUTRES MEMBRES DU JURY :

M. MARTIN Nicolas	Chargé de recherche, Université de Strasbourg

INVITÉ

M. PUZIA Thomas	Professeur, Institute of Astrophysics at the Pontificia Universidad Catolica

ABSTRACT

Star clusters are groups of self-gravitating stars that are linked together. There are mainly two categories of star clusters, globular clusters and open clusters. While open clusters are relatively young and less populated, globular clusters are generally very old and are more populated than open clusters. The main focus of this study is on globular clusters. Globular clusters (GCs) can contain up to a million stars that are generally formed at the same time and thus share similar chemical abundances. Since these stars in GCs were born at roughly the same time, they evolve together, and their evolution depends on their initial masses. The most massive stars at birth evolve faster than the less massive stars. Thus, at any given epoch, a GC will host stars from all stages of evolution, making it an ideal site to learn about stellar evolution and validate our understanding of stellar physics.

Because GCs mostly form at a very early stage in the life of their own host systems, they also witness the formation, evolution, and merger history of their systems. Their kinematic and chemical properties are studied to understand the systems of which they are part. It is also known that the number of GCs in a galaxy is an indication of the total amount of dark matter it possesses. All of these characteristics make globular clusters a very versatile piece that completes the big picture.

In this work, we exploit the globular cluster as an individual entity to assess our understanding of the physical processes taking place within a star by using the various stellar libraries available and testing their performance against each other. We also take leverage of the GCs as part of a larger system to study the influence of the environment on the properties of the GC system as a whole. In this part of the work, we use photometric data from objects around M49, the brightest elliptical galaxy in the Virgo cluster of galaxies. We have reduced the 20 Tbs of near-infrared data and combined it with optical and UV data to obtain a broader spectral energy distribution. We study various color combinations for GCs in different environments and find the difference in their color-color distributions. We also compared the trends in our dataset with the GCs around another massive elliptical galaxy in the same galaxy cluster, M89.

Comparison of stellar libraries with NGC 6397

Stellar spectra libraries are of two types : empirical and theoretical. Empirical stellar libraries are made of stars that exist in nature, while theoretical libraries contain synthetic stars made from the stellar physics we know. If empirical libraries have the advantage

of containing real stars, they have the disadvantage of not completely sampling all possible stellar parameters (effective temperature, surface gravity and metallicity). This shortcoming is overcome by theoretical stellar libraries, but the latter have their own limitations because we cannot yet simulate the spectra of real stars with the desired accuracy (Lançon et al., 2021). Moreover, mathematical operations, such as interpolation, tend to introduce artifacts that we do not see in the same way in empirical libraries. In an ideal world, the two libraries complement each other and the results they produce are consistent. This was the main driver for our study. In this study, we compared the performance of a theoretical library, the Gttingen Spectral Library or GSL, from a previous work Husser et al. 2016, with that of the two empirical libraries, MILES and ELODIE, in the context of analyzing individual stars from o years of the Milky Way. We use the medium-resolution spectra of 5000 stars in the globular cluster NGC 6397. The spectra of these stars were used by Husser et al. 2016 to estimate stellar parameters by comparing the spectra to the theoretical spectral library, GSL.

In the study by Husser et al. 2016, the authors found a trend in metallicity that shows a dip in metallicity as the stars move up the evolutionary ladder from the main sequence to the sub-giant phase. This effect has been theorized for a very long time and corresponds to a manifestation of atomic diffusion in the presence of gravity. When stars move from the main sequence (MS) to the turn-off phase (TO), the metals on their surface have time to sink into the star and the surface metallicity decreases. When the star moves to the giant phase, the metals are redistributed to the surface by convection and the metallicity increases again.

In this work published in the journal A&A (Jain et al., 2020), we have pointed out the inconsistencies between different stellar libraries and listed some possible causes of these inconsistencies. On stellar libraries are ubiquitous in studies of stellar populations in the universe. It is of utmost importance to extend the coverage of available libraries and globular clusters are ideal laboratories to test the performance of different libraries.

Extra-galactic globular clusters - A complicated color-environment relationship

Globular clusters as a system are also a very important clue to the dynamical and chemical evolution of their host environments. We can use photometric information from extragalactic sources to study their formation history. In this project, we use photometric data around a massive elliptical galaxy in the Virgo cluster of galaxies, called M49. In a previous work, Powalka et al. 2016b studied the GCs system of a nearby elliptical galaxy, M87 and in the region around the galaxy. They found that the color-color distribution of the GC system is a function of their environment. To extend this study to a larger sample of galaxies, we

performed a similar analysis on the GC system around M49.

We reduced the near-infrared photometric data from a field of about 9 square degrees with M49 at its center, consisting of 20 TBs of data obtained with the European Southern Observatory's VIRCAM large camera. These data were observed in the framework of the Next Generation Virgo Cluster Survey in infrared (NGVS-IR). We have constrained the photometric catalogs in two near-infrared filters, J (1.1 μm) and Ks (2.2 μm). After calibrating these data against external standard photometric and astrometric catalogs, we combined IR photometry with optical and near-UV photometry to select globular clusters. With the broad coverage of SED (spectral energy density) in the UV, optical, and NIR using u,i and Ks band data (Muñoz et al., 2014), we obtain exceptional diagnostic power to select GCs from the sample of GCs, stars, and galaxies.

We used a 2-dimensional density-based probabilistic selection algorithm called the Gaussian mixture model to separate the GC sequence of stars and galaxies in the modified uiKs diagram using object size information. The size criterion is derived from the i-band photometric data and helps us separate point sources from slightly larger GCs and more extended objects such as galaxies.

This sample is then divided into subsamples based on location in the field. We divide the GCs into groups depending on whether they are located around M49, other smaller galaxies, or floating freely in the space between galaxies. We use the different colors available to study the differences in the spectral energy distribution between these groups.

We find that the color-color relationships of GCs that belong to different environments show variation in certain color combinations, specifically those involving the i, z and Ks filters. These differences arise from combined efforts of age, modified stellar compositions, and stellar distributions. The magnitude of these differences is small and we need more precise photometry and larger samples of GCs in the future to better understand the origin of these differences and to account for them in our evolutionary models. We expect an influx of high-precision photometry from a larger region of the sky with the upcoming launch of ambitious space telescopes like Euclid or the Nancy Grace Roman Space Telescope. The data from our study can be used to prepare for future missions.

ACKNOWLEDGMENTS

Life happens, coffee helps. Except for me, it didn't. What and who did make this journey possible, successful, and a pleasant one is what this acknowledgment is about.

My first thanks and acknowledgment is for my supervisor, mentor, and academic guardian, Prof. Ariane Lançon. People who know me know how much I idolize and adore Ariane for not only she is a great mentor but also a very kind person. She has always been very patient with me and my naive questions and doubts. Ariane has unique ways to approach problems and seek solutions. She is a very patient listener and a teacher and has inspired me in more ways than she is aware of.

And it might seem irrelevant but Ariane is a fun person to be around, and that is something that has made some very stressful days seem super easy and made my time in Strasbourg very memorable. I have thoroughly enjoyed our discussions on science and things other than science. She has taught me things that I can't possibly list here, but if I have to pick my favorite, it is the 'c'est la vie' attitude that is my keepsake. I think I got very lucky in the supervisor department.

I would also like to take this opportunity to thank my co-supervisor, Dr. Philippe Prugniel. Philippe had been a source of constant support towards the realization of this thesis. His keen eye and expertise have been very monumental in the shaping of the thesis. He has provided valuable comments and feedback and I have learned a lot from our conversations and discussions.

The name of some close collaborators needs a special mention. I am very thankful to Prof. Thomas Puzia to host me in Chile and provide my first exposure to the world of photometric data. He is also the PI of the datasets that are used in this work. I would also like to thank Dr. Carlos Gonzalez-Fernandes to help me with our questions on data reduction promptly. The visit to Cambridge has been very successful and was my last trip before the covid stopped the world, so I am always going to remember that one. I am also thankful to Prof. Lucimara Martins, Prof. Eric Peng, Dr. Karina Voggel, Dr. Paolo Bianchini, Dr. Nicolas Gillet for their guidance and suggestions from time to time in various stages of my Ph.D. Their suggestions and kind support have helped me in several ways. I would also like to acknowledge my master's thesis supervisor Prof. Vig for her constant guidance.

My special thanks to Dr. William Chantereau. We had a very small overlap in working time but even that short duration had been very fruitful for me to say the least. William has participated in the discussions and provided valuable inputs to my ideas and the project. I would also like to thank Dr. Anaïs Gonneau who has been a friend and a very fun person to go to advice for, be it about work or otherwise. Anaïs has a very comforting presence and I am happy to have met her.

The list will be incomplete if I didn't mention Thomas Lizee and Pierre-Antoine Oria with whom I have shared my office for the three years of my PhD. These two are the nicest office mates one can have. Thanks to them I know how to ask someone for tea in french, and I can name at least 10 different varieties of tea. I can't thank them enough to help me with everything from answering phone calls in french to decoding the various administration documents, they have done it all. You should know how easy you made my life and I am sure I have earned friends for life.

I would also like to thank all my colleagues at the observatory who have made this time a wholesome experience. I would also like to thank Veronique Trimbour and Sandrine Lagenbacher who have always been kind and very helpful with all the administrative procedures and the IT department, Thomas Keller and Christophe Salliard for helping me promptly with all my laptop troubles (which were a lot).

There are a lot of people who I have met because of this Ph.D. and who became an integral part of my life. Anu (Kundu, Dr.) has been one such person. Life in Strasbourg wouldn't have been the same without her. She gave me pep talks when I hit a block and felt useless and was always there to share my relentless love for food. She made me try things I never thought I would, like ice skating (good) and broccoli smoothie (not good). She also introduced me to some other amazing-ish people like Bengali (aka Sucheta) and Gobu (Aakansha). You guys are the world's okayest friend. And I can now be officially renounced of my 'first-year' title.

The list would be incomplete if I didn't mention Arpita Sarkar, who has been around to listen to me crib about the slightest inconvenince I was faced with. She was the one who made me believe that I can do it, my cheerleader and my confidante. I would also like to take a moment to acknowledge the very valuable (but mostly nonpractical) advice given by James Angthopo followed by some real zen-level words of wisdom and the option to choose between the two. Some of your words have helped, others made them into good funny stories. A very similar person who never gave me any advice is Sreelekshmi but was always there for me, you are the best, kutty. I am very thankful to Suvidya who has been my Friday coffee partner and has let me pick his brain on books, politics, movies, and whatnot. I would also like to thank Sambit who always has so many ideas and the broadest spectrum of perspectives on any topic under the sun. He has helped me with my coding and math problems but I am most thankful for all the good food he has cooked for us. An effort to count all the motivation and support I have received from my other amazing friends, Jyoti, Subhashini, Mayank, Smriti, Abhilash, Ayushi, Sanyogita, and Wissal. You guys are the best.

And last but not the least, a huge shoutout to Maa, Papa, and my little brothers Aditya and Akshay. I could not have done it without you guys.

Table of Contents

Page

1 GLOBULAR CLUSTERS - FOSSILS OF ASTRONOMY 1
1.1 Defining Globular Clusters 2
1.2 Resolved globular clusters - GCs in the Milky Way and neighbourhood . . . 3
1.3 Properties of resolved GCs 6
1.3.1 Ages 6
1.3.2 Absence of Dark matter 7
1.3.3 Multiple stellar populations 8
1.4 Properties of GC systems 10
1.4.1 Specific Frequency 10
1.4.2 Cluster Mass Function (CMF) 11
1.4.3 Bimodality 12
1.4.4 Sizes 13
1.4.5 GC mean metallicity and galaxy luminosity 13
1.4.6 Globular cluster Luminosity Function (GCLF) 15
1.5 Formation of the globular clusters 17
1.5.1 Formation of GCs as a resolved object 18
1.5.2 GC formation at high redshift 19
1.6 GCs as science drivers 21
1.6.1 Stars and Globular clusters - Probe to stellar evolution 21
1.6.2 Galaxy evolution and assembly 23
1.6.3 Dark matter content of a galaxy 25
1.6.4 GCs as distance indicators 26
1.6.5 Link between GCs and Ultra compact dwarf galaxies, and Nuclear star clusters 27
1.7 Observational Techniques 29
1.7.1 Methods for spatially resolved clusters 30

1.7.2 Methods for spatially unresolved clusters 31
1.8 Motivation and outline 32
1.8.1 Stellar libraries 32
1.8.2 Extra-galactic GCs and their color-environment relationship 33
1.8.3 Outline 33
1.9 Résumé 34
1.10 Définition des amas globulaires 35
1.11 Amas globulaires résolus - GCs dans la Voie lactée et son voisinage 36
1.12 Propriétés des GC résolus 38
1.12.1 Ages 38
1.12.2 Absence de matière noire 39
1.12.3 Populations stellaires multiples 40
1.13 Propriétés des systèmes GC 41
1.13.1 Fréquence spécifique 41
1.13.2 Fonction de masse du cluster (CMF) 42
1.13.3 Bimodalité 43
1.13.4 Tailles 44
1.13.5 Métallicité moyenne du GC et luminosité des galaxies 44
1.13.6 Fonction de luminosité des amas globulaires (GCLF) 45
1.14 Formation des amas globulaires 46
1.14.1 Formation des GC en tant qu'objet résolu 46
1.14.2 Formation du GC à haut redshift 48
1.15 GCs comme moteurs de la science 50
1.15.1 Etoiles et amas globulaires - Sonde de l'évolution stellaire 50
1.15.2 Évolution et assemblage des galaxies 51
1.15.3 Contenu en matière noire d'une galaxie 54
1.15.4 Les CG comme indicateurs de distance 55
1.15.5 Lien entre les GC et les galaxies naines ultra compactes, et les amas d'étoiles nucléaires. 56
1.16 Techniques d'observation 57
1.16.1 Méthodes pour les amas résolus dans l'espace 57
1.16.2 Spectroscopie stellaire 58
1.17 Motivation et plan 58
1.17.1 Bibliothèques stellaires 59
1.17.2 Les GC extra-galactiques et leur relation couleur-environnement 59

1.17.3 Outline . . . 59

2 NGC 6397 : TESTING STELLAR MODELS WITH ATOMIC DIFFUSION . . . 61
2.1 Atomic diffusion in stars . . . 61
2.2 Atomic diffusion in NGC 6397 - Introduction to earlier study . . . 63
2.3 Data and earlier analysis . . . 66
2.4 Re-analysis . . . 67
2.4.1 Method . . . 67
2.4.2 Assessment of the internal errors . . . 70
2.4.3 Assessment of the external errors (accuracy) . . . 71
2.4.4 Results . . . 72
2.5 Discussion . . . 74
2.5.1 Changes of the surface metallicity above the turn-off . . . 74
2.5.2 Spectroscopic surface gravity . . . 77
2.6 Conclusions . . . 77

3 WIDE-FIELD IMAGING OF THE VIRGO GALAXY CLUSTER IN THE NEAR-INFRARED : THE SURVEY AND DATA REDUCTION. . . . 81
3.1 The Virgo galaxy cluster . . . 82
3.2 The Next Generation Virgo Cluster Survey in the Near-Infrared (NGVS-IR) 85
3.3 Data Acquisition . . . 86
3.3.1 Observing strategy . . . 89
3.3.2 Data Quality . . . 90
3.4 Data Reduction . . . 90
3.5 Data processing . . . 92
3.5.1 Mask creation . . . 93
3.5.2 Sky subtraction . . . 94
3.5.3 Pre-stacking Photometric Calibration . . . 94
3.5.4 Astrometric Calibration and Stacking . . . 96
3.5.5 Galaxy Subtraction . . . 98
3.6 Photometry on Stacked Images . . . 100
3.6.1 Aperture Photometry . . . 101
3.6.2 Uncertainties on aperture corrections . . . 103
3.6.3 External Photometric calibration . . . 103
3.6.4 Final word on aperture correction values . . . 106
3.6.5 Calibration of galaxy subtracted optical band catalogs . . . 106

3.6.6 Extinction correction . . . 107
3.7 The Photometric Catalogs . . . 107

4 GLOBULAR CLUSTER SELECTION AND THE COLOR COLOR DIAGRAMS . . . 109
4.1 Color-color diagrams . . . 109
4.1.1 The *uiKs* color-color plane - The tool for effective GC selection . . . 110
4.1.2 Reasons for excellent diagnositic power of the *uiKs* diagram . . . 111
4.2 Selection of Globular Cluster candidates . . . 113
4.2.1 Ridge line . . . 116
4.2.2 Gaussian Mixture Models . . . 116
4.2.3 Final sample of Globular clusters . . . 121
4.3 Optical color correction . . . 121
4.4 Spatial grouping of the GCs . . . 125
4.4.1 GCs in the P89 field . . . 125
4.4.2 GCs in the P91 field . . . 126

5 RELATION BETWEEN GLOBULAR CLUSTER COLOR AND ENVIRONMENT . . . 128
5.1 Completeness and contamination . . . 129
5.1.1 Comparison with the ACS Virgo cluster survey GC candidates . . . 129
5.1.2 Comparison with spectroscopic GC candidates . . . 130
5.1.3 Contamination . . . 133
5.2 GCs in different environments and their general properties . . . 135
5.2.1 GC system of giant elliptical galaxies . . . 136
5.2.2 GC system of NGC 4526 and NGC 4365 . . . 138
5.2.3 Intra-cluster GCs . . . 139
5.3 Color-color diagrams . . . 140
5.3.1 Influence of the environment on GC colors . . . 143
5.3.2 Comparison with M87 GC colors . . . 144
5.3.3 Comparison with SSP tracks . . . 144
5.4 Colors and environment - Possible culprits . . . 147

6 SUMMARY AND CONCLUSION . . . 149
6.1 The importance of the Ks band . . . 151
6.2 Upcoming surveys . . . 151

Appendices

A First Appendix . . . 155

A.1 Color transformation from UKIDSS/WFCAM to VIRCAM. 155

References 181

Chapter One

Globular clusters - Fossils of astronomy

"Astronomy, as nothing else can do, teaches a man humility." - Arthur C. Clarke

Abstract

This chapter gives an overview about globular clusters (GCs) and their role in understanding the physics of stars and their evolution. We discuss the GCs as an individual entity and as a part of a larger system and their properties. In this chapter we talk about the GC system found in different types of environments, and their role in understanding their surroundings.

The universe is an extremely mysterious place and humans are curious creatures. We have used photons across the range in electromagnetic spectrum that finds its way to us, to exploit every piece of possible information it might carry. This has led us to discover a broad variety of extraterrestrial objects all of which form part of this huge enigmatic puzzle that we are trying to comprehend. Over time astronomy has witnessed a revolutionary incoming of high quality data which is made possible by improved ground based and space based telescopes across all wavelengths. This is additionally benefited by the advances in the field of data science and machine learning. By taking advantage of all the tools at our dispense we are able to uncover more and more secrets of the cosmos. Forming a small but important part of this big picture and a big part of this work at the centre stage are the Globular clusters, or GCs as we will name them from time to time in this manuscript.

The distribution of stars in a globular cluster is usually spherical in shape which has earned them their rightful name. A typical globular cluster can harbour hundreds of thousand stars within a relatively small region in space. They have typical outer radii of the order of tens of parsecs. Figure 1.1 shows a typical globular cluster, NGC 6139 that orbits the Milky Way.

Figure 1.1 NGC 6139 is a massive globular cluster in the constellation of Scorpius (the Scorpion). Image Credit: ESA/Hubble Space Telescope & NASA

Since these GCs are some of the oldest surviving relics in an astronomical system such as a galaxy or a cluster of galaxies and they retain the signatures of the conditions and the environment in which they were born and therefore they are sometimes referred to as the fossils of astronomy. GCs have very popularly been dubbed as simple stellar systems, a notion which has been proven an understatement with evolving time and more and more advancements in the field.

But apart from being the members of the bigger system, GCs are interesting even all by themselves. The resolved stellar population of a GC is a magnificent site to find stars in all evolutionary stages. The GCs have, therefore, served as laboratories for testing the validity of our understanding of stellar physics. With their impeccable regular shapes and symmetry, GCs are hiding their true colorful nature in plain sight. We will discuss in brief various aspects of a GC as an entity and its complicated stellar population, and GCs as part of a bigger system in the next few sections.

1.1 Defining Globular Clusters

Star clusters cover a broad range of mass and sizes, and differ from stellar associations and moving groups in the respect that the clusters are gravitationally bound systems. In terms of distinction between a star cluster and galaxies, it was earlier accepted that the first is contained in the other, so a hierarchical definition of GC can be derived. But some galaxies like Aquarius and Tucana do not host any clusters (Forbes et al., 2000) and some ultra-faint dwarf galaxies have fewer stars than massive GCs do (Belokurov et al., 2007). This called for a revision in this definition of a GC.

The clusters in the Milky Way are usually classified as either Globular clusters(GCs), which are found in the halo, or open clusters (OCs) which are found in the disk. These clusters were earlier understood to have distinct mass ranges and ages, but with new data these distinctions have begun fading. GCs are a type of star cluster and generally very old and more populous as compared to their younger cousins, open clusters, which are also much smaller in size and extent. In the Milky Way, the GCs were traditionally defined as star clusters found in the bulge and the halo of a galaxy having masses $> 10^4$ $M_\odot$ and older than 6 Gyr. With additional study of the GC system of other galaxies, we came to learn about GCs that are much younger (Kharchenko et al., 2013). The metallicity of the OCs are also found to have overlap with the GCs in the thick disk of the MW with [Fe/H] values > -0.8 (Zinn, 1985). Ages within stellar population in GCs are usually very similar with a small spread. A significant difference between other types of clusters and globular clusters is that stars in most GCs show typical anti-correlation among light elemental abundances and are host to multiple stellar populations (Renzini, 2013; Bastian and Lardo, 2018). All GCs show patterns such that the stars that have access of He, N and Na and are depleted in O and C.

A precise definition of a globular cluster, thus remains elusive to date. A very naive definition of globular clusters would then be a system of gravitationally bound co-evolving stars which share similar but not the same chemistry with certain peculiar trends in their light element abundances. This definition is far from complete or even exclusive, but it works in the present context, hence we will adopt this definition for the globular clusters in this work. Since we have chosen this definition of a GC,in the next section we will describe in brief the properties of the object that is identified as a GC with the above definition.

1.2 Resolved globular clusters - GCs in the Milky Way and neighbourhood

The star clusters in the Milky Way, the Magellanic Clouds, and M31 can be resolved down to individual stars with the resolution of *Hubble Space Telescope*. It is a bit more complicated than stated, and the resolution of stars is a function of luminosity and the crowding in the region being studied. In cases where the stars can be resolved the CMD of these stars can provide direct estimate of a number of cluster properties. The globular clusters of the MW because of their proximity to us are best studied.

In 1918, when Harlow Shapley measured the distances to the GCs known at the time assuming their spherical distribution, he discovered that the Milky Way was much bigger than previously thought. He also discovered from the spatial distribution of the known GCs, that we are not the center of the universe. According to a 2010 census by Harris (1996) (updated by Harris (2010)), there are at least 157 Milky Way GCs, most of which reside in the galaxy halo. This might be a biased picture owing to the fact that any GCs in the galaxy disk or bulge will be obscured from us because of the galactic dust lying between us and the centre of the galaxy. A distribution of known MW GCs is shown in figure 1.2. The concentration of the GCs at the centre of the plot is an obvious indication of the centre of the galaxy. The Milky Way GCs are found to be as old as 13 Gyr with an age spread of about 5 Gyr (Carretta et al., 2000).

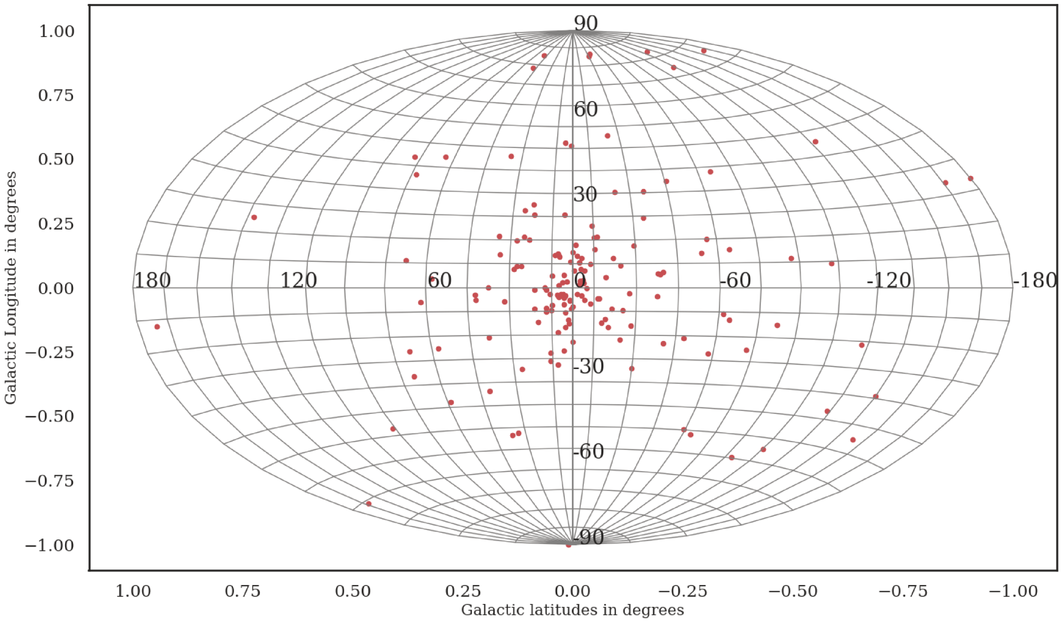

Figure 1.2 Distribution of the globular clusters of the Milky Way in the catalog of Harris (2010). The clusters are concentrated around the centre of the galaxy.

The Milky Way is home to GCs that have broad range of masses and integrated magnitudes (Meylan and Heggie, 1997). While most of the GCs are located within 20kpc from the centre of the galaxy, the farthest known Milky Way GC is Leavens-1 at staggering 145kpc from the galaxy's center (Laevens et al., 2014). The GC system of the MW is divided into two sub-groups, the GCs that lie within 10 kpc from the galactic centre are classified as the inner halo/bulge GCs, while the GCs that have distances $>$ 15 kpc are the outer halo GCs

(Kinman, 1959; Zinn, 1985; Armandroff, 1989). The halo population is typically metal-poor and shows little to no rotation, whereas the bulge population is relatively metal rich and has rotational velocities consistent with that of the disk stars. These properties are often linked to the origin of these population of GCs, as it will be discussed in the later sections, that metal-rich GCs are believed to have formed in-situ while the metal-poor GCs are most likely to have acquired by the Milky Way during in-fall and/or accretion episodes (Mackey and van den Bergh, 2005; Zinn, 1978; Zinn, 1993) The metallicity distribution of GC system of the Milky Way shows a bimodal distribution with peaks for MP and MR GC sub-population at [Fe/H] ∼ -1.59 and -0.55 respectively (Cote et al., 1999).

Age estimates of GCs from deep *HST* CMDs reveal that the majority of the GCs are rather old with their ages older than 10 Gyr (Marín-Franch et al., 2009; Vandenberg, 2003), and in terms of redshift these GCs were formed at z>2. This does not hold true for all of them and some of the GCs are found to have younger ages, for example, Palomar 12 and Terzan 7 which have ages ∼8 Gyr.

The age-metallicity relationship (AMR) for the GCs (Leaman et al., 2013) shows that metal rich GCs are younger on average. This observation can be explained as the older massive stars that will perish earlier and enrich the ISM make the subsequent generation of stars metal rich.

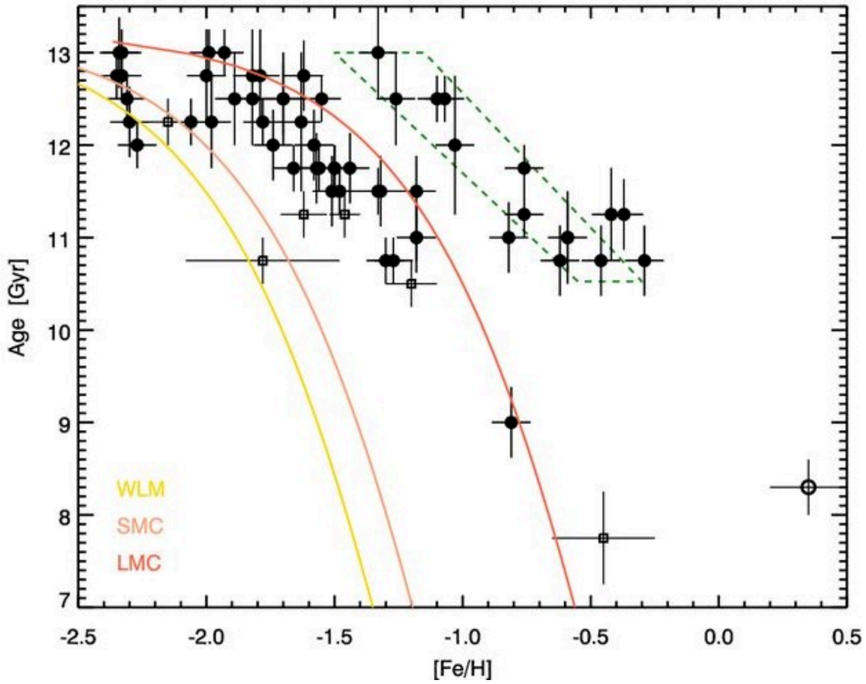

Figure 1.3 AMR for the GCs in halo and disk. The AMR for dwarf galaxies are overlaid on the top and they occupy the same region as halo GCs. The MW bulge GCs are enclosed within green dashed lines.(Figure taken from Leaman et al. 2013)

In figure 1.3 the AMR of the GCs are plotted overlaid with the expected AMR loci of the dwarf galaxies in our neighbourhood (WLM, and Magellanic clouds) and the MW bulge (green dashed region). The plot shows that the metal poor GCs are more consistent with the AMR of the neighbourhood dwarf galaxies and it makes it more likely that these clusters could have been accreted from the dwarf galaxies. This is a common scenario accepted for the formation of most massive galaxies and their GC systems.

In addition to the GCs of the MW, the better studied GC systems include the GCs of the Magellanic clouds which could be resolved due to their proximity to the MW, and M31 which could also be partially resolved. M31 is almost as massive as the MW (Evans and Wilkinson, 2000; Watkins et al., 2010) but it hosts 3 times the GC population of the MW ($\sim$ 400-450) (Barmby and Huchra, 2001). Some of the properties of M31's GC population are similar to those of MW GCs for instance both host an extended halo sub-population and a more centrally concentrated rotating disk population. The GC system of M31, however, does not exhibit the obvious bimodal color distribution which might indicate at shorter episodes of merger and in-falls.

In contrast with the MW GCs, the LMC clusters cover a broad range in ages and the GCs age distribution shows the 'famous' age-gap between the old and an intermediate age GC sub-systems (Jensen et al., 1988). The LMC clusters have an intermediate age GCs which have ages $\sim$ 3 Gyr. On the other hand, the SMC has only one old GC but a more continuous distribution of age between old and young clusters (Mighell et al., 1998).

In the next section, we will discuss the properties of the resolved globular clusters, the knowledge of which is primarily based on the Milky Way GCs, and the GCs in the neighbouring galaxies aided by numerical simulations. It is followed by the discussion of general properties of globular cluster systems as a whole.

1.3 Properties of resolved GCs

1.3.1 Ages

A knowledge of ages of GCs in the universe puts constraints on major star formation episodes in the universe. Coupled with their metallicities, they provide a key to understanding the major epochs of star formation in the Universe. GCs are typically older than 1 Gyr (as compared to open clusters which are generally younger) and sometimes they are survivors from the early universe, and relics of the major epochs of star formation in the history. Whether the GCs span a broad range in age, or if the majority of the GCs are formed at a particular epoch is still a topic of debate. A precise estimate of the age of a remote GC is still difficult because of the age-metallicity degeneracy (Worthey, 1994). Estimates of ages of

MW GCs are known with better precision because of their resolved nature. Ages of GCs in the Milky Way are measured from deep color-magnitude diagrams that come from the ACS instrument on-board HST. Almost 70 Milky Way GCs have their ages estimated from the HST CMDs, and their age-metallicity relationship reveals that most of the older GCs span a wide range in metallicity, while the ages of the younger GCs are anti-correlated with their metallicities (Marín-Franch et al., 2009; Forbes and Bridges, 2010; Oliveira et al., 2020) . In these studies, it was also found that in general the metal poor (MP) GC sub-population is somewhat older than their metal rich (MR) counterparts (12.5 Gyr for MP as compared to 11.5 Gyr for MR). But these age estimates are within the uncertainties and therefore the possibility of both the groups overlapping considerably cannot be ruled out. A few GCs have their age estimates obtained from the WD cooling sequence which is less sensitive to the metallicity but also need a much deeper CMD, and the ages were found to be consistent with the age estimates obtained via main sequence fitting (e.g. Hansen et al., 2013; García-Berro et al., 2014).

A new technique that could prove useful in deriving absolute GC ages uses deep near-IR CMDs. It probes main-sequence 'kinks' which are typically displayed at $\sim 0.5\ M_{\odot}$, which corresponds in color to *(J-K)* $\sim$ 0.8. The difference between the main sequence turn off and the kink is sensitive to age and metallicity. The location is insensitive to uncertainties in distance modulus, stellar models, and extinction values (Bono et al., 2010).

The ages of the MW GCs indicate that most of the GCs were formed 11.5-12.5 Gyr ago, that is at around $z \sim$ 3-6 in the standard cosmological model. This is one of the important constraints on the upper limit of the age of the universe (Krauss and Chaboyer, 2003). This is also important to assess the link between the re-ionization and the formation of the GCs and the impact of one on the other.

1.3.2 Absence of Dark matter

Kinematic studies of the globular clusters have established that the GCs are devoid of dark matter (DM). This is one of the striking differences between otherwise very similar dwarf Spheroidal galaxies (dSph) and the GCs. The mass-to-light ratio of the GCs is typically between 1-4, which indicates towards a deficiency in the DM content in the GCs. But based on formation channels usually accepted, it has been argued that if the GCs were formed in the DM dominated environment, it is unlikely that they are completely devoid of DM. Baumgardt and Mieske 2008 proposed that the GCs can be DM free in their center but should retain the dark matter in their halos. Ibata et al. 2013 also estimated the dark matter content of NGC 2419 in its halo and suspected that it could be twice as massive as its stellar component. This could explain the flattening of the velocity curve in the outskirt of some of the globular clusters (Drukier et al., 1998; Scarpa et al., 2007; Lane et al., 2010; Bellazzini et al., 2015; Bianchini et al., 2019). Such clusters would then call for a different formation scenario than the less massive ones, possibly similar to ultra compact dwarf galaxies (UCDs) that have a higher mass-to-light ratio and are similar to the GCs in other respects.

1.3.3 Multiple stellar populations

GCs were initially perceived as systems that host coeval simple stellar populations (e.g. Ashman and Zepf, 1998). But it is now widely accepted that this is not the case, and the stellar population in a GC is much more complicated than initially thought. GCs exhibit star-to-star variation in abundances of certain elements like He, C, N, O, Na, and Al. These peculiar patterns are particular to GCs and are absent in the field stars, and they are the telltale sign of high-temperature H burning (Gratton et al., 2004; Charbonnel, 2016). These patterns are seen in the GCs such that more enriched GCs are rich in He, N, and Na and have depleted abundances of O, and C. Figure 1.4 shows the plot of Na vs O abundances in 20 MW GCs. The anti-correlation between Na and O can be seen for almost all the clusters with varying amplitude (Carretta et al., 2009a; Carretta et al., 2009c).

It is noteworthy here that despite the strong anti-correlation among the stars,the [Fe/H] remains same amongst them. The anti-correlations give rise to what are known as multiple stellar populations (MSP) in the GCs which is reflected in the complex color-magnitude diagram of the clusters. Figure 1.14 shows the CMD of main sequence stars of NGC 2808. The distinct sequences of stars are very obvious.

The Hubble Space Telescope (HST) UV Legacy Survey of Galactic GCs (Piotto et al., 2015) observed 56 GCs with UV/blue filters primarily with the aim of identifying multiple populations in GCs. The findings from the survey were used to explain the possible origin of the enriched (or 2nd generation as referred in the series) population of stars (Renzini et al., 2015). The possible culprits include enrichment from the ejecta of first generation stars (Prantzos and Charbonnel, 2006), massive asymptotic giant branch (AGB) stars, fast rotating massive stars (Denissenkov et al., 2015) and interacting binaries. The models predict that the age difference between the two generation of stars is less than 150 Myr for clusters with ages 12 Gyr and older. Thus the stars can still be called co-eval.

These trends are not particular to MW GCs but are also known in the GCs outside of the MW. Mucciarelli et al. (2009) studied three GCs in the LMC and discovered the same trends between Na-O and Al-Mg as seen in the Galactic GCs. A number of similar studies on the GCs of the SMC, Fornax dwarf Spheroidal have also shown the presence of MSP (Hollyhead et al., 2017; Larsen et al., 2014). The amplitude of the variation of the elements is often linked to the mass and cluster age and metallicity such that older clusters (>8 Gyr) show

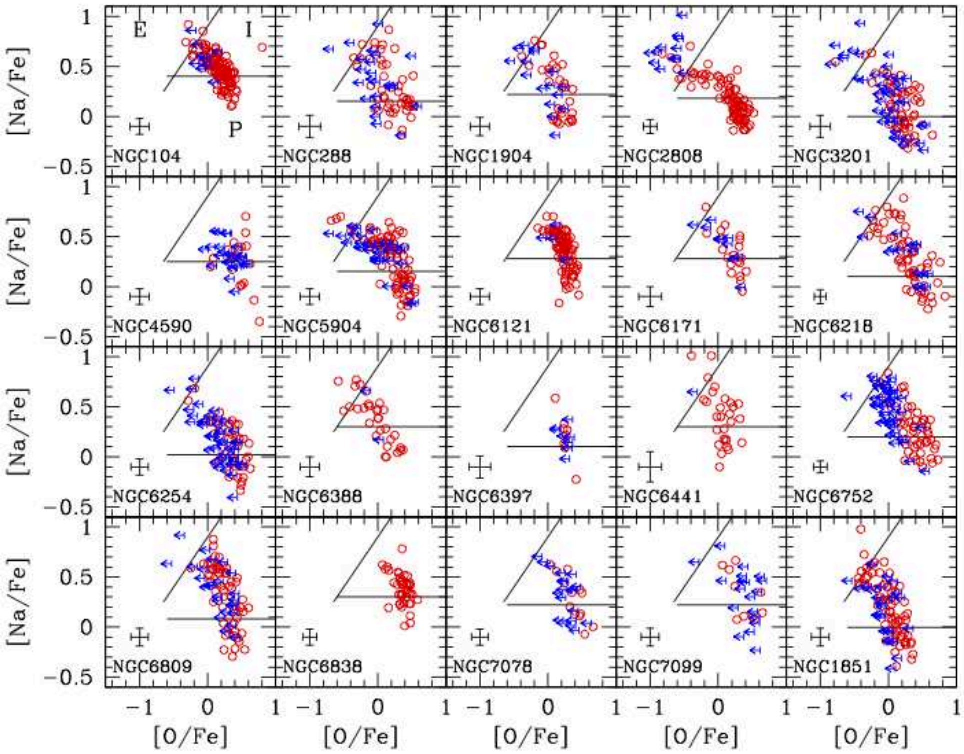

Figure 1.4 Na-O anti-correlations seen in 20 MW GCs.The lines mark the primordial, intermediate and extreme generation stars. The red circles show the stars with measurement for both Na and O, the blue data points only have measurement for Na but only upper limits for O (Gratton et al., 2012)

.

the presence of MSPs (Krause et al., 2016), with higher amplitude of variations observed in the more massive clusters (Milone et al., 2017). The fraction of enriched population of stars (also termed as 2nd generation or 2P stars) ranges from 40-90 % in old GCs (Gratton et al., 2019). These 2P stars are expected to have formed from the processed material from the 1P stars. With high-precision measurements many clusters have shown signatures of 3-4 subpopulations. There is tentative evidence that the MSPs are not only restricted to the GCs but can also be seen in other environments like dwarf galaxies, bulge/inner halos of galaxies and ETGs (Bastian and Lardo, 2018).

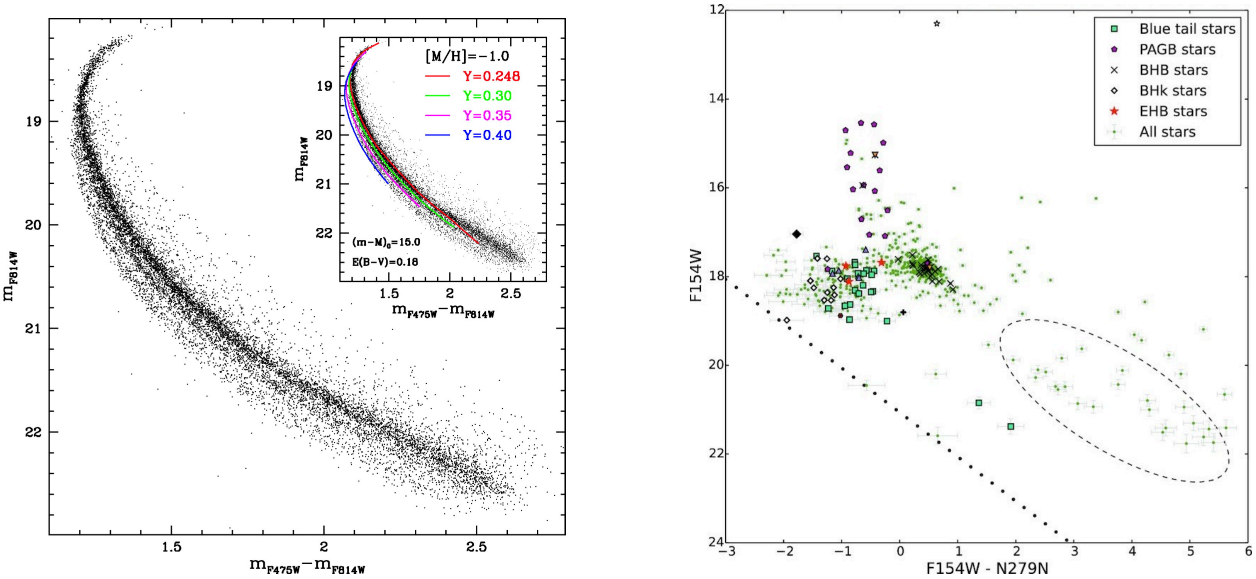

Figure 1.5 *Left*: Color-magnitude diagram of main sequence stars in the GC, NGC 2808. The multiple sequences are apparent in the CMD. In the inset, the CMD is fitted with four 12.5 Gyr isochrones with different He content (Piotto et al., 2007). *Right*: The FUV-NUV color magnitude diagram of horizontal branch stars of NGC 2808 showing the bimodal distribution of stars. (Jain et al., 2019)

1.4 Properties of GC systems

1.4.1 Specific Frequency

Specific frequency is defined as the number of globular clusters, N_{GC}, per unit galaxy luminosity, normalized to a galaxy with absolute V band magnitude of -15 (Harris and van den Bergh, 1981), and represents the efficiency of GC formation as compared to the stellar component of the galaxy.

$$S_N = N_{GC} 10^{0.4(M_V+15)} \tag{1.1}$$

The parameter was formulated to establish the relationship between galaxy luminosity and the number of GCs the galaxy hosts. S_N was found to have no simple relation with the M_V. However, S_N was found to differ based on the environment. It was found that ellipticals found in smaller and sparser groups have approximately two times fewer GCs for their size than the ellipticals that reside in richer environments (Harris, 1991). The average value of S_N for ellipticals is around 3.5, but large scatter exists. M87 has been shown to have a 2-3 times higher S_N than the other gE galaxies in the Virgo cluster, which themselves have a more populous GC population as compared to other field galaxies.

The value of S_N for disk galaxies is a little bit more challenging to determine directly because their M_V consists of light from both disk and Population I stars, which have little relation to the halo GCs. Moreover, the GCs are difficult to even detect on top of irregular background of the spiral galaxy especially if the galaxy is edge on (see figure 4 in Harris 1991). Their adjusted S_N is calculated from the ratio of N_{GC} to only the spheroidal light that excludes the disk.

The specific frequency was devised to compare the systems more easily without having the proportionality depend on the size of the galaxy. S_N is essentially the ratio of the number of GCs to the total stars in the galaxy, and is therefore insensitive to the galaxy mergers because both stars and GCs are formed when mergers take place.

Peng et al. (2008) studied the S_N for 100 galaxies in the Virgo cluster region and they found that the GC numbers were low in intermediate mass galaxies (-20.5 $< M_V <$ -18), increasing for both the lower and the higher mass galaxies in the region. Other independent studies have also confirmed the same results for ETGs (Zaritsky et al., 2015; Liu et al., 2019a) . In the beginning the S_N was parametrized to study the relation between the stellar population of a galaxy and its GC system, but lately it has been found to be an important factor that is regulated by the GC system environment.

1.4.2 Cluster Mass Function (CMF)

The exact nature of stellar systems in GCs is not easy to probe given the limitation in observation. Formation scenarios of GCs show that GCs could either form monotonically or through mergers of smaller sub-systems in larger molecular complexes (Bonnell et al., 2003). The confirmation of these scenarios require that we know the initial cluster mass function (ICMF) and its evolution. The ICMF can be a very important piece to reconstruct the formation of the clusters, but it is to be noted that it is unlikely to be observed since observations can only probe the present day cluster mass function. The present day CMF for the Milky Way GCs is described by a log-normal distribution which peaks at $\approx 2 \times 10^5$ $M_\odot$ (Whitmore et al., 1999; Fellhauer and Kroupa, 2005).

The mass function of the young systems could be approximated as the ICMF and used to infer the relationship between the current CMF and ICMF of older clusters. The mass function of a young cluster follows a power law function with exponential cutoff at the high mass end, and is given in the functional form as:

$$\frac{dN}{dM} \propto M^{-\beta} e^{-\frac{M}{M_c}} \tag{1.2}$$

The function is similar to the galaxy mass function (Press and Schechter, 1974) and is parameterized by $\beta \approx 2 \pm 0.3$ (Zhang and Fall, 1999; Bik et al., 2003; Hunter et al., 2003). To establish the relation between the Schechter like ICMF and current day CMF requires a knowledge of the mass-loss and other evolutionary processes that the clusters undergo during their lifetime and their dependence on mass.

1.4.3 Bimodality

GC systems of early galaxies were found to show bi-modal color distributions (Ostrov et al., 1993; Ashman and Zepf, 1993) and now it is established that the GC systems of most of the massive galaxies show a bi-modal color distribution (Larsen et al., 2001b; Kundu and Whitmore, 2001; Peng et al., 2006). This color differences had been explained to originate due to differences in metallicity or age or a combination of the two. Spectroscopic studies have shown that these differences are principally due to metallicity rather than age. The bimodality in colors translates to blue GCs as the metal poor (MP) ones, and the red GCs as the ones that are metal rich (MR). The presence of the two populations of GCs was first proposed by Zepf and Ashman (1993). The two distinct groups of GCs have significant differences in their characteristics and are proposed to have originated via different mechanisms or different events. The red clusters in disk galaxies have significant rotation as compared to the blue clusters. In elliptical galaxies, the red GCs have lower velocity dispersion than the blue GCs. The red GCs are also more centrally concentrated than the blue GCs in these systems (Brodie and Strader, 2006). However, the internal properties like masses, sizes, and ages at first glance are more similar in the two groups. This could mean that these clusters were formed in similar manner but the molecular clouds from which they were formed were assembled differently (Gnedin and Prieto, 2009). The consequences of existence of two distinct groups are significant in terms of formation and evolution of galaxies.

The GCs in the Milky Way are also known to exhibit bimodal color distribution (Zinn, 1985). The two groups in the MW have characteristic spatial distribution such that the MP GCs are found in halo of the Milky Way while the MR GCs are more commonly found in the disk and bulge. The blue and red peaks in the (V-I) color typically occurs at 0.95 ± 0.02, and 1.18 ± 0.04 (Larsen et al., 2001b) in ETGs. These color values correspond to [Fe/H] $\sim$ -1.5, and -0.5 for old GCs. This peak is not always the same for all galaxies.

On the contrary, some studies also propose that the color-metallicity relation might be non-linear, in which case a bimodal color distribution does not necessarily require that the metallicity will be bimodal too (Yoon et al., 2006b; Yoon et al., 2006a; Blakeslee et al., 2010). As shown in simulations by Yoon et al. (2006a), all colors exhibit bimodality, like g-z and V-I, but the impact is less obvious in optical-NIR colors like V-K. In terms of observation the number of galaxies with high quality optical-near IR data is low and will improve in the future.

1.4.4 Sizes

The surface brightness distributions of GCs can be approximated by King models (King, 1966). The King's model for the GC can be characterised as a function of the concentration parameter c, such that $c = log_{10}(r_t/r_c)$, where r_t is the tidal radius and r_c is the core radius. The surface luminosity of a cluster steadily decreases with the distance, and the tidal radius is the radius where the apparent surface luminosity falls to zero. Another parameter is the half-light radius r_h and it is the distance from the centre of the cluster where the encircled luminosity has risen to half of the total luminosity. Typically GCs have r_h less than 10 pc with some clusters having larger values, like Palomar13 ($r_h \sim 25$pc).

A correlation between the galactocentric distance and r_h has been observed (van den Bergh et al., 1991) such that metal poor GCs typically located far out are found to be 20% larger than the metal-rich GCs found at smaller distances (Kundu and Whitmore, 1998; Kundu et al., 1999; Jordán et al., 2005). This could point to differences in formation conditions for the two groups of clusters. It has also been proposed that this could be a result of projection effects (Larsen and Brodie, 2003). Another explanation could be the presence of stronger tidal forces at distances closer to the galaxy centre that limit r_t and in turn r_h (Jordán et al., 2005). It is possible that both projection and segregation might be responsible for the observed size trends but more studies are required to understand which effects are more important.

1.4.5 GC mean metallicity and galaxy luminosity

A relation between the mean metallicity of GC system and the luminosity of its parent galaxy was first proposed by van den Bergh (1975). Subsequently more studies have confirmed that such a relation of the form $Z \propto L^{0.4}$, which indicates that the GCs have same the enrichment history as their parent galaxies. The GC system of galaxies is better represented by two subsystems with distinct mean metallicities. Some studies have found the metallicity of metal rich GCs are more closely coupled to the host galaxy than the metal poor GCs, which means that the metallicity - galaxy luminosity relation could be dominated by the metal rich GCs (Forbes et al., 1997).

Peng et al. 2006 studied the optical colors of GCs in 100 galaxies in the Virgo cluster and they found that the colors of both blue and red GCs correlate with the luminosity and color of the host galaxy. Figure 1.6 shows the mean (g-z) color of red and blue GC sub-populations of the galaxies as a function of galaxy absolute magnitude.

The metal poor GCs are found in galaxies across the range in luminosity but the red GC population declines for fainter galaxies. On average, red GC form around 10% of total population of the faintest and bluest galaxies, and around 60 % of brightest and reddest

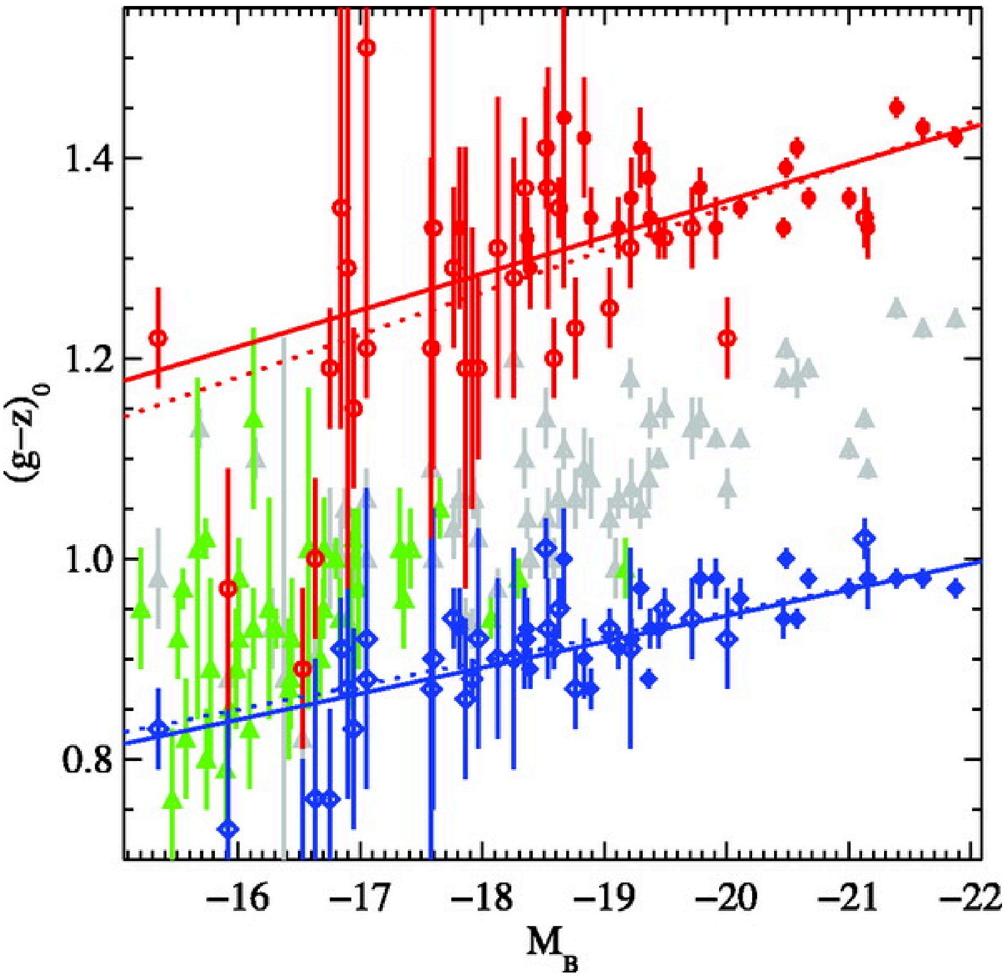

Figure 1.6 The colors of red and blue GC sub-populations of galaxies as a function of galaxy absolute magnitude. The grey triangles show the mean color of the composite GC populations, and the green triangles are mean color of GC population of the faint galaxies that do not show a bimodal distribution and are primarily rich in blue GCs.

galaxies (figure 1.7). Moreover, if the bimodal galaxies are group together with galaxies having unimodal GC metallicities, the metallicity of blue GCs span similar range in metallicity value for all galaxy luminosities, but the typical color of red GC population varies with galaxy luminosity.

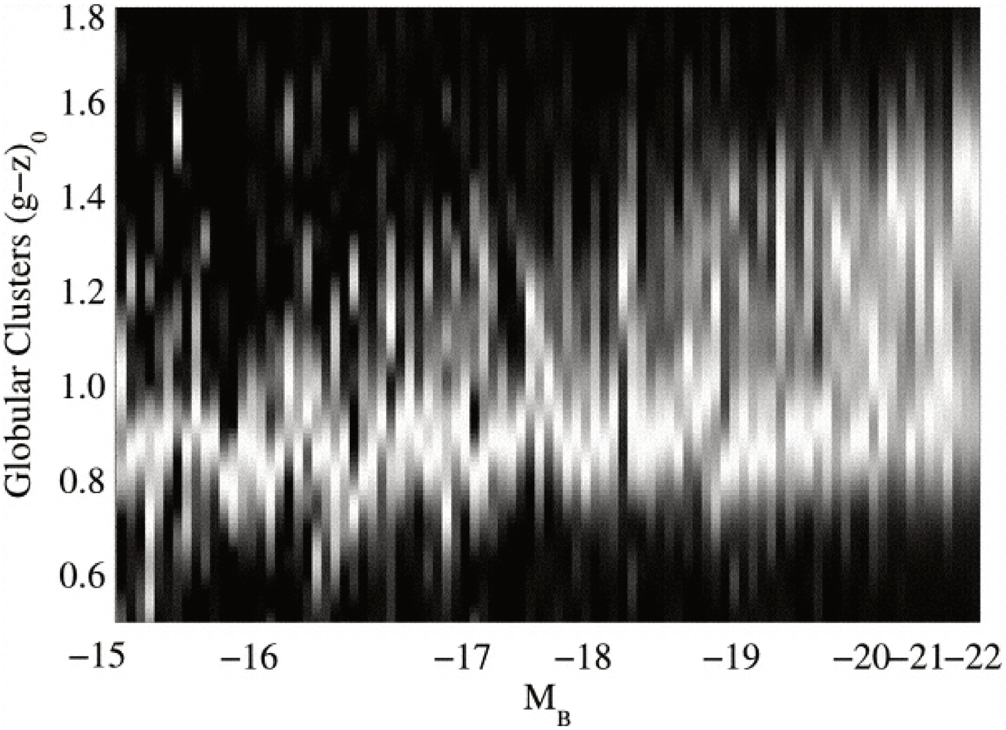

Figure 1.7 KDE distribution of *g-z* colors of GCs ordered by host galaxy absolute magnitude. The color and relative fraction of red GCs is a function of GC luminosity (figure taken from Peng et al. (2006)).

The relationship between GC metallicity and galaxy properties is indicative of the fact that the formation of both the sub-populations are closely linked to their host galaxies. As discussed in some of the GC formation scenarios in section 1.5, the MP GCs find their link to the episode of star formation that occurred early in the universe or shortly after re-ionization, whereas the MR population formation is associated with the formation of bulges and hence their numbers correlate with the mass of the galaxy, reinforcing the narrative.

1.4.6 Globular cluster Luminosity Function (GCLF)

The distribution of absolute magnitudes of globular clusters in a GC system can be approximated by a Gaussian,

$$\frac{dN}{dm} \sim \exp \frac{-(m-m_0)^2}{2\sigma^2} \tag{1.3}$$

where dN is the number of GCs in an apparent magnitude bin dm, m_0 is the turnover magnitude (TOM) and the σ is the width of the Gaussian distribution (Richtler, 2003). The term GCLF is a misnomer since it represents the magnitude distribution of the clusters and not the luminosity distribution. The shape of the GCLF is not a perfect gaussian, but it is peaked, unimodal, and almost symmetric in the V band in most studies and can be approximated by a gaussian function. Secker (1992) performed a maximum likelihood estimate on the GCLF of the MW and the M31 and demonstrated that the best fit is obtained with a t_5 distribution function given by,

$$\frac{dN}{dm} \sim \frac{1}{\sigma}(1 + \frac{-(m - m_0)^2}{5\sigma^2})^2 \tag{1.4}$$

In spite of the difference between the approximate and best fit, the GCLF TOM is very similar irrespective of the fit. The GCLF for MW GCs is shown in figure 1.8 fitted with a gaussian and a t_5 function.

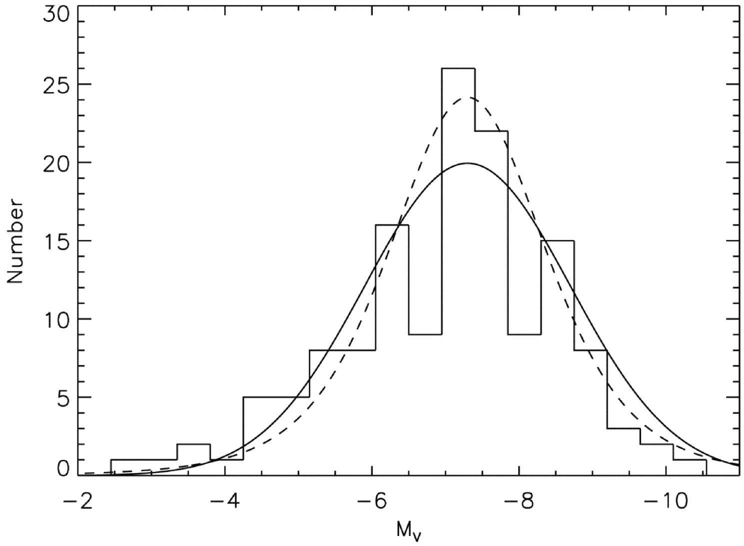

Figure 1.8 GCLF of the Milky Way globular clusters fitted with Gaussian (solid line) and t_5 function (dashed line) (Larsen et al., 2001b).

The typical values for elliptical galaxies is TOM, $m_0 \sim$ -7.5 and $\sigma \sim 1.4$ in the V band, and similar values for Spirals but $\sigma \sim 1.2$ being more accurate. The peak TOM magnitude corresponds to a mass of $\sim 2 \times 10^5 M_\odot$. The GCLF has a universal shape and is similar for different galaxies and the value of the TOM was thought to be the same universally (Hanes, 1977) and is now nuanced (Rejkuba, 2012). The GCLF is well known as a distance indicator on extra-galactic scale, but is only applicable to old GCs. The GCLF depends on the passbands of the observations, as expected in particular when the color distribution is bimodal (figure 1.9) (Taylor et al., 2017). The distances determined from the GCLF are found to be consistent with the distances determined from surface brightness fluctuations. The GCLF as a distance indicator is not very popularly used for spiral galaxies because of the difficulties in probing the GC population of spirals due to the presence of disks, dust lanes etc.

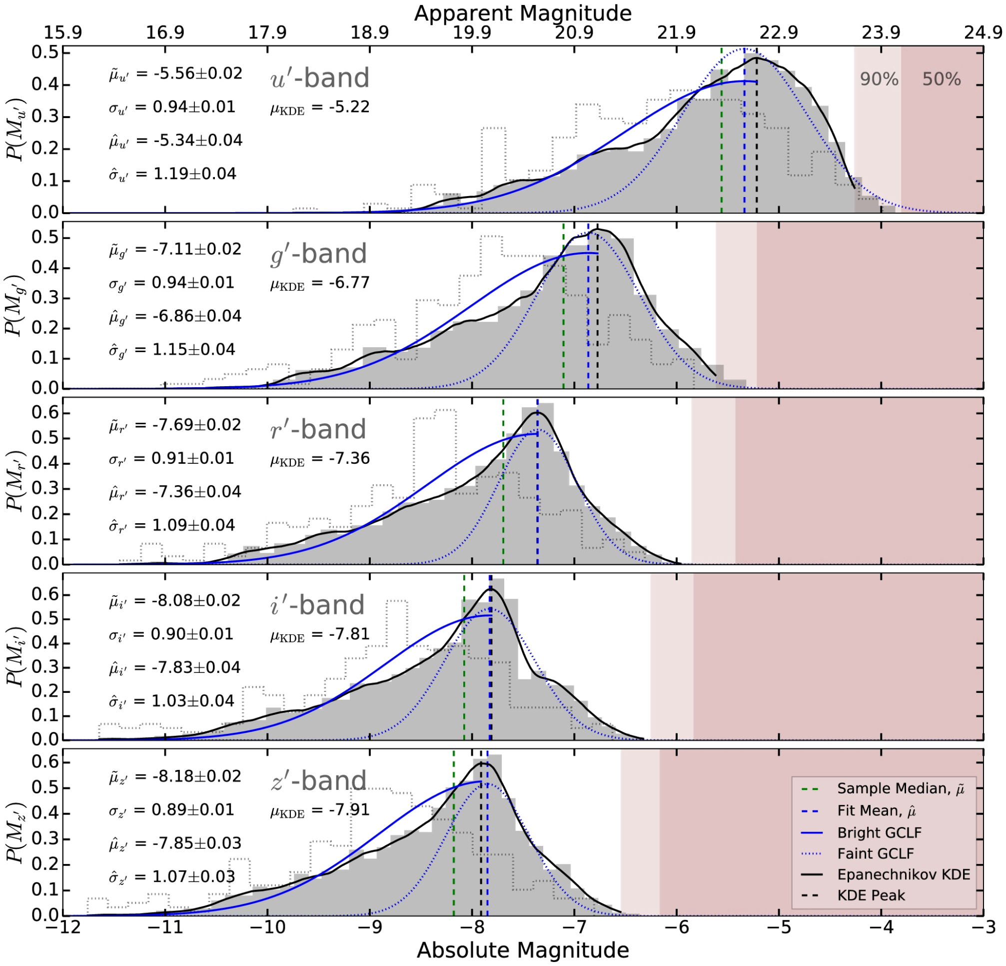

Figure 1.9 GCLF of GCs in Cen A in *u,g,r,i and z* bands. The different colors are the models fitted to bright (solid black curve), faint (solid blue curve) and their corresponding mean and median values (Taylor et al., 2017).

1.5 Formation of the globular clusters

Globular cluster formation in the early universe is not very well understood due to lack of direct observational evidence. We study the cluster formation in the local universe and extrapolate this to understand the formation of the clusters in the high redshift universe. Theoretical models and numerical simulations of the evolution of the gravitational systems in the cosmological framework guides this process. The origin of the GC system of the galaxies can be constrained by studying their integrated colors which are related to their chemical properties and ages. As such, an understanding of the GC system of a galaxy also sheds light on the formation history of the galaxy. In this section we will discuss the theories of formation of resolved GC, and the GC systems of the galaxies.

1.5.1 Formation of GCs as a resolved object

Molecular clouds are the densest regions in the interstellar medium. They are formed majorly from the molecular hydrogen and several other molecules. These clouds are known to have masses that range from $\sim 10^3$ to 10^7 $M_\odot$ and have hierarchical morphologies such that the denser regions are embedded in the less dense regions (Elmegreen and Falgarone, 1996). Globular clusters are formed in the dense regions where hierarchical collapse of giant molecular clouds triggers large scale star formation. The molecular clouds evolve by accreting copious amounts of atomic gas (Fukui et al., 2009). The common paradigm is that they are supported by some agent (thermal pressure, turbulence, or magnetism) against self-gravity and do not collapse all at once. The molecular clouds are supported by small scale, isotropic turbulence while locally they form shocks that can generate density fluctuations. The GMCs are cold and dense and hence reach their Jeans masses more rapidly than warm, diffuse gas (Gómez and Vázquez-Semadeni, 2014). The accretion makes them magnetically super-critical and they can no longer be supported against self-gravity and the cloud becomes gravitationally unstable. Since the cloud is non-uniformly dense it starts to form a cascade of collapses. The denser part of the cloud starts to collapse faster than the less dense parts, with a hierarchical collapsing scale, such that each one is accreting from the next larger scale (Vázquez-Semadeni et al., 2019). This onsets the formation of stars within a molecular cloud, and the bound star clusters are born.

Observationally it is known that the cold gas clouds are shrouded in envelopes of atomic gases, and have radii $\sim$ 10-30 pc. These observations are limited to the Milky Way and other nearby galaxies (LMC, SMC, M31 etc.) (Rosolowsky, 2007; Rosolowsky et al., 2007; Miville-Deschênes et al., 2017). It can be safely inferred that no stars are formed in isolation, and the stellar nurseries give birth to more than one star. However it is not always necessary that these cluster of stars born at the same site continue to survive as bound clusters and some of them get dynamically disrupted within a few Myr (Bressert et al., 2010).

Stellar feedback might play an important role in deciding the fate of the cluster. After being formed in the GMC, stars have the potential to modify their surroundings by means of proto-stellar outflows, photo-ionization, radiation, winds and supernovae (Dale, 2015). The impact of the stellar feedback can slow or quench the star formation (Murray, 2010;

Krumholz et al., 2014; Dale, 2015; Semenov et al., 2017), by expelling the gas out of the system, or initiate subsequent star formation in it by compressing the cloud by via shock-fronts (Koenig et al., 2012; Shima et al., 2017). In denser regions, the stellar wind feedback is not strong enough to remove the gas from the system, allowing retention of gas and possibly aiding the formation of multiple population of stars. Thus, the local environment plays a very vital role in determining the properties of the stellar objects formed.

1.5.2 GC formation at high redshift

The determination of the precise absolute ages of the GCs (see section 1.3.1) is still a challenge, mainly because of the age-metallicity degeneracy, and the ages are known with uncertainties of 1-2 Gyr which translates to the rough spread in redshift between $z \sim$ 4-10. Even then, the trends in the ages and metallicities of the GCs can be used to constrain the formation scenarios and the formation channels of the system and may also be informative about the formation and evolution of their host systems.

A major observational constraint on the formation of the GC systems come from the bi-modality observed in the color distribution in the GC system of some massive galaxies (Zinn, 1985; Gebhardt and Kissler-Patig, 1999; Larsen et al., 2001a; Peng et al., 2006) (see section 1.4.3). The bimodal color is often translated to bimodal metallicity which indicates the existence of two sub-systems in the GC system, the red GCs that are metal rich members, and the blue GCs, the metal poor population with a deficit of clusters in middle range values of the metallicity. In MW and M31 red GCs were found to be slightly younger and brighter than the blue GCs. While some galaxies like the Milky Way exhibit the bimodal population of the GC system, some others, like Andromeda lack this characteristic. Several scenarios have been proposed to address this bi-modal distribution of the GC sysytem.

- ***Formation in dark matter halos***

  Peebles and Dicke (1968) suggested the formation of GCs at a very high redshift in low metallicity medium. At this epoch the Universe has only expanded enough to allow the formation of the GCs but not the large scale structures like galaxies . When the primordial medium was metal poor and the temperature of the over-dense region reached $\sim$ 4000K the Jeans criteria could be achieved for the typical GC masses and sizes (Fall and Rees, 1985; Bromm and Clarke, 2002; Katz and Ricotti, 2014). This collapse is more likely to occur in the potential wells that contain the dark matter, therefore, the issue of the absence of DM in the GCs needs to be addressed. This scenario cannot explain the bimodal metallicity distribution of the GCs and also requires the GCs to be very old.

- ***Merger between galaxies***

  To explain the existence of distinct metallicities in the GC subsystem, Schweizer (1987) and Ashman and Zepf (1992) proposed a two step formation scenario to account for the age difference between the red and blue GCs. The blue clusters were formed at an early epoch when the universe was very metal poor. Due to the universe being denser, the mergers were more frequent and gas rich and thus the mergers would trigger more star formation. The older clusters would enrich their environments which would aid in the formation of the new GCs. This scenario requires gas-rich mergers and assumes that these produce globular clusters efficiently (as compared to small clusters that will be disrupted to become field stars), in order to explain an increase in the specific frequency after the merger. McLaughlin and Pudritz (1994) noted that the scenario struggles to reproduce the very large specific frequencies of cD galaxies in galaxy clusters.

- ***Multiphase collapse***

  In this scenario, proposed by Forbes (1997), the metal-poor clusters were formed during the collapse of the proto-galaxy before the re-ionization. This phase of GC formation was brought to halt as the re-ionization began and quenched star formation. Another phase of the GC formation was triggered in the disk of the galaxy when the ISM becomes dense enough to form stars. In this scenario, the observed kinematics and the distribution of the present day GC system could be fit when the system has a bimodal distribution, but this failed to explain the case of unimodal system of GCs, for instance the Andromeda galaxy.

  Age estimates of the blue MW GCs showed that these GCs were likely formed at $z \sim 6$, which is the end of the reionization (Forbes et al., 2015). The ages of red GCs have a mean value of 11.5 Gyr that corresponds to $z \sim 3$, which is prior to the onset of the disk formation predicted from the cosmological simulations (Agertz et al., 2011; Renaud et al., 2017). This suggested that the reionization was followed by the formation of GCs and is not the likely explanation of the observed bimodality.

- ***In-situ and ex-situ formation*** This scenario of GC formation was proposed by Côté et al. (1998) and Tonini (2013). In this scenario, the metal rich red GCs were formed at the site, while the blue and metal poor GCs were accreted via mergers. The properties of the accreted clusters are complicated because of variety in the properties of the donor galaxies. It is difficult to disentangle the contribution from each donor, and the epoch of the merger as well. This could contribute in smoothing out the metallicity distribution of the donated GCs (Forbes and Bridges, 2010). This scenario is consistent with cosmological simulations of formation of the Milky Way by Renaud et al. (2017).

This formation channel of the GC system of a galaxy is relatively more broadly accepted compared to the other scenarios, such that the metal-poor blue GCs are formed ex-situ in low mass galaxies, whereas the metal rich or the red GCs are formed in-situ within the accreting galaxy Tonini (2013).

1.6 GCs as science drivers

Our understanding of resolved GC populations and their properties comes from the GC system of the Milky Way and of other galaxies that are close to the Milky Way, like the LMC, the SMC, and M31. The GCs that are farther away and cannot be resolved with current technologies are also important to study the properties of the environments they reside in, and to uncover the events from the past. GCs can serve as a specimen for a variety of science cases ranging from their role in understanding the stellar physics to the knowledge of the dark matter content of a galaxy. In this section we will discuss the various science applications of GCs both as resolved and unresolved objects.

1.6.1 Stars and Globular clusters - Probe to stellar evolution

GCs in the Milky Way span a broad range in total mass and integrated magnitudes, ω Centauri being the most massive cluster in our galaxy with a total mass of about 10^6 $M_\odot$ and about 10 million stars while GCs like Pal 13 and AM 4 lie on the other end of the spectrum with masses in the range of 10^3 $M_\odot$. The variety available in the clusters makes them very interesting from a dynamical point of view, and the fact that their population consists of stars in all evolutionary stages but at similar ages and distances makes them even more desirable candidates to validate our understanding of stellar evolution.

In the beginning of the 20th century, Ejnar Hertzsprung and Henry Russell observed and analyzed the basic properties of a number of field stars and for nearby co-moving groups e.g. Pleiades and Hyades, (Russell, 1913; Russell, 1914), see figure 1.10). This work led to one of the most used, and important diagnostic tools, the HR diagram. An HR diagram shows the relationship between the luminosity and the spectral type of the star. These HR diagrams illustrated evidence that the stellar evolution is an orderly process and that the mass and the luminosity of the stars are correlated.

It was a clear evidence from the HR diagram of the Pleiades and Hyades clusters that these clusters have stellar populations that sample a range of stages of the stellar life cycle, and over the years the clusters were dubbed to be homes to simple stellar populations that co-evolve and share similar chemistries. This presented the clusters as ideal test beds to

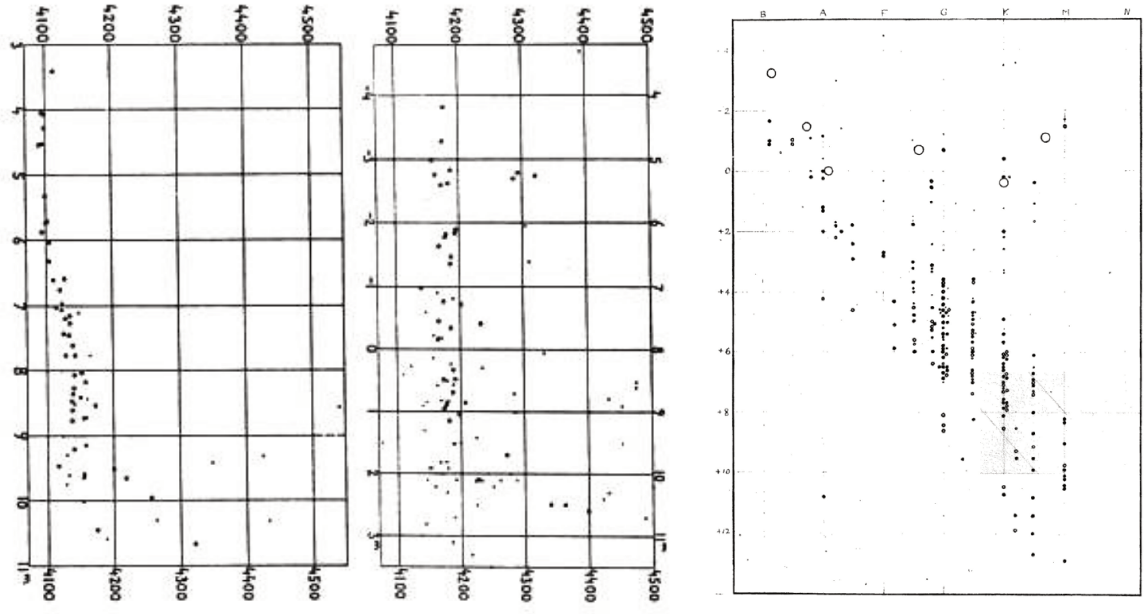

Figure 1.10 The first published HR diagram of the Pleiades and Hyades clusters (Hertzsprung (1911), left and centre respectively), and the field stars (extreme right; Russell (1914)). The vertical axis are the magnitudes with brighter stars on the top, and the horizontal axis is the peak wavelength or spectral type of the stars.

study the life of a star and our understanding of stellar physics. The GCs became the stills that made it possible to understand how the stars evolve at a given metallicity and age over the range of stellar masses. A stitched picture of a number of clusters with varying metallicities and ages facilitated the full picture of the evolution of the stars. This beautifully coincided with a development in the observation instruments at the time, which led Shapley to measure other photometric properties like the distances, sizes, luminosities etc. of several nearby clusters.

To interpret the observations of the clusters, the observations are compared against the theoretical HR diagrams produced from theoretical stellar evolution models. The synthetic HR diagram is obtained based on Monte Carlo simulations that produce pairs of mass and age for a given initial mass function, star-formation history and time interval. In case of globular clusters the star-formation histories are essentially a single peak of star birth followed by passive stellar evolution. Each star is placed in the observed HR diagram. The comparison can give constraints on fundamental properties of the cluster, like age, metallicity, and mass. This can also help in testing and quantifying the various processes that are expected to occur in the stellar interiors and are difficult to measure directly such as rotation of the core, atomic diffusion, gravitational settling, and core overshooting. Part I of this thesis is focused on one such scenario in which we test the performances of empirical stellar libraries against the theoretical stellar library to materialize the impact of atomic diffusion on the HR diagram of the globular cluster NGC 6397 (see Chapter 2). Studies like this make it evident that globular clusters are the way to calibrate our models and refine stellar evolution theories which, in turn are used to interpret the properties of distant galaxies (e.g. Bruzual and Charlot (2003)).

1.6.2 Galaxy evolution and assembly

Understanding galaxy formation and evolution is one of the major astrophysical challenges. It is still not well understood how the galaxies attain their present day morphologies or the form that we see at higher redshift. With a few exceptions globular clusters are ubiquitously found in galaxies of all types dwelling in all kind of environments. Several of their properties are also closely linked with their host galaxies, displaying scaling relations that now/then can serve to characterize new host systems. They are also useful to put constraints on the star formation episodes and the assembly histories of their host environments and efficient tracers of the formation history of early type galaxies, spiral bulges and halos.

- ***GC systems of Early Type Galaxies (ETGs)***

  GC systems of ETGs are the most thoroughly studied because of the relative ease of detecting GCs within such galaxies. ETGs also include the most massive known galaxies and host rich GC populations. Studies of the stellar populations of massive ETGs show that they are usually old ($\sim$ 10 Gyr), metal rich (metallicity equal to or higher than solar metallicity), and have a bottom heavy IMF (Trager et al., 2000; Renzini, 2006; La Barbera et al., 2013). The GC systems of ETGs typically have a bimodal metallicity distribution, and based on empirical relations derived from MW GCs and predictions from theoretical SSP models, the bimodality in color is usually dubbed as bimodality in metallicity distribution. It has also been argued that a bimodal color relation may not necessarily mean a bimodal metallicity (Yoon et al., 2006a) (see section 1.4.3) but the spectroscopic metallicity favors the linear color-metallicity relation (Romanowsky, 2009; Schuberth et al., 2010). It has also been suggested that GC colors-color relations can depend on their environment (Powalka et al., 2016a).

- ***GCs in Late type galaxies***

  The GC systems of late type galaxies are not as well studied as the GC systems of ETGs because of the difficulties in detecting the GCs over bulges and disks in addition to the hindrance caused by the dust internal to star forming disks. At a given luminosity they hosts smaller GC populations as compared to ETGs. Other then the MW the best studied GC system of a late type galaxy is that of the M31. It has a rich sample of 500 known GCs that lie at a distance of 780 kpc. The ages of the GCs could not precisely known from the deep HST CMDs, but the spectroscopic studies suggest that the GCs are typically old. The metallicity distribution spans a broad range but fails to display any hint of substructure in the distribution of metallicity (Caldwell et al., 2011). Tidal features and shell structures are detected around M31 and some of the GCs are associated with these structures which hints at accretion of GCs on the halo of M31 (Mackey et al., 2019). The GC systems of spiral galaxies outside the Local Group have shown the presence of GCs in the disks of the galaxies. These GCs have spatial distributions and properties like rotation that resemble the properties of the disk stellar population of the galaxy. This indicates on the possible formation of the disk GCs within the galaxy and if that is true the disks might have formed at a high redshift (z>2).

- ***GC population of Dwarf galaxies***

  The GC populations of dwarf galaxies are interesting to study for a number of reasons. The dwarf galaxies and their GCs can possibly be the building blocks of the halo of more massive galaxies. In the local group, 14 dwarfs are known to have GCs, and the census is more likely to increase with better resolution and wide field surveys. The most massive dwarf galaxy in our vicinity is the Large Megellanic Cloud (LMC) and it has 16 known GCs. Spectroscopic properties of these GCs show that they are old and metal poor which is very typical of GCs in dwarf galaxies. The GC systems of dwarf galaxies can give an insight about the dark matter content of these galaxies (Cole et al., 2012; Orkney et al., 2019).

One of the most widely accepted theory that explains the current state of the universe and try to establish the connection between the universe at its infancy and the current state is the *Lambda Cold Dark Matter* or the ΛCDM theory. According to the ΛCDM theory the baryonic structure of the universe continues to merge and grow under the influence of gravity. A very generic picture of the formation of elliptical galaxies and their GC systems under a λCDM regime starts with the formation of the first generation of stars that formed and then died while enriching the interstellar medium. This was the *in-situ* phase of the galaxy formation, and during this phase the progenitors of present day globular clusters were formed. These systems were formed in the gas rich disks of galaxies and went on to become the metal rich red GC subpopulation of the galaxy. The blue or metal-poor GCs were formed preferentially on low mass galaxies where the enrichment wasn't that common.

These galaxies were later accreted by the more massive galaxies and will form the halo population of the galaxy. This represents the *ex-situ* phase of galaxy formation. A similar scenario is also expected for the formation of spiral galaxies. However, the disk of MW and M31 are not very old and have ages ~ 5 Gyr which indicates that the formation of GCs in their disks cannot be very old.

The GC system colors and their kinematics are some of the properties that helped establish possible links between a galaxy's past and its present. The theoretical and observational studies on the GCs are progressively trying to connect the dots between the properties of the observed GC system and formation of the galaxy.

1.6.3 Dark matter content of a galaxy

All galaxies reside in dark matter halos, and the properties and history of these can be studied indirectly. A recent discovery of the relationship between the number of GCs in a galaxy and the mass of its DM halo has provided us with a means of estimating the mass of the DM halo. Unlike the stellar population of a galaxy, the number of GCs in a galaxy are independent of the type and environment of the galaxy and is one of the basic measures of a GC system in a galaxy. In theory, the total number of GC in a system, (N_{GC}) is estimated by counting GCs upto the peak of the globular cluster luminosity function (GCLF), and assuming a normal distribution the number of GCs is doubled to account for the missing fainter GCs.

It has been shown that the N_{GC} correlates positively with host galaxy's stellar mass M_*. In the left panel of figure 1.11 (taken from Hudson et al. (2014)), the plot shows the correlation between the galaxy stellar mass and the number of GCs hosted by the galaxy. The positive correlation is not surprising, as the more stars a galaxy will have the more GCs it will have formed. However, the plot shows the relation is not entirely linear, and low mass and high mass galaxies appear to have a better efficiency of GC formation than intermediate mass galaxies. A similar trend with galaxy mass is seen in the specific frequencies of the GCs (section 1.4.1).

The right panel shows the plot of number of GCs and the ha;p mass of the galaxy. The halo mass was estimated from the gravitational effects of the dark matter. The relationship between M_{halo} of galaxy and its N_{GC} is linear. This is an indication that a linear relation exists between the number of GCs a galaxy hosts and its dark matter. The origin of this relation is argued to have emerged from the central limit theorem and galaxy merging and it predicts that the merging of low and high mass halos and their galaxies give rise to average halo properties. The relationship between the N_{GC} and M_{halo} can be used to infer the mass of the dark matter in a galaxy by measuring the size of its GC system. Observationally that

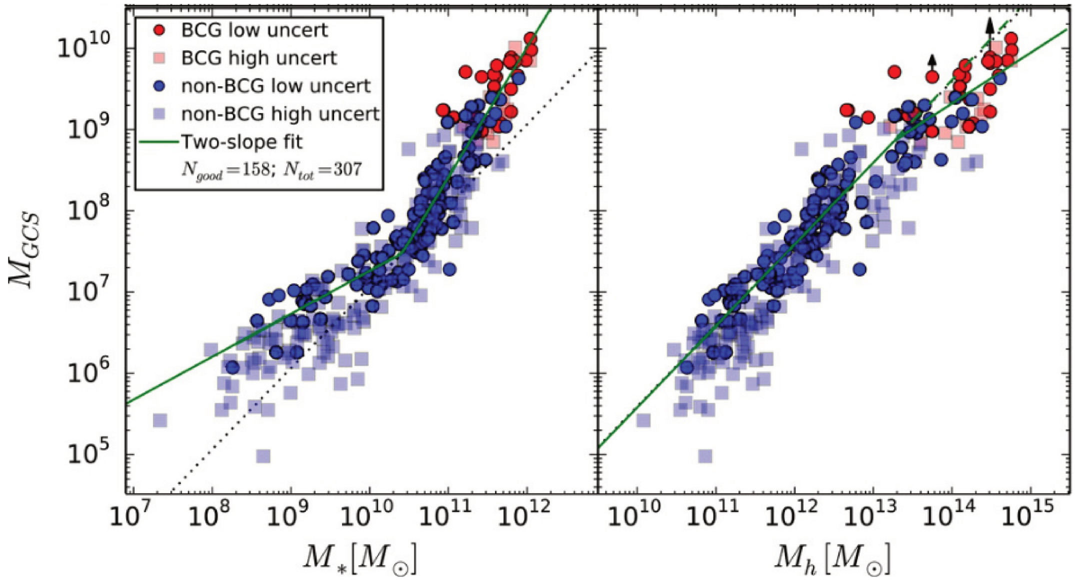

Figure 1.11 The plot shows relationship between the number of GCs and the stellar mass of the galaxy (*left*), and the relation between its halo mass (*right*).

is much easier and cheaper than obtaining spectra for these GCs in order to derive M_{halo} from the kinematics of the GC system. The DM halo masses for UDGs inferred from their GC population has been found to be consistent with other measurements from GC dynamic and stellar velocity dispersion.

1.6.4 GCs as distance indicators

Ideally, a standard candle should be bright, and commonly found in the universe and should have exactly the same absolute magnitude everywhere. Old globular clusters possess these properties (not individually but as a group), they are found in all types of galaxies, they are bright and only overshadowed by bright galaxies and supernova and can therefore be used as good distance indicators. The luminosity distribution of globular clusters is found to have a similar distribution in all galaxies and it peaks at an absolute magnitude of $M_V \sim -7.5$. This peak of the GCLF has been established as a standard distance indicator. The intrinsic accuracy of the method is estimated to be around ~ 0.2 mag (Rejkuba, 2012) which puts it at par with other standard candles.

The distance determination using GCLF is relatively simple and observationally less expensive. The GCs of the target galaxies need to observed upto sufficiently deep limiting magnitude, and compare the luminosity function with known magnitude distribution. Indeed, at 30 Mpc the peak of the GCLF is already shifted to $m_V \sim 25$ and locating the peak requires measurements that go 1-2 magnitudes deeper. The GCLF standard candle is calibrated against MW GCs based on accurate cluster distances which are derived from primary distance indicators. The turnover magnitude (TOM) (see section 1.4) is the value which is compared with the TOM of the MW or the M31 GCLF TOM. The estimates of the standard values are based on the RR Lyrae luminosity scale for the MW and Cepheid distances to the M31. The most common application of the distance measurement using GCLF is in early type galaxies. They have a rich GC population which is relatively easier to detect as compared to the spiral galaxies where the problem due to extinction and crowding is severe. GCLF measurements are also used to test the distances measured by other means like Cepheid distances, measuring distance using tip of RGB, surface brightness fluctuations etc. The GCLF TOM is also used in the early 60s to determine the value of Hubble's constant, H_0. Using individual cluster magnitudes around M87 the value of Hubble constant was determined to be 68 ± 10 km s^{-1} Mpc^{-1} (van den Bergh, 1985). It has been argued that the accuracy of this method depends on the environment of the galaxy (Villegas et al., 2010). It is recommended to use near-IR magnitudes and apply the method to metal-poor GCs.

1.6.5 Link between GCs and Ultra compact dwarf galaxies, and Nuclear star clusters

- *Nuclear star clusters (NSCs)*

  While discussing star clusters, it would be unfair to not mention the special category of clusters that consists of the nuclear star clusters. Nuclear star clusters are the dense and massive star clusters found at the center of most galaxies (figure 1.12) (Côté et al., 2006; Seth et al., 2006; Neumayer, 2012). They become rare only in the brightest elliptical galaxies and in the lowest luminosity dwarf galaxies (Eigenthaler et al., 2018; Sánchez-Janssen et al., 2019a). They are luminous and compact and are usually denser than GCs. They are found in galaxies with different morphological types which raises questions if they are formed and evolve in similar ways or if it depends on their host environments. Two most favored formation scenarios are suggested for the formation of NSCs. In the first proposed scenario which is called the *Globular cluster infall and merging* the massive clusters migrate to the centre of the galaxy and merge to form NSC (Tremaine et al., 1975). The second proposed channel is called the *In-situ* formation and it argues that galactic centre being the deep potential well is the place where most large-scale gas transportation takes place and the accumulated gas triggers the formation of massive stars that forms the NSC (Milosavljević, 2004).

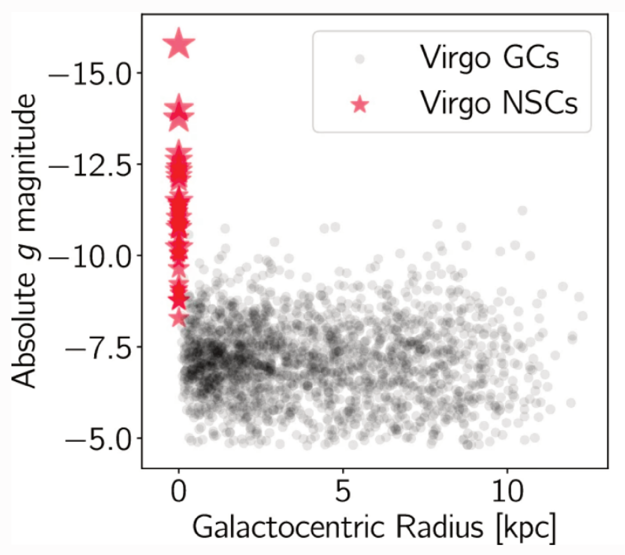

Figure 1.12 The diagram compares the magnitude of the NSCs and GCs in the Virgo cluster as a function of their distance from the centre of the parent galaxy. The NSCs are always concentrated in the centre of their hosts and are in general very luminous. (figure from Neumayer et al. 2020)

- *Ultra Compact Dwarf galaxies (UCDs)*

  Nearly two decades ago a new class of astrophysical objects was discovered in the Fornax galaxy cluster (Hilker et al., 1999; Drinkwater et al., 2000; Phillipps et al., 2001). These objects appeared to be the transition objects between GCs and early type galaxies. They had luminosities that were comparable with dwarf elliptical galaxies (dE) and sizes much smaller than typical dEs but larger for a normal globular cluster. Hence they were names ultra compact dwarf galaxies (UCDs). UCDs are characterized by old stellar populations and have typical radii of 10-100 pc and masses that range from $10^6 - 10^8 M_\odot$.

  In comparison with GCs, the mass-radius relationship between the GCs and UCDs is different and this indicates the possibility of the two having different evolution histories, while the continuous transition in sizes can mean a similar origin scenario (Dabringhausen et al., 2008). As compared to GCs, UCDs typically have twice as high an M/L ratio (Drinkwater et al., 2003) which can either mean that they possess dark matter or they are home to stellar population that have initial mass function different from the canonical MW resolved GCs.

  Several formation scenarios are suggested for the formation of UCDs. One possible scenario proposes that UCDs could be most luminous GCs forming the bright end tail of the GCLF (Mieske et al., 2002), or they could be a result of mergers of massive clusters (e.g. - Fellhauer and Kroupa (2002)). In another proposed scenario they are thought of as the nucleus of nucleated galaxies that had their low brightness envelopes removed during tidal stripping (e.g. Bekki et al. (2001)). Bassino et al. (1994) suggested that a nucleated dwarf galaxy undergoing tidal stripping would lose all its material except the most robust members of the galaxy, that is its nuclear star cluster, and the resulting object would be a UCD. But in order to explain the high mass to light ratio observed in UCDs which is likely to be absent in NSCs if they are indeed formed from GCs there have to be other explanations. It is widely accepted that the possibility of multiple formation channels for UCDs cannot be denied (Mieske, 2006; Brodie et al., 2011; Norris and Kannappan, 2011)

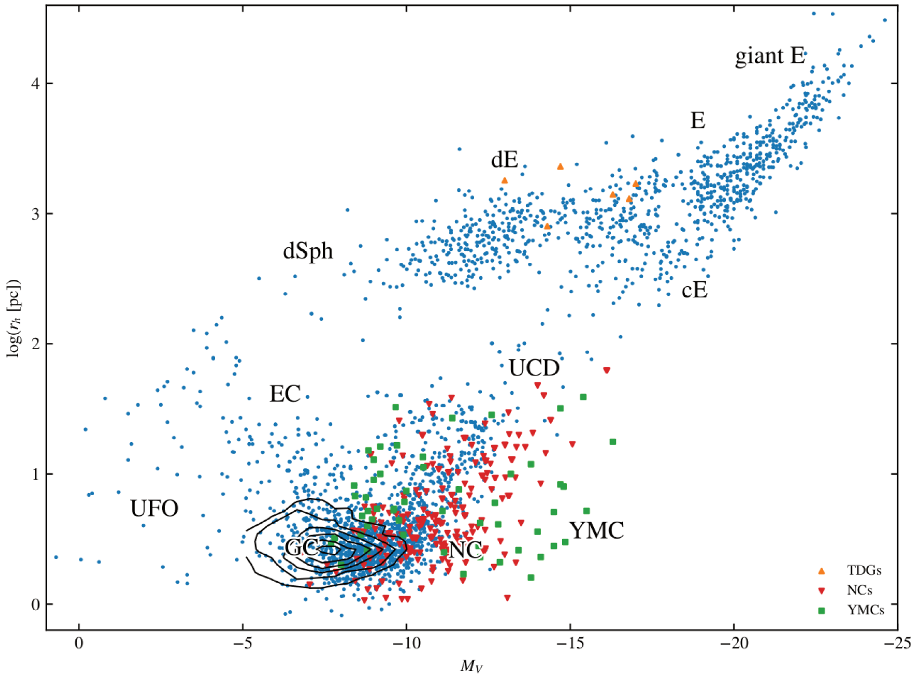

Figure 1.13 Relationship between luminosity and the size of dynamically hot stellar objects. The x-axis has the absolute V band magnitude plotted against half-light radius of the objects for different classes of objects. The GCs are taken from Jordán et al. (2009) and are represented by the density contours (Figure courtesy - Renaud (2018)).

1.7 Observational Techniques

The observation strategies adopted to study star clusters can be divided into two kinds, the methods adopted for resolved star clusters, that is clusters with distance < 1 Mpc, and methods adopted for unresolved star clusters. Resolved clusters can be studied using photometry

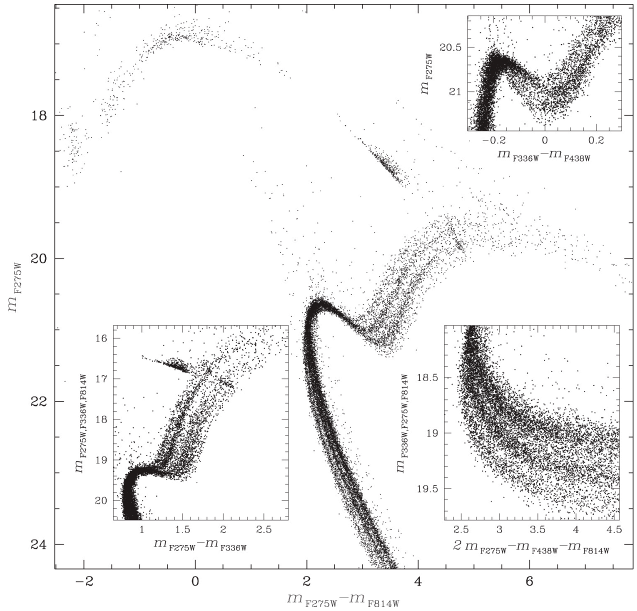

Figure 1.14 Color-magnitude diagram of NGC 2808 highlighting the multiple sequences along main sequence, red-giant and sub-giant branch respectively (Milone et al., 2015).

or spectroscopy of individual stars, and these methods can be used for GCs in the Milky Way and other galaxies in the Local group. The spatially unresolved clusters are observed using photometry and spectroscopy for their integrated luminosity. The techniques for observation are similar but the analysis is different for the spatially resolved and unresolved clusters.

1.7.1 Methods for spatially resolved clusters

Photometry

Photometry is a very common method to measure stellar fluxes of resolved cluster stars and it finds wide application in constructing the color-magnitude diagrams, which are used to estimate other cluster parameters like their age, metallicity, and distance. Color-magnitude diagrams are also instrumental in detecting the multiple stellar population in GCs. Figure 1.14 shows the color magnitude diagram of the galactic GC NGC 2808 constructed using UV and visible magnitudes from *HST* UVIS/WFC3 and ACS/WFC. The plot shows various combinations of magnitudes and colors that highlight the presence of multiple sequence of stars in the GC in various evolutionary stages.

Stellar spectroscopy

Spectroscopy is often employed to study the chemical abundances of cluster stars with the help of high resolution spectra. A medium resolution spectrum can be used to estimate atmospheric parameters of stars (T_{eff}, log g, and [Fe/H]). The spectra of the stars are compared against stellar libraries to determine these parameters. Various stellar models are available in different wavelength ranges that can be used for determination of the abundances and cluster parameters. The available stellar libraries are typically either theoretical libraries that use synthetic stars, and empirical stellar libraries that consist of real stars with known atmospheric parameters. There are advantages and disadvantages to both the libraries. In Chapter-2 we will discuss the determination of cluster atmospheric parameters using empirical stellar libraries and compare the obtained values with the ones obtained from the theoretical stellar libraries.

Spectroscopy finds frequent application in determining radial velocities of stars in clusters. The *Hubble Space Telescope* and *GAIA* has revolutionized the field by providing radial velocities and parallaxes for all the known GCs in the Milky Way. This led to providing precise orbits of the GCs and better estimate of the mass of the Milky Way. Recently, the combination of adaptive optics with 3D spectrographs have made it possible to measure spectra from the ground in crowded areas previously inaccessible (e.g. the instrument MUSE on the Very Large Telescope of the European Southern Observatory).

1.7.2 Methods for spatially unresolved clusters

The observation of the unresolved GC population means capturing the integrated light of the GC. These are often interpreted using the stellar population synthesis models.

Integrated Photometry

Photometry of extra-galactic sources using broad-band filters in various bands is used to measure integrated flux of a GC. Optical colors are capable of giving useful information about the age and metallicity of the objects but they suffer from age-metallicity degeneracy (Worthey, 1994). But using near-UV and near-IR colors can help break the degeneracy. The colors that span a broad range in electromagnetic spectrum are known to be very effective in selection of GC in extra-galactic field. We will discuss this in detail in Chapter-3. The magnitudes in various apertures based on the quality of the data, can be used to mimic the function of various other parameters like size of the GCs. Several elaborate studies on extra-galactic GCs at larger distances are based on photometry where spectroscopy is relatively inefficient and observationally expensive. A large part of this thesis is based on study carried out using photometric data in the Virgo cluster of galaxies which lies at a distance of 16.5 Mpc from us.

Integrated spectroscopy

Integrated spectra of GCs are useful in determining the chemical abundance ratios in addition to velocity measurements. Line strengths in the spectra can be compared against the model grids or a full spectrum fitting that can help estimating the metallicity of the clusters.

In principle, the age of a GC can also be estimated from spectra of GCs. The lines that are sensitive to the age of a GC are the Balmer series in absorption (Hα, Hβ, Hγ, etc.). The Balmer lines are sensitive to temperature and vary in strength with the location of main-sequqnce turn off (MSTO). There are still some challenges in modelling the hot population of GCs that also contribute to the strength of Balmer lines, such as horizontal branch stars and blue stragglers. This introduces large uncertainties in age determination specially for metal-poor GCs.

1.8 Motivation and outline

In this chapter we tried to cover some of the important aspects of globular cluster science, and it is still far from comprehensive. But it is clear from what we know about these deceptively simple looking astrophysical objects that they are truly complicated and mysterious. An understanding of GCs is also monumental in understanding the bigger pillars of the universe, like galaxies, and smaller bricks that form these pillars that is the stars.

1.8.1 Stellar libraries

Resolved globular clusters in our galaxy are home to tens of millions of stars and based on their initial masses these stars can be found in different stages of their evolutionary lifetimes. This makes the globular clusters an ideal site to study the stars and testify out theoretical understanding of their evolution. In the first part of this thesis we take advantage of this very fact that GCs are host to stars in all evolutionary stages to test the performances of stellar libraries. We use spectra of $\sim$ 6000 stars in a galactic globular cluster, NGC 6397 and estimate their atmospheric parameters using two empirical stellar libraries. We compare these values with the values of atmospheric parameters estimated in another work using a theoretical stellar library. We present the differences between the various estimates and highlight the problem with the consistency between the different stellar libraries. These stellar libraries are the standard data that are used to derive the physical parameters for observed stellar systems, and it is of prime importance to know the shortcomings of the libraries being used and if possible device methods to minimize these shortcomings.

1.8.2 Extra-galactic GCs and their color-environment relationship

One of the ways to bridge the gap between the standard libraries and real data is to compare the predictions of the simple stellar population (SSP) models with approximate simple stellar systems, that is the globular clusters. All our present empirical libraries are devised, for obvious reasons, from galactic stars. It is important to assess how well or not the extra-galactic simple stellar system agree with the models we have. In some previous work on extra-galactic GC system it has been found that the color-color distribution of the GCs can be a function of their environments (Powalka et al., 2016b). In the second part of the thesis we do a similar analysis for the GC system of M49, one of the most massive elliptical galaxies in the Virgo cluster. It deals with the near-IR photometry in the fields around M49 and uses the color-color information of the objects to identify globular clusters. In the later part of the thesis we will study the relationship between the colors of the GCs and their environment.

1.8.3 Outline

In Chapter-2 we discuss the atomic diffusion in stars and its theory. Atomic diffusion is expected to change the surface abundances in stars and its effect is seen in the main sequence turn off (MSTO) stars where the metals sink to the bottom and consequently lowers the surface metallicity of the MSTO stars. We use two empirical libraries called ELODIE and MILES to estimate the atmospheric parameters of $\sim$ 6000 stars in the GC NGC 6397 using medium resolution MUSE spectra. In this chapter we compare the trends in metallicity seen in the H-R diagram predicted by the two empirical libraries with the trends predicted by theoretical library GSL adop ted from a previous work.

Chapter-3 transitions to the second part of the thesis and this chapter explains the data reduction of near-IR data in the 9.5 square degrees around M49 and $\sim$13 square degrees in the intracluster region between M87 and M49, and extraction of GCs in the survey area. We describe the survey and data acquisition, followed by first pass of data reduction at the CASU (Cambridge Astronomy Survey Unit) and the subsequent background subtraction performed by us. We adopt the optical data for our field from CADC archive to cross-match it with the objects detected in the near-IR bands. We also describe the galaxy subtraction of M49 and object detection in the galaxy subtracted field in the near-IR as well as the optical bands. The chapter also discusses the photometric and astrometric data calibration and other other additional steps towards making of the catalog of objects in the field and finally the catalog generated for the field.

In Chapter-4 we describe the selection of globular cluster candidates in the field using the *uiKs* diagram (Muñoz et al., 2014). These GC candidates are subjected to various tests that uses limits in magnitudes and morphological parameters derived using the information in the optical bands to reduce the contamination from the stars and the galaxies in the sample. We further divide this sample into groups that are classified according to their environments.

In chapter-5 we discuss the completeness and contamination in the GC catalog by comparing our sample with the ACSVCS GC data in the field and with a sample of spectroscopically confirmed GCs around M49. In this chapter we also talk about the color distributions of GCs that belong to different environments followed by their color-color distribution. We compare the color-color trends of different groups and with the GCs of M87. We conclude the chapter with discussion on possible reasons for the observed differences.

In chapter-6 we summarize the thesis.

1.9 Résumé

L'univers est un endroit extrêmement mystérieux et les humains sont des créatures curieuses. Nous avons utilisé les photons dans toute la gamme du spectre électromagnétique qui nous parvient, afin d'exploiter toutes les informations qu'ils peuvent contenir. Cela nous a conduit à découvrir une grande variété d'objets extraterrestres, qui font tous partie de cet immense puzzle énigmatique que nous essayons de comprendre. Au fil du temps, l'astronomie a connu un afflux révolutionnaire de données de haute qualité, rendu possible par l'amélioration des télescopes terrestres et spatiaux dans toutes les longueurs d'onde. Les progrès réalisés dans le domaine de la science des données et de l'apprentissage automatique y contribuent également. En tirant parti de tous les outils à notre disposition, nous sommes en mesure de découvrir de plus en plus de secrets du cosmos. Les amas globulaires, ou GC comme nous les appellerons de temps en temps dans ce manuscrit, constituent une partie petite mais importante de cette grande image et une grande partie de ce travail au centre de la scène.

La distribution des étoiles dans un amas globulaire est généralement de forme sphérique, ce qui leur a valu leur nom. Un amas globulaire typique peut abriter des centaines de milliers d'étoiles dans une région relativement petite de l'espace. Leur rayon extérieur typique est de l'ordre de quelques dizaines de parsecs. La figure 1.1 montre un amas globulaire typique, NGC 6139 qui tourne autour de la Voie lactée.

Comme les GC sont les plus anciennes reliques d'un système astronomique, tel qu'une galaxie ou un amas de galaxies, et qu'elles conservent la signature des conditions et de l'environnement dans lesquels elles sont nées, on les appelle parfois les fossiles de l'astronomie.

Les GC ont été très populairement surnommés les systèmes stellaires simples, une notion qui s'est avérée être un euphémisme avec l'évolution du temps et de plus en plus de progrès dans le domaine.

Mais en plus d'être les membres d'un système plus grand, les GC sont intéressants en eux-mêmes. La population stellaire résolue d'un GC est un site magnifique pour trouver des étoiles à tous les stades de l'évolution. Les GCs ont donc servi de laboratoires pour tester la validité de notre compréhension de la physique stellaire. Avec leurs formes régulières et leur symétrie impeccables, les GCs cachent à la vue de tous leur véritable nature colorée. Dans les prochaines sections, nous aborderons brièvement divers aspects d'un CG en tant qu'entité et de sa population stellaire complexe, ainsi que les CG en tant que partie d'un système plus vaste.

1.10 Définition des amas globulaires

Les amas d'étoiles couvrent un large éventail de masses et de tailles, et se distinguent des associations stellaires et des groupes mobiles par le fait que les amas sont des systèmes liés gravitationnellement. En ce qui concerne la distinction entre un amas d'étoiles et les galaxies, il était auparavant admis que le premier était contenu dans l'autre, de sorte qu'une définition hiérarchique des GC peut être dérivée. Mais certaines galaxies comme Aquarius et Tucana n'hébergent aucun amas (Forbes et al., 2000) et certaines galaxies naines ultra-faibles ont moins d'étoiles que les GC massives (Belokurov et al., 2007). Cela a nécessité une révision de cette définition d'un GC.

Les amas de la Voie lactée sont généralement classés en amas globulaires (GC), qui se trouvent dans le halo, et en amas ouverts (OC), qui se trouvent dans le disque. Ces amas étaient auparavant considérés comme ayant des gammes de masse et des âges distincts, mais avec les nouvelles données, ces distinctions ont commencé à s'estomper. Les GC sont un type d'amas d'étoiles et sont généralement très vieux et plus peuplés que leurs cousins plus jeunes, les amas ouverts, qui sont également beaucoup plus petits en taille et en étendue. Dans la Voie lactée, les GC étaient traditionnellement définis comme des amas d'étoiles trouvés dans le bulbe et le halo d'une galaxie ayant des masses $> 10^4$ $M_\odot$ et âgés de plus de 6 Gyr. Avec l'étude complémentaire du système GC d'autres galaxies, nous avons appris l'existence de GC beaucoup plus jeunes (Kharchenko et al., 2013). La métallicité des OCs se chevauche également avec celle des GCs dans le disque épais de la MW avec des valeurs de [Fe/H] $>$ -0.8 (Zinn, 1985). Les âges au sein de la population stellaire dans les GCs sont généralement très similaires avec un petit écart. Une différence importante entre les autres types d'amas et les amas globulaires est que les étoiles dans la plupart des GCs montrent une anti-corrélation typique entre les abondances des éléments légers et sont l'hôte de multiples populations stellaires (Renzini, 2013; Bastian and Lardo, 2018). Tous les GC présentent des modèles tels que les étoiles qui ont accès à He, N et Na et sont appauvries en O et C.

Une définition précise d'un amas globulaire, reste donc insaisissable à ce jour. Une définition très naïve des amas globulaires serait alors un système d'étoiles en co-évolution liées gravitationnellement qui partagent une chimie similaire mais pas identique avec certaines tendances particulières dans leurs abondances en éléments légers. Cette définition est loin d'être complète ou même exclusive, mais elle fonctionne dans le contexte actuel, c'est pourquoi nous adopterons cette définition pour les amas globulaires dans ce travail. Puisque nous avons choisi cette définition d'un GC, nous allons décrire brièvement dans la section suivante les propriétés de l'objet qui est identifié comme un GC avec la définition ci-dessus.

1.11 Amas globulaires résolus - GCs dans la Voie lactée et son voisinage

Les amas d'étoiles dans la Voie lactée, les nuages de Magellan et M31 peuvent être résolus jusqu'aux étoiles individuelles avec la résolution du *Télescope spatial à bulle*. C'est un peu plus compliqué qu'indiqué, et la résolution des étoiles est fonction de la luminosité et de l'encombrement de la région étudiée. Dans les cas où les étoiles peuvent être résolues, le CMD de ces étoiles peut fournir une estimation directe d'un certain nombre de propriétés de l'amas. Les amas globulaires de la MW sont les mieux étudiés en raison de leur proximité avec nous.

En 1918, lorsque Harlow Shapley a mesuré les distances aux GCs connus à l'époque en supposant leur distribution sphérique, il a découvert que la Voie lactée était beaucoup plus grande qu'on ne le pensait. Il a également découvert, à partir de la distribution spatiale des GC connus, que nous ne sommes pas le centre de l'univers. Selon un recensement effectué en 2010 par Harris (1996) (mis à jour par Harris (2010)), il existe au moins 157 GC de la Voie lactée, dont la plupart résident dans le halo de la galaxie. Il s'agit peut-être d'une image biaisée, car tout GC situé dans le disque ou le bulbe de la galaxie sera masqué par la poussière galactique qui se trouve entre nous et le centre de la galaxie. La figure 1.2 montre une distribution des GC connus de MW. La concentration des GC au centre du graphique est une indication évidente du centre de la galaxie. Les GC de la Voie lactée sont vieux de 13 ans avec un écart d'âge d'environ 5 ans (Carretta et al., 2000).

La Voie lactée abrite des GC dont les masses et les magnitudes intégrées sont très variées (Meylan and Heggie, 1997). Alors que la plupart des GC sont situés à moins de 20kpc du centre de la galaxie, le GC le plus éloigné connu de la Voie lactée est Leavens-1, situé à

145kpc du centre de la galaxie (Laevens et al., 2014). Le système de GC de la MW est divisé en deux sous-groupes, les GC qui se trouvent à moins de 10 kpc du centre galactique sont classés comme les GC du halo interne/bulge, tandis que les GC qui ont des distances $>$ 15 kpc sont les GC du halo externe (Kinman, 1959; Zinn, 1985; Armandroff, 1989). La population du halo est typiquement pauvre en métaux et montre peu ou pas de rotation, tandis que la population du bulbe est relativement riche en métaux et a des vitesses de rotation compatibles avec celles des étoiles du disque. Ces propriétés sont souvent liées à l'origine de ces populations de GCs, comme nous le verrons dans les sections suivantes, les GCs riches en métaux sont supposés s'être formés in-situ tandis que les GCs pauvres en métaux sont très probablement acquis par la Voie lactée lors d'épisodes de chute et/ou d'accrétion (Mackey and van den Bergh, 2005; Zinn, 1978; Zinn, 1993) La distribution de la métallicité du système GC de la Voie lactée montre une distribution bimodale avec des pics pour les sous-populations GC MP et MR à [Fe/H] $\sim$ -1,59 et -0,55 respectivement (Cote et al., 1999).

Les estimations de l'âge des GC à partir des CMD profonds *HST* Les CMDs révèlent que la majorité des GCs sont plutôt vieux avec des âges supérieurs à 10 Gyr (Marín-Franch et al., 2009; Vandenberg, 2003), et en termes de décalage vers le rouge, ces GCs ont été formés à $z>2$. Ceci n'est pas vrai pour tous et certains des GCs ont des âges plus jeunes, par exemple, Palomar 12 et Terzan 7 qui ont des âges $\sim$8 Gyr.

La relation âge-métallicité (AMR) pour les GCs (Leaman et al., 2013) montre que les GCs riches en métaux sont plus jeunes en moyenne. Cette observation peut être expliquée par le fait que les étoiles massives les plus anciennes, qui meurent plus tôt et enrichissent le MIS, rendent la génération suivante d'étoiles riches en métaux.

Dans la figure 1.3, l'AMR des GCs est superposé aux lieux d'AMR attendus des galaxies naines de notre voisinage (WLM, et nuages de Magellan) et du bulbe MW (région en pointillés verts). Le graphique montre que les GC pauvres en métaux sont plus cohérents avec l'AMR des galaxies naines du voisinage et il est plus probable que ces amas aient pu être accrétés par les galaxies naines. C'est un scénario commun accepté pour la formation de la plupart des galaxies massives et de leurs systèmes GC.

En plus des GC du MW, les systèmes GC les mieux étudiés comprennent les GC des nuages de Magellan qui ont pu être résolus en raison de leur proximité avec le MW, et M31 qui a également pu être partiellement résolu. M31 est presque aussi massif que le MW (Evans and Wilkinson, 2000; Watkins et al., 2010) mais il héberge 3 fois la population de GC du MW ($\sim$ 400-450) (Barmby and Huchra, 2001). Certaines des propriétés de la population de GC de M31 sont similaires à celles des GC de MW ; par exemple, les deux hébergent une sous-population étendue de halo et une population de disques rotatifs plus concentrée au centre. Le système GC de M31, cependant, ne présente pas la distribution bimodale évidente des couleurs qui pourrait indiquer des épisodes plus courts de fusion et de chute.

Contrairement aux GCs de MW, les amas du LMC couvrent une large gamme d'âges et la distribution d'âge des GCs montre le fameux écart d'âge entre les vieux sous-systèmes GC et ceux d'âge intermédiaire (Jensen et al., 1988). Les amas des LMC ont des GC d'âge intermédiaire dont l'âge est ~ 3 Gyr. D'autre part, le SMC n'a qu'un seul vieux GC mais une distribution d'âge plus continue entre les vieux et les jeunes amas (Mighell et al., 1998).

Dans la section suivante, nous discutons des propriétés des amas globulaires résolus, dont la connaissance est principalement basée sur les GC de la Voie Lactée, et les GC des galaxies voisines aidés par des simulations numériques. Elle est suivie par la discussion des propriétés générales des systèmes d'amas globulaires dans leur ensemble.

1.12 Propriétés des GC résolus

1.12.1 Ages

La connaissance des âges des GCs dans l'univers permet d'établir des contraintes sur les principaux épisodes de formation d'étoiles dans l'univers. Couplés à leurs métallicités, ils fournissent une clé pour comprendre les principales époques de formation d'étoiles dans l'Univers. Les GCs sont typiquement plus vieux que 1 Gyr (comparé aux amas ouverts qui sont généralement plus jeunes) et parfois ils sont des survivants de l'univers primitif, et des reliques des époques majeures de formation d'étoiles dans l'histoire. La question de savoir si les GCs couvrent une large gamme d'âge, ou si la majorité des GCs ont été formés à une époque particulière, reste un sujet de débat. Une estimation précise de l'âge d'un GC éloigné est encore difficile à cause de la dégénérescence âge-métallicité (Worthey, 1994). Les estimations de l'âge des GCs de MW sont connues avec une meilleure précision en raison de leur nature résolue. Les âges des GCs de la Voie Lactée sont mesurés à partir des diagrammes couleur-magnitude profonds qui proviennent de l'instrument ACS à bord de HST. Les âges de près de 70 GC de la Voie lactée ont été estimés à partir des CMD du HST, et leur relation âge-métallicité révèle que la plupart des GC les plus anciens couvrent une large gamme de métallicité, tandis que les âges des GC les plus jeunes sont anti-corrélés avec leurs métallicités (Marín-Franch et al., 2009; Forbes and Bridges, 2010; Oliveira et al., 2020) . Dans ces études, on a également constaté qu'en général, la sous-population GC pauvre en métaux (MP) est un peu plus âgée que ses homologues riches en métaux (MR) (12,5 Gyr pour MP contre 11,5 Gyr pour MR). Mais ces estimations d'âge sont dans les limites de l'incertitude et donc la possibilité que les deux groupes se chevauchent considérablement ne peut être exclue. Pour quelques GC, les estimations d'âge ont été obtenues à partir de la séquence de refroidissement des WD, qui est moins sensible à la métallicité, mais qui nécessite également un CMD beaucoup plus profond, et les âges se sont avérés cohérents avec les estimations d'âge obtenues par ajustement de la séquence principale (par exemple Hansen et al., 2013; García-Berro et al., 2014). Une nouvelle technique qui pourrait s'avérer utile pour dériver les âges absolus des GC utilise les CMD profonds dans le proche IR. Elle permet de sonder les "couloirs" de la séquence principale qui sont généralement affichés à $\sim$ 0,5 $M_{\odot}$, ce qui correspond en couleur à *(J-K)* $\sim$ 0,8. La différence entre le tournant de la séquence principale et le coude est sensible à l'âge et à la métallicité. L'emplacement est insensible aux incertitudes du module de distance, des modèles stellaires et des valeurs d'extinction (Bono et al., 2010).

Les âges des GCs MW indiquent que la plupart des GCs se sont formés il y a 11,5-12,5 Gyrs, c'est-à-dire à environ $z \sim$ 3-6 dans le modèle cosmologique standard. Ceci est une des contraintes importantes sur la limite supérieure de l'âge de l'univers (Krauss and Chaboyer, 2003). Ceci est également important pour évaluer le lien entre la réionisation et la formation des GCs et l'impact de l'une sur l'autre.

1.12.2 Absence de matière noire

Les études cinématiques des amas globulaires ont établi que les GCs sont dépourvus de matière noire (DM). C'est l'une des différences frappantes entre les galaxies naines sphéroïdales (dSph), par ailleurs très similaires, et les GC. Le rapport masse/lumière des GC est généralement compris entre 1 et 4, ce qui indique une carence en matière noire dans les GC. Mais sur la base des canaux de formation généralement acceptés, il a été avancé que si les GC se sont formés dans un environnement dominé par le DM, il est peu probable qu'ils en soient complètement dépourvus. Baumgardt and Mieske 2008 a proposé que les GC puissent être exempts de DM en leur centre mais qu'ils conservent la matière noire dans leur halo. Ibata et al. 2013 a également estimé le contenu en matière noire de NGC 2419 dans son halo et soupçonne qu'il pourrait être deux fois plus massif que sa composante stellaire. Cela pourrait expliquer l'aplatissement de la courbe de vitesse dans la périphérie de certains des amas globulaires (Drukier et al., 1998; Scarpa et al., 2007; Lane et al., 2010; Bellazzini et al., 2015; Bianchini et al., 2019). Ces amas nécessiteraient alors un scénario de formation différent de celui des amas moins massifs, peut-être similaire à celui des galaxies naines ultra compactes (UCD) qui ont un rapport masse-lumière plus élevé et sont similaires aux GC à d'autres égards.

1.12.3 Populations stellaires multiples

Les GC étaient initialement perçus comme des systèmes hébergeant des populations stellaires simples coexistantes (par exemple, Ashman and Zepf, 1998). Mais il est maintenant largement admis que ce n'est pas le cas, et que la population stellaire d'un GC est beaucoup plus compliquée qu'on ne le pensait initialement. Les GC présentent des variations d'étoile à étoile dans les abondances de certains éléments comme He, C, N, O, Na et Al. Ces modèles particuliers sont propres aux GC et sont absents dans les étoiles de champ, et ils sont le signe révélateur d'une combustion de H à haute température (Gratton et al., 2004; Charbonnel, 2016). Ces modèles sont observés dans les GCs, de sorte que les GCs les plus enrichis sont riches en He, N et Na et ont des abondances appauvries en O et C. La figure 1.4 montre le tracé des abondances de Na par rapport à O dans 20 GCs MW. L'anti-corrélation entre Na et O est visible pour presque tous les amas avec une amplitude variable (Carretta et al., 2009a; Carretta et al., 2009c).

Il est intéressant de noter que malgré la forte anti-corrélation entre les étoiles, le [Fe/H] reste le même parmi elles. Les anti-corrélations donnent lieu à ce que l'on appelle des populations stellaires multiples (MSP) dans les GCs, ce qui se reflète dans le diagramme couleur-magnitude complexe des amas. La figure **??** montre le CMD des étoiles de la séquence principale de NGC 2808. Les séquences distinctes d'étoiles sont très évidentes.

Le Hubble Space Telescope (HST) UV Legacy Survey of Galactic GCs (Piotto et al., 2015) a observé 56 GCs avec des filtres UV/bleus principalement dans le but d'identifier des populations multiples dans les GCs. Les résultats de l'enquête ont été utilisés pour expliquer l'origine possible de la population d'étoiles enrichie (ou de 2e génération comme indiqué dans la série) (Renzini et al., 2015). Les coupables possibles incluent l'enrichissement par les éjectas des étoiles de première génération (Prantzos and Charbonnel, 2006), les étoiles massives de la branche géante asymptotique (AGB), les étoiles massives en rotation rapide (Denissenkov et al., 2015) et les binaires en interaction. Les modèles prédisent que la différence d'âge entre les deux générations d'étoiles est inférieure à 150 Myr pour les amas d'âge 12 Gyr et plus. Ainsi, les étoiles peuvent encore être qualifiées de coéternelles. Les écarts d'âge mesurés pour les deux générations d'étoiles dans les GC du halo et du bulbe par Oliveira et al. (2020) montrent que la différence d'âge est de ~ 50 Myr.

Ces tendances ne sont pas particulières aux GCs du MW mais sont également connues dans les GCs en dehors du MW. Mucciarelli et al. (2009) ont étudié trois GCs dans le LMC et ont découvert les mêmes tendances entre Na-O et Al-Mg que celles observées dans les GCs galactiques. Un certain nombre d'études similaires sur les GCs du SMC, la sphéroïde naine de Fornax ont également montré la présence de MSP (Hollyhead et al., 2017; Larsen et al., 2014). L'amplitude de la variation des éléments est souvent liée à la masse, à l'âge de l'amas et à la métallicité de sorte que les amas les plus anciens ($>$8 Gyr) montrent la présence de MSPs (Krause et al., 2016), avec une plus grande amplitude des variations observées dans les amas les plus massifs (Milone et al., 2017). La fraction de la population enrichie d'étoiles (également appelée étoiles de 2ème génération ou 2P) varie de 40 à 90% dans les vieux GCs (Gratton et al., 2019). Ces étoiles 2P sont censées s'être formées à partir de la matière transformée des étoiles 1P. Grâce à des mesures de haute précision, de nombreux amas ont montré des signatures de 3-4 sous-populations. Il existe des preuves provisoires que les MSP ne sont pas seulement limitées aux GCs mais peuvent également être observées dans d'autres environnements comme les galaxies naines, le bulbe/halo interne des galaxies et les ETGs (Bastian and Lardo, 2018).

1.13 Propriétés des systèmes GC

1.13.1 Fréquence spécifique

Fréquence spécifique est défini comme le nombre d'amas globulaires, N_{GC}, par unité de luminosité de la galaxie, normalisé à une galaxie avec une magnitude absolue de la bande V de -15 (Harris and van den Bergh, 1981), et représente l'efficacité de la formation des GC par rapport à la composante stellaire de la galaxie.

$$S_N = N_{GC} 10^{0.4(M_V+15)} \tag{1.5}$$

Le paramètre a été formulé pour établir la relation entre la luminosité des galaxies et le nombre de GCs que la galaxie héberge. On a constaté que le S_N n'avait pas de relation simple avec le M_V. Cependant, on a constaté que le S_N diffère en fonction de l'environnement. On a constaté que les elliptiques trouvées dans des groupes plus petits et plus clairsemés ont environ deux fois moins de GCs pour leur taille que les elliptiques qui résident dans des environnements plus riches (Harris, 1991). La valeur moyenne de S_N pour les elliptiques est d'environ 3,5, mais une grande dispersion existe. Il a été démontré que M87 a un S_N 2 à 3 fois plus élevé que les autres galaxies gE de l'amas de la Vierge, qui ont elles-mêmes une population de GC plus importante que les autres galaxies de champ.

La valeur de S_N pour les galaxies à disque est un peu plus difficile à déterminer directement car leur M_V est constitué de la lumière provenant à la fois du disque et des étoiles de la population I, qui ont peu de rapport avec les GC du halo. De plus, les GCs sont difficiles à détecter sur le fond irrégulier de la galaxie spirale, surtout si la galaxie est de bord (voir figure 4 dans (Harris, 1991)). Leur S_N ajusté est calculé à partir du rapport de N_{GC} à la seule lumière sphéroïdale qui exclut le disque.

La fréquence spécifique a été conçue pour comparer plus facilement les systèmes sans que la proportionnalité dépende de la taille de la galaxie. $\mathbf{S}_N$ est essentiellement le rapport entre le nombre de GC et le nombre total d'étoiles dans la galaxie, et est donc insensible aux fusions de galaxies car les étoiles et les GC se forment lors des fusions.

Peng et al. (2008) ont étudié le S_N pour 100 galaxies dans la région de l'amas de la Vierge et ils ont constaté que le nombre de GC était faible dans les galaxies de masse intermédiaire ($-20,5 < M_V < -18$), augmentant à la fois pour les galaxies de masse inférieure et supérieure dans la région. D'autres études indépendantes ont également confirmé les mêmes résultats pour les ETGs (Zaritsky et al., 2015; Liu et al., 2019a) . Au début, le $\mathbf{S}_N$ était paramétré pour étudier la relation entre la population stellaire d'une galaxie et son système GC, mais récemment, il s'est avéré être un facteur important qui est régulé par l'environnement du système GC.

1.13.2 Fonction de masse du cluster (CMF)

La nature exacte des systèmes stellaires dans les GCs n'est pas facile à sonder étant donné la limitation des observations. Les scénarios de formation des GCs montrent que ces derniers pourraient se former soit de manière monotone, soit par fusion de sous-systèmes plus petits dans des complexes moléculaires plus grands (Bonnell et al., 2003). La confirmation de ces scénarios nécessite de connaître la fonction de masse initiale de l'amas (ICMF) et son évolution. L'ICMF peut être une pièce très importante pour reconstruire la formation des amas, mais il est à noter qu'il est peu probable qu'elle soit observée puisque les observations ne peuvent sonder que la fonction de masse actuelle des amas. La FMC actuelle des GC de la Voie lactée est décrite par une distribution log-normale qui culmine à environ 2 fois 10^5 $M_\odot$ (Whitmore et al., 1999; Fellhauer and Kroupa, 2005).

La fonction de masse des jeunes systèmes pourrait être approximée comme l'ICMF et utilisée pour déduire la relation entre l'ICMF actuel et l'ICMF des amas plus anciens. La fonction de masse d'un jeune amas suit une fonction de loi de puissance avec une coupure exponentielle à l'extrémité de masse élevée, et est donnée sous la forme fonctionnelle suivante :

$$\frac{dN}{dM} \propto M^{-\beta} e^{-\frac{M}{M_c}} \tag{1.6}$$

Cette fonction est similaire à la fonction de masse des galaxies (Press and Schechter, 1974) et est paramétrée par $\beta \approx 2 \pm 0.3$ (Zhang and Fall, 1999; Bik et al., 2003; Hunter et al., 2003). Pour établir la relation entre l'ICMF de type Schechter et le CMF actuel, il faut connaître la perte de masse et les autres processus d'évolution que subissent les amas au cours de leur vie, ainsi que leur dépendance à la masse.

1.13.3 Bimodalité

On a découvert que les systèmes GC des premières galaxies présentaient des distributions de couleurs bimodales (Ostrov et al., 1993; Ashman and Zepf, 1993) et il est maintenant établi que les systèmes GC de la plupart des galaxies massives présentent une distribution de couleurs bimodale (Larsen et al., 2001b; Kundu and Whitmore, 2001; Peng et al., 2006). Ces différences de couleur avaient été expliquées comme étant dues à des différences de métallicité ou d'âge ou une combinaison des deux. Des études spectroscopiques ont montré que ces différences sont principalement dues à la métallicité plutôt qu'à l'âge. La bimodalité des couleurs se traduit par le fait que les GC bleus sont pauvres en métaux (MP), et les GC rouges sont riches en métaux (MR). La présence de ces deux populations de CG a été proposée pour la première fois par Zepf and Ashman (1993). Les deux groupes distincts de GCs présentent des différences significatives dans leurs caractéristiques et sont proposés comme ayant été créés par des mécanismes ou des événements différents. Les amas rouges des galaxies à disque ont une rotation importante par rapport aux amas bleus. Dans les galaxies elliptiques, les GC rouges ont une dispersion de vitesse plus faible que les GC bleus. Les GC rouges sont également plus concentrés au centre que les GC bleus dans ces systèmes (Brodie and Strader, 2006). Cependant, les propriétés internes comme les masses, les tailles et les âges à première vue sont plus similaires dans les deux groupes. Cela pourrait signifier que ces amas se sont formés de manière similaire mais que les nuages moléculaires à partir desquels ils se sont formés ont été assemblés différemment (Gnedin and Prieto, 2009). Les conséquences de l'existence de deux groupes distincts sont importantes en termes de formation et d'évolution des galaxies.

Les GC de la Voie lactée sont également connues pour présenter une distribution bimodale des couleurs (Zinn, 1985). Les deux groupes de la Voie lactée ont une distribution spatiale caractéristique : les GC MP se trouvent dans le halo de la Voie lactée tandis que les GC MR se trouvent plus souvent dans le disque et le bulbe. Les pics bleu et rouge de la couleur (V-I) se produisent généralement à 0,95 ± 0,02, et 1,18 ± 0,04 (Larsen et al., 2001b) dans les ETGs. Ces valeurs de couleur correspondent à [Fe/H] $\sim$ -1.5, et -0.5 pour les vieux GCs. Ce pic n'est pas toujours le même pour toutes les galaxies.

Au contraire, certaines études proposent également que la relation couleur-métallicité pourrait être non linéaire, auquel cas une distribution bimodale de la couleur ne nécessite pas nécessairement que la métallicité soit bimodale également (Yoon et al., 2006b; Yoon et al., 2006a; Blakeslee et al., 2010). Comme le montrent les simulations de Yoon et al. (2006a), toutes les couleurs présentent une bimodalité, comme g-z et V-I, mais l'impact est moins évident dans les couleurs optiques-NIR comme V-K. En termes d'observation, le nombre de galaxies disposant de données optiques-IR proche de haute qualité est faible et s'améliorera dans le futur.

1.13.4 Tailles

Les distributions de luminosité de surface des GC peuvent être approximées par des modèles de King (King, 1966). Le modèle de King pour le GC peut être caractérisé comme une fonction du paramètre de concentration c, tel que $c = log_{10}(r_t/r_c)$, où r_t est le rayon de marée et r_c est le rayon du noyau. La luminosité de surface d'un amas diminue régulièrement avec la distance, et le rayon de marée est le rayon où la luminosité de surface apparente tombe à zéro. Un autre paramètre est le rayon de demi-lumière r_h et c'est la distance du centre de l'amas où la luminosité encerclée a atteint la moitié de la luminosité totale. Généralement, les GC ont une r_h inférieure à 10 pc, certains amas ayant des valeurs plus élevées, comme Palomar13 ($r_h \sim 25$pc).

Une corrélation entre la distance galactocentrique et r_h a été observée (van den Bergh et al., 1991) de telle sorte que les GC pauvres en métaux, typiquement situés loin, sont 20% plus grands que les GC riches en métaux trouvés à de plus petites distances (Kundu and Whitmore, 1998; Kundu et al., 1999; Jordán et al., 2005). Cela pourrait indiquer des différences dans les conditions de formation des deux groupes d'amas. Il a également été proposé que cela pourrait être le résultat d'effets de projection (Larsen and Brodie, 2003). Une autre explication pourrait être la présence de forces de marée plus fortes à des distances plus proches du centre de la galaxie qui limitent r_t et à leur tour r_h. (Jordán et al., 2005). Il est possible que la projection et la ségrégation soient toutes deux responsables des tendances de taille observées, mais d'autres études sont nécessaires pour comprendre quels effets sont les plus importants.

1.13.5 Métallicité moyenne du GC et luminosité des galaxies

Une relation entre la métallicité moyenne d'un système GC et la luminosité de sa galaxie mère a été proposée pour la première fois par van den Bergh (1975). Par la suite, d'autres études ont confirmé qu'une telle relation de la forme $Z \propto L^{0.4}$, ce qui indique que les GC ont la même histoire d'enrichissement que leurs galaxies parentes. Le système de galaxies GC est mieux représenté par deux sous-systèmes avec des métallicités moyennes distinctes. Certaines études ont trouvé que la métallicité des GC riches en métaux est plus étroitement couplée à la galaxie hôte que celle des GC pauvres en métaux, ce qui signifie que la relation métallicité - luminosité de la galaxie pourrait être dominée par les GC riches en métaux (Forbes et al., 1997).

Peng et al. 2006 ont étudié les couleurs optiques des GCs dans 100 galaxies de l'amas de la Vierge et ont trouvé que les couleurs des GCs bleus et rouges sont en corrélation avec la luminosité et la couleur de la galaxie hôte. La figure 1.6 montre la couleur moyenne (g-z) des sous-populations de GC rouges et bleus des galaxies en fonction de la magnitude absolue de la galaxie.

Les GC pauvres en métaux se retrouvent dans toutes les galaxies, quelle que soit leur luminosité, mais la population des GC rouges diminue dans les galaxies les moins lumineuses. En moyenne, les GC rouges forment environ 10 % de la population totale des galaxies les plus faibles et les plus bleues, et environ 60 % des galaxies les plus brillantes et les plus rouges (figure 1.7). De plus, si les galaxies bimodales sont regroupées avec les galaxies ayant des métallicités GC unimodales, la métallicité des GC bleues couvre une gamme similaire de valeurs de métallicité pour toutes les luminosités de galaxies, mais la couleur typique de la population GC rouge varie avec la luminosité de la galaxie.

La relation entre la métallicité des GC et les propriétés des galaxies indique que la formation des deux sous-populations est étroitement liée à leurs galaxies hôtes. Comme discuté dans certains des scénarios de formation des GC dans la section 1.14, les GC MP trouvent leur lien avec l'épisode de formation d'étoiles qui s'est produit au début de l'univers ou peu après la réionisation, tandis que la formation de la population MR est associée à la formation des bulbes et donc leur nombre est corrélé avec la masse de la galaxie, renforçant le récit.

1.13.6 Fonction de luminosité des amas globulaires (GCLF)

La distribution des magnitudes absolues des amas globulaires dans un système GC peut être approximée par une gaussienne,

$$\frac{dN}{dm} \sim \exp \frac{-(m-m_0)^2}{2\sigma^2} \tag{1.7}$$

où dN est le nombre de GC dans un bin de magnitude apparente dm, m_0 est la magnitude de renouvellement (TOM) et le σ est la largeur de la distribution gaussienne (Richtler, 2003). Le terme GCLF est mal choisi car il représente la distribution de magnitude des amas et non la distribution de luminosité. La forme de la FCLG n'est pas une gaussienne parfaite, mais elle présente un pic, est unimodale et presque symétrique dans la bande V dans la plupart des études et peut être approximée par une fonction gaussienne. Secker (1992) ont effectué une estimation du maximum de vraisemblance sur la FCMG du MW et du M31 et ont démontré que le meilleur ajustement est obtenu avec une fonction de distribution t_5 donnée par,

$$\frac{dN}{dm} \sim \frac{1}{\sigma}(1 + \frac{-(m - m_0)^2}{5\sigma^2})^2 \tag{1.8}$$

Malgré la différence entre l'ajustement approximatif et le meilleur ajustement, le TOM du GCLF est très similaire quel que soit l'ajustement. La figure 1.8 montre le GCLF pour les GC de MW, ajusté avec une gaussienne et une fonction t_5. Les valeurs typiques pour les galaxies elliptiques sont TOM, m_0 ∼ -7,5 et σ ∼ 1,4 dans la bande V, et des valeurs similaires pour les spirales mais σ ∼ 1,2 étant plus précis. Le pic de magnitude du TOM correspond à une masse de ∼ 2 $\times 10^5$. $M_\odot$. La FCMG a une forme universelle et est similaire pour différentes galaxies et la valeur du TOM était considérée comme étant la même universellement (Hanes, 1977) et est maintenant nuancée (Rejkuba, 2012). Le GCLF est bien connu comme indicateur de distance à l'échelle extra-galactique, mais n'est applicable qu'aux vieux GCs. La FCMG dépend des bandes passantes des observations, comme prévu en particulier lorsque la distribution des couleurs est bimodale (figure 1.9) (Taylor et al., 2017). Les distances déterminées à partir du GCLF s'avèrent cohérentes avec les distances déterminées à partir des fluctuations de la luminosité de surface. Le GCLF comme indicateur de distance n'est pas très populairement utilisé pour les galaxies spirales en raison des difficultés à sonder la population GC des spirales en raison de la présence de disques, de couloirs de poussière, etc.

1.14 Formation des amas globulaires

La formation des amas globulaires dans l'univers primitif n'est pas très bien comprise en raison du manque de preuves observationnelles directes. Nous étudions la formation des amas dans l'univers local et l'extrapolons pour comprendre la formation des amas dans l'univers à haut redshift. Des modèles théoriques et des simulations numériques de l'évolution des systèmes gravitationnels dans le cadre cosmologique guident ce processus. L'origine du système GC des galaxies peut être limitée par l'étude de leurs couleurs intégrées qui sont liées à leurs propriétés chimiques et à leurs âges. En tant que telle, la compréhension du système GC d'une galaxie éclaire également l'histoire de la formation de la galaxie. Dans cette section, nous discuterons des théories de formation des GC résolus, et des systèmes GC des galaxies.

1.14.1 Formation des GC en tant qu'objet résolu

Les nuages moléculaires sont les régions les plus denses du milieu interstellaire. Ils sont formés principalement d'hydrogène moléculaire et de plusieurs autres molécules. On sait que ces nuages ont des masses allant de $\sim 10^3$ à 10^7 $M_\odot$ et ont des morphologies hiérarchiques telles que les régions les plus denses sont encastrées dans les régions les moins denses (Elmegreen and Falgarone, 1996). Les amas globulaires se forment dans les régions denses où l'effondrement hiérarchique de nuages moléculaires géants déclenche la formation d'étoiles à grande échelle. Les nuages moléculaires évoluent en accrétant de grandes quantités de gaz atomique (Fukui et al., 2009). Le paradigme commun est qu'ils sont soutenus par un agent (pression thermique, turbulence ou magnétisme) contre l'auto-gravité et ne s'effondrent pas d'un seul coup. Les nuages moléculaires sont soutenus par une turbulence isotrope à petite échelle, tandis que localement ils forment des chocs qui peuvent générer des fluctuations de densité. Les GMCs sont froids et denses et atteignent donc leurs masses de Jeans plus rapidement que les gaz chauds et diffus (Gómez and Vázquez-Semadeni, 2014). L'accrétion les rend magnétiquement super-critiques et ils ne peuvent plus être soutenus contre l'auto-gravité et le nuage devient gravitationnellement instable. Comme le nuage n'a pas une densité uniforme, il commence à former une cascade d'effondrements. La partie la plus dense du nuage commence à s'effondrer plus rapidement que les parties les moins denses, avec une échelle d'effondrement hiérarchique, telle que chacune d'entre elles s'accrète à partir de l'échelle plus grande suivante (Vázquez-Semadeni et al., 2019). Cela déclenche la formation d'étoiles dans un nuage moléculaire, et les amas d'étoiles liés sont nés. La formation d'étoiles dans ces nuages est très efficace car la rétroaction stellaire n'est pas aussi efficace dans les régions denses qui empêchent le gaz d'être expulsé.

D'un point de vue observationnel, on sait que les nuages de gaz froid sont enveloppés de gaz atomiques et ont un rayon de 10-30 pc. Ces observations sont limitées à la Voie lactée et à d'autres galaxies proches (LMC, SMC, M31 etc.) (Rosolowsky, 2007; Rosolowsky et al., 2007; Miville-Deschênes et al., 2017). On peut en déduire sans risque qu'aucune étoile ne se forme isolément et que les pouponnières stellaires donnent naissance à plus d'une étoile. Cependant, il n'est pas toujours nécessaire que ces amas d'étoiles nées au même endroit continuent à survivre en tant qu'amas liés et certains d'entre eux sont dynamiquement perturbés en quelques myr (Bressert et al., 2010).

La rétroaction stellaire pourrait jouer un rôle important dans la décision du destin de l'amas. Après leur formation dans le GMC, les étoiles ont le potentiel de modifier leur environnement par le biais d'écoulements proto-stellaires, de photo-ionisation, de rayonnement, de vents et de supernovae (Dale, 2015). L'impact de la rétroaction stellaire peut ralentir ou éteindre la formation d'étoiles (Murray, 2010; Krumholz et al., 2014; Dale, 2015; Semenov et al., 2017), en expulsant le gaz hors du système, ou initier une formation d'étoiles subséquente dans celui-ci en comprimant le nuage par des fronts de chocs (Koenig et al., 2012; Shima et al., 2017). Dans les régions plus denses, la rétroaction du vent stellaire n'est pas assez forte pour éliminer le gaz du système, permettant la rétention du gaz et aidant éventuellement à la formation de multiples populations d'étoiles. Ainsi, l'environnement local joue un rôle très important dans la détermination des propriétés des objets stellaires formés.

1.14.2 Formation du GC à haut redshift

La détermination des âges absolus précis des GC (voir la section 1.12.1) reste un défi, principalement en raison de la dégénérescence âge-métallicité, et les âges sont connus avec des incertitudes de 1 à 2 Gyrs, ce qui se traduit par un écart approximatif du décalage vers le rouge entre $z \sim$ 4-10. Même dans ce cas, les tendances des âges et des métallicités des GC peuvent être utilisées pour contraindre les scénarios de formation et les canaux de formation du système et peuvent également être informatives sur la formation et l'évolution de leurs systèmes hôtes.

Une contrainte observationnelle majeure sur la formation des systèmes GC provient de la bi-modalité observée dans la distribution de couleur dans le système GC de certaines galaxies massives (Zinn, 1985; Gebhardt and Kissler-Patig, 1999; Larsen et al., 2001a; Peng et al., 2006) (voir la section 1.13.3). La couleur bimodale est souvent traduite par une métallicité bimodale qui indique l'existence de deux sous-systèmes dans le système GC, les GC rouges qui sont des membres riches en métaux, et les GC bleus, la population pauvre en métaux avec un déficit d'amas dans les valeurs moyennes de la métallicité. Dans les galaxies MW et M31, les GC rouges sont légèrement plus jeunes et plus brillants que les GC bleus. Alors que certaines galaxies, comme la Voie lactée, présentent la population bimodale du système GC, d'autres, comme Andromède, ne présentent pas cette caractéristique. Plusieurs scénarios ont été proposés pour expliquer cette distribution bimodale du système GC.

- ***Formation dans les halos de matière noire***

  Peebles and Dicke (1968) a suggéré la formation de GCs à un redshift très élevé dans un milieu à faible métallicité. A cette époque, l'Univers s'est juste suffisamment étendu pour permettre la formation des GCs mais pas des structures à grande échelle comme les galaxies. Lorsque le milieu primordial était pauvre en métaux et que la température de la région surdense atteignait $\sim$ 4000K, les critères de Jeans pouvaient être atteints pour les masses et tailles typiques des GCs (Fall and Rees, 1985; Bromm and Clarke, 2002; Katz and Ricotti, 2014). Cet effondrement est plus susceptible de se produire dans les puits de potentiel qui contiennent la matière noire, par conséquent, la question de l'absence de DM dans les GC doit être abordée. Ce scénario ne peut pas expliquer la distribution bimodale de la métallicité des GC et nécessite également que les GC soient très vieux.

- ***Fusion entre galaxies***

Pour expliquer l'existence de métallicités distinctes dans le sous-système des GC, Schweizer (1987) et Ashman and Zepf (1992) ont proposé un scénario de formation en deux étapes pour expliquer la différence d'âge entre les GC rouges et bleus. Les amas bleus se sont formés à une époque précoce où l'univers était très pauvre en métaux. En raison de la densité de l'univers, les fusions étaient plus fréquentes et riches en gaz, et les fusions ont donc déclenché plus de formation d'étoiles. Les amas plus anciens ont enrichi leur environnement, ce qui a contribué à la formation des nouveaux GC. Ce scénario nécessite des fusions riches en gaz et suppose que celles-ci produisent efficacement des amas globulaires (par rapport aux petits amas qui seront perturbés pour devenir des étoiles de champ), afin d'expliquer une augmentation de la fréquence spécifique après la fusion. McLaughlin and Pudritz (1994) a noté que le scénario peine à reproduire les très grandes fréquences spécifiques des galaxies cD dans les amas de galaxies.

- ***Effondrement multiphase***

  Dans ce scénario, proposé par Forbes (1997), les amas pauvres en métaux se sont formés pendant l'effondrement de la proto-galaxie avant la réionisation. Cette phase de formation des GC s'est arrêtée lorsque la réionisation a commencé et a éteint la formation des étoiles. Une autre phase de formation des GC a été déclenchée dans le disque de la galaxie lorsque l'ISM est devenu suffisamment dense pour former des étoiles. Dans ce scénario, la cinématique observée et la distribution du système GC actuel pourraient être adaptées lorsque le système a une distribution bimodale, mais cela n'explique pas le cas d'un système unimodal de GC, par exemple la galaxie d'Andromède.

  Les estimations de l'âge des galaxies MW bleues montrent que ces galaxies se sont probablement formées à $z \sim 6$, ce qui correspond à la fin de la réionisation (Forbes et al., 2015). L'âge des GC rouges a une valeur moyenne de 11,5 Gyr qui correspond à $z \sim 3$, ce qui est antérieur au début de la formation du disque prédit par les simulations cosmologiques (Agertz et al., 2011; Renaud et al., 2017). Cela suggère que la réionisation a été suivie par la formation de GCs et n'est pas l'explication probable de la bimodalité observée.

- ***Formation in-situ et ex-situ*** Ce scénario de formation des GC a été proposé par Côté et al. (1998) et Tonini (2013). Dans ce scénario, les GC rouges riches en métaux se sont formés sur le site, tandis que les GC bleus et pauvres en métaux ont été accrétés via des fusions. Les propriétés des amas accrétés sont compliquées en raison de la variété des propriétés des galaxies donneuses. Il est difficile de distinguer la contribution de chaque donneur, ainsi que l'époque de la fusion. Cela pourrait contribuer à lisser la distribution de la métallicité des GCs donnés (Forbes and Bridges, 2010). Ce scénario est cohérent avec les simulations cosmologiques de la formation de la Voie lactée par Renaud et al. (2017).

Cette voie de formation du système GC d'une galaxie est relativement plus largement acceptée par rapport aux autres scénarios, tels que les GC bleus pauvres en métaux sont formés ex-situ dans les galaxies de faible masse, tandis que les GC riches en métaux ou les GC rouges sont formés in-situ au sein de la galaxie en accrétion Tonini (2013).

1.15 GCs comme moteurs de la science

Notre compréhension des populations résolues de GC et de leurs propriétés provient du système GC de la Voie lactée et d'autres galaxies proches de la Voie lactée, comme le LMC, le SMC et M31. Les GC qui sont plus éloignés et qui ne peuvent pas être résolus avec les technologies actuelles sont également importants pour étudier les propriétés des environnements dans lesquels ils résident, et pour découvrir les événements du passé. Les GCs peuvent servir de spécimen pour une variété de cas scientifiques allant de leur rôle dans la compréhension de la physique stellaire à la connaissance du contenu en matière noire d'une galaxie. Dans cette section, nous discuterons des diverses applications scientifiques des GC, qu'il s'agisse d'objets résolus ou non résolus.

1.15.1 Etoiles et amas globulaires - Sonde de l'évolution stellaire

Les amas globulaires de la Voie lactée couvrent un large éventail en termes de masse totale et de magnitudes intégrées, ω Centauri étant l'amas le plus massif de notre galaxie avec une masse totale d'environ 10^6 $M_\odot$ et environ 10 millions d'étoiles, tandis que des amas globulaires comme Pal 13 et AM 4 se situent à l'autre extrémité du spectre avec des masses de l'ordre de 10^3 $M_\odot$. La variété disponible dans les amas les rend très intéressants d'un point de vue dynamique, et le fait que leur population soit composée d'étoiles à tous les stades d'évolution mais à des âges et distances similaires en fait des candidats encore plus désirables pour valider notre compréhension de l'évolution stellaire.

Au début du 20e siècle, Ejnar Hertzsprung et Henry Russell ont observé et analysé les propriétés de base d'un certain nombre d'étoiles de champ et de groupes proches en mouvement conjoint (par exemple, les Pléiades et les Hyades, (Russell, 1913; Russell, 1914), voir figure 1.10). Ces travaux ont donné naissance à l'un des outils de diagnostic les plus utilisés et les plus importants, le diagramme HR. Un diagramme HR montre la relation entre la luminosité et le type spectral de l'étoile. Ces diagrammes HR ont illustré la preuve que l'évolution stellaire est un processus ordonné et que la masse et la luminosité des étoiles sont corrélées.

Le diagramme HR des amas des Pléiades et des Hyades montre clairement que ces amas ont des populations stellaires qui échantillonnent une série d'étapes du cycle de vie stellaire, et au fil des ans, les amas ont été considérés comme abritant des populations stellaires simples qui co-évoluent et partagent des chimies similaires. Les amas sont donc devenus des bancs d'essai idéaux pour étudier la vie d'une étoile et notre compréhension de la physique stellaire. Les GC sont devenus les alambics qui ont permis de comprendre comment les étoiles évoluent à une métallicité et un âge donnés sur toute la gamme des masses stellaires. Une image cousue d'un certain nombre d'amas avec des métallicités et des âges différents a facilité l'image complète de l'évolution des étoiles. Cela a coïncidé avec un développement des instruments d'observation de l'époque, qui a conduit Shapley à mesurer d'autres propriétés photométriques comme les distances, les tailles, les luminosités, etc. de plusieurs amas proches.

Pour interpréter les observations des amas, les observations sont comparées aux diagrammes HR théoriques produits à partir de modèles théoriques d'évolution stellaire. Le diagramme HR synthétique est obtenu à partir de simulations de Monte Carlo qui produisent des paires de masse et d'âge pour une fonction de masse initiale, une histoire de formation d'étoiles et un intervalle de temps donnés. Dans le cas des amas globulaires, l'histoire de la formation des étoiles est essentiellement un pic unique de naissance d'étoiles suivi d'une évolution stellaire passive. Chaque étoile est placée dans le diagramme HR observé. La comparaison peut donner des contraintes sur les propriétés fondamentales de l'amas, comme l'âge, la métallicité et la masse. Elle peut également aider à tester et à quantifier les différents processus qui devraient se produire à l'intérieur des étoiles et qui sont difficiles à mesurer directement, comme la rotation du noyau, la diffusion atomique, le tassement gravitationnel et le dépassement du noyau. La première partie de cette thèse se concentre sur un tel scénario dans lequel nous testons les performances des bibliothèques stellaires empiriques par rapport à la bibliothèque stellaire théorique afin de matérialiser l'impact de la diffusion atomique sur le diagramme HR de l'amas globulaire NGC 6397 (voir chapitre 2). Des études comme celle-ci rendent évident que les amas globulaires sont le moyen de calibrer nos modèles et d'affiner les théories de l'évolution stellaire qui, à leur tour, sont utilisées pour interpréter les propriétés des galaxies lointaines (par exemple Bruzual and Charlot (2003)).

1.15.2 Évolution et assemblage des galaxies

Comprendre la formation et l'évolution des galaxies est l'un des défis majeurs de l'astrophysique. On ne sait pas encore très bien comment les galaxies atteignent leur morphologie actuelle ou la forme que nous voyons à un décalage vers le rouge plus élevé. A quelques exceptions près, les amas globulaires sont omniprésents dans les galaxies de tous types et dans toutes sortes d'environnements. Plusieurs de leurs propriétés sont également étroitement liées à leurs galaxies hôtes, présentant des relations d'échelle qui peuvent désormais servir à caractériser de nouveaux systèmes hôtes. Ils sont également utiles pour établir des contraintes sur les épisodes de formation d'étoiles et l'histoire de l'assemblage de leurs environnements hôtes, et sont des traceurs efficaces de l'histoire de la formation des galaxies de type précoce, des bulbes spiralés et des halos.

- ***Systèmes GC des galaxies de type précoce (ETGs)***

  Les systèmes GC des galaxies de type précoce (ETG) sont les plus étudiés en raison de la facilité relative de détection des GC dans ces galaxies. Les ETGs comprennent également les galaxies connues les plus massives et abritent de riches populations de GC. Les études des populations stellaires des ETGs massives montrent qu'elles sont généralement vieilles ($\sim$ 10 Gyr), riches en métaux (métallicité égale ou supérieure à la métallicité solaire), et ont un FMI lourd de fond (Trager et al., 2000; Renzini, 2006; La Barbera et al., 2013). Les systèmes GC des ETGs ont typiquement une distribution bimodale de la métallicité, et sur la base des relations empiriques dérivées des GCs MW et des prédictions des modèles théoriques SSP, la bimodalité de la couleur est généralement surnommée la bimodalité de la distribution de la métallicité. Il a également été avancé qu'une relation de couleur bimodale ne signifie pas nécessairement une métallicité bimodale (Yoon et al., 2006a) (voir section 1.13.3) mais la métallicité spectroscopique favorise la relation linéaire couleur-métallicité (Romanowsky, 2009; Schuberth et al., 2010). Il a également été suggéré que les relations couleur-métallicité des GC peuvent dépendre de leur environnement (Powalka et al., 2016a).

- ***CGs dans les galaxies de type tardif***

  Les systèmes GC des galaxies de type tardif ne sont pas aussi bien étudiés que les systèmes GC des ETGs en raison des difficultés à détecter les GC sur les bulbes et les disques en plus de la gêne causée par la poussière interne aux disques de formation d'étoiles. A une luminosité donnée, ils accueillent des populations de GC plus petites que les ETGs. A part la MW, le système GC le mieux étudié d'une galaxie de type tardif est celui de M31. Elle possède un riche échantillon de 500 GCs connus qui se trouvent à une distance de 780 kpc. L'âge des GCs ne peut pas être connu précisément à partir des CMDs profonds du HST, mais les études spectroscopiques suggèrent que les GCs sont typiquement vieux. La distribution de la métallicité s'étend sur une large gamme mais ne montre aucun signe de sous-structure dans la distribution de la métallicité (Caldwell et al., 2011). Des caractéristiques de marée et des structures de coquille sont détectées autour de M31 et certains GCs sont associés à ces structures, ce qui laisse supposer une accrétion des GCs sur le halo de M31 (Mackey et al., 2019). Les systèmes GC des galaxies spirales en dehors du Groupe local ont montré la présence de GC dans les disques des galaxies. Ces GCs ont des distributions spatiales et des propriétés comme la rotation qui ressemblent aux propriétés de la population stellaire du disque de la galaxie. Cela indique la formation possible des GCs dans le disque de la galaxie et si cela est vrai, les disques pourraient s'être formés à un redshift élevé ($z>2$).

- ***Population GC des galaxies naines***

  Les populations GC des galaxies naines sont intéressantes à étudier pour un certain nombre de raisons. Les galaxies naines et leurs GC peuvent être les éléments constitutifs du halo de galaxies plus massives. Dans le groupe local, 14 galaxies naines sont connues pour avoir des GCs, et le recensement est susceptible d'augmenter avec une meilleure résolution et des études à grand champ. La galaxie naine la plus massive dans notre voisinage est le Grand Nuage de Mégellan (LMC) et elle possède 16 GCs connus. Les propriétés spectroscopiques de ces GCs montrent qu'ils sont vieux et pauvres en métaux, ce qui est très typique des GCs des galaxies naines. Les systèmes GC des galaxies naines peuvent donner un aperçu du contenu en matière noire de ces galaxies (Cole et al., 2012; Orkney et al., 2019).

L'une des théories les plus largement acceptées qui explique l'état actuel de l'univers et tente d'établir le lien entre l'univers à ses débuts et l'état actuel est la *Lambda Cold Dark Matter* ou la théorie ΛCDM. Selon la théorie ΛCDM, la structure baryonique de l'univers continue de fusionner et de croître sous l'influence de la gravité. Une image très générique de la formation des galaxies elliptiques et de leurs systèmes GC sous un régime λCDM commence par la formation de la première génération d'étoiles qui se sont formées puis sont mortes tout en enrichissant le milieu interstellaire. C'était la phase *in-situ* de la formation des galaxies, et c'est au cours de cette phase que se sont formés les progéniteurs des amas globulaires actuels. Ces systèmes se sont formés dans les disques riches en gaz des galaxies et sont devenus la sous-population des GC rouges riches en métaux de la galaxie. Les GC bleus ou pauvres en métaux se sont formés de préférence dans les galaxies de faible masse où l'enrichissement n'était pas si courant. Ces galaxies ont ensuite été accrétées par les galaxies plus massives et formeront la population du halo de la galaxie. Ceci représente la phase *ex-situ* de la formation des galaxies. Un scénario similaire est également attendu pour la formation des galaxies spirales. Cependant, les disques de MW et de M31 ne sont pas très vieux et ont des âges ~ 5 Gyr ce qui indique que la formation des GCs dans leurs disques ne peut pas être très ancienne.

Les couleurs des systèmes GC et leur cinématique sont quelques-unes des propriétés qui ont permis d'établir des liens possibles entre le passé et le présent d'une galaxie. Les études théoriques et observationnelles sur les GCs tentent progressivement de relier les points entre les propriétés du système GC observé et la formation de la galaxie.

1.15.3 Contenu en matière noire d'une galaxie

Toutes les galaxies résident dans des halos de matière noire, et les propriétés et l'histoire de ceux-ci peuvent être étudiées indirectement. Une découverte récente de la relation entre le nombre de GCs dans une galaxie et la masse de son halo de DM nous a fourni un moyen d'estimer la masse du halo de DM. Contrairement à la population stellaire d'une galaxie, le nombre de GC dans une galaxie est indépendant du type et de l'environnement de la galaxie et constitue l'une des mesures fondamentales d'un système GC dans une galaxie. En théorie, le nombre total de GC dans un système (N_{GC}) est estimé en comptant les GC jusqu'au pic de la fonction de luminosité des amas globulaires (GCLF), et en supposant une distribution normale, le nombre de GC est doublé pour tenir compte des GC moins lumineux manquants.

Il a été démontré que le N_{GC} est en corrélation positive avec la masse stellaire de la galaxie hôte M_*. Dans le panneau gauche de la figure 1.11 (tiré de Hudson et al. (2014)), le graphique montre la corrélation entre la masse stellaire de la galaxie et le nombre de GCs hébergés par la galaxie. La corrélation positive n'est pas surprenante, car plus une galaxie a d'étoiles, plus elle a formé de GCs. Cependant, le graphique montre que la relation n'est pas entièrement linéaire, et les galaxies de faible masse et de masse élevée semblent avoir une meilleure efficacité de formation de GC que les galaxies de masse intermédiaire. Une tendance similaire avec la masse de la galaxie est observée dans les fréquences spécifiques des GCs (section 1.13.1).

Le panneau de droite montre le tracé du nombre de GC et de la masse du halo de la galaxie. La masse du halo a été estimée à partir des effets gravitationnels de la matière noire. La relation entre M_{halo} de la galaxie et son N_{GC} est linéaire. Ceci indique qu'il existe une relation linéaire entre le nombre de GCs d'une galaxie et sa matière noire. L'origine de cette relation proviendrait du théorème de la limite centrale et de la fusion des galaxies. Elle prédit que la fusion des halos de faible et de forte masse et de leurs galaxies donne lieu à des propriétés moyennes du halo. La relation entre N_{GC} et M_{halo} peut être utilisée pour déduire la masse de la matière noire dans une galaxie en mesurant la taille de son système GC. D'un point de vue observationnel, cela est beaucoup plus facile et moins coûteux que d'obtenir les spectres de ces GC afin de déduire M_{halo} de la cinématique du système GC. Les masses du halo de DM pour les UDGs déduites de leur population de GC se sont avérées cohérentes avec d'autres mesures de la dynamique des GC et de la dispersion des vitesses stellaires.

1.15.4 Les CG comme indicateurs de distance

Idéalement, une bougie standard devrait être brillante, se trouver couramment dans l'univers et avoir exactement la même magnitude absolue partout. Les anciens amas globulaires possèdent ces propriétés (non pas individuellement mais en tant que groupe), on les trouve dans tous les types de galaxies, ils sont brillants et seulement éclipsés par des galaxies brillantes et des supernovas et peuvent donc être utilisés comme de bons indicateurs de distance. La distribution de la luminosité des amas globulaires est similaire dans toutes les galaxies et atteint son maximum à une magnitude absolue de $M_V. \sim -7.5$. Ce pic de la FCG a été établi comme un indicateur de distance standard. La précision intrinsèque de la méthode est estimée à environ $\sim$ 0,2 mag (Rejkuba, 2012) ce qui la place au même niveau que les autres bougies standard.

La détermination de la distance à l'aide de la FCG est relativement simple et moins coûteuse d'un point de vue observationnel. Il suffit d'observer les GC des galaxies cibles jusqu'à une magnitude limite suffisamment profonde, et de comparer la fonction de luminosité avec la distribution de magnitude connue. En effet, à 30 Mpc le pic de la FCG est déjà décalé à $m_V \sim 25$ et la localisation du pic nécessite des mesures qui vont 1-2 magnitudes plus profondes. La bougie standard du FSCG est calibrée par rapport aux GCs de MW en se basant sur des distances d'amas précises qui sont dérivées d'indicateurs de distance primaires. La magnitude de rotation (TOM) (voir section 1.13) est la valeur qui est comparée à la TOM du MW ou à la TOM du GCLF M31. Les estimations des valeurs standard sont basées sur l'échelle de luminosité RR Lyrae pour le MW et les distances des céphéides par rapport à M31. L'application la plus courante de la mesure de distance à l'aide du GCLF concerne les galaxies de type précoce. Elles possèdent une riche population de GC qui est relativement plus facile à détecter que les galaxies spirales où le problème dû à l'extinction et à l'encombrement est sévère. Les mesures du FGCL sont également utilisées pour tester les distances mesurées par d'autres moyens comme les distances des Céphéides, la mesure de la distance en utilisant la pointe du RGB, les fluctuations de la luminosité de surface, etc. Le TOM du GCLF est également utilisé au début des années 60 pour déterminer la valeur de la constante de Hubble, H_0. En utilisant les magnitudes des amas individuels autour de M87, la valeur de la constante de Hubble a été déterminée comme étant de 68 ± 10 km s^{-1} Mpc^{-1} (van den Bergh, 1985). Il a été avancé que la précision de cette méthode dépend de l'environnement de la galaxie (Villegas et al., 2010). Il est recommandé d'utiliser les magnitudes du proche IR et d'appliquer la méthode aux GC pauvres en métaux.

1.15.5 Lien entre les GC et les galaxies naines ultra compactes, et les amas d'étoiles nucléaires.

- *Nuclear star clusters (NSC)*

  Lorsque l'on parle d'amas d'étoiles, il serait injuste de ne pas mentionner la catégorie spéciale d'amas que sont les amas d'étoiles nucléaires. Les amas d'étoiles nucléaires sont les amas d'étoiles denses et massifs que l'on trouve au centre de la plupart des galaxies (figure 1.12) (Côté et al., 2006; Seth et al., 2006; Neumayer, 2012). Elles ne deviennent rares que dans les galaxies elliptiques les plus brillantes et dans les galaxies naines les moins lumineuses : (Eigenthaler et al., 2018; Sánchez-Janssen et al., 2019a). Elles sont lumineuses et compactes et sont généralement plus denses que les GC. On les trouve dans des galaxies de différents types morphologiques, ce qui soulève la question de savoir si elles sont formées et évoluent de manière similaire ou si cela dépend de leur environnement hôte. Deux scénarios de formation les plus favorisés sont suggérés pour la formation des NSCs. Dans le premier scénario proposé qui est appelé le *Globular cluster infall and merging* les amas massifs migrent vers le centre de la galaxie et fusionnent pour former le NSC (Tremaine et al., 1975). La deuxième voie proposée s'appelle la *Formation in situ* et soutient que le centre galactique, étant le puits de potentiel profond, est l'endroit où la plupart des transports de gaz à grande échelle ont lieu et le gaz accumulé déclenche la formation d'étoiles massives qui forment la NSC (Milosavljević, 2004).

  Il y a près de deux décennies, une nouvelle classe d'objets astrophysiques a été découverte dans l'amas de galaxies Fornax (Hilker et al., 1999; Drinkwater et al., 2000; Phillipps et al., 2001). Ces objets semblaient être des objets de transition entre les GCs et les galaxies de type précoce. Ils avaient des luminosités comparables aux galaxies elliptiques naines (dE) et des tailles beaucoup plus petites que les dEs typiques mais plus grandes pour un amas globulaire normal. On les a donc nommées galaxies naines ultra compactes (UCD). Les UCDs sont caractérisées par de vieilles populations stellaires et ont des rayons typiques de 10-100 pc et des masses qui varient de $10^6 - 10^8$. $M_\odot$.

  En comparaison avec les GC, la relation masse-radius entre les GC et les UCD est différente, ce qui indique la possibilité que les deux ont des histoires d'évolution différentes, tandis que la transition continue dans les tailles peut signifier un scénario d'origine similaire (Dabringhausen et al., 2008). Comparés aux GCs, les UCDs ont typiquement un rapport M/L deux fois plus élevé (Drinkwater et al., 2003) ce qui peut signifier qu'ils possèdent de la matière noire ou qu'ils abritent une population stellaire qui a une fonction de masse initiale différente de celle des GCs canoniques résolus en MW.

Plusieurs scénarios de formation sont suggérés pour la formation des UCDs. L'un d'eux propose que les UCD soient les GC les plus lumineux formant la queue de l'extrémité brillante du GCLF (Mieske et al., 2002), ou qu'ils soient le résultat de fusions d'amas massifs (par exemple - Fellhauer and Kroupa (2002)). Dans un autre scénario proposé, ils sont considérés comme le noyau de galaxies nucléées dont les enveloppes de faible luminosité ont été éliminées lors d'un décapage par effet de marée (par exemple : Bekki et al. (2001)). Bassino et al. (1994) a suggéré qu'une galaxie naine nucléée subissant un effet de marée perdrait tout son matériel à l'exception des membres les plus robustes de la galaxie, c'est-à-dire son amas d'étoiles nucléaires, et l'objet résultant serait un UCD. Mais pour expliquer le rapport élevé entre la masse et la lumière observé dans les UCDs, qui est probablement absent dans les NSCs si elles sont effectivement formées à partir de GCs, il doit y avoir d'autres explications. Il est largement admis que la possibilité de canaux de formation multiples pour les UCDs ne peut être niée (Mieske, 2006; Brodie et al., 2011; Norris and Kannappan, 2011)

1.16 Techniques d'observation

Les stratégies d'observation adoptées pour étudier les amas d'étoiles peuvent être divisées en deux types, les méthodes adoptées pour les amas d'étoiles résolus, c'est-à-dire les amas dont la distance est < 1 Mpc, et les méthodes adoptées pour les amas d'étoiles non résolus. Les amas résolus peuvent être étudiés en utilisant la photométrie ou la spectroscopie d'étoiles individuelles, et ces méthodes peuvent être utilisées pour les GC de la Voie lactée et d'autres galaxies du groupe local. Les amas spatialement non résolus sont observés par photométrie et spectroscopie pour leur luminosité intégrée. Les techniques d'observation sont similaires mais l'analyse est différente pour les amas spatialement résolus et non résolus.

1.16.1 Méthodes pour les amas résolus dans l'espace

Photométrie

La photométrie est une méthode très courante pour mesurer les flux stellaires des étoiles d'amas résolus et elle trouve une large application dans la construction des diagrammes couleur-magnitude, qui sont utilisés pour estimer d'autres paramètres des amas comme leur âge, leur métallicité et leur distance. Les diagrammes couleur-magnitude sont également utiles pour détecter la population stellaire multiple dans les GC. La figure 1.14 montre le diagramme couleur-magnitude du GC galactique NGC 2808 construit à partir des magnitudes UV et visibles de *HST* UVIS/WFC3 et ACS/WFC. Le diagramme montre différentes combinaisons de magnitudes et de couleurs qui mettent en évidence la présence de multiples séquences d'étoiles dans le GC à différents stades d'évolution.

1.16.2 Spectroscopie stellaire

La spectroscopie est souvent employée pour étudier les abondances chimiques des étoiles en amas à l'aide de spectres à haute résolution. Un spectre de résolution moyenne peut être utilisé pour estimer les paramètres atmosphériques des étoiles (T_{eff}, log g, et [Fe/H]). Les spectres des étoiles sont comparés à des bibliothèques stellaires pour déterminer ces paramètres. Plusieurs modèles stellaires sont disponibles dans différentes gammes de longueurs d'onde et peuvent être utilisés pour déterminer les abondances et les paramètres des amas. Les bibliothèques stellaires disponibles sont généralement soit des bibliothèques théoriques qui utilisent des étoiles synthétiques, soit des bibliothèques stellaires empiriques qui consistent en des étoiles réelles dont les paramètres atmosphériques sont connus. Ces deux types de bibliothèques présentent des avantages et des inconvénients. Dans le chapitre 2, nous discuterons de la détermination des paramètres atmosphériques des amas à l'aide de bibliothèques stellaires empiriques et nous comparerons les valeurs obtenues avec celles obtenues à partir des bibliothèques stellaires théoriques.

La spectroscopie est souvent utilisée pour déterminer les vitesses radiales des étoiles dans les amas. Le *Télescope spatial de Hubble* et le *GAIA* ont révolutionné le domaine en fournissant des vitesses radiales et des parallaxes pour tous les GC connus dans la Voie lactée. Cela a permis de fournir des orbites précises des GC et une meilleure estimation de la masse de la Voie lactée. Récemment, la combinaison de l'optique adaptative avec des spectrographes 3D a permis de mesurer des spectres depuis le sol dans des zones encombrées auparavant inaccessibles (par exemple l'instrument MUSE sur le Very Large Telescope de l'Observatoire Européen Austral).

1.17 Motivation et plan

Dans ce chapitre, nous avons essayé de couvrir certains des aspects importants de la science des amas globulaires, et nous sommes encore loin d'être exhaustifs. Mais il est clair, d'après ce que nous savons de ces objets astrophysiques d'apparence si simple, qu'ils sont vraiment compliqués et mystérieux. La compréhension des amas globulaires est également essentielle pour comprendre les grands piliers de l'univers, comme les galaxies, et les petites briques qui forment ces piliers, à savoir les étoiles.

1.17.1 Bibliothèques stellaires

Les amas globulaires résolus de notre galaxie abritent des dizaines de millions d'étoiles et, en fonction de leur masse initiale, ces étoiles se trouvent à différents stades de leur vie évolutive. Cela fait des amas globulaires un site idéal pour étudier les étoiles et tester notre compréhension théorique de leur évolution. Dans la première partie de cette thèse, nous profitons du fait que les amas globulaires accueillent des étoiles à tous les stades de leur évolution pour tester les performances des bibliothèques stellaires. Nous utilisons les spectres de $\sim$ 6000 étoiles dans un amas globulaire galactique, NGC 6397 et estimons leurs paramètres atmosphériques en utilisant deux bibliothèques stellaires empiriques. Nous comparons ces valeurs avec les valeurs des paramètres atmosphériques estimés dans un autre travail utilisant une bibliothèque stellaire théorique. Nous présentons les différences entre les diverses estimations et soulignons le problème de cohérence entre les différentes bibliothèques stellaires. Ces bibliothèques stellaires sont les données standard qui sont utilisées pour dériver les paramètres physiques des systèmes stellaires observés, et il est primordial de connaître les défauts des bibliothèques utilisées et si possible de mettre en place des méthodes pour minimiser ces défauts.

1.17.2 Les GC extra-galactiques et leur relation couleur-environnement

L'une des façons de combler le fossé entre les bibliothèques standard et les données réelles est de comparer les prédictions des modèles de population stellaire simple (SSP) avec des systèmes stellaires simples approximatifs, à savoir les amas globulaires. Toutes nos bibliothèques empiriques actuelles sont conçues, pour des raisons évidentes, à partir d'étoiles galactiques. Il est important d'évaluer dans quelle mesure les systèmes stellaires simples extra-galactiques correspondent ou non aux modèles dont nous disposons. Dans certains travaux antérieurs sur le système extra-galactique des GCs, il a été trouvé que la distribution des couleurs des GCs peut être une fonction de leurs environnements (Powalka et al., 2016b). Dans la deuxième partie de la thèse, nous effectuons une analyse similaire pour le système GC de M49, l'une des galaxies elliptiques les plus massives de l'amas de la Vierge. Elle traite de la photométrie dans l'infrarouge proche dans les champs autour de M49 et utilise les informations de couleur des objets pour identifier les amas globulaires. Dans la suite de la thèse, nous étudierons la relation entre les couleurs des GCs et leur environnement.

1.17.3 Outline

Dans le chapitre 2, nous abordons la diffusion atomique dans les étoiles et sa théorie. On s'attend à ce que la diffusion atomique modifie les abondances de surface dans les étoiles et son effet est visible dans les étoiles MSTO (Main Sequence Turn Off) où les métaux coulent vers le bas, ce qui réduit la métallicité de surface des étoiles MSTO. Nous utilisons deux bibliothèques empiriques appelées ELODIE et MILES pour estimer les paramètres atmosphériques de 6000 étoiles dans le GC NGC 6397 en utilisant des spectres MUSE de moyenne résolution. Dans ce chapitre, nous comparons les tendances de la métallicité observées dans le diagramme H-R prédites par les deux bibliothèques empiriques avec les tendances prédites par la bibliothèque théorique GSL adoptée dans un travail précédent. adoptée dans un travail précédent.

Le chapitre 3 fait la transition vers la deuxième partie de la thèse et ce chapitre explique la réduction des données dans l'infrarouge proche dans les 9,5 degrés carrés autour de M49 et les 13 degrés carrés dans la région intra-amas entre M87 et M49, et l'extraction des GC dans la zone d'étude. Nous décrivons l'étude et l'acquisition des données, suivies du premier passage de la réduction des données au CASU (Cambridge Astronomy Survey Unit) et de la soustraction du bruit de fond réalisée par nos soins. Nous adoptons les données optiques de notre champ à partir des archives du CCDA pour les comparer aux objets détectés dans les bandes du proche infrarouge. Nous décrivons également la soustraction des galaxies de M49 et la détection des objets dans le champ soustrait des galaxies dans le proche infrarouge ainsi que dans les bandes optiques. Le chapitre traite également de la calibration des données photométriques et astrométriques et d'autres étapes supplémentaires pour la réalisation du catalogue d'objets dans le champ et enfin du catalogue généré pour le champ.

Dans le chapitre 4, nous décrivons la sélection des candidats amas globulaires dans le champ en utilisant le diagramme *uiKs* (Muñoz et al., 2014). Ces candidats GC sont soumis à divers tests qui utilisent des limites dans les magnitudes et les paramètres morphologiques dérivés en utilisant l'information dans les bandes optiques pour réduire la contamination des étoiles et des galaxies dans l'échantillon. Nous divisons ensuite cet échantillon en groupes qui sont classés en fonction de leur environnement.

Dans le chapitre 5, nous discutons de la complétude et de la contamination du catalogue de GC en comparant notre échantillon avec les données de GC de l'ACSVCS dans le champ et avec un échantillon de GC confirmés par spectroscopie autour de M49. Dans ce chapitre, nous parlons également de la distribution des couleurs des GCs qui appartiennent à différents environnements, suivie de leur distribution couleur-couleur. Nous comparons les tendances couleur-couleur de différents groupes et avec les GCs de M87. Nous concluons le chapitre par une discussion sur les raisons possibles des différences observées.

Dans le chapitre 6, nous résumons la thèse.

CHAPTER TWO

NGC 6397 : TESTING STELLAR MODELS WITH ATOMIC DIFFUSION

"The Universe seems neither benign nor hostile, merely indifferent." - Carl Sagan

Abstract

In this chapter we compare the performance of empirical and theoretical stellar libraries in the metal poor regime most relevant to the globular clusters. We use these libraries to determine atmospheric parameters of about 5000 stars in the GC NGC 6397. We use medium resolution VLT/MUSE spectra of the stars in the GC and estimate their atmospheric parameters like effective temperature and metallicity by comparing the spectra with those of the empirical libraries MILES and ELODIE. In previous work that used a theoretical spectral library called the Göttingen Spectral Library (GSL) to obtain these parameters, a metallicity gradient between the turn off and the red giant stars was found which was interpreted as a possible evidence of atomic diffusion in stars. We show that the analysis of the same data with the empirical libraries cannot reproduce the trends. On one hand this calls for confirmation of the trends with the given grids of synthetic spectra. On the other hand our study highlights the need to improve the empirical spectral libraries in the low-metallicity regime.

This chapter is based on the article : **NGC 6397: The metallicity trend along the isochrone revisited**, 2020, Rashi Jain, Philippe Prugniel, Lucimara Martins, and Ariane Lançon, submitted to A & A 635,A161 (ADS entry to the article).

2.1 Atomic diffusion in stars

Important constraints on the conditions under which stars formed can be inferred from the atomic composition and this has been a major driver of many spectrscopic surveys. This association of chemical properties of stars with their home environments is called chemical tagging. But over the course of its life-cycle the surface abundance of a star is altered owing to various processes taking place withing its fiery interior. The eventual surface abundance of a star is modified heavily and is no more the same as its initial abundance. These two abundances (initial and surface) of a star are not interchangeable. In order to better estimate the parameters of a star (age, mass and radius) it is important to correctly address this distinction in the stellar evolutionary models. Age estimates of the objects such as GCs can be biased if the surface abundances of selected stars are assumed to represent their initial abundances.

Given the repercussions on the evolutionary models, it is important to address the causes of alteration of the initial chemical composition of a star on its surface. During the life cycle of a star a number of transport processes are in action. These transport processes can be broadly classified into microscopic (like atomic diffusion) and macroscopic (like convection) processes. Atomic diffusion is a consequence of a tussle between radiation pressure that tries to push the larger atoms upwards, and gravitational settling that tries to gravitate the heavy atoms towards the centre of the star. In the pursuit of equilibrium, there are gradients of pressure, densities, and temperature that produces selective transfer of chemical elements. This process either leads to a local depletion or to accumulation of the chemical element but the net effect depends on a lot of factors such as the nature of the element, its total abundance, its ionization state, etc. (Deal et al., 2020).

The macroscopic transport processes transport the material on a larger scale. These processes are in direct competition with the microscopic processes. The effect of these processes is a largely dependant on the time-scale of their action. If the time scale of microscopic processes is larger then the effects of the atomic diffusion are mostly wiped out. In most of the stellar models convection is most commonly accounted for macroscopic transportation process but convection by itself is found to be inadequate to explain the abundances in observed stars.

Figure 2.1 shows an over-simplified illustration of gravitational settling working against the radiative acceleration procedure in the convection zone of a low mass main sequence star.

The effect of including atomic diffusion in stellar evolutionary codes on the predicted ages of the globular clusters is known to make a difference of about 10-12 % (VandenBerg et al., 2002b). The age estimates with models that do not account for mixing processes to distinguish surface abundance from initial abundance reach values around 15 Gyr, which are unlikely given that even the universe is not that old. If the distinction between the initial and surface abundance is made in the models the age estimates are reduced by 10%-12% and the cluster ages drop to 13.5 Gyr .

The term atomic diffusion has been theorized more than a century ago by Chapman,

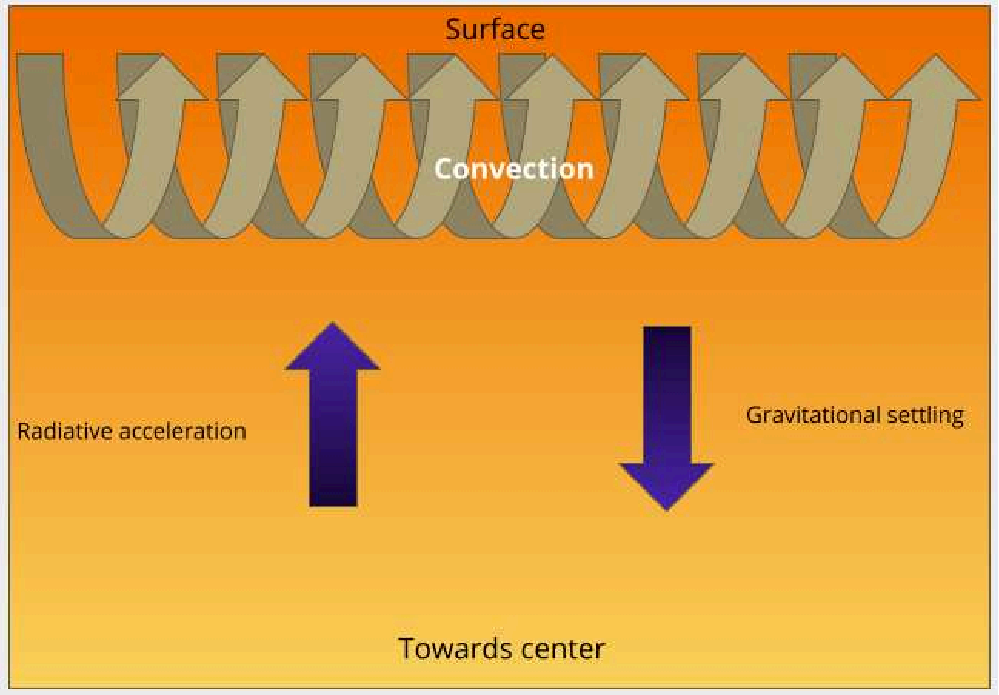

Figure 2.1 Simplified diagram of interior of a relatively low mass main sequence star demonstrating atomic diffusion. The top of the block is the surface of the star while the bottom of the figure is towards the center.

1917a. The mixing processes (e.g. convection and turbulent mixing) within a star are constantly competing against the gravitational settling and thus attempting to neutralize any depletion of the heavy elements. There is no clear theoretical description of the efficiency of these forces at work and the only way to quantify their effects is to do observational studies. Globular clusters are the perfect site to test these effects because of the advantage that they host co-evolving stars that had same initial metallicity. Husser et al. (2016, hereafter H16) performed such a study for the GC NGC 6397. They used medium resolution spectra of 12000 stars, estimated their stellar parameters, and found a trend in metallicity in the HR diagram that could be attributed to atomic diffusion. We will describe the findings of this work, which is also the basis of our analysis, in detail in the next section.

2.2 Atomic diffusion in NGC 6397 - Introduction to earlier study

The data in the work of H16 were obtained with wide-field integral spectrograph MUSE (Bacon et al., 2014) mounted at UT4 (Yepun) of the ESO Very Large Telescope (VLT). MUSE has a field of 1 arcminute which makes it convenient to observe an entire globular cluster in a reasonable number of pointings. This has the advantage of covering numerous stars in a single pointing. Medium resolution spectra might not provide us the details to study abundances of a star, but they are very well suited to determine the stellar parameters via full spectrum fitting. Koleva and Vazdekis (2012) have shown that the stellar atmospheric parameters like effective temperature (T_{eff}), surface gravity ($log\ g$), and metallicity ($[Fe/H]$) can be obtained from spectra of resolution $\lambda/\delta\lambda \sim 1000$ without the lower resolution affecting precision or introducing significant biases. In the present data set there are stars with a wide range of apparent magnitudes and hence with a variety of signal-to-noise ratio (SNR), therefore a full spectrum fitting is of great advantage.

In their work, H16 reduced 18932 spectra of 12307 stars extracted from a mosaic of 23 MUSE pointings. They performed a full spectrum fitting by comparing the spectra against a grid of models (Husser et al., 2013, the *Göttingen Spectral Library*, GSL) computed with the *PHOENIX* synthesis code (Allard and Hauschildt, 1995) and interpolated to minimize the residuals. In that work, the authors have found a metallicity trend along the isochrone such that the metallicity of the Turn-Off (TO) stars is the minimum and it increases along both the Main sequence (MS) and the sub-Giant branch (sGB). The magnitude of this trend is 0.2-0.3 dex. This trend could be interpreted as a result of atomic diffusion, which is expected to cause a reduction in the surface abundance of metals due to inefficient mixing processes near the turn-off (Richard et al., 2002).

Nordlander et al. (2012a) conducted a detailed abundance analysis on individual stars of NGC 6397 and found a similar trend in metallicty, albeit less strong. The effect was of the order of $\sim$ 0.1 dex but it was based on a smaller number of stars taken in each evolutionary phase of interest. That work highlighted the sensitivity of the metallicity trend to the model aspects such as the efficiency of the turbulent mixing, the temperature scale, non-local thermal equilibrium (NLTE) and 3D effects.

H16 computed the model grid using 1D spherical models. Their reference stellar library, GSL, has spectra calculated at regular intervals of T_{eff}, *log g*, [Fe/H], and [α/Fe] parameter space. The steps in metallicity are of 1 dex for [Fe/H] $<$ -2.0, and 0.5 for [Fe/H] $>$ -2.0. Figure 2.2 shows the distribution of the GSL spectra in the log g vs T_{eff}, and [Fe/H] vs T_{eff} planes plotted over the individual cluster stars of NGC 6397. The cluster metallicity is [Fe/H] $\sim$ 2.02 dex and the whole metallicity range is well withing -1.5 and -3.0.

The magnitude of the metallicity variations along the GC isochrone are only a fraction of the step of the metallicity grid of reference synthetic spectra. It cannot be entirely ruled out that the observed trend in H16's work is a result of spline interpolation in the grid The results directly impact our understanding of mixing procedures in stars which are known to have implications on general star cluster properties like their ages and location of turn-off (TO) stars. In our study we re-assess the stellar parameters by comparing the

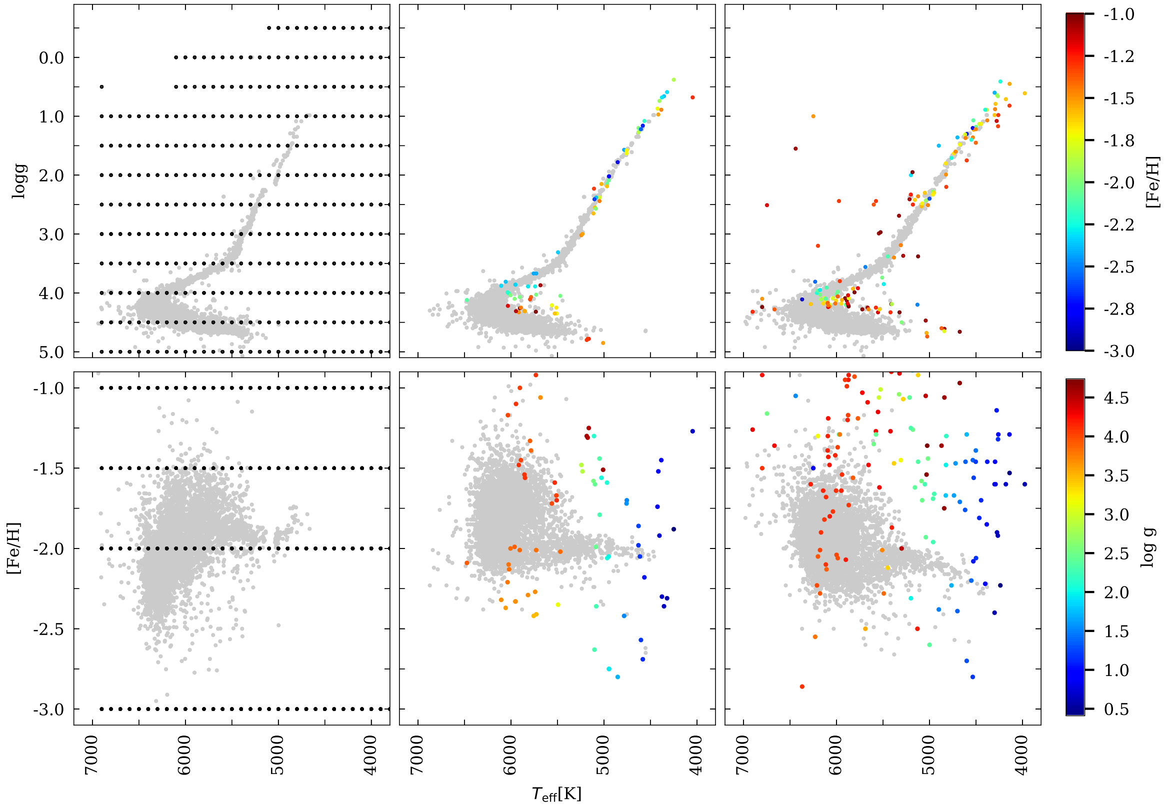

Figure 2.2 Distribution of the library spectra in the region of the parameter space occupied by the cluster stars. The gray dots represent the H16 measurements of the cluster members. The top graphics are the projections in the log g vs. $T_{\rm eff}$ plane and the bottom graphics show the [Fe/H] vs. $T_{\rm eff}$ projections. The over-plotted colored points are the location of the reference spectra in the three libraries used in this work. The left panel shows the Göttingen Spectral Library used by H16, the central panel shows the ELODIE library, and the right panel the MILES library. These last two libraries were used in our reanalysis. Only the library stars corresponding to the region mapped by the our sample are shown: $T_{\rm eff} < 7000$ K, and $3.04 <$ [Fe/H] < 0.88 dex (77 stars for ELODIE and 137 for MILES, including 40 and 46 stars, respectively with [Fe/H] < 1.7 dex). The color scales for the ELODIE and MILES libraries are indicated on the right.

MUSE spectra of stars in NGC 6397 against empirical libraries, ELODIE and MILES. By comparing the spectra with a different kind of reference library than H16, we introduce a set of different biases. Differences with the results of H16 will provide an assessment of systematic uncertainties, and the basis for future improvements.

2.3 Data and earlier analysis

The observations of a 5 x 5 mosaic[1] reaching out to a distance of $\sim$ 3.5 arcmin from the cluster centre were made during MUSE commissioning, between July 26nd to August 3rd, 2014 (ESO program identifier `60.A-9100(C)`). They consisted in 127 pointings of exposure time of not more than 60 s to avoid the saturation of the bright giant stars, for a total integration time of 95 min. Each pointing covers a field of 1 x 1 arcmin with a spatial step of 0.2 arcmin, and the seeing was in the range 0.6” to 1”.

The data reduction was done by the MUSE consortium using the official pipeline, and the extraction of the individual stellar spectra was described in H16, with a de-blending approach presented in Kamann et al. (2013, implemented in the PampelMuse software, publicly available). This method relies on a photometric and astrometric input catalogue, which in this particular case was the Anderson et al. (2008) table derived from images obtained with ACS on-board the Hubble Space Telescope. An initial Point-Spread-Function (PSF) model, set to be the seeing, is used to create a mock image that is cross-correlated with each wavelength layer of the MUSE cube to find the coordinates transformations. The most isolated and bright spectra are used to iteratively refine the PSF by subtracting all the other spectra. The final wavelength-dependent PSF is derived by smoothing the PSF obtained for each layer, and it is used to extract the spectra. In total, 18 932 spectra of 12 307 stars were extracted. The stars in the overlapping regions between the different fields were observed multiple times. The line spread function (LSF) varies with the wavelength from a full-width at half maximum (FWHM) of about 2.82 Å at λ = 4750Å (equivalent to an instrumental velocity dispersion, $\sigma_{ins} = 80$ km s^{-1}), to about 2.54 Å at λ = 7000Å ($\sigma_{ins} = 46$ km s^{-1}), and stay approximately constant further in the red. The actual LSF also varies across the 24 spectrographs forming MUSE by roughly 0.1 Å.

Out of the 18 932 extracted spectra, 14 271, with an SNR greater than 5, are distributed on the MUSE web site[2] (the raw data are available in the ESO archive[3]).

To determine the atmospheric parameters, H16 proceeded in three steps. First they obtained T_{eff} and log g by fitting the HST photometry to an isochrone. They then used these

---

[1] Two of the planned fields, located at the periphery, were not observed; 23 fields are available.

[2] http://muse-vlt.eu/science/globular-cluster-ngc-6397

[3] http://archive.eso.org/

parameters to generate interpolated models that they cross-correlated with the observations to derive the radial velocity ($v_{\rm rad}$). At the third step, they performed an optimisation to produce the final $T_{\rm eff}$, [Fe/H], $v_{\rm rad}$, line broadening, and telluric absorption spectrum. They used their own full-spectrum fitting procedure, using GSL interpolated by cubic-spline as reference. The interpolation cannot be a simple linear interpolation, because the optimisation method requires its derivative to be continuous. It shall be noted that log g is not optimised; the adopted value is the photometric one. The authors justify this choice as precautionary approach to prevent a possible degeneracy between log g and the broadening.

This analysis provided parameters for 5 882 spectra of 4 132 stars having SNR $>$ 20, above which the formal error on $T_{\rm eff}$ is lower than 100 K, and on [Fe/H] lower than 0.16 dex. The tables with results were kindly provided to us by Tim-Oliver Husser. For 367 of these spectra log g was not determined, and consequently neither $T_{\rm eff}$ nor [Fe/H] were measured. To clean the sample of the non-member stars, we select the spectra within an ellipse centered on $v_{\rm rad}$ = 17.8 km s^{-1}, and [Fe/H] = -1.96 dex (mean parameters of the cluster), and semi axes of 29 km s^{-1} and 1.08 dex (corresponding approximately to the selection area measured on the figure 7 of H16; the actual values are not mentioned in the text of this work). The sample is reduced to 5 510 spectra of 4 089 distinct cluster members. Furthermore, in this chapter we are interested in the TO and red giant branch (RGB), and as the method of determining the stellar parameters by full spectrum fitting has never been validated for the hot stars, we will follow H16 and limit the sample to $T_{\rm eff}$ $<$ 7000 K. The latter criterion excludes the hot horizontal-branch stars. Finally, the sample counts 5 400 spectra of 4 053 distinct cluster members.

2.4 Re-analysis

2.4.1 Method

The immediate aim of this work is to repeat H16's analysis of the metallicity trend along the cluster sequence with other reference libraries, in order to check its robustness. Alternatives to GSL are amongst others, the ELODIE and MILES empirical libraries. Synthetic and empirical libraries are seen as complementary, with each having their advantages and drawbacks. On the one hand, synthetic spectra can be computed at any point in the parameter space, and are therefore not limited to the region populated with stars that can be observed (i.e. essentially stars from the Solar neighbourhood). They are also free of noise and observational signatures, and their spectral resolution can be as high as necessary. However, synthetic spectra still fail to accurately match observed spectra, because of the limitations of the physical models and of the lists of atomic and molecular transitions (Martins et al., 2014; Lançon et al., 2021). On the other hand, empirical libraries can accurately reproduce observed spectra, and this is why they are extensively used to model integrated spectra of stellar populations (Martins et al., 2019).

ELODIE is an empirical library, initially presented in Prugniel and Soubiran (2001) and later upgraded to increase the coverage in the parameter space. We use the latest version (version 3.2), described in (Wu et al., 2011), containing 1962 spectra at a constant FWHM resolution of 0.55 Å over the wavelength range 3900 – 6800 Å (R $\approx$ 10 000). The second library, MILES (Sánchez-Blázquez et al., 2006), contains spectra of 985 stars at a resolution about 2.55 Å (R $\approx$ 2000) in the wavelength range 3536-7410 Å. The distribution of the stars populating the region of the cluster in the parameter space are represented in the central and right panels of Fig. 2.2, for respectively ELODIE and MILES. Both libraries sample reasonably well the region of the RGB, down to almost the TO. Along the MS, most of the stars are on the high-metallicity side compared to the cluster, and only a few have the cluster's metallicity. It is also noticeable that the libraries MS are shifted toward lower gravities by about 0.1 dex compared to the cluster stars gravities determined by isochrone fitting. We found indications that this may be at least partly due to an under-estimate of the gravities given with the libraries.

The fitting procedure to be used for stellar parameters estimation requires to interpolate through the libraries, to compute a spectrum for any set of T_{eff}, log g, and [Fe/H]. To this purpose, we are using polynomial interpolators computed using stellar parameters of the library stars compiled from the literature, generally obtained through detailed abundances studies using high-resolution spectroscopy. The ELODIE interpolator is described in Wu et al. (2011), and for MILES, we use the one described in Sharma et al. (2016). The quality of the interpolated spectra naturally depends on the distribution of the stars in the parameter space: the densest it is, the best we can expect the interpolation to be. It also depends on the accuracy of the input stellar parameters used when computing the interpolators, and on the intrinsic accuracy of the interpolators. At the margin of the parameter space, the interpolators use synthetic spectra to extend the validity range, however with a lower quality. The main sequence of the cluster is at the edge of the validity region of the interpolators. However, using the procedure described below, we successfully fitted synthetic spectra from Coelho et al. (2005) and from GSL chosen to map this regime. This gave us some confidence in our ability to analyse MS spectra. However, similar tests with the cluster's spectra failed to restore the correct gravity. The solutions were found at a correct temperature, but located on the giant branch. The reasons for this difficulty are not completely clear, but are probably related to the drop in SNR from ∼60 near the turn-off to ∼20 on the lower MS, and to larger effects of contamination by other cluster stars for the fainter objects. In the present analysis, we prefer to restrict the spectral analysis to logg<4.2 and high SNR. and are subject to a strong light contamination by the other cluster's stars. Although in the present analysis we will follow H16 and adopt the isochrone's gravities, we prefer to restrict the present analysis to the RGB, logg < 4.2. This sample counts 1 587 spectra of 1 063 stars.

The determination of the atmospheric parameters is made with the ULySS package (Koleva et al., 2009) by minimising the squared residuals between the MUSE observation and an interpolated spectrum:

$$S(\lambda) = P_n(\lambda) \times G(v_{\mathrm{rad}}, \sigma_{\mathrm{rel}}) \otimes \mathrm{TGM}(T_{\mathrm{eff}}, \mathrm{logg}, [\mathrm{Fe/H}], \lambda), \tag{2.1}$$

where $P_n(\lambda)$ is a series of Legendre polynomials up to degree n, meant to absorb the instrumental spectral response and line-of-sight extinction; we are using $n = 20$. $G(v_{\mathrm{rad}}, \sigma_{\mathrm{rel}})$ is a Gaussian function centered at v_{rad} and with standard deviation σ_{rel}. The spectra are binned in logarithmic wavelength, so that the Doppler shift can be expressed by a convolution. TGM is the spectral interpolator. The free parameters are T_{eff}, [Fe/H], v_{rad}, σ_{rel} and the coefficients of $P_n(\lambda)$. See Arentsen et al. (2019) for other details on the procedure.

σ_{rel} was let free in order to account for the variation of instrumental broadening from spectrum to spectrum (as mentioned in Sect. 2.3, the MUSE LSF varies between the individual spectrographs). The relative LSF between MUSE and the libraries changes significantly over the wavelength range, and we therefore ingested this variation pattern in the interpolated spectra, before the minimization. This was made with a step-wise convolution of the library (see the ULY_LSF_CONVOL function in the ULySS package). The LSF injection improves the quality of the fits and slightly reduces the errors of the estimated parameters, but it does not affect the general trends.

In the case of the ELODIE library, the injected LSF was chosen so that the interpolated spectrum has a higher resolution than the MUSE spectrum. The observation is then fitted letting σ_{rel} free. For the MILES library, the resolution after the LSF injection is very close to the MUSE's one, but because of the spectrum-by-spectrum variations by 0.1 Å, it is sometimes lower. In such cases, detected because the first fit fails to determine σ_{rel}, we convolved the observation with a Gaussian with a dispersion of 30 $\mathrm{km\,s^{-1}}$, and then let the fitting procedure determine σ_{rel}.

A difference between the present procedure and H16's is that the latter adjusts the telluric absorption together with the stellar parameters and broadening. Telluric absorption features are prominent in the red part of the spectra that are not in the currently analysed region, and we more simply masked (i. e. ignored) the two strongest features. The first one is the water absorption near the NaD line affecting both the ELODIE and MILES, and the B band, near 6887 Å (Fraunhofer, 1817; Fraunhofer, 1821) affecting MILES.

No error spectra are associated with the extracted observations, but a *mean* SNR is provided. We used it to determine a noise level that we assume identical throughout the spectrum, meaning that all the wavelength bins have the same weight. This assumed error sets the scale of the fitting errors on the parameters that will be tuned in Sect. 2.4.2 into internal errors, by matching the repeated observations of stars in the overlaps of the different pointings.

In order to keep the re-analysis as close as possible to H16's, we carried it out by fixing log g to their photometric value (but see Sect. 2.5.2, where we also determine log g spectroscopically). As first guesses, for $T_{\rm eff}$, we used the photometric value, and for [Fe/H] we used -2.0 dex, which is an approximation of the cluster's metallicity.

2.4.2 Assessment of the internal errors

The full catalogue contains 5 510 measurements for 4 089 stars (including the stars from the MS to the RGB). For the 1 200 stars with two or more repeated observations, the spectra differ by the noise and by the propagation of systematics introduced by the spectrograph and data-reduction. We assessed the precision by comparing the atmospheric parameters measured on each pair of observations as in Arentsen et al. (2019). We computed for each pair of observations i:

$$\Delta \mathrm{P}_i = \frac{\mathrm{P}_{1,i} - \mathrm{P}_{2,i}}{\sqrt{\epsilon_{1,i}^2 + \epsilon_{2,i}^2}}, \tag{2.2}$$

where P can be $T_{\rm eff}$ or [Fe/H], ϵ is the formal ULySS error on the respective parameters, and 1 and 2 indicate the observation of each spectrum of the pair. This distribution should be nearly Gaussian, and if the errors are properly scaled, their standard deviation should be one. For both parameters we find $\Delta \mathrm{P} = 2.2$ and 1.8 respectively for ELODIE and MILES. Because we assumed a constant noise scaled to produce the average SNR determined by the data-reduction and spectra extraction pipeline, we indeed expected deviations from unity. We also assumed that all the pixels are independent, which cannot be the case because the spectra were rebinned into evenly sampled wavelength (this process necessarily introduces a correlation in the noise), and this leads to an underestimation of the errors.

We checked that these distributions are similar throughout all the parameter space, and we found only a marginal indication that they may depend on SNR, in a way consistent with an additional source of noise independent of SNR. The effect is of the order of 15 K and 0.01 dex to be quadratically added on respectively the errors on $T_{\rm eff}$ and [Fe/H], which is very small.

The fact that the distributions are similar for the two parameters is a satisfactory sanity check of our analysis, and we will not investigate further the deviations from unity as they have no incidence on the present discussion. We rescaled the errors by the aforementioned factors when computing the errors in the final table (see Sect. 2.4.4).

2.4.3 Assessment of the external errors (accuracy)

For an estimate of the external errors, we compare our measurements with previous works. First of all, the comparison of 1587 measurements with H16 indicates $T_{\rm eff}(\textsc{h16}) - T_{\rm eff}(\textsc{elodie/miles}) =$ 92 K with a dispersion of 40 K. For the metallicity, the bias is different for ELODIE or MILES: [Fe/H]($\textsc{h16}$) − [Fe/H]($\textsc{elodie}$) = −0.07 dex, and [Fe/H]($\textsc{h16}$) − [Fe/H]($\textsc{miles}$) = 0.03, with a dispersion of 0.15 dex. Since the three series used the same reduced spectra, they can be similarly affected by systematics due to the data. These figures shall therefore be regarded as lower-limits to the errors, and comparisons with independent measurements should give a more complete assessment of the external errors.

Five previous studies determined the parameters of a significant number of stars in this cluster. Carretta et al. (2009d) measured 13 stars at high spectral resolution, with the UVES spectrograph attached to the VLT, and Carretta et al. (2009b) measured 144 stars at intermediate resolution, with GIRAFFE on the same telescope, all giants with $T_{\rm eff} < 5400$ K. Lovisi et al. (2012) measured 146 stars, but those in common with the MUSE sample are mostly blue stragglers, which are not discussed in this work. Finally, Korn et al. (2007), and Lind et al. (2008) observed stars with respectively, the UVES (18 stars) and GIRAFFE (116 stars) spectrographs, but in more peripheral fields lying outside the MUSE pointings.

The comparisons with the two first datasets are very similar, so that we can merge them and report only the total comparison. We find $T_{\rm eff}(\rm lit) - T_{\rm eff}(\textsc{elodie}) = 15$ K with a dispersion of 30 K, and $T_{\rm eff}(\rm lit) - T_{\rm eff}(\textsc{miles}) = 48$ K with a dispersion of 25 K. For the metallicity, we find no differences with ELODIE, and [Fe/H](lit) − [Fe/H]($\textsc{miles}$) = 0.07 dex, in both cases with a dispersion of 0.05 dex.

The comparison between the H16 measurements and the literature displays the following differences: $T_{\rm eff}(\rm lit) - T_{\rm eff}(\textsc{h16}) = -100$ K and [Fe/H](lit) − [Fe/H]($\textsc{h16}$) = −0.08 dex, with dispersions of 48 K and 0.06 dex on the two parameters. In all cases the log g values are very consistent with the literature, which is understandable as they were in all cases determined photometrically with very similar methods.

The picture emerging from these comparisons is that (i) $T_{\rm eff}$ measured by H16 are on average hotter than the literature and our own measurements, (ii) [Fe/H] are reasonably consistent between the different series, our measurements being marginally more consistent with the literature than those of H16, and (iii) the consistency is similar for our two analyses, with a marginally better performance of ELODIE.

For the observations compared with the literature, the mean estimated internal errors, after the re-scaling described in Sect. 2.4.2, are 18 and 25 K on $T_{\rm eff}$, and 0.04 and 0.05 dex on [Fe/H] for respectively ELODIE and MILES, which is about 1.25 times less than the external dispersions estimated here. Since this dispersions include both the errors on our and on the literature measurements, we conclude that our estimates of the internal errors properly reflect the external errors, or accuracy of the measurements.

2.4.4 Results

Our measurements of the atmospheric parameters for the 1 587 spectra are available in electronic form in Vizier.

Figure 2.3 presents the distribution of the measurements in the log g vs T_{eff} plane. The vertical axis is the photometric gravity, and the horizontal axis is the T_{eff} from H16, ELODIE and MILES, respectively for the left, central and right panels. The data points are colour coded according to the metallicity. This can be compared with the figure 8 of H16. The RGB harbours an un-physical break in the H16 data near $T_{\mathrm{eff}} = 5000\,\mathrm{K}$. We cannot provide a final explanation for this break, but it may correspond to a discontinuity of the opacities used for GSL, at a threshold temperature where some molecular bands are considered. Globally, this RGB is hotter than in our analysis, reflecting the systematic difference quantified in Sect. 2.4.3, and also found when H16 is compared to earlier measurements. The small T_{eff} difference between ELODIE and MILES is consistent with the uncertainties on the temperature calibration of the RGB.

Figure 2.4 shows the distribution of the sample in the [Fe/H] vs T_{eff} plane. The top panel shows the result from H16 analysis, and the middle and lower panels are the results with the ELODIE and MILES interpolators respectively. In the three cases, the small dispersion around the observed trend reveals a high internal consistency. The mean [Fe/H] dispersion around the cluster isochrone, estimated as the average rms computed in the T_{eff} bins shown on Fig. 2.4, is about 0.07 dex. Compared to the 0.05 dex external error reported in Sect. 2.4.3, we do not see a clear indication of a cosmic dispersion.

Beside this internal consistency, the three analyses display different patterns of metallicity variation. The results with ELODIE would be consistent with a constant metallicity. The H16 metallicity steadily increases along the sGB, while the MILES trend is wavy, with a pronounced [Fe/H] decline immediately above the TO.

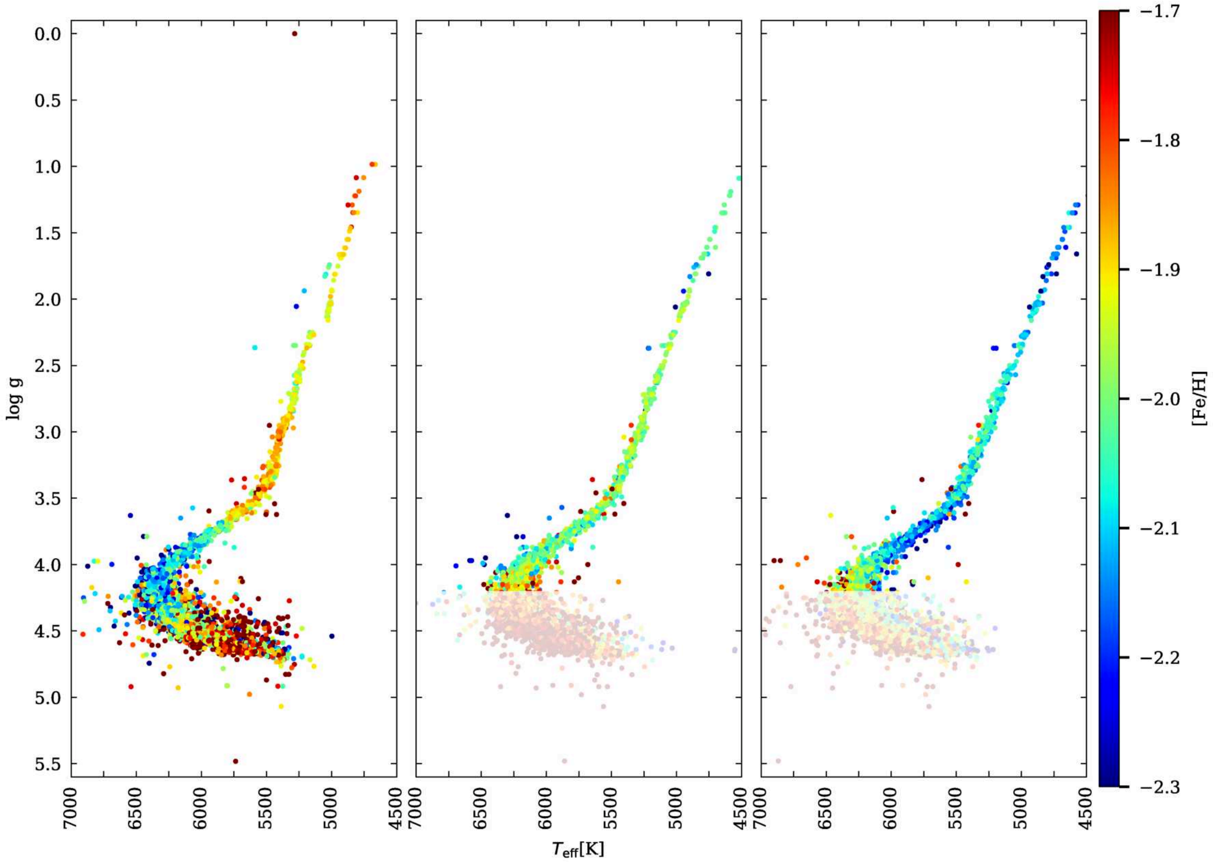

Figure 2.3 Distribution of the parameters measurements for the 5 400 spectra of cluster members with good quality spectra in the log g vs. $T_{\rm eff}$ plane. The left panel is the H16 catalogue, the central and right ones are the re-analysis presently carried-on with respectively the ELODIE and MILES interpolators. The colour scale, figuring the metallicity, is shown in the right margin. The region of the diagram excluded from the present discussion (logg $<$ 4.2), is shown with paler colours.

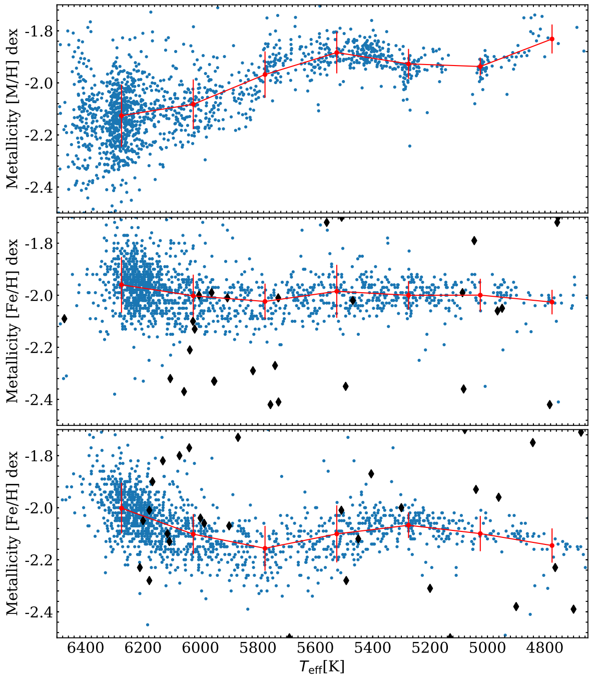

Figure 2.4 [Fe/H] vs. $T_{\rm eff}$ for the giants (logg < 4.2 dex). The top panel is the H16 catalogue, and the middle and bottom panels respectively our re-analysis with the ELODIE and MILES interpolators (blue dots). The solid red line connects the mean values and standard deviations of the metallicity in 250 K wide bins. The black dots show the location of the ELODIE and MILES library stars, respectively on the middle and bottom panels. The mean [Fe/H] dispersion in [Fe/H] of stars taken in bins of 250 K for H16 is 0.076, for ELODIE is 0.075 and that for MILES is 0.079 calculated for stars having $T_{\rm eff} < 6\,500$K.

2.5 Discussion

2.5.1 Changes of the surface metallicity above the turn-off

Considering that chemical tagging (the ability to associate individual stars with their birth environment) has been a science driver for many of the large surveys now underway, the ability to differentiate surface from initial abundances is a crucial necessity of stellar evolution models. Many processes can alter the surface abundance of a star during its life time, atomic diffusion being one of the mostly discussed of these processes. It encompasses different processes that operate in the radiative regions of the stars causing the redistribution of elements, mainly by the migration of heavier elements towards its center, and consequently lowering its surface metallicity. Although atomic diffusion in stars has been theorized more than a century ago by Chapman (1917b), its real effect on stellar evolution remains debated (VandenBerg et al., 2002a). Mixing processes (e.g. convection and turbulent mixing), are competing against the gravitational settling to weaken the actual depletion in heavy elements. The efficiency of these processes, at variance with the pure atomic diffusion, has no well-established physical description, and can only be determined through comparison with observations. For instance, Dotter et al. (2017) investigated models with and without these effects and finds that the differences in ages obtained through isochrones might reach up to 20%. Star clusters, where a coeval stellar population which, in principle, is initially chemically homogeneous, are the perfect laboratory to test the balance between the different phenomena.

It is expected that because of atomic diffusion, the surface abundance of heavy elements should be minimum at the TO, increasing both, down the MS and towards the RGB. Metallicity trends near the TO of globular clusters have been previously discussed in NGC 6752 by Gruyters et al. (2013), and in M 30 Gruyters et al. (2016), and in the M 67 open cluster by Bertelli Motta et al. (2018), Souto et al. (2018), Gao et al. (2018), and Liu et al. (2019b). In particular, for NGC 6397, Gratton et al. (2001), and more recently Lovisi et al. (2012) found no difference between the abundances of TO stars and base-RGB stars. At variance, Korn et al. (2007), Lind et al. (2008) and Nordlander et al. (2012b) found a clear trend. The latter three works found similar trends for the iron metallicity from the TO to the RGB, obtaining maximum metallicity differences of about $0.15 - 0.20$ dex. They argue that their results indicate the need of atomic diffusion with weak efficiency of turbulent mixing, but also that, given the uncertainties from modeling techniques, the possibility that this might be just an artifact cannot be ruled out. For example, the figure 7 of Lind et al. (2008) shows that, although they and Korn et al. (2007) find a very similar trend in [Fe/H] along the HR-diagram, the systematic differences between their values is around 0.15 dex, which they explain as possible differences between the NLTE corrections. In other clusters, the measured amplitude of variations are smaller, or no effect was detected. All these works attempted to determine chemical abundances with state of the art techniques, addressing and trying to take into account model weaknesses like the NLTE and 3D effects.

In this work we found different [Fe/H] trends above the TO using three different stellar libraries, which is casting some suspicion about the reality of the detection of the effect of atomic diffusion.

Regarding the H16 results, we remind that the magnitude of the trend is significantly smaller than the GSL grid mesh and that the synthetic spectra themselves can introduce systematics due to calculation details. The non-uniform distribution of the cluster stars along the sequence in the the top panel of Fig. 3 is a hint that some finite-grid effects are indeed present along the temperature axis in that analysis, but how this projects to other parameters remains unclear. At variance, the ELODIE and MILES interpolators do not suffer of this wide-mesh drawback, but they are limited by the small number of stars in this region of the parameter space (about 40 stars for both libraries in the ±0.3 dex slice around the cluster's metallicity, see Fig. 2.4). Also, these observed library spectra are subject to noise and to the effect of peculiarities of individual stars. In well populated regions of the parameter space (typically close to Solar metallicity) these effects are averaged-out thanks to the presence of a fair number of stars with similar parameters, but in this low-metallicity regime, every single star might have a strong influence on the interpolator.

The distribution of the ELODIE stars (the black dots in Fig. 2.4) is uniform except in the region $T_{\mathrm{eff}} > 6100\,\mathrm{K}$ where there is only one star with [Fe/H] < -1.7 dex. In the case of MILES, we note that in the range: $5500 < T_{\mathrm{eff}} < 5850\,\mathrm{K}$ there is only one library star with [Fe/H] < -1.7 dex, HD 140283, with [Fe/H] ≈ -2.57 dex. The MILES pattern in this regime may therefore be an artifact of the interpolation. The interpolator we are using here is an improvement of the one initially published by Prugniel et al. (2011). The improvement concerned the cool stars ($T_{\mathrm{eff}} < 4800K$), and consisted in refining the parameters of the stars by critically scrutinizing the literature and tuning the interpolator. The number of terms in the polynomial development was also increased, essentially to reflect better the variation between the giants and the dwarfs, and this can affect its behavior at warmer temperature. We hereby repeated the analysis with this first version interpolator, in order to check the robustness of the metallicity trend with respect to the change of the interpolator, and we did not notice any significant difference. During the preparation of this improved MILES interpolator, a series of interpolators were constructed, where for each one a single star was excluded. They are called *X-interpolators* in Sharma et al. (2016), and they were used to check the stability of the results. We[4] repeated here the analysis with all the X-interpolators of the library stars in the region of the parameters we are analyzing, to see if for some of these stars the trend would be modified. We found the trend to be robust, hence ruling out any strong bias due to a single individual star. We also compared the parameters used to compute the MILES interpolator with an updated compilation of the literature, and did not find any discrepancy. Finally, we re-determined the parameters of the MILES spectra by fitting in the same way as the MUSE observation (self-inversion of the interpolator), and we also found no systematic effect.

At this point, the difference between the trends found for the three analyses is not understood. Each analysis approach has its merits and drawbacks, and we found no reason

---

[4] in collaboration with P. Prugniel

to support one more that the others.

2.5.2 Spectroscopic surface gravity

H16 did not fit log g from the spectra because of concerns of degeneracy between the instrumental broadening and the surface gravity. As the MUSE LSF cannot be precisely assessed for the spectra extracted from the final cubes, they preferred to adopt log g from their photometric fit to the isochrone. Although for individual spectral lines observed at high spectral resolution the line width is a major indicator for the gravity, at medium resolution and for full-spectrum fitting, where all the lines are used, notwithstanding their sensitivity to gravity, the degeneracy between the broadening and the gravity may not be important.

To test the influence of the gravity on the results for the metallicity, we performed a separate analysis with log g as an additional free parameter. Figure 2.5 compares the two values. For the high signal-to-noise spectra, (SNR> 50), the differences in log g do not exceed 0.5 dex between the two methods. When we compare the new values with literature values (see Sect. 2.4.3), we find $\mathrm{logg(lit)} - \mathrm{logg(spectro)} = 0.15$ dex, with a dispersion of 0.25 dex. T_{eff} obtained with free log g are lower by ~ 40 K (ELODIE) and 85 K (MILES) compared to the values when log g was fixed.

The [Fe/H] trends with this analysis, presented in Fig. 2.6, are not significantly modified in this new analysis (compare with Fig. 2.4).

2.6 Conclusions

We repeated the analysis of 1 587 MUSE spectra of 1 063 stars located above the TO of NGC 6397 originally performed by H16. While their analysis used a grid of synthetic stellar spectra, we have used two empirical stellar libraries, ELODIE and MILES, to determine T_{eff} and [Fe/H] of these stars. These spectra have SNR $\gtrsim 50$, and comparisons with H16 and earlier studies suggest that the errors in our determinations are ~ 25 K and 0.05 dex on the two parameters respectively. The metallicity dispersions of the measurements, ~ 0.07 dex, agree with these figures.

Despite this fair consistency, the metallicity trends along the sGB and RGB are different in the three analyses. No trend was found with ELODIE and the one found with MILES does not match the theoretical expectations. Previous observational studies of this and other clusters also lead to contradictory results about the reality of this variation, and the detection of the effect of atomic diffusion.

These empirical libraries contain only a limited number of stars in this low-metallicity regime (they do not have enough stars on the MS, which renders impossible to explore the

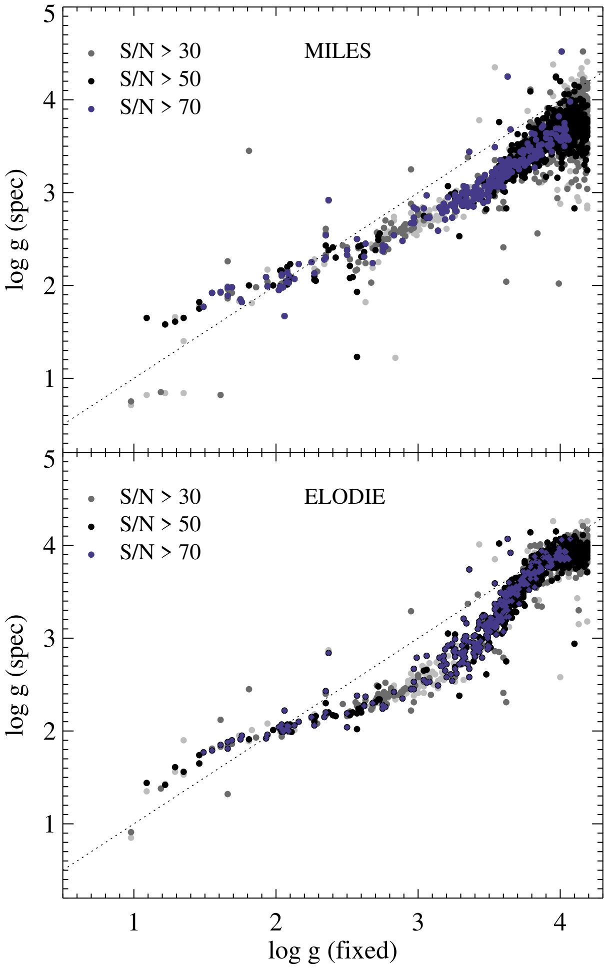

Figure 2.5 Comparison between the spectroscopic and photometric log g. The dotted line is the 1:1 correspondence, the colour of the symbol reflects SNR as indicated in the Figure. The top panel is for MILES analysis and the bottom one ELODIE.

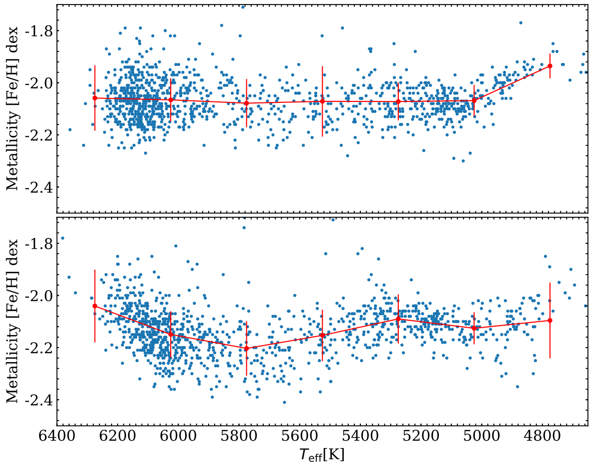

Figure 2.6 [Fe/H] vs. $T_{\rm eff}$ for the giants (logg < 4.2 dex), with log g determined spectroscopically. The top panel is with the ELODIE interpolator, and the bottom with the MILES one. The solid red line connects the mean values and standard deviations of the metallicity in 250 K wide bins. The difference with Fig. 2.4 is that log g was this time determined by the full-spectrum fitting, rather than by photometry.

trend below the TO). Despite this limitation, the empirical libraries are essential to validate the synthetic libraries, and they are still unavoidable ingredients for models of integrated spectra of stellar populations, used in extragalactic astronomy. Therefore, the motivation to continue to improve the empirical libraries remains strong. The present work clearly identifies the regime of [Fe/H] ~ -2 as an area where the libraries deserve to be improved.

The metallicity trend found by H16 qualitatively reproduces the expected effect of atomic diffusion. But the reference grid of synthetic spectra has a wide metallicity mesh, questioning the capability to resolve the small physical effect. If one relates the grids' meshes to the generally accepted accuracy of the determination of the atmospheric parameters, most of the grids presently used for population analysis are too coarse in their metallicity coverage. Typically, for $T_{\rm eff} \sim 6\,000$ K, the mesh size is 200 K, which is roughly four times the admitted precision on measurements. On log g it is 0.5 dex, ie. about five times the precision, and on [Fe/H], 0.5 dex, about ten times the precision. For example, for GSL the meshes sizes are 100 K, 0.5, and 0.5 dex, and for Coelho (2014) they are 200 K, 0.5, and 0.5 dex on the three parameters respectively. Only recently, libraries with a finer metallicity sampling became available. For example, (Franchini et al., 2018, INTRIGOS) and Allende Prieto et al. (2018) have mesh sizes of 250 K, 0.5, and 0.25 dex. Adopting finer sampling is naturally challenging in terms of both the computing time necessary to produce the large number of spectra, and the volume of data to manipulate which is yet in the 100s GB for Allende Prieto et al. (2018). For a proper resolution of the metallicity trends due to atomic diffusion, or of the other surface abundances alterations due to other processes, a mesh size of 0.1 dex would be required.

From the high resolution abundance analysis point of view, there is also a large space for improvement, as the limitations like the treatment of NLTE and 3D effects are still a large source of uncertainty.

This work illustrates the limits of the present libraries at low metallicity. While observations of Galactic globular clusters are classical benchmark for population models, the empirical libraries are at the best, limited near the TO of these clusters, and the interpolated spectra used by the models are crudely approximate. The latest library, XSL Arentsen et al., 2019, has a more uniform coverage of the metallicity range than earlier libraries, but also suffers of a relative shortage of TO and MS stars in the low metallicity regime. Both for the stellar population models, and for the validation of synthetic spectra, it is desirable to extend the coverage of these libraries.

CHAPTER THREE

WIDE-FIELD IMAGING OF THE VIRGO GALAXY CLUSTER IN THE NEAR-INFRARED : THE SURVEY AND DATA REDUCTION.

"If you don't succeed at first, try two more times so that your failure is at least statistically significant." - Anon.

Abstract

In this chapter we will discuss the reduction of photometric data in two infra-red bands (J and Ks) which were observed as a part of Next Generation Virgo cluster Survey in IR (NGVS-IR). These data cover about 23 square degrees in the Virgo cluster region. The field is divided in two parts, one of the fields covers ∼9 square degrees around M49 and the other part covers the intracluster region between M49 and M87. In the first part we will describe the NGVS and NGVS-IR survey and their contribution to the community followed by the details of acquisition and quality of the acquired data. This will be followed by a description of data reduction that involves background subtraction and stacking. We will also discuss the various calibrations that have been performed on the data, and conclude the chapter with a few comments on the photometric catalogs produced.

Globular clusters have been formed in the context of an expanding universe, together with galaxies, galaxy clusters and large scale structures. In recent times, a number of surveys have been dedicated to the study of the early universe and have helped to improve our understanding of the formation of hierarchical structure within the ΛCDM paradigm. These surveys provide observations of complex stellar systems from enormous galaxy clusters down to very low mass dwarf galaxies and star clusters on large areas of the sky. The data from these dedicated surveys aids in our quest to test and tune our models and the physics therein. These surveys give us an integrated picture over many orders of magnitude in mass which is statistically powerful. An ideal site to study stellar systems would be a dense galaxy cluster with a large area survey.

The Virgo cluster of galaxies is the richest galaxy cluster at low red-shift in the nearby universe (Tully, 1982; Klypin et al., 2003). At the distance of only ∼16.5 Mpc (Mei et al., 2007) due to its diverse population it is an ideal target to point our telescopes at. The Next Generation Virgo cluster Survey (NGVS) is curated with these objectives in mind. It is a wide-field comprehensive optical survey that covers the Virgo cluster using MegaCam instrument mounted on the Canada-France-Hawaii telescope (CFHT). The NGVS has been an instrumental step towards completing the stellar census in the Virgo cluster which will also serve as specimen for upcoming space-based and ground-based surveys like Euclid, and LSST, for instance.

3.1 The Virgo galaxy cluster

The Virgo cluster of galaxies is the nearest galaxy cluster to the Milky Way. With a virial cluster mass of $6.3 \pm 0.9 \times 10^{14}$ $M_\odot$ (Kashibadze et al., 2020) the cluster has a dense mass concentration in the local universe. In a cosmological sense, the Virgo cluster lies at the centre of the Local Supercluster (de Vaucouleurs, 1953; de Vaucouleurs, 1958; Klypin et al., 2003), the outskirt of which is occupied by the Milky Way. The Virgo galaxy cluster, because of its proximity, is the best mapped galaxy cluster and owing to its rich population of equidistant galaxies of different morphologies and luminosities is of prime astronomical importance. The cluster is also home to a number of low surface brightness stellar systems but even at the distance of Virgo these systems remain challenging to detect and hence a large number of diffuse cluster members might still be unexplored.

Relative to other galaxy clusters the Virgo Cluster is loosely concentrated and has a high fraction of Spiral galaxies among its bright cluster members. The other class of more regularly shaped galaxies like E and S0 are relatively fewer in number which points to dynamical youth when compared with, for example, the Coma cluster (at a distance of 100 Mpc). A distribution of known Virgo cluster galaxies is shown in figure 3.1. The image is adopted from the work of Ferrarese et al. (2012), and it shows the Virgo field covered by Binggeli et al. (1985) more than two decades ago as a part of moderately deep photographic survey of the Virgo field in optical light. The catalog still serves as reference for the Virgo Cluster and has about 2096 candidate members. The catalog is known as the Virgo Cluster Catalog (VCC) and it contains morphological and dynamical information of the member galaxies. The VCC has contributed immensely towards understanding a wide range of astronomical problems that includes photometric and morphological properties of galaxies, the abundance of bright and faint galaxies in a dense environment, the distribution of dark matter among a number of other aspects.

Despite serving as the reference for the Virgo cluster and clusters in general, the VCC is no longer up to date. The Sloan Digital Sky Survey (SDSS; York et al. 2000) has provided an extension in five optical bands simultaneously (*u,g,r,i,* and *z*) with its wide field imaging camera (CCDs). The use of CCDs in SDSS was an upgrade from photometric plates used earlier for VCC observations and CCDs provided a linear response and more homogeneous data in SDSS, but the shorter exposure times in SDSS did not provide a deeper coverage than what was already achieved in VCC. The Virgo Cluster has since been observed across a broad range in electromagnetic spectrum including radio at 1.4 GHz as a part of Very Large Array (VLA) Faint Images of the Radio Sky at Twenty centimeters survey (FIRST; Becker et al. 1995; White et al. 1997), NRAO VLA Sky Survey (NVSS; Condon et al. 1998) among others. In the far infrared the cluster has been covered by the Herschel Virgo Cluster Survey (HeViCS; Davies et al. 2010 and other papers in the series), and others that make targeted observations like the Hershel Reference Survey (HRS; Boselli et al. 2010).

In the near-infrared, the Two Micron All Sky Survey (2MASS; Skrutskie et al. 2006) provided entire coverage of the cluster in J, H and K_s bands aided by the Large Area Survey as a part of the UKIRT Infrared Deep Sky Survey, or UKIDSS (Lawrence et al., 2007) that provides coverage pf 4000 deg^2 in Y, J, H and K. Optical coverage of the cluster is provided prominently by SDSS in (*u,g,r,i,* and *z*), the Advanced Camera for Surveys (ACS) Virgo Cluster Survey (ACSVCS; Côté et al. 2004) and $ATLAS^{3D}$ (Cappellari et al., 2011). The ACSVCS data was the reference for the X-ray follow up program carried out with Chandra (Gallo et al., 2008; Gallo et al., 2010) and also 8.4 GHz observations from the VLA (Capetti et al., 2009).

The Next Generation Virgo Cluster Survey (NGVS; Ferrarese et al. 2012) is an addition to the caravan of the surveys of the Virgo Cluster in optical bands and it covers about 104 deg^2 around the cores of Virgo subclusters A and B. The 50 % completeness limit is 2 magnitudes deeper than the VCC detection limit (Ferrarese et al., 2020), which, for instance led to the addition of 154 uncategorized galaxies in just the central $\sim$ 4 square degrees. It is complemented by its infrared counterpart called NGVS-IR survey that covers a sub-field around M87 and M49 and the intra-cluster region between the two galaxies in near-IR bands J and Ks. In the next two sections we will describe these surveys and their contributions in adding to the knowledge of the Virgo cluster and galaxy clusters in general.

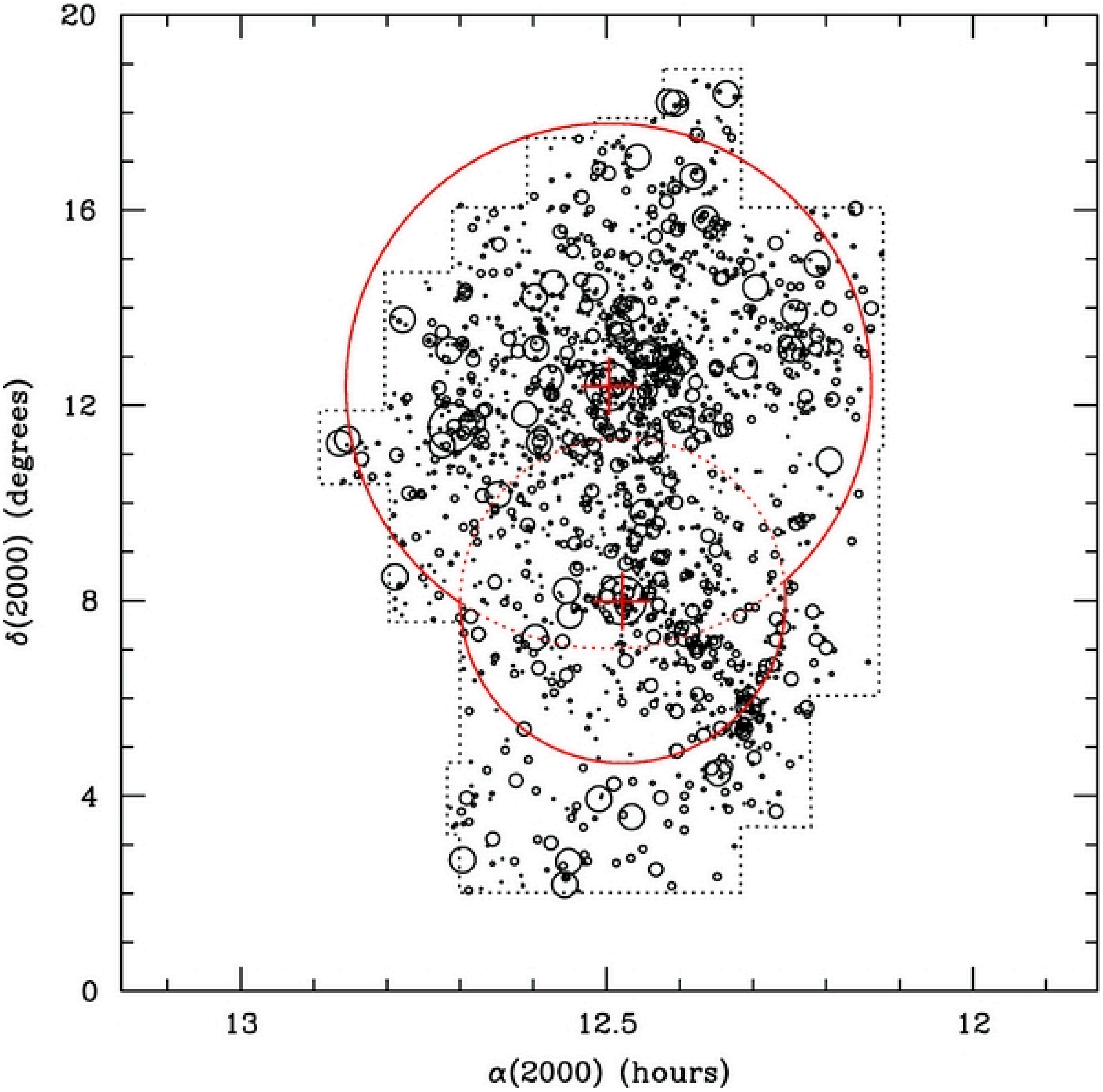

Figure 3.1 Spatial distribution of Virgo cluster galaxies. The size of the symbol scales with galaxy's B-band luminosity. The sample includes the galaxies from the Virgo cluster catalog from Binggeli et al. 1985 and the region enclosed within dashed boundaries is the region observed as a part of their studies. There are additional galaxies which were not classified in VCC as a part of the Virgo cluster but were later added as cluster members (Ferrarese et al., 2020). The red crosses are the locations of M87 and M49 and the red circles mark their virial radii Ferrarese et al. (2012). The values are based on X-ray measurements of the host intracluster gas and on radial velocity measurements for the galaxies and are taken from McLaughlin (1999).

3.2 The Next Generation Virgo Cluster Survey in the Near-Infrared (NGVS-IR)

The Next Generation Virgo cluster Survey (NGVS; Ferrarese et al. 2012) is a multi passband optical survey carried out with the wide-field optical imager MegaCam at the Canada-France-Hawaii Telescope (CFHT), which is a 3.6 meter telescope located at Mauna Kea, Hawaii. The survey covers a field of 104 square degrees around M87 and M49 out to their virial radii in u^*, g , r, i, and z optical bands. The survey provides typical depth of ∼25 mag (AB) in i and ∼26 mag in g and u^* (Table 2 in Ferrarese et al. 2012). The seeing FWHM in all the optical bands is well below 1", with i band having exceptional seeing FWHM less than 0.6" across the field to facilitate the study of compact stellar systems (Longobardi et al., 2018; Liu et al., 2020; Lim et al., 2020), nuclear star clusters of the Virgo cluster (Ordenes-Briceño et al., 2018; Sánchez-Janssen et al., 2019b), and the measurement of distances using surface brightness fluctuation (SBF) (Cantiello et al., 2018). The photometry and astrometry of the NGVS data is calibrated against the SDSS-DR7 survey which also covers the entire NGVS footprint.

The science driver of the NGVS survey includes the determination of galaxy luminosity function with the motivation of obtaining the cosmological constraints on galaxy formation (Ferrarese et al., 2016). The multi-band photometry also proved useful in understanding the stellar populations of the individual galaxies. The broad coverage along the wavelength aids in breaking the metallicity-age degeneracy in stellar systems. Alongside the galaxy luminosity function, the survey provides opportunity to study the galaxy scaling relations in terms of photometry, dynamics and structure that gives deeper insight on the assembly history of the galaxies (Roediger et al., 2017; Powalka et al., 2018; Longobardi et al., 2018; Lim et al., 2020). One of the major aspects of the survey is its advantage in studying the origin of compact stellar systems that include Globular clusters (GCs), Ultra Compact Dwarfs (UCDs), and nucleated galaxies.

Surveys like the ACSVCS (Côté et al., 2004) and the ACSFCS (Jordán et al., 2007a) paved a way for observing large samples of GCs associated with early-type galaxies (Villegas et al., 2010; Liu et al., 2011; Wang et al., 2013; Jordán et al., 2015; Liu et al., 2016; Liu et al., 2019c). This was pivotal in understanding the relationship between the host systems and their GCs. These surveys were carried out with the HST which provided excellent angular resolution and photometric precision that could resolve GCs with effective radii r_h ∼3pc at the distance of the Virgo cluster. NGVS added the wide-field, and homogeneous sample of data in the field which was an advantage over small pointed fields covered with HST.

The survey was extended beyond optical into the near-infrared and the extended survey was named NGVS-IR. NGVS-IR covers a part of the NGVS footprint, including M87 and M49, the two dominant early-type galaxies the Virgo cluster and the intra-cluster region between the two. It provides deep and uniform data in the J and the Ks bands. The first part of the NGVS-IR survey was observed with the *Wide-field Infrared camera* (WIRCam; Puget et al. (2004)) at CFHT (Muñoz et al., 2014). This covered around 4 square degrees around the galaxy M87, a field referred to as the Pilot Field. The second part of the survey covered the region around M49 and the intra-cluster region between M87 and M49. The second part of the survey was observed with a 4-meter class telescope, the Visible and Infrared Telescope for Astronomy (VISTA; Dalton et al. 2006; Sutherland et al. 2015) of the European Southern Observatory (ESO) on Cerro Paranal, Chile, in two semesters. The second part will be the focus of the data reduction in this chapter. The program IDs of the two observations are 89B-0521 and 91B-0397 (proposal PIs respectively, are Robert Muñoz and Thomas Puzia)). We will refer to these as P89 and P91, respectively. The observations under the program P89 cover around 9.5 square degrees around M49 and the data observed as a part of P91 covers around 13.5 square degrees between M87 and M49. In total the NGVS-IR covers more than 20 square degrees in the core region of the Virgo cluster.

Figure 3.2 shows the NGVS-IR observation fields on the NGVS footprint. The background image shows a mosaic of NGVS images in the g band that illustrate the survey footprint (image courtesy J. C. Cuillandre). The highlighted regions are the fields that also have an infrared counterpart observed as a part of the NGVS-IR survey. The red block shows the 4 square degrees around M87 that have been studied earlier and forms the reference for this work. The region enclosed within the solid black box is the region around M49 (program P89) and the dashed black region is the intra-cluster region observed as a part of the P91 program between M87 and M49. The field to the West of M87 includes the elliptical galaxies M86 and M84.

3.3 Data Acquisition

In this section we will describe in detail the instrument and the data acquisition, observation strategy, and data quality for both the data sets used, P89 and P91. As discussed in the previous section, both the data sets in this work have been observed in Service Mode with the Visible and Infrared Camera (VIRCAM) mounted on the VISTA telescope (Sutherland et al., 2015). The telescope has a 4.1 meter diameter primary mirror and has a quasi Ritchey-Chretien design with Cassegrain focus. It has an alt-azimuth mount. The telescope is kept within a 19 meter diameter enclosure which helps minimizing local seeing effects. The telescope was primarily designed for large area sky surveys because of its wide field of

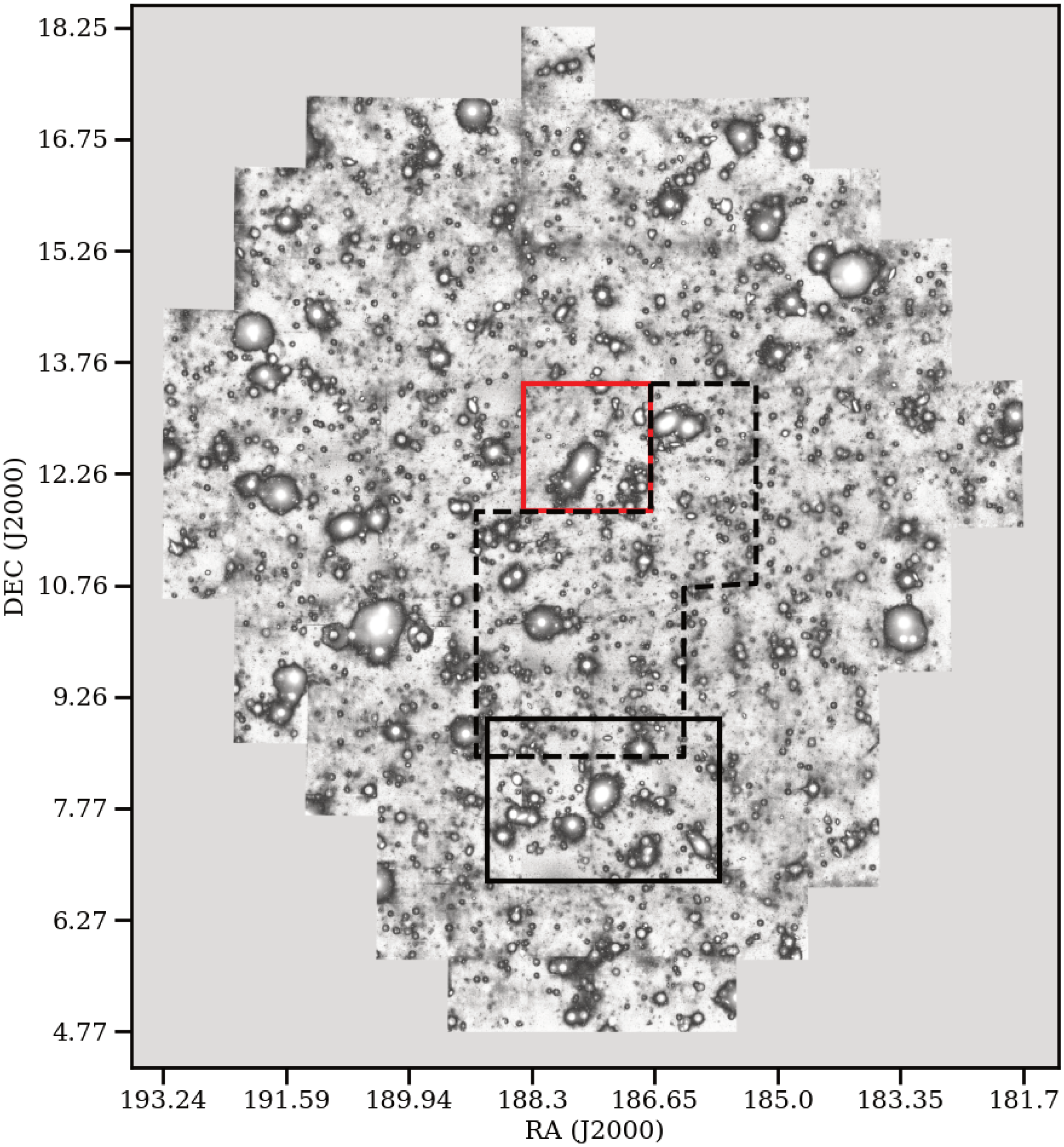

Figure 3.2 The NGVS-IR fields on top of the NGVS optical footprint. The major galaxies are shown on the plot. The solid red box is the pilot field observed as a part of NGVS-IR survey with M89 at it's center. The solid black box is the P89 field with M49 roughly at its center, and the dashed black region is the P91 field that covers intra-cluster region between M49 and M87 (Image courtesy - J. C. Cuillandre).

view and moderately large aperture size. Therefore about 75% of the telescope observing time is dedicated to large area sky survey programs, like VVV (Minniti et al., 2010), VIDEO (Jarvis et al., 2013), UltraVISTA (McCracken et al., 2012) among others.

VIRCAM was the largest wide-field near-IR imager at the time of the NGVS-IR observations (2012-2014). It has 16 Raytheon VIRGO HgCdTe IR detectors arranged in a rectangular array of 4×4. The spacing between each detector is 90% of the active width in the y-direction, and 42.5% of the active width in the orthogonal direction. A schematic of the detector assembly is shown in figure 3.3. Each detector has a grid of 2048×2048 pixels and a total of 67 megapixels.

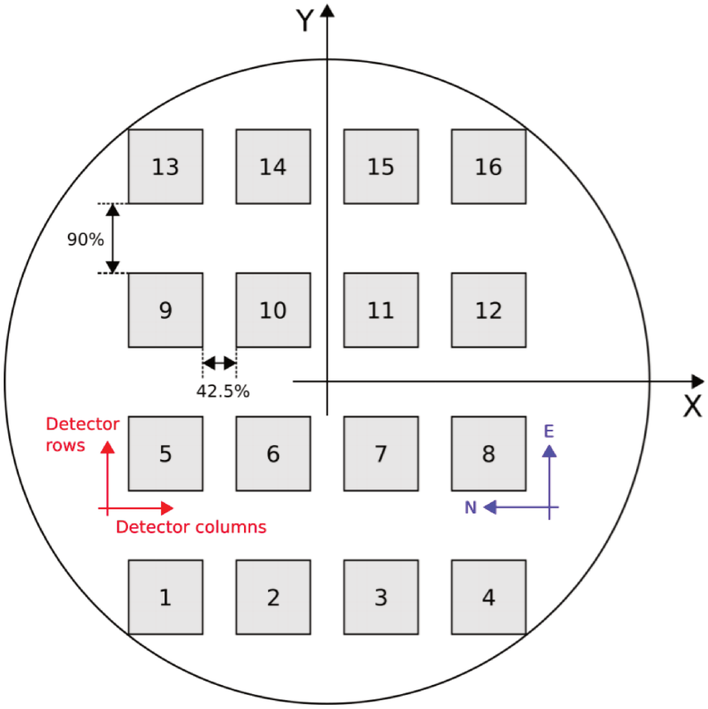

Figure 3.3 The schematic of VIRCAM detector assembly (Image courtsey - González-Fernández et al. (2018)).

The detectors perform at 90% quantum efficiency in the wavelength range from 1.0-2.35 μm. The detectors have certain cosmetic defects that account for about 1% of the total pixels, which are time invariant and can usually be eliminated during processing. The read out noise is $\sim$24 e^- for a single integration and dark current contributes typically 0.2 e^-/s. The detectors have considerable non-linearity of about 2-4% which is corrected using polynomial fits to series of dome flats. The flat-fielding correction, however, is done using twilight flats taken over a period of about a month.

A single observed unit is called a readout and it has an exposure time which is called DIT and it is short for Detector Integration Time. Readouts are converted to digital units with

Program	Filter	DIT	NDIT	G_{eff}
P89	J	25s	2	8.38
P89	Ks	10s	3	12.57
P91	J	25s	2	8.38
P91	Ks	8s	3	12.57

Table 3.1 The exposure time and effective gain for each dataset. The reference gain is the median gain of 4.19 e^-/ADU and G_{eff} is derived as explained in 3.3.

a median system gain of 4.19 e^-/ADU. The exposures are usually generated by co-adding multiple readouts before they are saved to the disk. For example, one readout of the *Ks* band in the NGVS-IR program has a DIT of 10s or 8s, and the *J* band has a DIT of 25 seconds. A *Ks* band exposure consists of 3 frames (NDIT=3) of 10s (or 8s), and *J* band exposure are 2 co-added frames (NDIT = 2) of 25s each.

3.3.1 Observing strategy

As discussed in the previous section, the detectors on the VIRCAM are sparsely arranged, so in order to make a contiguous tile the telescope has standard pointing schemes that make sure that there are no empty gaps in the final stacked image. In one of the observing strategies the telescope covers a part of sky in six successive pointings. The first three are offset by 47.5 % in the y-direction between them. This gives a continuous observation which has a width of about 1.02 degrees. The telescope then moves with an offset of 95% in the x-direction and repeats the procedure again figure (3.4). The six stacked pointings can make a complete tile that covers 1.07×1.47 square degrees. This strategy is called Tile6n. All the objects on the tile, except those on the edge of the stack are observed at least twice in the single sequence.

In the other strategy which is called Tile3nx, the telescope covers a part of the sky in three pointings offset in y-direction and then it moves to another part of the sky and then moves back and forth repeating the same pattern. The program P89 uses Tile6n strategy while P91 is observed with Tile3nx. The sequence of telescope pointings is illustrated for both the programs in figure 3.4.

A stack of one set of pointings is called a tile. The survey's target area is divided into pairs of tiles. After each completed set of six (or three) exposures on the sky within one tile, a larger slew moves the telescope to the other tile region of the pair, performing the same sequence of observation adding an extra offset with respect to any previous visit to avoid exact superimposition. The acquisition sequences bypass the dithering at a given location, present in the standard VIRCAM survey procedures (González-Fernández et al. 2018, hereafter GF2018), to concentrate on larger offsets. This specific strategy allows dealing both with small-scale

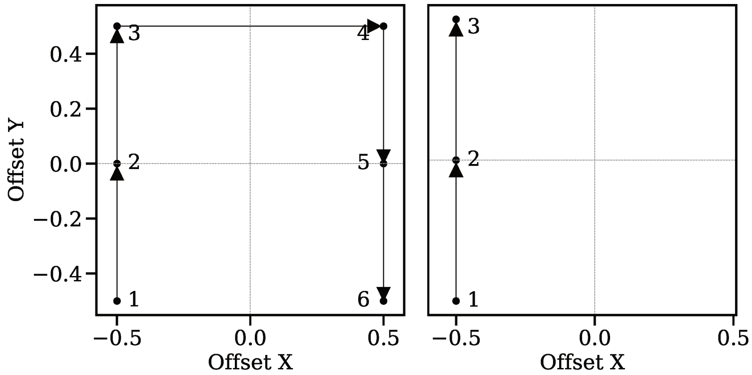

Figure 3.4 Observing pattern tile6n and tile3nx adopted for P89 and P91 respectively. The offsets are in relative units.

Table 3.2 Log of the VIRCAM observations

Prog/Filter	Date of first and last exposure	Used frames	T_{int} (sec)	FWHM	Obs Pattern
P89-J	20/04/2012, 08/06/2012	435	25	0.78”	Tile6n
P89-Ks	29/03/2012, 30/06/2012	1813	10	0.8 ”	Tile6n
P91-J	02/04/2013, 06/06/2013	540	25	0.8”	Tile3nx
P91-Ks	29/03/2013, 07/02/2014	3228	8	0.71”	Tile3nx

cosmetics and with larger areas of contiguous defects and improves the sampling of the sky when the field contains large galaxies.

3.3.2 Data Quality

The pixel scale varies across the detector field because of the geometry of the focal plane of the detector system. To minimize this effect, we have derived zero-point magnitudes per chip in each exposure which will be discussed later in the calibration section. The value of the pixel scale increases from the centre to the edge and its mean value is 0.339 arcsec. The mean seeing FWHM for J band in both the programs is about 0.8”. This is the mean FWHM determined from the point sources in each exposure. The Ks band in P91 has a slightly better seeing of 0.71” as compared to the Ks band of P89 which has 0.8” FWHM. An overview of the observations is provided in Table 6.1.

3.4 Data Reduction

The IR detectors are inherently more unstable than their optical counterparts. In addition, the sky background in IR is approximately 100 times brighter than the objects of interest and varies spatially and temporally rapidly. The observing techniques that are employed to counter these issues produce large volumes of data. To minimize the volume of the data a number of basic pre-processing steps are carried out in VISTA data acquisition system (DAS).

In the first step the observed data from VISTA at Paranal undergo a simplified data reduction at the summit for basic quality control. This processing is very rapid and the pipeline uses an already prepared calibration information. The raw observed data are then transmitted from the telescope site to the ESO's headquarter in Garching, Germany. There, the data are fed to ESO's raw data archive, and it undergoes a general quality check to ensure instrument's health, collecting calibration information and to provide calibration frames for the Paranal pipeline. After archive ingestion is finished the data is forwarded to Cambridge where a more elaborate science data reduction is performed by the Cambridge Astronomy Survey Unit (CASU)[1]. At this stage of data processing, CASU has access to the entire night (or week) of observed data which is treated as a single entity The pipeline at Cambridge performs a number of data reduction procedures which we will discuss briefly in the next section.

The processing performed at CASU is described on their web page and for typical VISTA surveys in González-Fernández et al. (2018). To discuss the specific choices made for our data we have interacted directly with C. González-Fernández in Cambridge. The following steps are performed at CASU to treat the raw data products from the telescope.

1. **Reset Correction** - This step takes place at the Data Acquisition System (DAS) before the pre-processing starts to remove the bias given to the driving electronics.

2. **Dark correction** - Dark current frames are estimated from a series of exposures taken with the dark filter and are subtracted from the exposures. In addition to the dark correction, this step also addresses other additive electronic effects.

3. **Linearity correction** - The VISTA imager has 16 detectors, and their response is not perfectly linear. The non-linearity is estimated from the information on the readout timing, the exposure time and the reset image timing using dome flat fields.

4. **Flat field correction** - This step uses a mean twilight flatfield image and each exposure is divided by the normalized flatfield. This step minimizes the effects due to small amplitude QE variation and large amplitude camera vignetting profile. In this step the detector gains are also normalized to have a common output gain (4.19 e^-/ADU).

---

[1] http://casu.ast.cam.ac.uk/

5. **Sky subtraction** - CASU removes large scale artifacts that are introduced as a result of the atmosphere, the thermal emission of the telescope, and other additive effects. A 2-dimensional background map is estimated from the science exposures after masking the objects and rejection of bad pixels.

6. **De-striping** - A low level horizontal striped pattern is introduced in the VISTA images as a result of readout electronics. The patterns are the same for the detectors that are read-out from the same channel. The pattern is modelled by taking the median of each row and then subtracted from each pixel in the row.

After the pre-processing of the frames, the exposures are stacked and used for photometry. The catalogs so obtained have the flux information, positions, and shape description of the objects and serve as the basis for calibration and quality check. These catalogs are used to calibrate the data astrometrically and photometrically. The pipeline uses transformed 2MASS magnitudes to calculate photometric zero points for each chip. CASU also provides stacked images which they refer to as tiles, and the deep catalogs obtained from the stacked tiles in addition to the unstacked reduced pawprints and their respective catalogs.

The data processing at CASU removes most of the artifacts from the images but even then the background of the pre-processed images displays residual patterns of the scale of large astronomical sources. Therefore, before we stack the individual exposures to construct a stacked image, we implement another pass of data processing. In the next section, we will enumerate various steps of a second pass of sky subtraction, and the subsequent calibration procedures.

3.5 Data processing

We use the data pre-processed by CASU and subsequently apply a few more steps of processing the data. We have used IDL procedures (inherited from Robert Mñoz and Yasna Ordenes-Briceño) already adopted for reduction of VISTA data. The procedures in the IDL pipeline was questioned and tested at each step and have been adapted to suit the needs of our dataset. In this section we will discuss parameter adjustments corrections and additions made to the procedure.

Our second-pass sky subtraction rests on a smooth model of the spatial distribution of these residuals that is constructed for each chip using that chip-image itself. Objects must be masked aggressively for this purpose, and we exploit the depth of stacked images to build such masks. The masks also flag bad pixels. To construct the mask for the objects, we first stack the exposures after doing a very basic average sky subtraction. In this step, we take a median of the background over multiple frames that are temporally adjacent and then subtract this average value from the respective exposure. These exposures are co-added to obtain the full stacked image. We use the Swarp package [2] (Bertin et al., 2002) for stacking the frames. We estimate the background in each exposure after masking the bright objects. This background is subtracted from the exposures, which are then calibrated astrometrically against GAIA using Scamp (V 2.6.7, Bertin, 2006) [3] and then stacked to make the final image. This image is then used for flux measurement of the objects. All these steps are explained in detail in the next few subsections.

3.5.1 Mask creation

The objective of a mask is to shield the bright objects in the exposure so that they are not accounted for while calculating the background. But to obtain the mask we first need the stacked image which will be used to locate the objects and determine their sizes. This first stack is created from the exposures after a first basic pass of sky subtraction without mask. In this step of sky subtraction, for each frame we use 8-10 temporally adjacent frames to estimate the background. We take a median of the background for each pixel which gives a sky image and subtract the sky image from the frame. These frames are then stacked using Swarp. Photometry is performed on the stacked frame using Sextractor [4] (Bertin and Arnouts, 1996). Sextractor produces segmentation maps for the images in addition to the catalogs and other diagnostic files. Segmentation maps are images that match exact pixels of the objects in the input images and have pixel values of either 0 or 1 depending on whether they are associated or not with a source. They are extensively used for creating object masks. The segmentation map provided by the Sextractor does not provide masking regions broad enough to include the low surface brightness halos of galaxies, so we use this map and convolve the map with a Gaussian kernel. Once convolved we digitize the pixel values to 0 and 1 again.

The mask so produced is projected on each pawprint using Swarp. The stacked image has served its purpose of producing a mask and is discarded after this step. The first sky subtraction that was used for this stacking is also discarded. The pawprint masks are combined with a bad pixel mask which masks all the hot and damaged pixels on the detector and the pixels affected by cosmic microwave background radiation. Figure 3.5 shows a typical

---

[2] SWarp is a re-sampling and co-adding software that comes as a part of the Astromatic package. It uses standard WCS projections to co-add the images.

[3] Scamp is an astrometric calibration package designed to evaluate astrometric solutions using catalogs that are generated by SExtractor.

[4] SExtractor or Source Extractor is a widely used software for generating photometric catalogs from wide field astronomical images.

mask of a paw print. The dark regions are the location of the objects and have pixel values 0 and the white region is the background and has pixel value 1.

3.5.2 Sky subtraction

The next step in the procedure is our final pass of sky subtraction. In this step we use the masks created in the previous step to reprocess the images from CASU. Each chip with masked astronomical sources, is divided into smaller grids. A median background is estimated in each of these grids, and a low-order polynomial is used to interpolate the sky background to get a higher resolution sky map. This sky map is subtracted from each image.

The individual exposures have a low amplitude striped pattern across the images. An additional de-striping procedure is performed on the images. A clipped median is calculated along each detector line in the masked image and is subtracted from that line.

The effect of our additional sky subtraction and artifact removal can be assessed by comparing the sky statistics before and after the sky subtraction. Images from CASU have an artificially added constant elevation in the sky. For example the median sky before sky subtraction in a J band image is ~ 4300 with a standard deviation of ~ 340. After our sky subtraction, the median sky value is 0.0 with a standard deviation of 5.2. Despite the background subtraction we fail to fully eliminate the systematic dark patches in the background around the brightest objects that come as a part of CASU pre-processed images. They are a result of median sky subtraction around bright objects without sufficient masking. However, they are not a severe threat for point source science, as they are dealt with later by a local background subtraction while measuring source fluxes.

3.5.3 Pre-stacking Photometric Calibration

Each observed frame has 16 chips with slightly time-dependent detector sensitivities which are not removed by the monthly flat-fields. Due to changing weather conditions, and other instrumental factors, the frame-to-frame zero point also varies over time. To homogenize the exposures it is required that a zero-point that is particular to each exposure and each chip is derived, which will provide a scaling factor. An initial zero-point per chip is already in place supplied by the CASU pipeline and these are derived by comparing the point source photometry against the 2MASS Point source catalog (PSC). In an attempt to improve the calibration, by using more stars per field than is possible with 2MASS we repeated the same procedure keeping UKIDSS as our target calibration system.

The flat-fielding procedure implemented in the pre-processing pipeline is a classical one, that assumes a uniform sky brightness over the field of view; but field distortions in VISTA

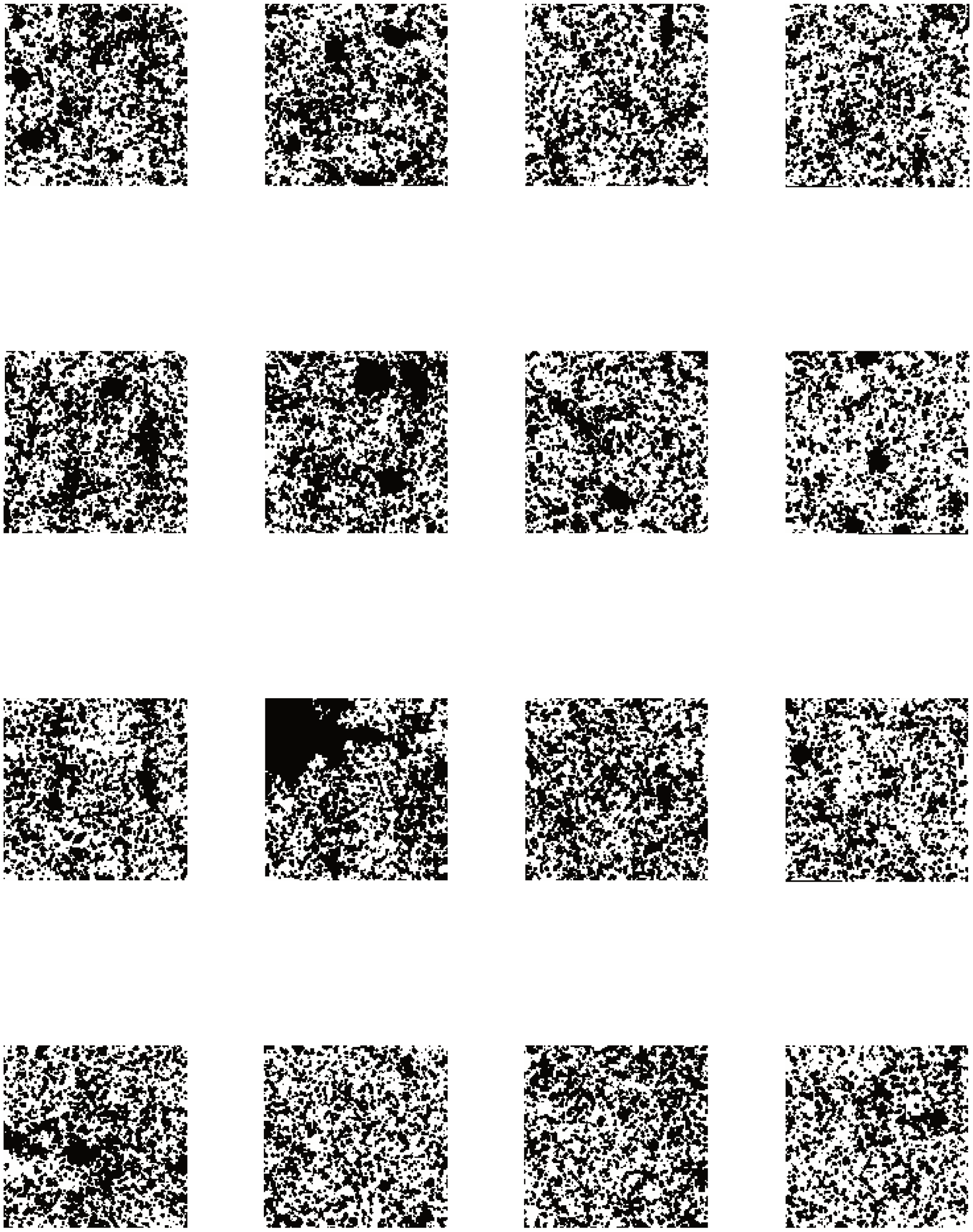

Figure 3.5 The object mask for one exposure. The dark patches are the regions where the objects are detected and the pixel value in the mask is 0. This mask is a combination of the object mask and the bad pixel mask.

mean that pixels at the edge of the field of view cover 3.6 % less sky area than pixels near the center (GF2018, Sutherland et al. 2015). Hence the flat-fielding procedure overestimates the light received in outer parts of the camera's field of view. Similarly, stellar fluxes near the edges are overestimated. The determination of one zero point per chip reduces the residuals of this radial trend to less than 1 %, so that the subsequent averages of numerous observations at different detector-positions further reduce the effect to a negligible level. We use the catalogs for each chip supplied by CASU that is generated after the pre-processing of the data. These catalogs have aperture correction values calculated at CASU which are used to calculate the zero-point magnitudes per chip.

The zero points per chip are derived using a strategy akin to the UberCal alogorithm[5] (Padmanabhan et al., 2008). It makes use of multiple detections of point sources that are observed at different epochs and on different detector chips, to correct for relative flux discrepancies amongst the chips while at the same time also calibrating the data to an external standard database. The algorithm constructs a χ^2 sum of differences between magnitudes in any pair of observations of any well-measured star, as well as differences between observed and target magnitudes of stars that have a UKIDSS counterpart. The unknowns are the zero points. Sparse matrix tools are used to minimize the χ^2.

We use these zero point magnitudes to evaluate the scaling factor for a common output zero point and multiply the fluxes of objects in individual chips to bring them all to the same level before stacking them together.

3.5.4 Astrometric Calibration and Stacking

Astrometric calibration

The astrometry of the CASU images is tied to 2MASS. Because of the limited depth of the 2MASS survey, 2MASS and VISTA have an overlap of less than 2 magnitudes for the selection of point sources with a good signal-to-noise ratio (SNR) that are bright enough and unsaturated. Moreover, the native astrometry of 2MASS is accurate to 70-80 mas for stars with Ks magnitudes brighter than 14 mag, and precision is of the same order. In pursuit of more precise astrometry, we re-calibrate our data against GAIA positions using the astrometry package Scamp. We have resorted to GAIA for re-calibration primarily for two reasons, the first one is the number of objects common to the GAIA and VISTA database for our field, which is almost double the number of cross matches we achieved with 2MASS. And secondly, GAIA-DR1 promises astrometry that is precise to 0.2-0.7 mas.

At the time of our calibration work, GAIA-DR1 was the latest release the then available

---

[5] We have used the implementation of the algorithm in Python and the scripts were obtained from Carlos González Fernández.

version of Scamp could work with (Jordi et al., 2016; Lindegren et al., 2016). The GAIA-DR1 astrometric precision is almost 100 times better than that of 2MASS, and the accuracy is also improved by a factor of a few. Using GAIA-DR1 roughly doubled the number of stars that could be used as astrometric references. More advanced versions of both GAIA and Scamp are available now, but in this work we retain the GAIA-DR1 calibrated astrometric solutions. A more accurate astrometry also ensures a narrower PSF in the resulting co-added image and hence a more precise flux measurement.

Stacking

After the improved astrometric calibration, the images are co-added using the Swarp package. Swarp is fed with the scaling factors that account for variable chip responses and instrumental and temporal variations (section 3.5.3) and with astrometric solutions from Scamp.

The mean pixel scale in the J and the Ks bands is 0.34"/pixel and in the optical bands it is 0.18"/pixel. To match the plate scale of the optical images we have resampled the IR band data to 0.18"/pixel. The parameter in Swarp that needs to be changed is PIXELSCALE_TYPE that is set to MANUAL and PIXEL_SCALE to 0.18.

For resampling the data, swarp provides a number of interpolation options. We use LANCZOS2 interpolation between pixels as a good compromise between retaining the signal and not creating strong artifacts around discontinuities. The pixels are combined with a clipped average (keyword COMBINE_TYPE set to CLIPPED), which SWarp implements following Gruen et al., 2014.

The effective gain of the exposures must be provided to Swarp. It is important because the photon noise scales as square root of the effective gain of the exposure. It is a function of the number of individual readouts (NDIT that make one exposure, and of the gain of a single CASU processed readout which is 4.19 e^{-}/ADU. After the co-addition at the telescope, the NDIT is set to 1 in the final data product at CASU without appropriately re-scaling the gain of the exposure. What was the sum of NDIT readouts is not the average of NDIT readouts. So, the effective gain of an exposure will be 4.19 × NDIT e^{-}/ADU. Alternatively, one can also divide the gain (4.19 e^{-}/ADU) by the BSCALE value, as BSCALE is 1/NDIT and is given in the header of the CASU-processed exposure, unlike NDIT. The typical NDIT in the J band is 2 and that in the Ks band is 3, so the effective gain (G_{eff}) for J band images is $8.38e^{-}$/ADU and for Ks band images is $12.4e^{-}$/ADU. This parameter is fed to Swarp via keyword GAIN, and is crucial to clip the noisy pixels.

Additional parameters that are specific to CLIPPED co-addition are CLIP_AMPFRAC and CLIP_SIGMA which control the tolerance of the procedure to PSF inhomogeneity over the field; they are set to 0.5 and 4.0 respectively. An oversampling of 2×2 is used for all the frames to avoid aliasing. The target zero point in the output image is fixed to 30 for both J and Ks.

Figure 3.6 shows the number of frames that contributed to a typical pixel. J band images have a higher exposure time than the Ks band images and therefore have smaller number of frames that are co-added to make a pixel. The maximum number of frames per pixel in the J band is about 118 and in Ks about 600. The field P89 is made up of four tiles and P91 is made up of 6 tiles. The edges of the tiles have a slightly smaller number of frames than the centre, which is partially compensated by overlap with other tiles. The stacked images of field P89 in the J band is shown in figure 3.7.

The optical images and catalogs that we will use to construct color-color diagrams later are taken from the NGVS database at CADC (Canadian Astronomy Data Center) [6]. They are divided into grids of size 1 × 1 square degrees. We also divided our fields into the same layout by projecting the size information of the optical band data to our stacked images. This makes data handling easier in terms of size of the data.

3.5.5 Galaxy Subtraction

The radial profiles of GC number densities around a galaxy fall off from the center outwards, so that an important fraction of the GCs lie close to the galaxy core. However, automatic GC detection and precise photometry are difficult on a bright and spatially varying galaxy background. We are, in particular, interested in the GC system of M49, a case for which galaxy subtraction prior to detection is necessary. We have used the IRAF subroutine ISOFIT/ELLIPSE in conjunction with CMODEL (Ciambur, 2015) to model the galaxy. ISOFIT/CMODEL are the tasks specially aimed at modelling the galaxies with peculiar profiles, such as the ones having boxy/disky profiles, bars in disks, and complex isophote shapes, by implementing the modelling of higher order harmonics.

At this point in time we have only subtracted M49, for which the subtraction has a significant impact on total GC numbers. We modelled and subtracted the galaxy in J, Ks, and the optical bands and, after inspection of the residual images, used the *u*-band galaxy-subtracted image as the detection image in the dual mode of the SExtractor software (Bertin and Arnouts, 1996) to obtain GC photometry in other optical bands. The optical band data for other parts of the field has been taken from the CADC repository, and therefore the photometry on the galaxy-subtracted optical images needed to be re-calibrated to the CADC photometry. This is explained in the later sections (see section 3.6.5). The photometry on the galaxy subtracted IR images was performed in the same way as for other tiles followed by same post-photometry calibrations.

---

[6] http://www.cadc-ccda.hia-iha.nrc-cnrc.gc.ca/en/community/ngvs/

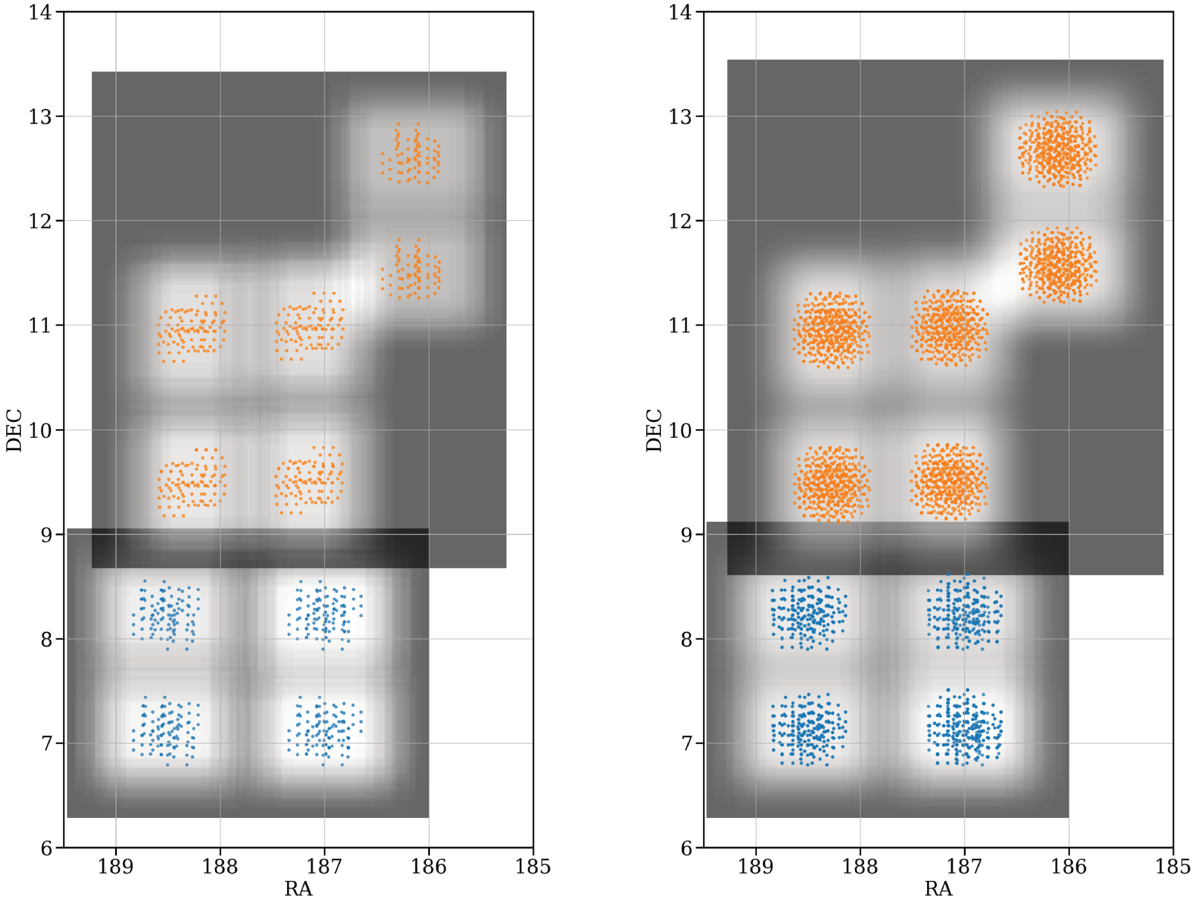

Figure 3.6 The figure shows frames per pixel for J and Ks bands (left and right, respectively). The Northern field is P91 and the Southern field is P89 in both the panels. The blue circles represents the centre of each pointing in the P89 field, and the orange circles are the center of the pointings in the P91 field. The color of the pixel is whiter when more frames go into making the pixel, the gray regions have little to no coverage.

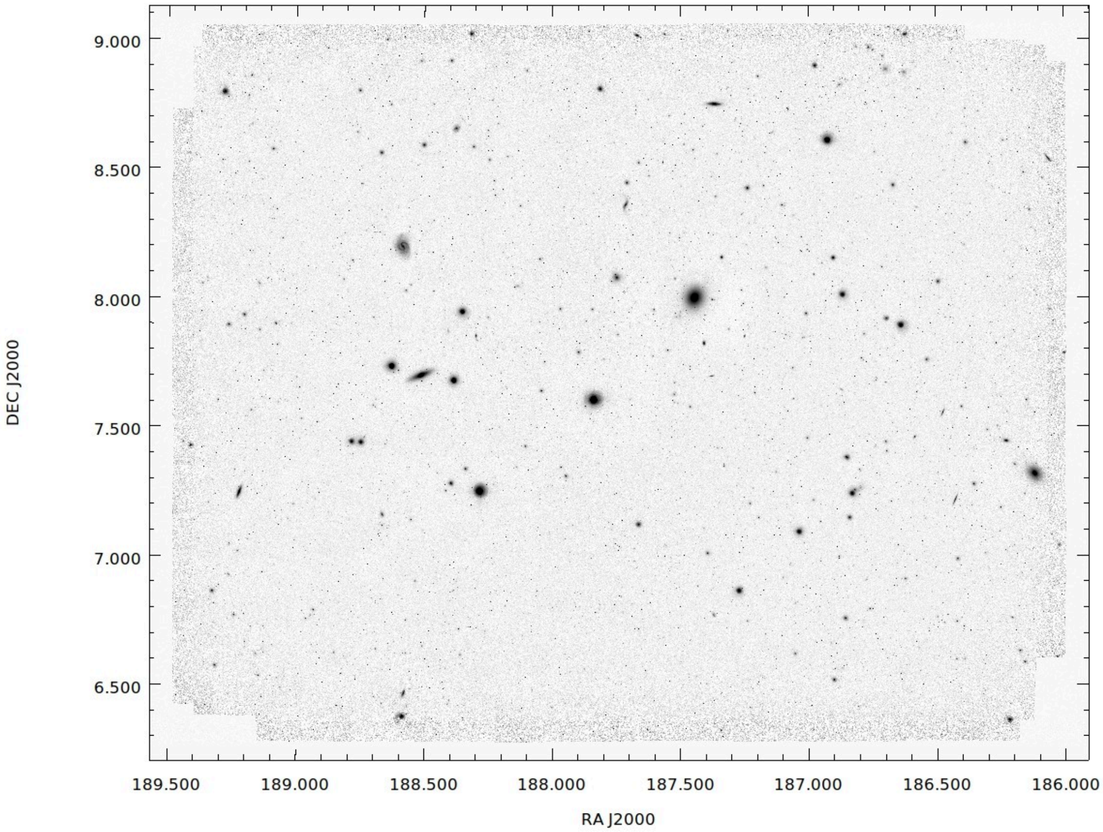

Figure 3.7 Sky subtracted stacked image of P89 field in the J band. The size of the field is around $\sim 3.5 \times 3.0$ square degrees.

Even when using CMODEL the central part of the galaxy-subtracted image remains irregular and noisy, so we exclude GC detection within a 20 arcsecond radius of the core. The objects only detected after galaxy subtraction are merged with the other objects and go through the same calibration and corrections as described in the upcoming sections.

3.6 Photometry on Stacked Images

In the next step we convert the information in stacked images to object catalogs using the Sextractor package which is used for object detection and flux measurement. We work with images that are the size of CADC fields, which make it easier in terms of handling the images, and are more convenient to cross-match with the optical data. The P89 field has 4 full CADC-NGVS fields and 12 partial fields, and the field P91 has 20 fields. The field that we are working with covers a broad region in the sky and was observed under varying atmospheric and instrumental conditions, therefore it is of utmost importance that we address the inevitably varying PSF over the field. We thus use Sextractor for fixed

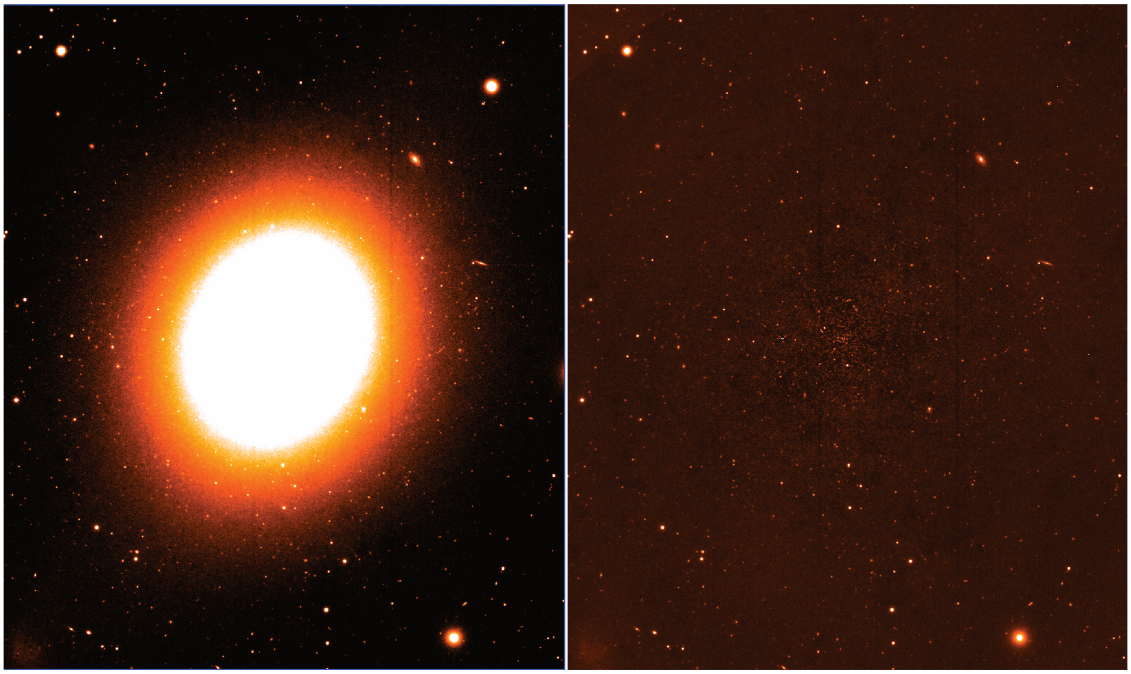

Figure 3.8 The galaxy subtracted image as compared to the image with galaxy on it. The galaxy in the image is M49 in the Ks band. The right panel shows the region after the galaxy is subtracted using ISOFIT/ELLIPSE.

aperture photometry and compute fluxes in multiple apertures with successively increasing radii, which are then used to compute aperture corrections. An additional step that compares the aperture corrected magnitude with an external database (in our case UKIDSS) ensures the absorption of any residual PSF trends that might remain after aperture correction.

In this section we will describe various steps that were carried out to generate the object catalogs with aperture photometry and subsequent additional calibration steps. In addition we will also discuss the calibration of optical galaxy subtracted catalogs with respect to the CADC-NGVS catalogs.

3.6.1 Aperture Photometry

A fixed aperture photometry is not viable in a wide field as a fixed aperture does not account for the varying PSF, and is also insufficient to capture maximum flux from all the objects. To deal with these issues one can perform aperture photometry. We adopt the standard aperture magnitudes provided by Sextractor in apertures of requested radii. In both J and Ks bands, we allow Sextractor to measure the flux and magnitudes of the objects in circular apertures of radii ranging from 0.5" to 6". We select the point sources in the field and construct a curve of growth (CoG) by taking median of aperture magnitude differences in successive apertures.

The point sources are selected using Sextractor parameters MAG_AUTO, and FLUX_RADIUS for magnitude and radius limits for bright and unsaturated point sources. For the J band we choose objects with FLUX_RADIUS values between 2.1 and 3.0 pixels and 2.2 and 2.8 for the Ks band. The magnitude range is from MAG_AUTO 13.0 to 16.2 Vega magnitudes for both the bands.

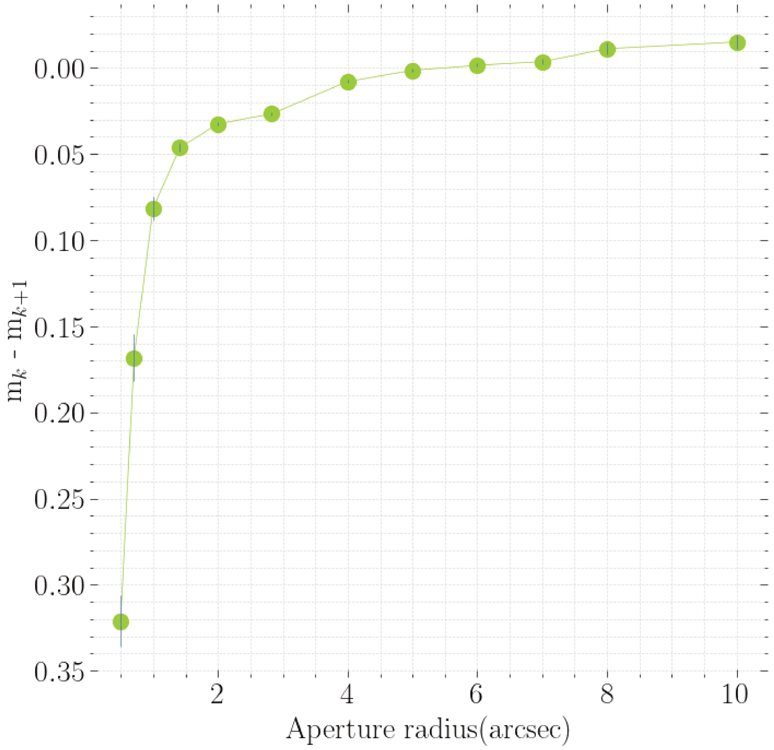

Figure 3.9 The curve of growth for point sources in the Ks band (P89). The *x-axis* displays the aperture size in arcseconds, and the *y-axis* shows the median difference between the magnitue in corresponding aperture and the subsequent aperture (*k* and *k+1*). In this particular band, the difference between m_k and m_{k+1} for k=4 is zero, which indicates that aperture of radii 5" encloses the maximum flux and the subsequent apertures starts to get dominated by more and more noise.

Figure 3.9 shows a curve of growth for the Ks band for P89. The green data points are the median of the differences between the aperture magnitudes in k^{th} and $k{+}1^{th}$ aperture for the point sources in the field, and the blue bar is the standard error on the median. As long as the difference between the two successive magnitudes is positive the flux dominates the noise and increases as aperture radii increases, and when the curve hits 0 the magnitudes in the two corresponding apertures is almost the same, post which the noise starts to dominate.

The bigger aperture of the data point where the curve hit 0 is the aperture to which the corrections will be made and we will call it the reference aperture. For the J band in P89 dataset the CoG gives aperture with radii 6” as the reference aperture that should be used for correction, while for Ks in P89 and J, and Ks in P91 the reference aperture is aperture with radii 5”.

The aperture corrections are calculated for each aperture and we use the point sources selected in the previous step for the same. For each source in the field, we locate n nearest point sources and take the median of the difference between i^{th} aperture and the reference aperture magnitudes, which is the aperture correction for that source. This is implemented using the Python implementation of the k-d tree algorithm, where k in this case the dimension of the dataset and is 2 (RA and Dec), and n is the number of nearest neighbours, which is set to 25 for calculating aperture corrections.

A comparison of the variation of the FWHM of the point sources and the calculated aperture corrections for all the objects is shown in figure 3.10. The bottom panel shows the aperture corrections for the aperture of radius 1” for objects in Ks band. The pattern of the the variation of the FWHM is very well replicated in the high resolution aperture correction map.

The two corrections above constitute the aperture correction for the magnitudes. In the next section we will discuss the uncertainties on the aperture corrections and their contribution to the total error budget.

3.6.2 Uncertainties on aperture corrections

The uncertainties on the aperture corrections are estimated from the map of residual differences between the real value of aperture correction and the inferred values. The real value of aperture correction is the difference between the aperture magnitudes in smaller aperture and the reference aperture, whereas the inferred aperture correction is the value of local median aperture correction derived as described in the previous section. The error on the aperture correction values is estimated by taking the local standard deviation of these residuals divided by the square root of $n-1$, where n is the number of stars in the local patch. The uncertainties in the aperture corrections remain well below 0.02 magnitude in all the fields that P89 and P91 are comprised of.

3.6.3 External Photometric calibration

We carry out an additional step that is required to absorb the leftover effects of varying PSF. While the aperture correction captures large amplitude the variations in the PSF, there are

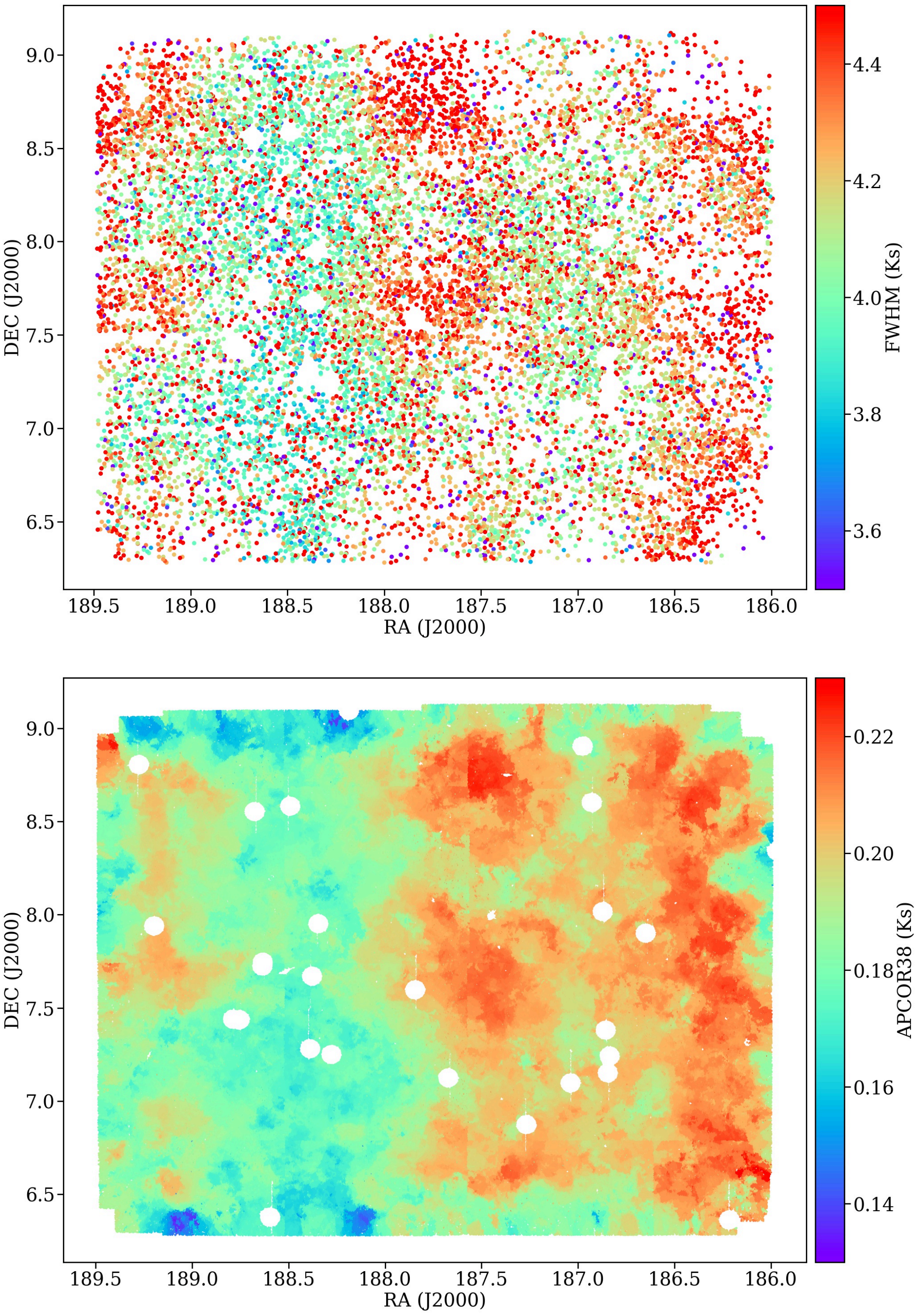

Figure 3.10 The comparison of the variation of FWHM map (top panel), and the aperture correction values for Ks band (P89) as a function of the location of objects. The top panel shows variation of the FWHM of the selected point sources across the field. The bottom panel shows the aperture correction values calculated from the point sources for all the objects in the top panel for aperture of radius 1” (APCOR38).

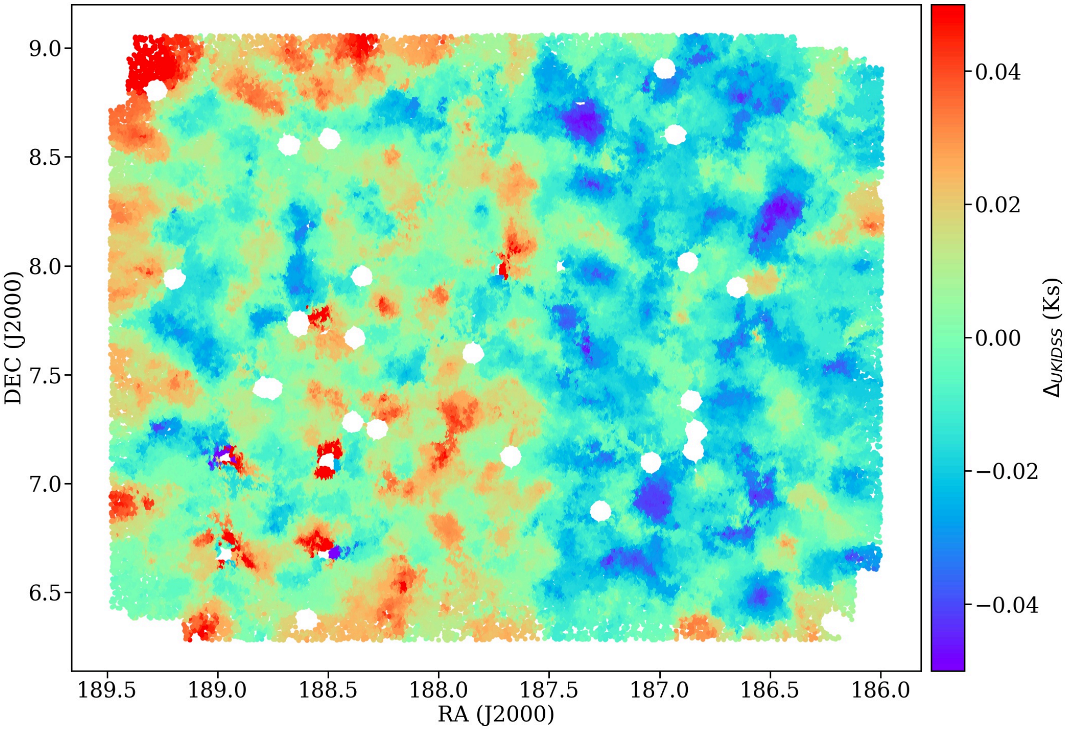

Figure 3.11 The map of the offset between transformed UKIDSS magnitudes and Ks band aperture corrected magnitude in aperture of radius 1".

small amplitude trends that the reference aperture also suffers. To counter these trends we compared the stellar magnitudes with transformed UKIDSS magnitudes. The color - transformation between UKIDSS and VIRCAM are explained in appendix A.1. We compare the aperture corrected magnitudes of the point sources with the transformed UKIDSS magnitudes and use the k-d tree algorithm to calculate the offset between our J and Ks band aperture corrected magnitudes and UKIDSS J band and K band magnitudes. We denote this offset by Δ_{UKIDSS}. The Δ_{UKIDSS} varies between -0.05 to 0.05 for smaller apertures and -0.05 to 0.1 for larger apertures in the Ks band, whereas for the J band it varies from -0.06 to 0.07 in all apertures. Figure 3.11 shows the variation of Δ_{UKIDSS} for Ks band aperture corrected magnitude for aperture radius 1". The map shows the apparent dependence of the offset on RA more than DEC.

By default, these magnitudes are in the Vega system and it was transformed from Vega to AB system by applying appropriate transformations. The values for a given set of filters can be derived from info on the SVO [7] pages for Paranal. For J band the offset to be subtracted from Vega magnitude is 0.925 and for Ks band it is 1.836.

---

[7] Click here for the link to SVO page for Paranal.

3.6.4 Final word on aperture correction values

The final value that needs to be subtracted from the Sextractor aperture magnitudes is a consolidated sum of all the corrections that we have calculated in the previous sections, including the UKIDSS to VIRCAM shifts, and the Vega to AB offset. Therefore, the consolidated aperture correction values for J band is,

$$J\_apcor_i = apcor_i + \Delta_i - 0.925 \tag{3.1}$$

and, for Ks band,

$$Ks\_acpor_i = apcor_i + \Delta_i - 1.836 \tag{3.2}$$

where i is the i_{th} aperture. This value is subtracted from the Sextractor aperture magnitudes to obtain aperture corrected magnitudes which are calibrated against UKIDSS, and are in the AB magnitude system.

3.6.5 Calibration of galaxy subtracted optical band catalogs

As discussed briefly in section 3.5.5, we have to perform a galaxy subtraction in all the optical bands in addition to the infrared band images. The other optical NGVS catalogs in the dataset come from the CADC repository and have been created and calibrated in a certain way that is almost impossible to replicate completely. While performing photometry on optical galaxy subtracted catalogs we tried to maintain the parameters and configuration files as similar to the original NGVS ones as we could, but there were still some inevitable differences between the magnitudes in our optical catalogs and the CADC catalogs. After photometry on the galaxy subtracted optical images, we calculated the aperture corrections for all the bands. We compared the aperture corrected magnitudes of the point sources in the part of the field, with the aperture corrected magnitudes of their counterparts in CADC catalogs. The difference between the two for the point sources was used to construct a smooth interpolation for the correction to be applied to other objects in the field. This correction was applied to the respective aperture corrected magnitudes from our galaxy subtracted optical images. The median residual between the galaxy subtracted aperture corrected magnitudes and the CADC magnitudes after correction is less than 0.01 magnitudes in all the optical bands.

3.6.6 Extinction correction

The typical values of the foreground extinction based on dust maps from Schlegel et al., 1998[8] in the direction of the Virgo cluster are in the range 0.06 $<$ A(V) $<$ 0.16.

Extinction coefficients for J and Ks are taken from the SVO filter services and for *u, g, r, i,* and, z bands from Muñoz et al., 2014. The values for IR filters are based on the extinction law by Fitzpatrick, 1999 improved in the near-infrared by Indebetouw et al., 2005, and those for the optical filters on the work of Cardelli et al. (1989); both sources adopt $R_V = 3.1$.

The average values of the extinction correction are 0.05 for *(u-i)* and 0.03 for *(i-Ks)*, with a standard deviation of one tenth of those values.

3.7 The Photometric Catalogs

The final data product that results after the stacking, photometry, and additional calibrations is the catalog of objects in the J and Ks bands. The 5 - σ detection limit in the J band is 23.1 AB mag, and in Ks band is 23 AB mag. The catalog is cross matched with the optical catalogs obtained from the CADC-NGVS repository, and the bands consists of u, g, i, and z bands and partial coverage in the r band. The position information of objects in infrared bands is calibrated against GAIA-DR1 (P89 data) and 2MASS (P91 data) and other optical bands that are calibrated against the SDSS catalog where available, otherwise on 2MASS. In our catalog we only provide coordinates calibrated against GAIA-DR1 (P89) and 2MASS (P91). A density plot of objects in P91 field is shown in figure 3.12. The figure shows objects that are common to near-IR and optical bands. The missing portion in the catalog (between DEC 12.5 and 13.00 degrees and RA 12h28m00s and 12h25m00s) is because the optical data is not available in that part of the field.

The photometric parameters come from Sextractor and have aperture magnitudes in the aperture of radii - (1) 0.5" (2) $1/\sqrt{2}$ " (3) 1" (4) $\sqrt{2}$ " (5).$2\sqrt{2}$" (6). 4" (7). 5" (8). 6". The subscript corresponds to the serial number in the parenthesis and is appended to prefix APCOR to identify the aperture. The optical bands have aperture magnitudes in radii ranging from 0.5" to 1.5".

The optical magnitudes are aperture corrected and calibrated against the SDSS database that are in the AB magnitude system.

---

[8] We have used Python package SFDmap to access Schlegel extinction map.

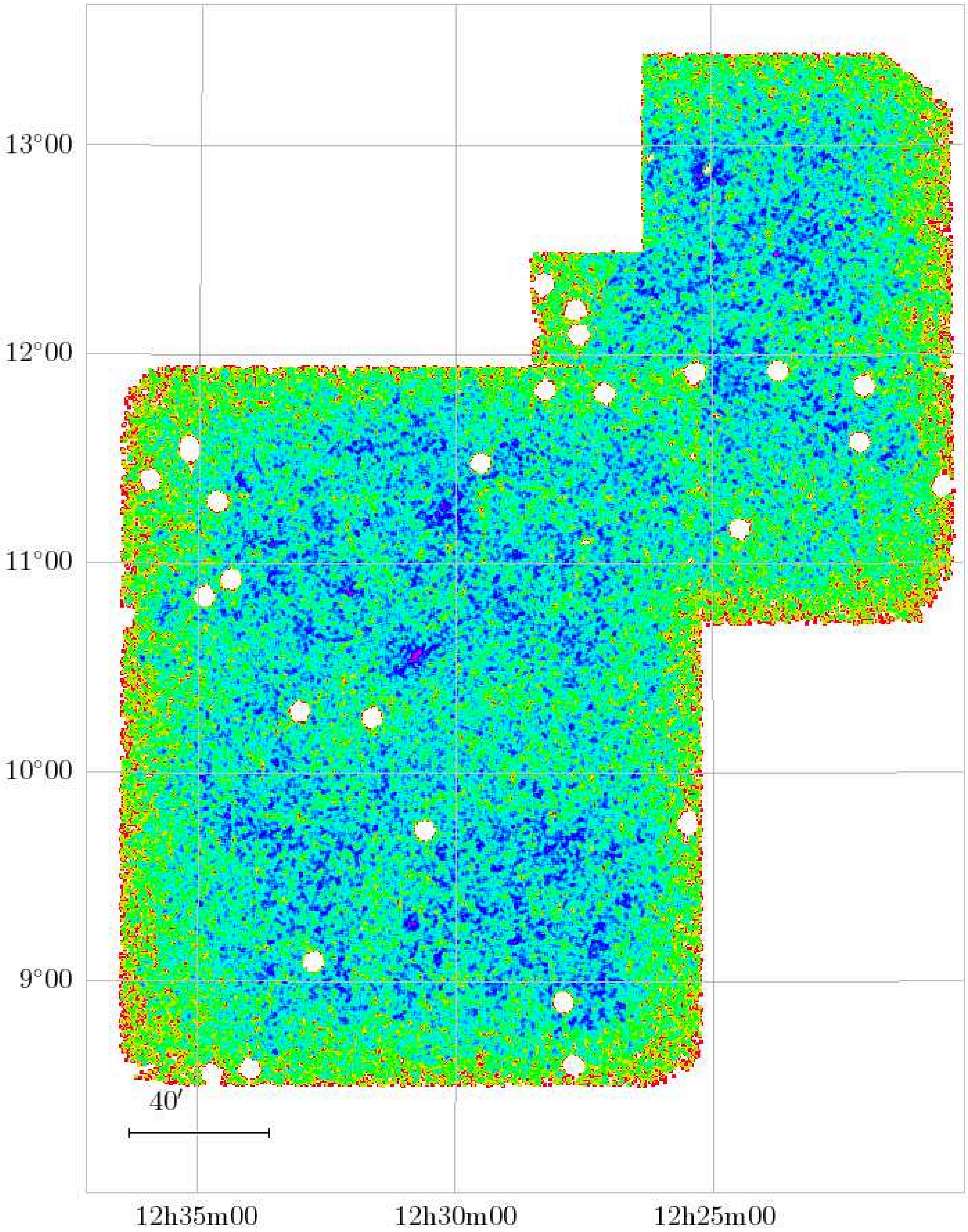

Figure 3.12 The density plot of the objects in P91 field. The objects are extracted using Sextractor. The holes are the location of bright saturated stars. The field covers ∼ 13 square degrees.

Chapter Four

Globular cluster selection and the color color diagrams

"I haven't failed, I have found a thousand ways that don't work." - Thomas Edison

Abstract

In this chapter we will describe the selection of the GCs in the Virgo fields of our new infrared observations using the *uiKs* color-color diagram. The *uiKs* color-color diagram combines the near-ultraviolet, optical and near-infrared data and is a very strong diagnostic tool. We will detail the various steps of the GC candidate selection. The later parts of the chapter deal with the corrections that are applied to the data to homogenize the colors. We conclude the chapter with the description of various GC groups in different environments within the Virgo galaxy cluster.

4.1 Color-color diagrams

The need to extend the NGVS observations to infrared was to develop an efficient classification procedure that utilizes the photometric information from near-UV to near-IR. The objectives of the NGVS-IR survey include the study of star formation histories and mass profiles of Virgo galaxies, the identification of GCs and ultra compact dwarf (UCD) galaxies, and characterising the UCD and GC stellar populations by combining the optical, near-UV and near-IR data. The combination is useful to break the age-metallicity and mass degeneracies much more efficiently than just using optical colors.

One of the most important goals of the NGVS-IR survey was to provide a clean sample of any kind of objects, in particular the globular clusters, UCDs and dwarf galaxies. The broad band colors, when available across a wide range of the electromagnetic spectrum, are capable of delivering very robust results. Daddi et al., 2004 demonstrated the diagnostic power of a combination of (B-z) and (z-K) colors that was used to classify passive and star-

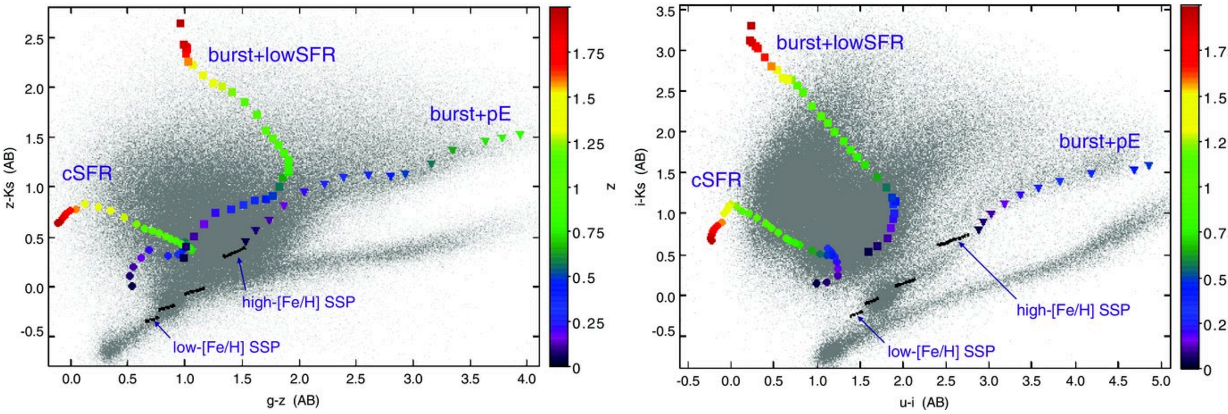

Figure 4.1 Color-color distribution of objects in the NGVS/NGVS-IR images of 4 square degrees around M87. Overlaid on top of the color-color diagram are the stellar population tracks for different ages and different star forming histories color coded by metallicity values (Muñoz et al., 2014)

.

forming galaxies at redshifts higher than 1.4. Since then the *BzK* diagram is broadly used in conjunction with extra-galactic surveys to segregate low and high red-shift passive and star forming sources. The closest NGVS equivalent of the *BzK* diagram is the *gzKs* diagram. Both the *BzK* and the *gzKs* diagrams have GC sequence that merge with the low redshift galaxies at the redder end and with the stellar sequence at the bluer end.

4.1.1 The *uiKs* color-color plane - The tool for effective GC selection

The exceptional diagnostic capability of the *uiKs* diagram to classify compact stellar systems like GCs composed of old stars, and UCDs has been demonstrated by Muñoz et al. (2014). The *uiKs* diagram combines the photometry from the near-IR, optical and near-UV filters and it provides a more prominent segregation between background galaxies, foreground stars and other compact stellar systems. This is very useful in terms of identifying the GCs as the distinction is much better defined than in other color combinations discussed.

In figure 4.1 the *gzKs* and *uiKs* color-color diagrams are compared to each other and to the simple stellar population (SSP) models computed using the PEGASE library (Fioc and Rocca-Volmerange, 1997) for NGVS+NGVS-IR filters. The SSP tracks (shown as solid black lines) are calculated for Z = 0.0004, 0.001, 0.004, and 0.02 for ages 8 to 13 Gyr. These tracks coincide with the GC locus on the color-color planes. Additionally, the tracks of red-shift evolution of three prototypical galaxies which were born at z=3 are also displayed. The three type of systems are, in order of color ranging from blue to red, a continuously star forming galaxy, a galaxy that had major star formation at the earliest epoch and then evolved with a lower star formation, and a passively evolving galaxy that had its major star forming episode at z=3.

4.1.2 Reasons for excellent diagnositic power of the *uiKs* diagram

In the *gzKs* diagram the SSP tracks that correspond to the compact stellar systems overlap with the passively evolving galaxies on the red end and with the stellar sequence on the blue end. The distinction between the SSP tracks in the *uiKs* diagrams is distinctly defined.

The GC sequence at the blue end in the *gzKs* diagram at *g-z*∼1.0 and *z-Ks*∼0-0.5 also suffers from contamination by star-forming galaxies with redshift z∼0.5-1. The spectra of star-forming galaxies display a strong Balmer jump at $\lambda \sim 4000$Å. When the associated drop in flux (at 3000Å $< \lambda <$ 4000Å) is moved into the *g* band by the redshift, the observed *(g-z)* is quite red, creating the confusion with GCs. This contamination by star forming galaxies is reduced drastically in *uiKs* color-color plane and the GC sequence is neatly separated from the star-forming galaxy sequence at the blue end and the stellar sequence at the red end. The dip in flux rapidly moves out of the u-band. By redshift 0.25 the *u* band sees the steep rise in near-UV flux typical of star formation and so (*u-i*) is very blue. This blue-ward shift creates a better distinction between the metal poor GCs and the galaxies with active star formation at higher red shift. The red-shift evolution in SEDs of the passive galaxies pushes the low red-shift passive galaxies towards the cooler side on both color axes.

The separation at the stellar end comes from the fact that the *Ks* band is sensitive to cooler red giant branch (RGB) stars and (*i-Ks*) color is representative of effective temperature of RGB population. On the other hand (*u-i*) is sensitive to the hot stellar population (main sequence turn-off and horizontal branch) in the GCs. This makes the separation between the GCs and stellar sequence of the MW more efficient. The stars on the hotter end of the stellar sequence in the *uiKs* diagram are the main sequence turn-off stars in the Milky Way halo while the ones on the cooler end are lower main sequence stars in the disk.

Given the advantages of the *uiKs* color-color diagram over other color combinations, specifically in identifying the globular clusters, we will exploit this diagnostic capability using our data.

We use dereddened aperture corrected magnitudes in the *u, i* and *Ks* bands. For optical bands, we have taken the aperture corrected magnitudes based on apertures of diameter 3", and for the *J* & *Ks* band we have taken the aperture corrected magnitude based on apertures of diameter 2". The choice of aperture is a compromise between minimizing the dispersion and capturing maximum flux in the object of interest, the globular clusters. Evidently, at the distance of the Virgo cluster (∼16 Mpc), the GCs are marginally resolved, and therefore

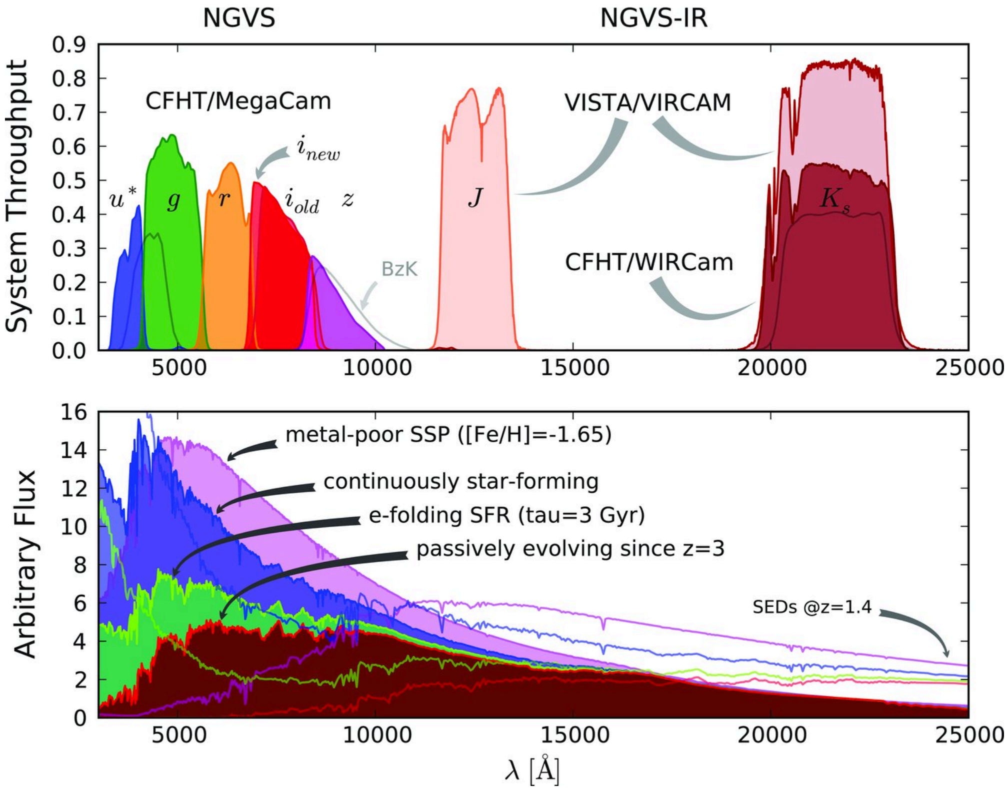

Figure 4.2 *Top panel*:Comparison of throughput curves of NGVS+NGVS IR filters. The detector efficiency for the two *Ks* bands is different for the two instruments. *Bottom panel:* Comparison of four different types of SEDs. For comparison all the SEDs are normalized at z = 0 to the flux at 2.2 μm which roughly corresponds to effective wavelength of *Ks* band. The open SED curves correspond to the same SEDs as they would appear at z = 1.4. (Figure courtesy - Muñoz et al. (2014)).

an aperture correction based on point sources will not entirely ensure that the aperture corrected magnitudes will all have the same magnitudes. This possible issue is minimized when aperture and initial magnitude is large enough. In the near-IR, the background is noisier than in optical images and as a result the optimal measurement aperture is smaller.

We can further use the fact that GCs are marginally resolved to our advantage by curating a factor that holds size information. The size information comes from a difference between aperture corrected magnitudes in a smaller and a bigger aperture and we will call this parameter compactness index or iC. In the present context, this parameter is the difference between aperture corrected i band magnitude in the apertures of size 1” and 3”. In the case of point sources the iC will be close to zero but will increase for more extended objects. Since GCs are slightly more extended than the point sources, the iC of the GCs takes a small positive value on average.

The effect of size information on the separation between GCs and other sources can be visualized with 3-D plotting tools, using *(u-i)*, (*i-Ks*) and iC on the three axes. Projection onto certain planes of that 3-D space maximizes the separation; if we subtract the iC from the *u-i* color and add it to the *i-Ks* color the separation between the different morphological objects becomes more distinct. We call this projected color-color diagram a modified *uiKs* diagram. Figure 4.3 shows the de-reddened and modified *uiKs* diagram for the objects in the P89 field that have Sextractor errors smaller than 10%.

The objects are colored according to their iC values. The point sources have a neatly defined sequence and have iC values which are centered around 0. The galaxies have larger values of iC, and the GCs lie in between the galaxy region and the stellar sequence and have iC values ranging between 0.05 to 0.25.

In the next section we will explore various techniques to select the GC candidates from the *uiKs* diagram detailing the steps implemented by steps to reduce contamination from stars and background galaxies in the GC sample.

4.2 Selection of Globular Cluster candidates

The *uiKs* diagram provides an excellent tool for identifying the GCs, and we will demonstrate some of the methods that we have tried to isolate the GCs from the rest of the objects. In the processes that we have adopted to pre-select the GC candidates, inevitably contaminants creep in. We have adopted certain rejecting criteria which are common for all the pre-selection procedures and we will briefly describe each rejection criterion before returning to the pre-selection procedure.

Rejecting contaminants

The contaminants in a pre-selected GC sample can be either point sources or the background galaxies. To separate the galaxies from the rest of the objects the iC is a very strong parameter. In the modified *uiKs* the majority of the extended objects move away from the GC sequence and they can, therefore, be discarded right away. Thus selecting GC samples from a modified *uiKs* diagram is more efficient than selecting GCs from a normal *uiKs* diagram. A very few extended objects still make their way to the GC sample selected using a modified *uiKs* diagram and can be removed by putting an upper limit on the iC. Anything that has an iC larger than 0.25 is very unlikely to be a GC.

The contamination due to point sources cannot be fully eliminated by using the morphological parameter (iC) because of the natural dispersion in iC values. The iC values of the point sources are centered around zero but they have a typical standard deviation of 0.02. This also applies for the red GCs which have smaller values of iC and therefore their iCs

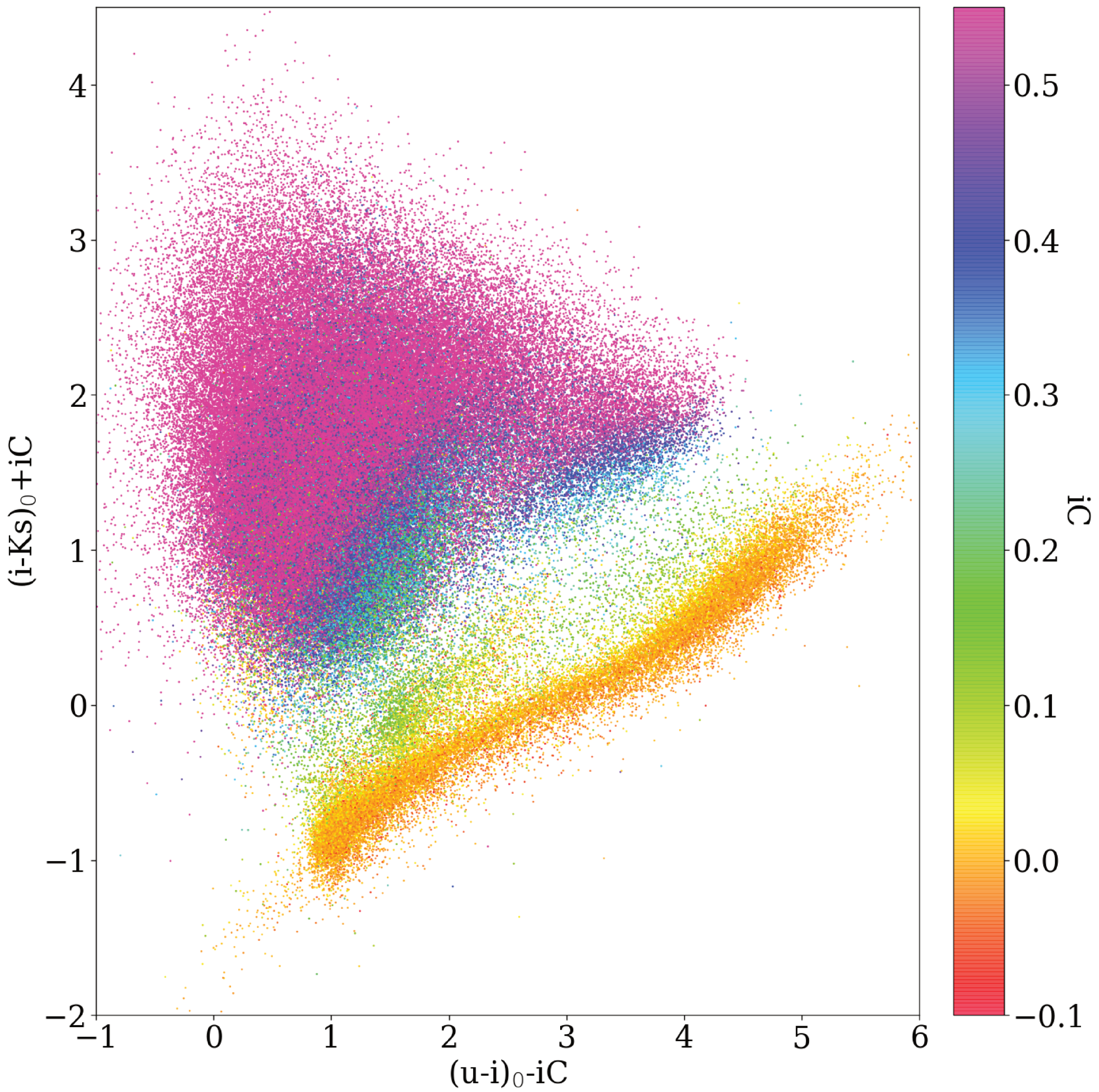

Figure 4.3 The modified *uiKs* color-color diagram for the objects in the P89 field colored by the compactness index or iC.

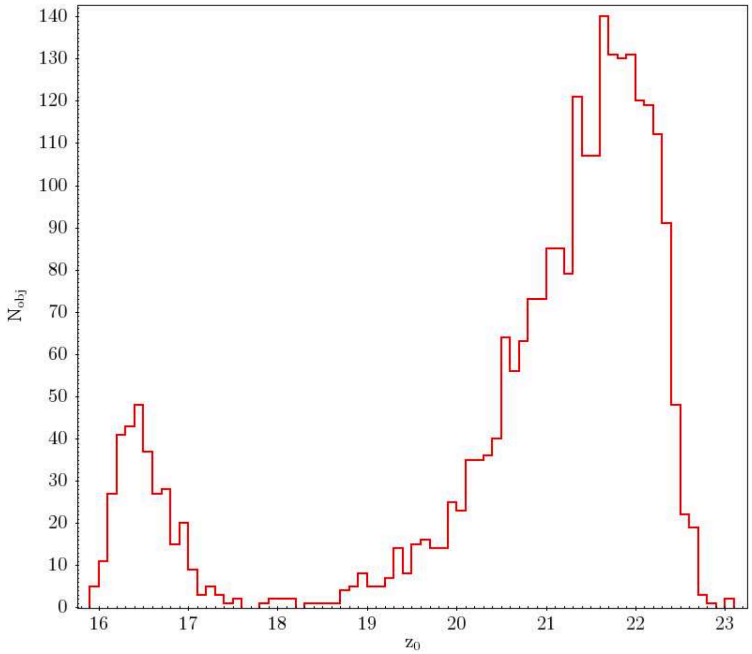

Figure 4.4 Distribution of z band AB magnitude for the objects in the pre-selected GC sample from the modified *uiKs* diagram having -0.1 < iC < 0.3. The objects that are brighter than 18 magnitude are more likely to be stars than GCs.

overlap with the point sources. So we extend the value of iC from 0 to -0.1 to allow more red GCs in the sample thereby also increasing contamination due to stars.

The Globular Cluster Luminosity Function (GCLF) of M49 based on the areas imaged with the Hubble Space Telescope peaks at magnitude 23 (AB) in the z band (Jordán et al., 2007b; Jordán et al., 2009). We do not expect to find any GCs brighter than 18 mags in the z band and we can reject anything that is brighter than that limit. Figure 4.4 shows the z-band magnitude distribution for the objects in a GC sample obtained with the ridge line method(see section 4.2.1) with iC values smaller than 0.25. The distribution is strikingly bimodal and the objects brighter than 18 AB mag are unlikely to be GCs and can be safely removed.

These are the two major steps that will remove the majority of the false candidates. In addition one can use other color-magnitude diagrams, like J vs *(J-Ks)* or the i vs *(g-i)* CMD. The point sources form a separate sequence at the brighter end on the magnitude axis in the CMDs.

These rejection steps can be applied to any GC candidate sample irrespective of the way it was pre-selected. In the next subsection we will discuss a few techniques that can be used to pre-select a GC rich sample in the initial modified *uiKs* diagram.

4.2.1 Ridge line

In the first method we have used a sample of cluster candidates identified spectroscopically in our survey region. It was provided by NGVS collaborators. The uiKs colors of the bonafide GC candidates are used to construct a ridge line which is then used to select objects that lie along the line as GCs in our sample. The sample thus selected is contaminated with stars and background galaxies. We further use concentration index and magnitude in z band to filter the objects that are not likely to be GCs (figure 4.4).

We use a sample of about 480 spectroscopically confirmed GCs to construct the fiducial color-color distribution in the *uiKs* plane. The ridge line is constructed by taking equal bins in $(u\text{-}i)_0$ and taking the median of $(i\text{-}k)_0$ in each bin of $(u\text{-}i)_0$ to obtain the fiducial line. This line serves as the guide to mark the region where the GCs are likely to occupy the color-color region. We do not use the same fraction above and below the fiducial line across the range in $(u\text{-}i)_0$, since the spread of the GC sequence is not uniform. We divide the range on the $(u\text{-}i)_0$ axis from 1.4 to 2.2 in 5 unequal bins. The algorithm selects a portion of objects above and below the line, and masks the objects that lie above and below the line terminating the selection areas on the $(i\text{-}k)_0$ where the stellar sequence and the galaxies start (Fig 4.5). The selected sample is heavily contaminated. A simple rejection based on size (iC) and *Ks* band magnitudes removes the majority of the contaminants. These conditions were discussed earlier in 4.2. We always adopt the same criteria to filter objects after a preliminary selection. An object is classified as a GC when it has concentration index iC (Durrell et al., 2014) in the range -0.1 and 0.25 and a Ks band magnitude fainter than 18 AB mag.

After applying the filtering criterion we have $\sim$ 2300 objects left that are the GC candidates in the field. The figure 4.6 shows the position of the selected objects in the RA-Dec plane. The gray dots are the objects that are rejected and the blue dots are the GC candidates. As it is expected, the rejected objects are more dispersed in the field than the final sample of GC candidates, which tend to cluster around major galaxies.

The advantage with using this pre-selection method is that it is insensitive to the magnitude error unlike the other methods that we have used and will review in later part of this section. The disadvantage of using this method is that it uses a known GC sample around M49 which may introduce a selection bias. This bias might have little effect, if any, as compared to the other methods we will discuss in the forthcoming sections.

4.2.2 Gaussian Mixture Models

In this section we will discuss two other methods to pre-select the GCs in the *uiKs* color-color diagram. These methods are more statistically oriented and use a Python implementation

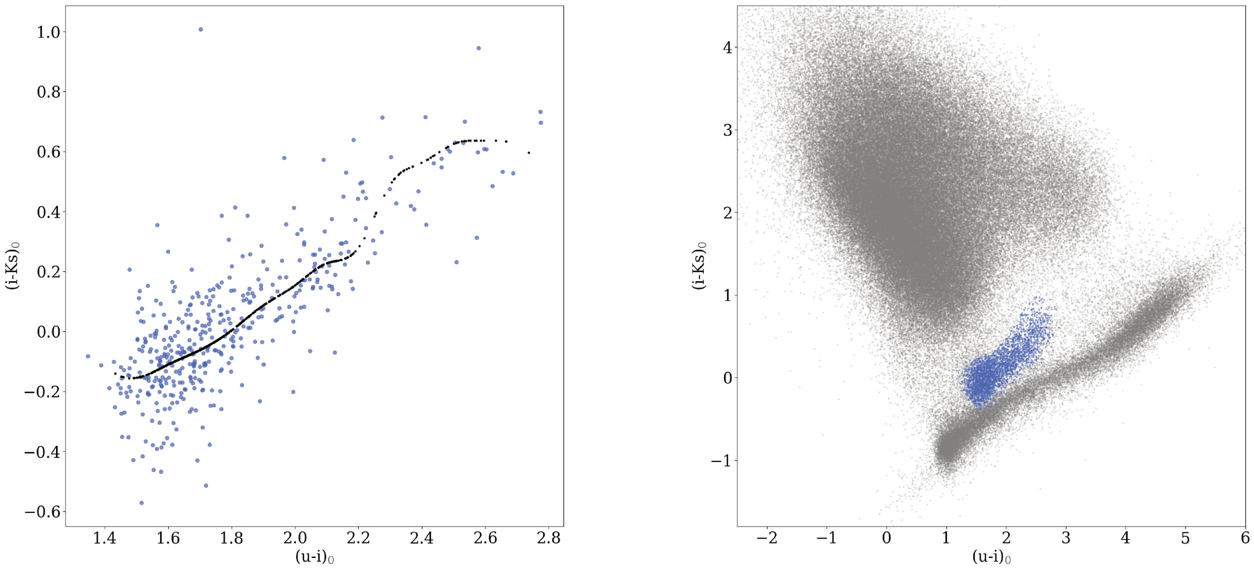

Figure 4.5 *Left*:spectroscopically confirmed GCs in the field on *uiKs* plane. The black circles show the fiducial line which is used to classify cluster candidates in the *uiKs* diagrams. *Right*:The blue circles are the GC candidates classified using the ridge line and after the further selection criterion are applied as discussed in section 4.2.1

of the clustering algorithm called Gaussian Mixture Model (GMM). We will briefly describe the GMM technique in this section.

To recall, a Gaussian Distribution, also known as Normal distribution is a bell shaped distribution in which the data points are symmetrically distributed around the mean value. It is characterised primarily by two parameters, mean (μ) and variance (σ^2). A 2-dimensional Gaussian distribution has elliptical contours and is characterized by its mean, teo variances and a covariance.

A clustering algorithm is one that groups data points together that share similar values. GMM is one such technique that assumes that the data is composed of multiple Gaussian distributions and it tries to group the data points together and associate them with respective Gaussians. Behind the scene, a maximum likelihood calculation determines the best parameters for the gaussians. The number of Gaussian components that could be fit to the data distribution can be left as a free parameter or it can be chosen by the user. One can force the algorithm to fit a certain number of Gaussians in the model if we know intuitively what kind of model best fits the data but a more sophisticated approach would require certain parameters that could quantify the quality of fit. Generally, to get the best GMM one can use the Akaike information criterion (AIC) or the Bayesian Information Criterion (BIC). AIC and BIC are both penalized Maximum likelihood criteria which are employed to avoid

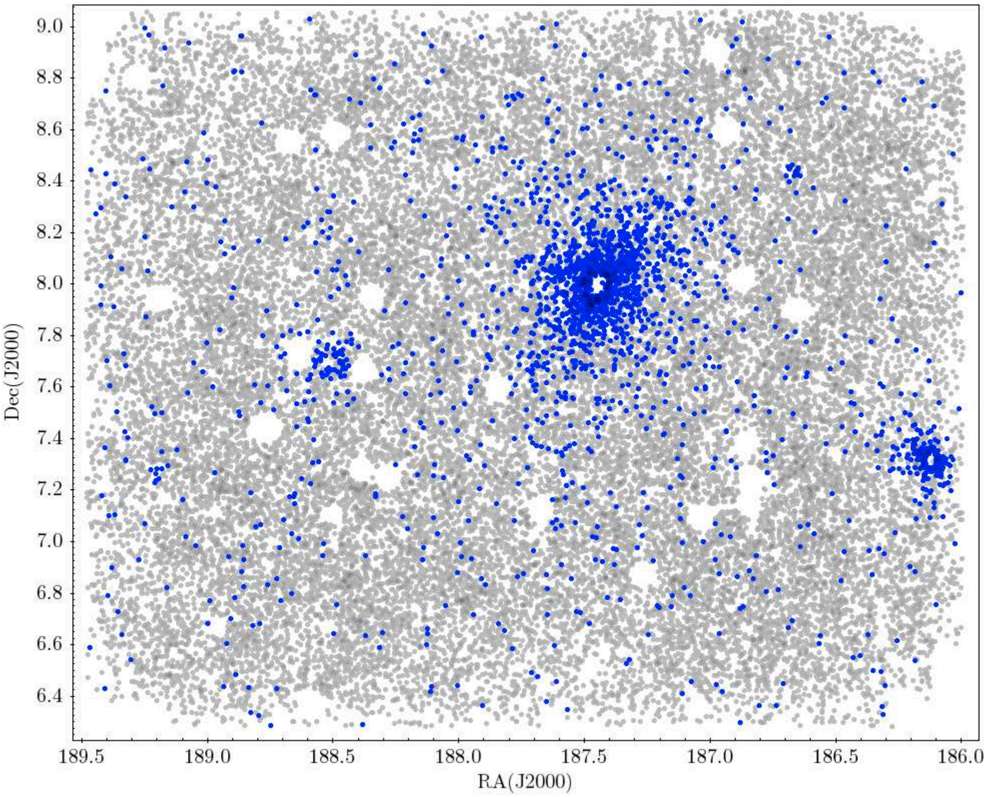

Figure 4.6 Spatial distribution of objects identified as GCs using the ridge line. The gray dots are the candidates before filtering was applied and the blue dots are objects that pass the compactness criteria and magnitude cut.

over-fitting. BIC is the parameter that tells us how well the model predicts our distribution whereas AIC tells us how close the model is to our data. An optimum estimate of the number of components is the value for which AIC and/or BIC is minimum. In our case we take AIC as the deciding parameter.

Another parameter that affects 2D fits such as those performed in color-color space is covariance type. In the Python implementation of GMM, this input parameter can assume any type among the following - *full*, *tied*, *diagonal*, and *spherical*. A covariance type '*full*' allows the gaussian to assume an shape and orientation, whereas *tied* means all the gaussians will have the same shape but that shape can be anything, in *diagonal* type the contours can have any shape but they are always oriented along the axes, and *spherical* has spherical contour (see figure 4.7). We adopted the *full* covariance type because of the flexibility it allows in terms of shape and orientation of the Gaussians.

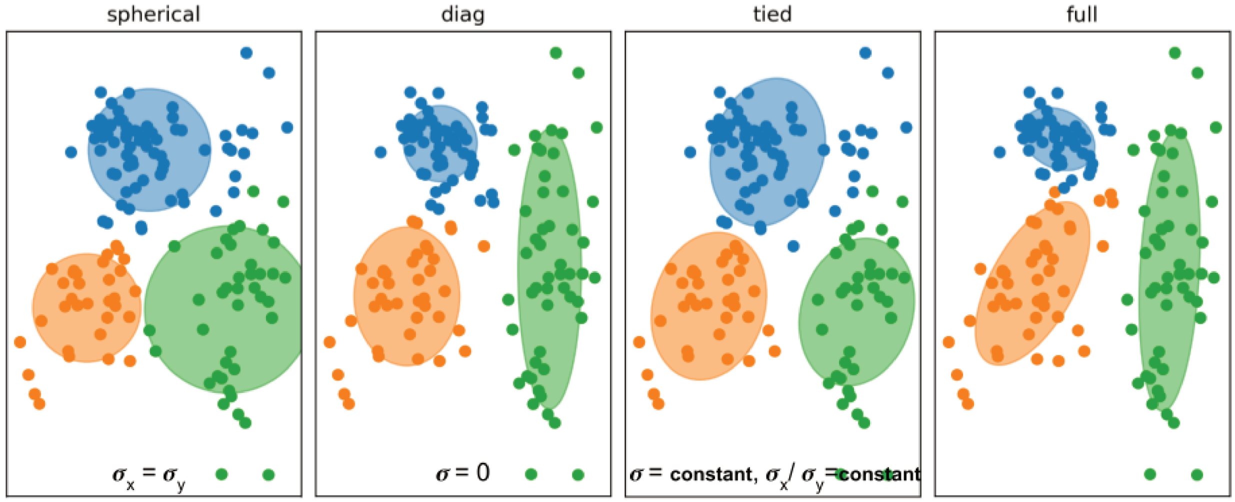

Figure 4.7 Python implementation of the GMM using different type of covariances. Image taken from the github page of Python scikit learn package.

1-dimensional Gaussian Mixture Model

This method uses a 1d GMM model that is fit to a rotated *uiKs* diagram. To facilitate fitting a 1d GMM model to the *uiKs* diagram we rotated the diagram by 26 degrees (0.45 radians) such that the orientation of the distribution is parallel to the *(u-i)* axis (figure 4.8). The rotated (u-i) axis values are divided into overlapping intervals across the range. In each of these interval, we run the GMM model on the $(i\text{-}Ks)_{rot}$ with the number of components that gives best AIC score.

The algorithm groups the objects in such a way that the entire distribution is a sum of multiple gaussians. The figure 4.9 shows the objects in one of the $(u\text{-}i)_{rot}$ intervals. The different colors show the sub-groups that GMM groups the objects in, and a gaussian fitted to each group externally. At the end of the procedure, the trail of groups that form the GC are separated from the rest of the dataset. An initial selection of the GC sample gives about 4500 objects, which, after rejection, retains about 2400 objects.

This selection scheme is free from prior bias unlike the one explained in the previous section that uses a set of already identified GCs. The disadvantage with this algorithm is that the classification is sensitive to the noise. A noisier data makes it difficult to group the objects, especially the GCs that lie in between the stellar sequence and the galaxy sequence and that are not as dense as the stars or the galaxies in the color-color diagram. For this algorithm to work efficiently there should be relatively smaller dispersion within the different groups of objects in the color-color diagram. This could be partially achieved by only allowing objects with smaller errors. But if we restrict the objects with very small errors, we risk losing many GC candidates.

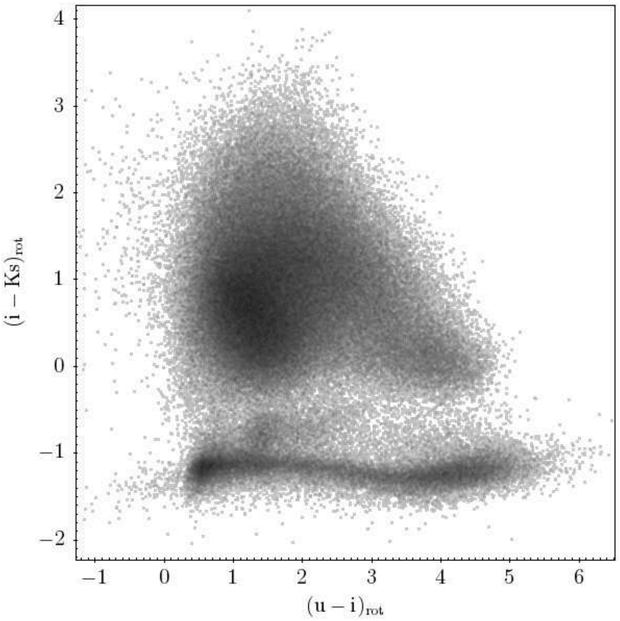

Figure 4.8 The *uiKs* diagram rotated by 26 degrees in clockwise direction to make the plot parallel to the *(u-i)* axis.

In the next part we will explain the GC selection using a 2-D GMM model.

2-dimensional Gaussian Mixture Model

In this method we use a Python implementation of the 2-D GMM. We use AIC to determine the number of Gaussian components, which in the case of our data is 15. This method can work fine with the original modified *uiKs* diagram with the covariance type set to *full*, so we do not need to rotate the color-color plot.

This method of selecting GC candidates is also sensitive to the noise in the data, but provides are better selection. We applied this selection strategy to the dataset with magnitude errors smaller than 6%. The sample selected by this algorithm then undergoes the rejection criterion described earlier. After removing more extended objects, and brighter objects most likely to be stars we get around 1800 objects as GC candidates in P89.

We also use the borders of the region that is marked by the selected GC objects by this method to extend the selection to the GCs that have errors on magnitude higher than 6%. After applying the rejection criteria to this sample, we get around 4500 GC candidates in the field. We expect a lot more contamination in the field GC candidates in this sample. Figure 4.13 shows the distribution of the extended sample as grey data points. The colored data points are the GC candidates that have magnitude errors smaller than 6%. The various colors denoted the different groups the GCs will be assigned to in section 4.4.

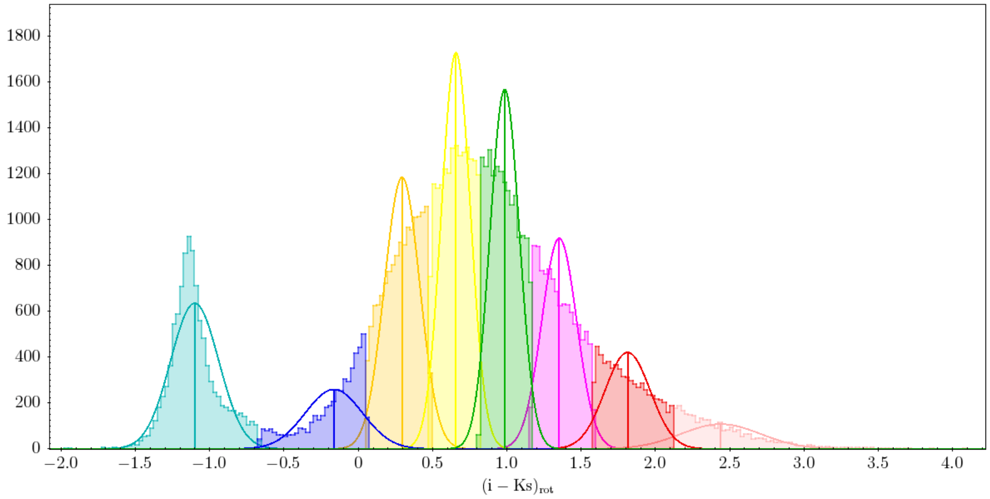

Figure 4.9 The histogram of $(i\text{-}Ks)_{rot}$ color for one of interval of $(u\text{-}i)_{rot}$. The Gaussians are fitted to each sub-group externally to roughly represent the gaussians that were fitted by the 1-D GMM. This figure only shows a part of the $(u\text{-}i)_{rot}$ color. The violet region is most likely region occupied by GCs. The figure is only to display how the 1-D GMM works, we did not use the sample of GCs selected uisng this algorithm.

4.2.3 Final sample of Globular clusters

Of the three methods described above, the 2D GMM gives the GC sample with the least contamination. Also including the GCs that are extracted after subtracting the main galaxy (see section 3.5.5), we have 2049 objects in the P89 field with magnitude errors smaller than 6%. In the P91 field, following the same selection and rejection criteria we have 1580 clusters with magnitude uncertainty less than 6%. The selected GCs in the P91 field are shown in figure 4.10. The spatial structure of GCs in this map is consistent with the GC density map shown in Durrell et al. (2014) (their figure 9), but our sample is less densely populated due the constraint on photometric errors on our GC sample. The only major galaxies in the P91 field are M84, and M86 which are the most crowded regions in the field. A big fraction of the sample are free floating clusters which also includes the clusters around smaller galaxies in the field.

In the next section, we will derive the correction for homogenized colors for these candidates.

4.3 Optical color correction

The NGVS optical band data is calibrated against the *Sloan Digital Sky Survey (SDSS)*. The two surveys have a relatively narrow overlap in magnitude hence a relatively small

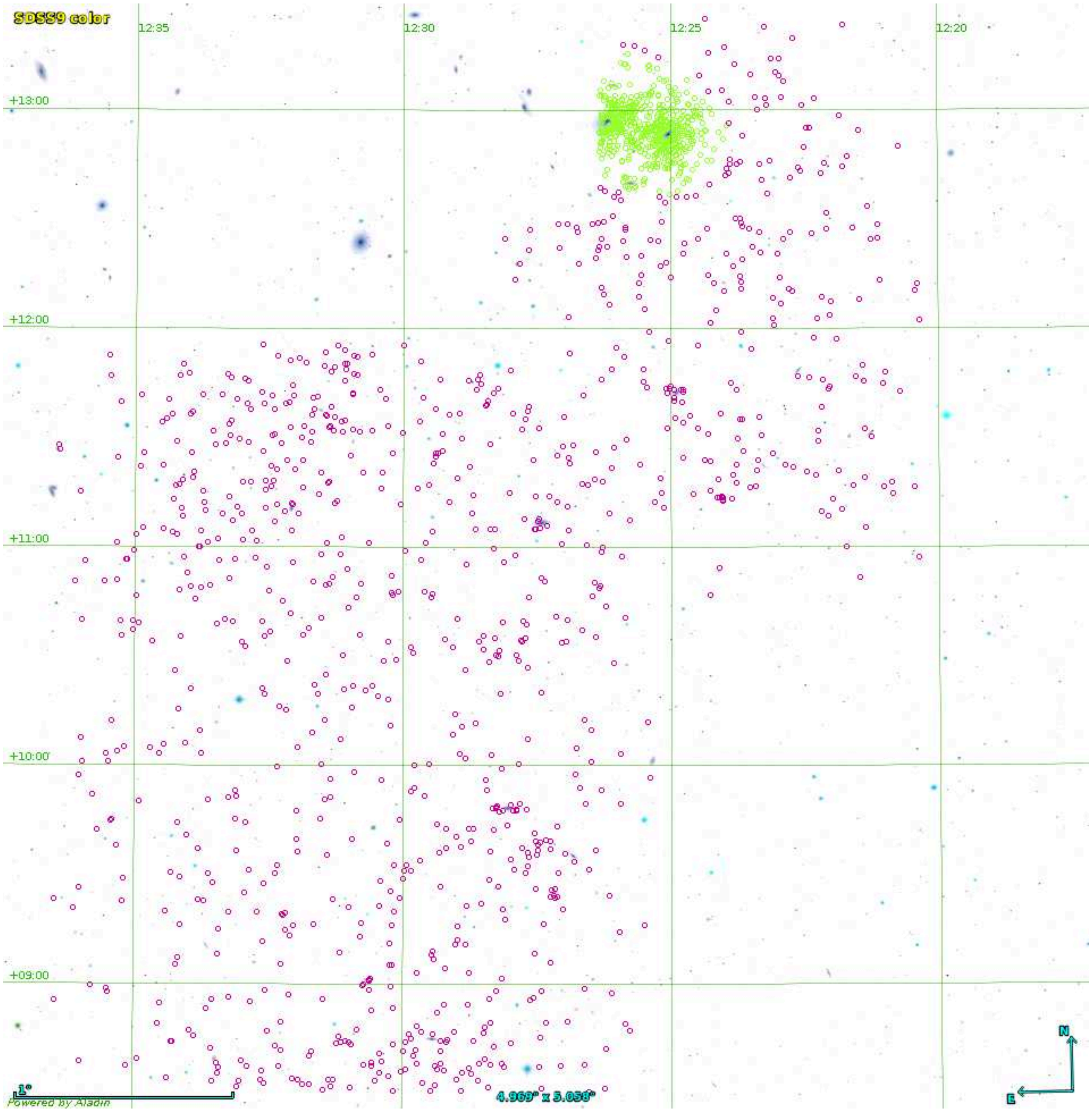

Figure 4.10 Globular clusters in the P91 field selected using Python implementation of GMM clustering. The green circles are the GCs which belong to M84 and M86, and the magenta circles are the field clusters.

number of common point sources; this gives rise to spatial variations in the photometric calibration. Before comparing the colors of our objects of interest between different areas, we must evaluate and address these effects. The goal is to homogenize the colors of the GCs over the entire field. As in Powalka et al. (2018), we estimate corrections by assuming that the colors of the most common Milky Way stars are homogeneous across the field of view. We emphasize that this method produces a statistical correction of colors, not magnitudes: the corrected colors should not be used to re-evaluate individual stellar magnitudes.

Point sources are selected with the aid of the *uiKs* diagram combined with size information that serves to reduce contamination from extended objects. In the bottom panel of figure 4.11 we have plotted g vs *(g-i)* for the selected point sources. The objects that have *(g-i)* < 0.5 are mostly main sequence turn-off (MSTO) stars of the Milky Way (MW) halo and of the Sgr stream that crosses the Virgo field (Durrell et al. 2014, Lokhorst et al. 2016). The region from *(g-i)* $= 0.6$ to 1.15 is occupied by a mix of GCs in the Virgo field ($g >$ 20.0 mag), main sequence stars in the inner MW halo, and sub-giant and red giant stars in the Sgr stream. The objects at *(g-i)* > 2 are faint MW disc dwarf stars. There is residual contamination by galaxies at the faintest magnitudes in all bands.

The color distribution in figure 4.11 is too broad to be used as it is to homogenize colors, considering the available spatial density of stars; but a large fraction of the stars reside in a narrow range of colors at the blue end, and they constitute an adequate subset. Our magnitude selection for the color-correction sample is set at the faint end by the curved aspect of the main stellar locus when the end of the MW halo is reached, as well as by galaxy contamination; at the bright end it is set to avoid saturation in all bands and at all positions ($19.8 < g < 22.2$ AB mag). The color cut at *(g-i)* < 0.5 is a compromise to include enough stars from the dominant peak in all bands without being contaminated by GCs.

The selected sample of point sources is used to evaluate optical color corrections for the GC candidates in the field. The underlying scheme uses a global average for the field which is used as a reference target value for the color in question. The local average color is calculated on a smaller patch. The difference between the two at a coordinate is the deviation from the global average color value and thus the correction value at that location. The global average color is the median for the respective color in a smaller neighborhood after applying 2.7σ clipping. We apply an adaptive filter-based approach to calculate the local median and use k nearest neighbor stars around any GC to calculate the average stellar color around that position. A larger value of k will ensure a more precise estimate of the local average but this comes at the cost of a lower spatial resolution. Balancing the two factors, we selected k=40 to exploit the $\sim$5000 and $\sim$7000 stars selected in the P89 and the P91 field respectively. The difference between the global median and the local median, Δ is the correction to be added to original colors. The map of the Δ for all available colors is shown in figure 4.12.

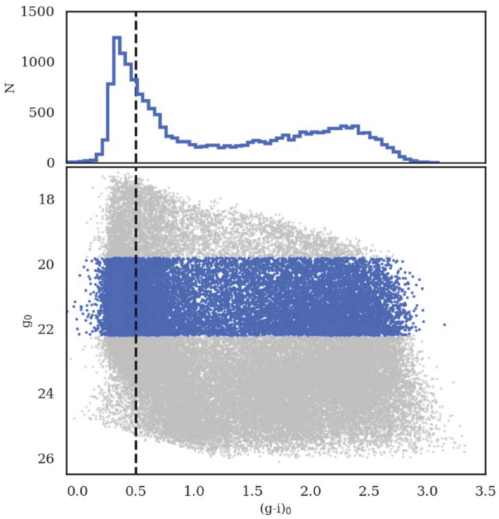

Figure 4.11 Selection of stars for the color-corrections of section 4.3. The bottom panel shows the *g* vs *(g-i)* CMD of all the stars initially selected using in the modified *uiKs* color-color diagram. The blue symbols identify stars that pass the extra magnitude criteria described in section 4.3; their color distribution is shown in the top panel. The dotted line marks the color cut applied to isolate the dominant peak of the color distribution.

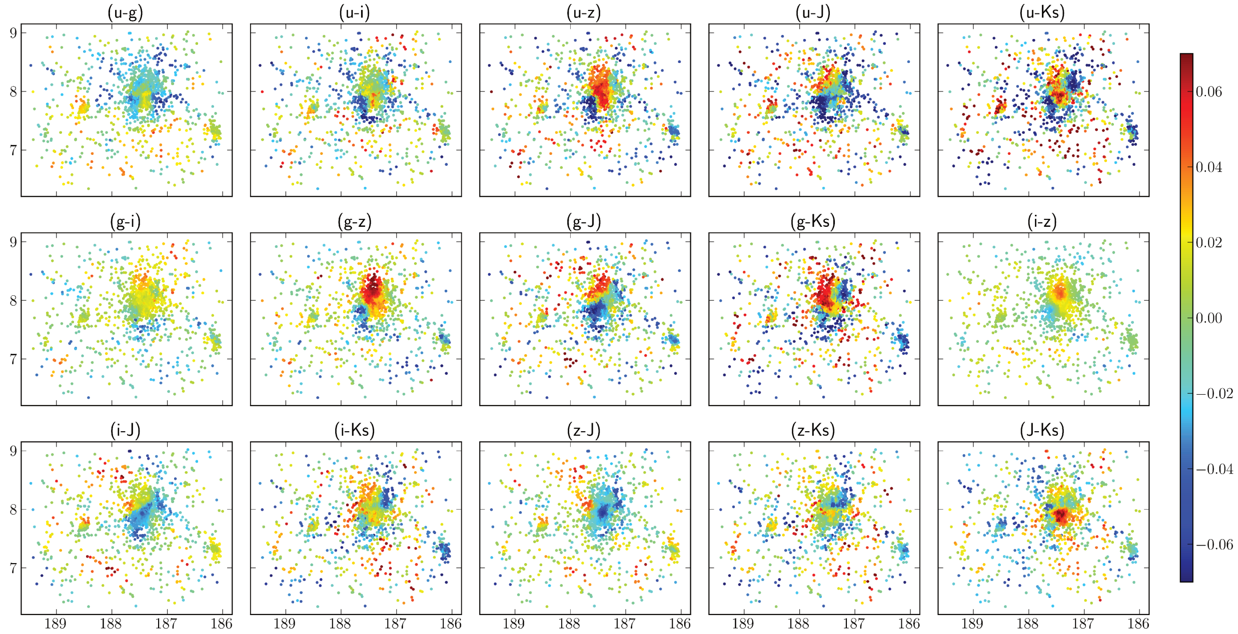

Figure 4.12 Color correction values for GC candidates in the field. The map shows the difference Δ between the global median color and local median of the selected point sources at the location of each GC.

The correction maps show the correction factors to be added to respective colors at the respective locations. The typical range of variation is 0.1 - 0.2 magnitudes. Some colors are more dramatic than the others in terms of magnitude of variation while others show higher frequency fluctuation across the field, (u-Ks) for instance. Correlations between maps of (u-z), (g-z), and (i-z) can be observed specially around the center of M49. The three colors have z band in common and it is likely that z band is the origin of the butterfly shaped feature seen at the center of M49 in these three bands. The absence of any common features between colors with no common band is also an indication that these corrections are meaningful.

This calculation attempts to minimize the non-homogeneity in colors which further reduces the chances of any spatial structures seen in GC colors being an artifact of non-homogeneous calibration.

4.4 Spatial grouping of the GCs

4.4.1 GCs in the P89 field

The main motivation behind our work is to study the dependence of the colors of the GCs as a function of their environment. In this section, we will spatially classify the cluster candidates selected in the previous section.

In the first group of objects, designated as e0, we have selected clusters that are within the effective radius of M49. The effective radius is derived from the galaxy surface brightness profile obtained from the ELLIPSE and CMODEL tasks within STSDAS in IRAF. The effective radius of the galaxy is found to be 244.8" in *Ks* band. This value is comparable to the 263" reported by Kormendy et al. (2009) in the V band and by Hartke et al. (2017) which is derived from fitting 2D profile to V band diffuse light of the galaxy. The corresponding minor axis value in Ks is 191.5" and the corresponding position angle of the ellipse is about 141 degrees East of North. For the first group of clusters, we select all the objects that lie within this region. We note that this excludes objects with projected distances to the galaxy center smaller than about 20" as in this region the background is dominated by the bright core of M49.

The second group of objects, e1, hosts the clusters that lie outward of the e0 region but within an ellipse with a semi-major axis of 0.5 degrees. Most of the clusters in e1 belong to M49, but there are also a few elliptical galaxies projected within the region, such as NGC 4467 and NGC 4471, and the irregular dwarf UGC 7636 which is allegedly being stripped off by M49 (Patterson and Thuan, 1992; Irwin and Sarazin, 1996). Therefore, this region might contain some clusters that belong to the GC system of smaller galaxies than M49.

The next group of objects, e2, consists of clusters around the lenticular galaxy NGC 4526,

Table 4.1 Parameters of the regions for spatial classification the GCs (candidates with error on magnitudes < 0.06)

Region	RA,Dec (deg)	PA [1]	α, β(deg)	No of Objects
e0	187.4448, 8.005	141.18	0.068, 0.053	395
e1	187.4448, 8.005	141.18	0.5, 0.35	863
e2	188.515, 7.689	135	0.15, 0.1	54
e3	186.195, 7.3189	45	0.2, 0.15	120
e4	-	-	-	617
e5	-	-	-	597
e6	-	-	-	983

and group e3 of objects belong to the elliptical galaxy towards the South-West of M49, NGC 4365. The parameters for the regions and other details are given in table 4.1.

The group of field clusters in P89, e4, consists of all the other GCs and most of its members are candidate clusters of the Virgo intracluster field. A few of them belong to the GC system of intermediate mass ellipticals in the field but since they are less numerous we merge them with the field clusters.

4.4.2 GCs in the P91 field

The P91 field include two major elliptical galaxies, M84 and M86. We have classified the GCs in P89 in only two categories, the GCs that belong to the two galaxies and the field clusters. We call these groups e5 and e6, respectively. There are 597 GCs in the e5 group and 983 field GCs. The field GCs consists of GCs that belong to smaller galaxies in the region in addition to the free floating clusters.

The GC groups are illustrated in figure 4.13. They are representative of cluster environments such that we have clusters that belong to the region close to the core of a massive early type galaxy and the region in the outskirts of the same galaxy. The other regions represent less massive ellipticals and spirals in the region and the clusters floating in the inter galactic region. In the next section we will look at the colors of these groups of clusters and then compare the differences in their color-color distributions.

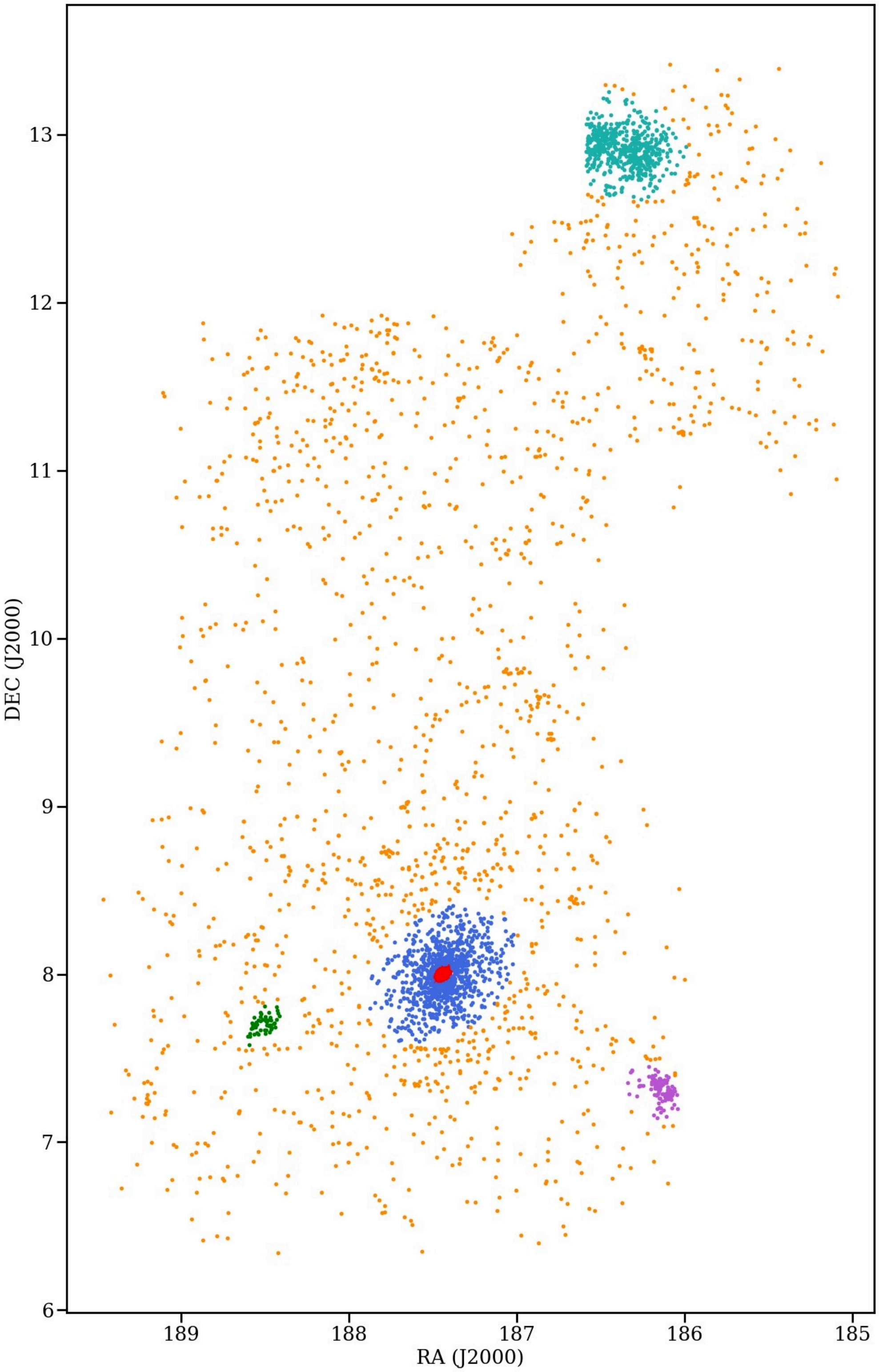

Figure 4.13 Globular clusters in the region colored based on the region they belong to. The red, blue, green, violet, cyan and orange colored circles belong to groups e0, e1, e2, e3, e5 and the field clusters (e4 and e6) respectively.

Chapter Five

Relation between globular cluster color and environment

"Somewhere something incredible is waiting to be known." - Carl Sagan

Abstract

In this chapter we will use different groups of GCs classified based on their environment within Virgo and study their color-color properties. We assess the completeness and possible contamination in our GC sample. We find the spectral energy distributions in the various groups to be very similar, with a few difference that are reminiscent of those found in a previous study by Powalka et al. (2016a). We conclude the chapter by discussing some of the reasons that could explain the color-color trends and their differences.

Before discussing the color distributions and color-color relations of the GC candidates in our photometric catalogs, we briefly examine the completeness and contamination in our samples. We recall that because our main objective is to study the color-color relations, we have given purity preference over completeness. Our main GC sample also has limits set by the requirement of small photometric errors, which means it is not representative of the full depth of the NGVS-IR images.Our secondary, extended sample includes the main one, but without the tight limits on photometric errors. Nevertheless, even that catalog is limited intrinsically by the fact that the first selection step occurs in the *uiKs* diagram, which implies detection at all wavelengths, *u*-band depth restricts the detection of the red clusters, while *Ks* band objects limits the detection of blue objects.

Because of complex color-dependent selection effects, artificial object experiments would have had to involve simultaneous simulations of GCs of various colors in all the wavebands (including the optical ones), in areas sufficiently numerous to cover variations in seeing and in relative proximity to galaxies. This represented a prohibitive amount of time and resources. Hence we turned to more restricted but nevertheless informative comparisons with external catalogs. In sections section 5.1.1 and 5.1.2 we discuss completeness, and in section 5.1.3 we turn towards contamination.

5.1 Completeness and contamination

5.1.1 Comparison with the ACS Virgo cluster survey GC candidates

We first compare our GC catalog with the ACSVCS GC catalog adopted from Jordán et al. (2009). Thanks to the spatial resolution of HST, the GCs in Virgo are extended objects on ACS images and hence the GC catalogs have little or no stellar contamination. The ACSVCS catalog includes bona fide GCs in 100 galaxies in the Virgo cluster selected using photometry in optical bands equivalent of g and z bands of SDSS and GC profile fitting using King models (King, 1962). Their fields of observations are mostly pointed towards the center of galaxies and are very small ($\sim 200'' \times 200''$) and therefore do not contain any field GCs. Therefore the overlap between our GC catalog and their GC catalog is very small. We use the only reasonably overlapping region which is centred around M49 to assess the completeness of our GC catalog. We use the entire extended GC catalog with no bar on magnitude error.

The ACSVCS survey is $\sim$ 1.5 magnitudes deeper in the z band (Figure 5.1). The magnitude distribution of our catalog peaks at 21.9 AB mag (z), which is about a magnitude brighter than the peak of the intrinsic GC luminosity function at the distance of Virgo. Based on that distribution our completeness appears to drop to 80 % at approximately z = 22.2. We restrict the comparison with the ACSVCS catalog to the magnitude range in which we expect to be close to complete, i.e. to objects with z $\geq$ 21.9 AB mag.

The P89 field has 195 GCs and ACSVCS has 369 GCs in the co-incident part of the field with magnitudes brighter than 21.9 AB mag in z. When we cross-match the two catalogs we find that there are 165 common objects in ACSVCS and our GC catalog. In other words 204 of the 369 relevant ACSVCS objects are not in our GC catalog. The reason for this discrepancy is not that the objects are not detected in NGVS, but rather that we have not selected them as candidate clusters. If we cross-match the ACSVCS catalog with our all object catalog we find the number of common objects increases to 338 from 165 which elevates the completeness relative to ACSVCS to 91.5%. On overlaying the two sets of cross match on the modified *uiKs* diagram (figure 5.2) we find that many of the GCs in the ACSVCS catalog lie outside the range of modified colors we have accepted. About two thirds of the ACSVCS objects that we excluded are in the regions of the diagram still compatible with a GC nature, but in which the fraction of contaminants is higher than 50 %; we rejected

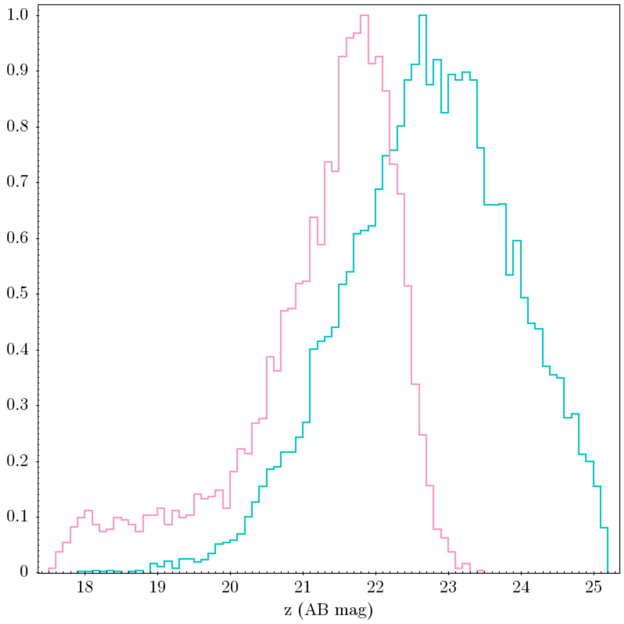

Figure 5.1 Distribution of z band magnitude for GCs in the ACSVCS catalog (cyan curve) and our catalog (magenta curve). The ACSVCS catalog is ~ 1.5 magnitudes deeper than our catalog.

these to conserve sample purity. The other third has modified colors very far from those of the GCs. On the side with negative values of (i-Ks), these are the objects with large errors in the Ks band; on the other side, these are a combination of objects with large errors in Ks and a few objects that might be mistaken background galaxies in the ACSVCS.

Figure 5.3 shows the ACSVCS clusters and all cross-matched objects in the co-incident field. It is clear from the figure that the majority of the GCs that are missing in our ground-based data are the ones that are close to the bright galaxy core around both the galaxies.

5.1.2 Comparison with spectroscopic GC candidates

We also compare our GC candidates with a spectroscopic sample of GCs obtained via private communication thanks to Youkyung Ko and Eric Peng. This catalog has objects that are likely to be GCs in the P89 field with a value of the corresponding probability (p_gc). We select the objects in their catalog that have a probability of being a GC higher than 50% and cross-match it with our sample. That gives us a sample of 462 objects. A comparison with that catalog will allow us to check our selection in a broader field than the ACSVCS data. The disadvantage is that the spectroscopic catalog itself is partially complete and contains only bright objects.

---

[1] https://aladin.u-strasbg.fr/

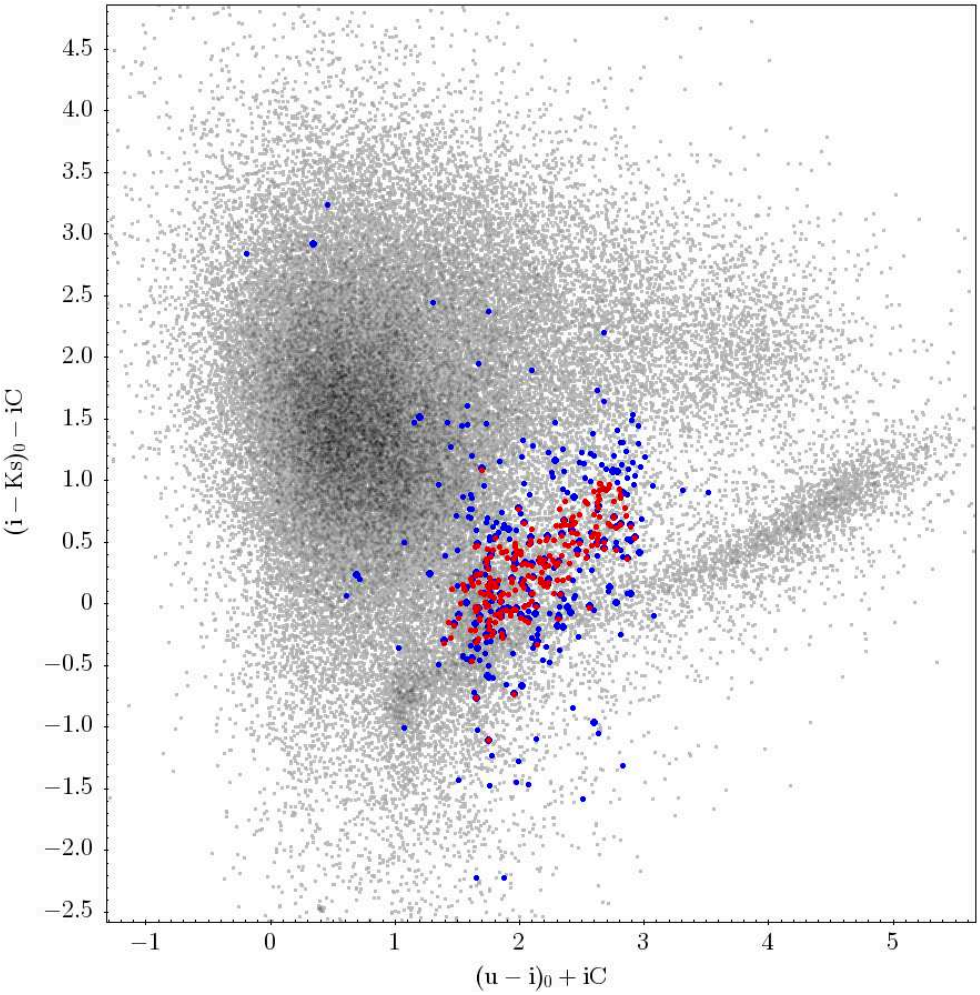

Figure 5.2 The *uiKs* color-color diagram for the cross-matched candidates with the ACSVCS catalog. The red objects are the common objects in our GC catalog and the ACSVCS catalog whereas the blue objects are those common to our all object catalog and the ACSVCS catalog.

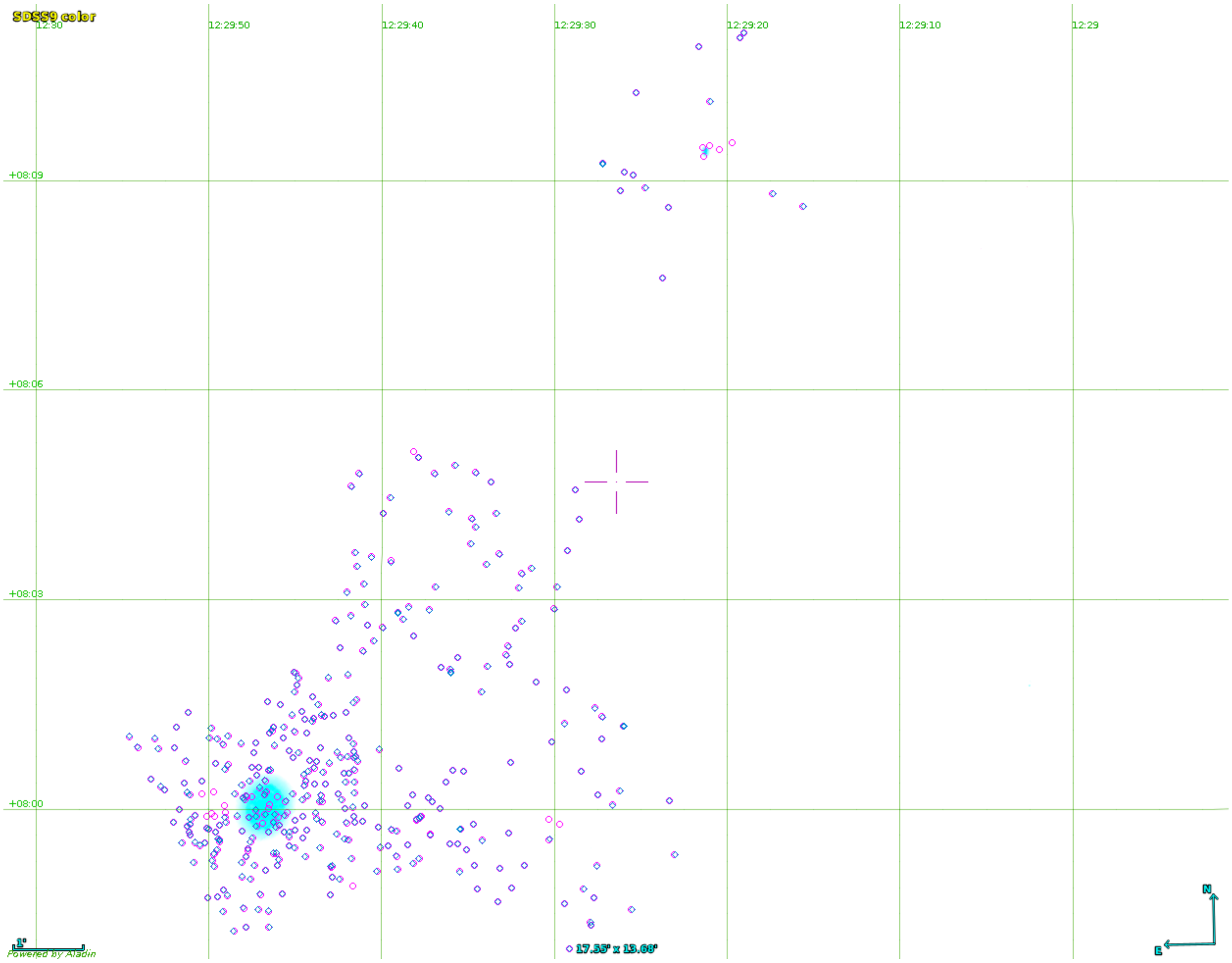

Figure 5.3 GCs in the ACSVCS GC catalog and in our catalog overlaid on the SDSS image in CDS/Aladin archive exploration tool [1]. The brightest galaxy is M49. The figure shows only the objects that are brighter than z=21.9 AB mag. The magenta diamonds are the ACSVCS GCs, and the cyan diamonds are the NGVS objects (not all of them are GCs) in our catalog, i.e. the objects shown as blue circles in Fig 5.2.

We select the objects that have a probability of being a GC higher than 50% and that are brighter than z=21.9 AB mag. Out of the 462 spectroscopic GC candidates thus selected we have 439 common objects. The relative completeness of our photometric catalog based on this cross-match can be stated as 95% below 21.5 z band AB magnitude.

In figure 5.4 the objects with p_gc > 0.5 are shown. The objects are colored by the radial velocity measurement for the objects. The GCs that we do not have in our catalog probably lie outside our photometric selection criteria, as was the case for ACSVCS objects. Ongoing work will verify this statement. Ongoing work will also extend the completeness test to the P91 field. Spectroscopically selected samples of GCs and UCDs have been published by Ko et al. (2017). The overlap between their study and the P91 field extends over roughly 1

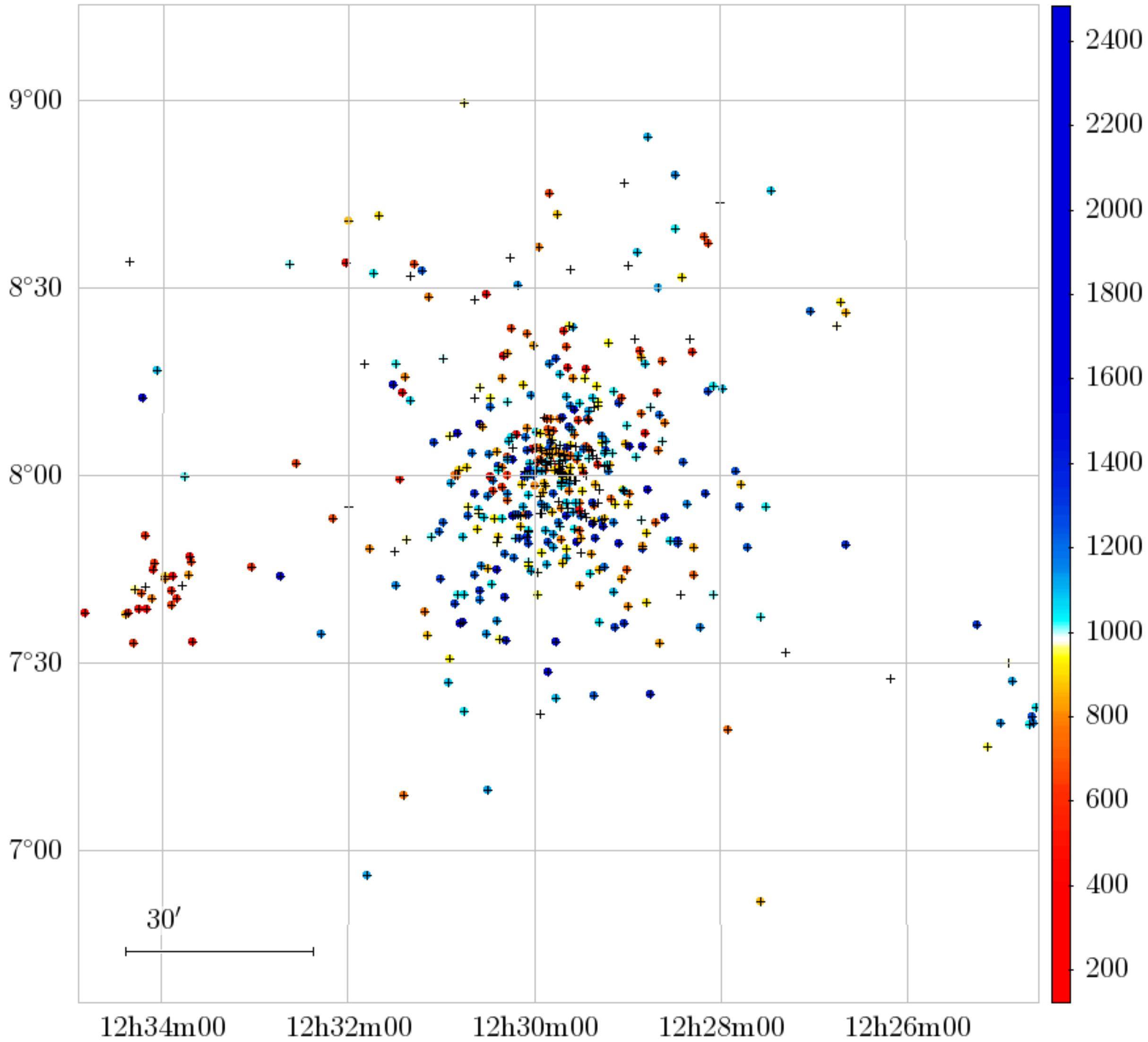

Figure 5.4 The filled circles are the objects in the spectroscopic sample that has probability of being a GC > 0.5, colored by radial velocity measurements given in the catalog. The crosses are over-plotted on top of these objects to show the common objects in spectroscopic sample and our catalog.

square degree, in which their GC sample lists about 130 objects.

5.1.3 Contamination

The selection of GCs from the *uiKs* color-color plane is not immune to contamination from stars and galaxies. We have implemented steps to reduce the contamination that include magnitude, color and morpholgical constraints, but the catalog can still not be entirely contaminant free. To estimate contaminants we compared our GC candidates with the

ACSVCS catalog mentioned in the previous section and searched for objects that are in our GC catalog but not listed in the space based one. We find 29 such objects, of which 19 are on the edges of the field (figure 5.5) which makes it uncertain if the part of the field was included in the ACSVCS catalog. Based on this number the contamination is 29/195 $\sim$ 15% and if we exclude the objects that are on the edge of the ACSVCS field then the contamination drops to 5% (10/195).

The above estimate refers to bright objects (z $\leq$ 21.9 AB mag). Contamination increase at fainter magnitudes. And although the number of contaminants per unit sky surface is expected to be roughly constant, the fraction of contaminants will be larger in areas in which the space-density of GCs is smaller.

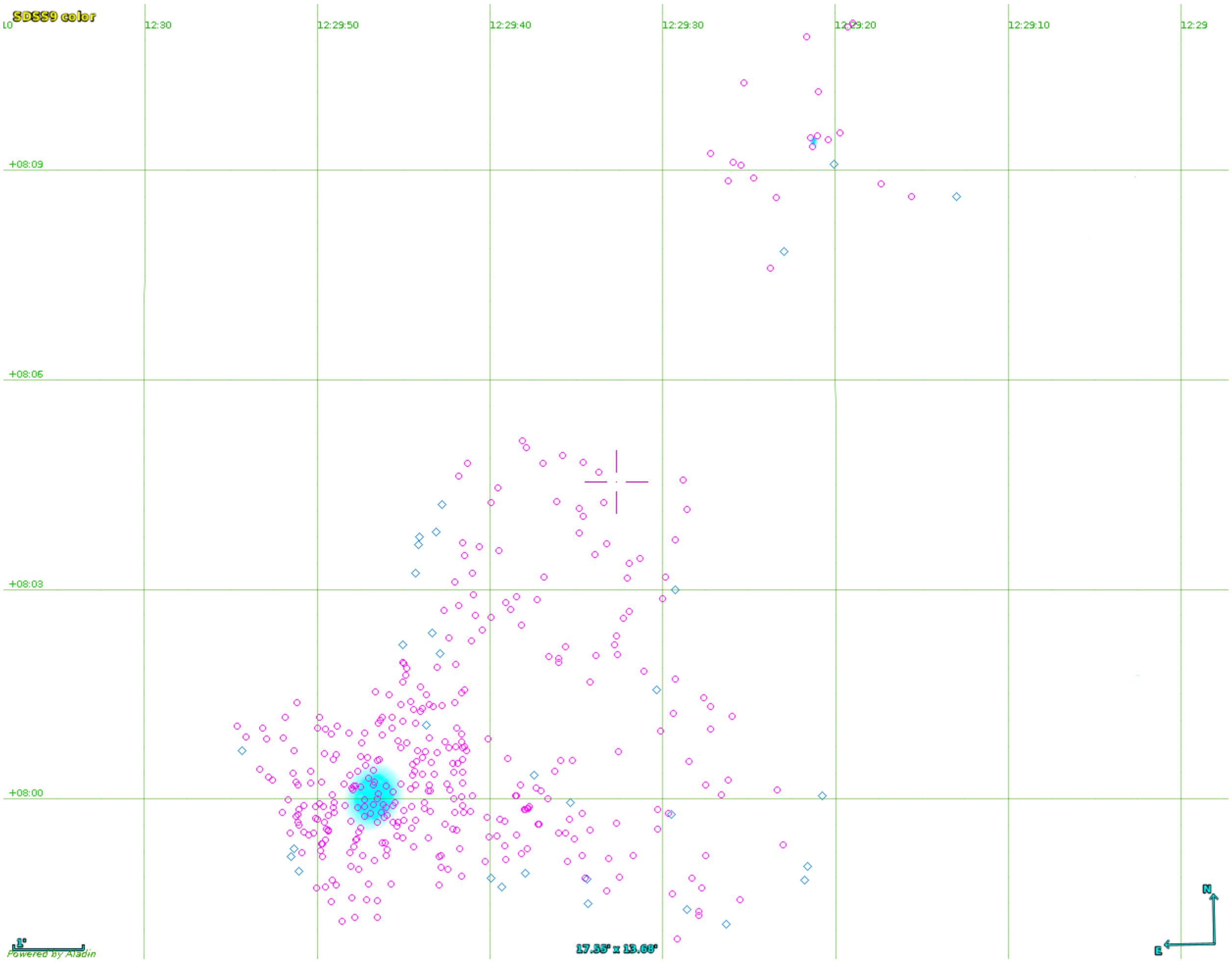

Figure 5.5 Possible contaminants in our GC catalog overlaid on top of SDSS image of the field. The objects represented by cyan diamonds are the objects detected in our catalog but that are absent in the ACSVCS catalog. It can be seen that most of these objects are on the edge of the ACSVCS fields.

5.2 GCs in different environments and their general properties

The central issue of discussion is the role of the environment on GC colors and their color-color distributions. The GCs in our data set belong to different types of environments. There are elliptical galaxies of various scales in the field (including M86 and M84 although these are sometimes referred to as lenticular galaxies), there is one S0 galaxy (NGC 4526) and there are field clusters that also include GCs from other smaller galaxies in the survey area. Figure 5.6 shows the KDE plot for the $(u\text{-}i)_0$ color for different groups. In the left panel, we compare the color distribution of GCs in group e5 (GCs of M84 and M86, cyan curve) with that of combined e0 and e1 (GCs of M49, with and without galaxy subtracted GCs, black and grey curves respectively). The blue peak of the color distribution of both the systems coincide with each other, whereas the red peaks show considerable difference. The e5 group seems to have relatively few red GCs as compared to M49. It must be noted here that e5 does not include the GCs in the most central region of M86 and M84 because the galaxy subtraction has not been implemented for the P91 data. The central regions of the galaxies are where the red GCs are most likely to be populated which could explain the deficiency of red GCs in e5.

The comparison of the color distributions of field GCs in the two survey regions (figure 5.6, right panel) shows mainly similarity. Again the blue peaks coincide; the red GCs in the P89 field sample are on average slightly bluer than those in the P91 field. The color of the red peak in the P89 distribution is consistent with the color of the red globulars in the external parts of M49 (black curves in the two panels); the presence of this massive galaxy at the centre of the P89 field, which drives the dynamics of the whole area, could be responsible for that peak.

Where exactly the reddest objects in the field sample of P91 are located (e6) remains to be confirmed (ongoing work); we expect they may be associated with the numerous smaller galaxies that populate that area. Despite the slight difference the two color distributions are similar (in other colors as well, not displayed here) and thus we have merged the two groups (e4 and e6) together.

A detailed comparison of color distribution between fields requires a knowledge of the local completeness functions in all bands (including detection and selection) much more extensive than is available to us today. The loci of color-color distributions is much less sensitive to selection biases, and we examine these in section 5.3.

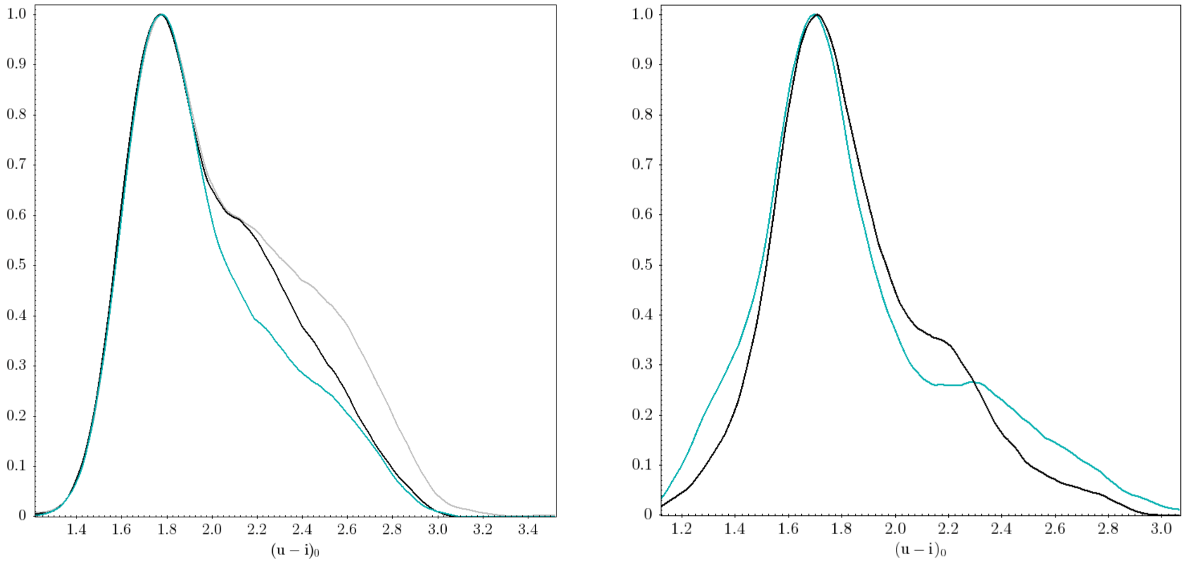

Figure 5.6 *Left panel:* Normalized KDE (Kernel density estimation) plot of $(u-i)_0$ color distribution of GCs in M49 (black and grey curve, the grey curve includes GCs in the galaxy subtracted region) and combined GCs of M84 and M86 (cyan curve). The blue peak of the two systems is coincident, but our samples of M86 and M84 have a smaller fraction of red GCs. *Right panel*: KDE plot of $(u-i)_0$ color distribution of field GCs in P89 (black curve) and P91 (cyan curve). The two curves are similar but the red GCs in the field around M49 seem to be slightly bluer on average than those in the P91 field.

5.2.1 GC system of giant elliptical galaxies

The three giant elliptical galaxies in our field are M49 (NGC 4472), M84 (NGC 4374) and NGC M86 (NGC 4406). While M49 is the brightest and one the two most massive Virgo cluster galaxies, M84 and M86 are the two other massive galaxies which are classified as elliptical or lenticular galaxies. Despite being the most luminous galaxy in the cluster M49 hosts around 6800 GCs (Cohen et al., 2003) with specific frequency 3.6 which is significantly smaller than the neighbouring giant elliptical galaxy, M87. M87 hosts around 13500 GCs and sits in the dynamical centre of the Virgo cluster while M49 is located in relatively less active region of the cluster. The GC system of M86 is known to be home to around 3800 GCs and the galaxy have a specific frequency $S_N = 3.5 \pm 0.5$ (Rhode and Zepf, 2004). The GC system of M84 hosts around 1800 GCs (Gómez and Richtler, 2004) and have a specific frequency $S_N = 1.6 \pm 0.3$ which is rather unusually low for a giant elliptical galaxy.

- **Spatial distribution of GCs**

  The GCs in most massive galaxies have bimodal color distributions dividing the GC system of the galaxy in blue and red sub-populations. Some global properties of these sub-populations are found to be uniform among galaxies of similar masses and morphological types. The red GC sub-population is found to be more centrally concentrated and on average have smaller sizes as compared to the blue GCs sub-population.

These properties are used to explain the formation and evolution history of the parent galaxies and possible timeline of formation of these sub-systems. We have plotted the $(u\text{-}g)_0$ color of all the GCs of M49 in our data set as a function of their concentration index (iC) color coded by the square of their radial distance from the center of M49 (figure 5.7). The filled triangles are GCs inward of 4' radius from the centre of M49 and the solid squares are the GCs that lie outside of this distance. The blue GCs are span a broader range of size and are predominantly farther away from the galaxy, while the red GCs are smaller and concentrated towards the centre.

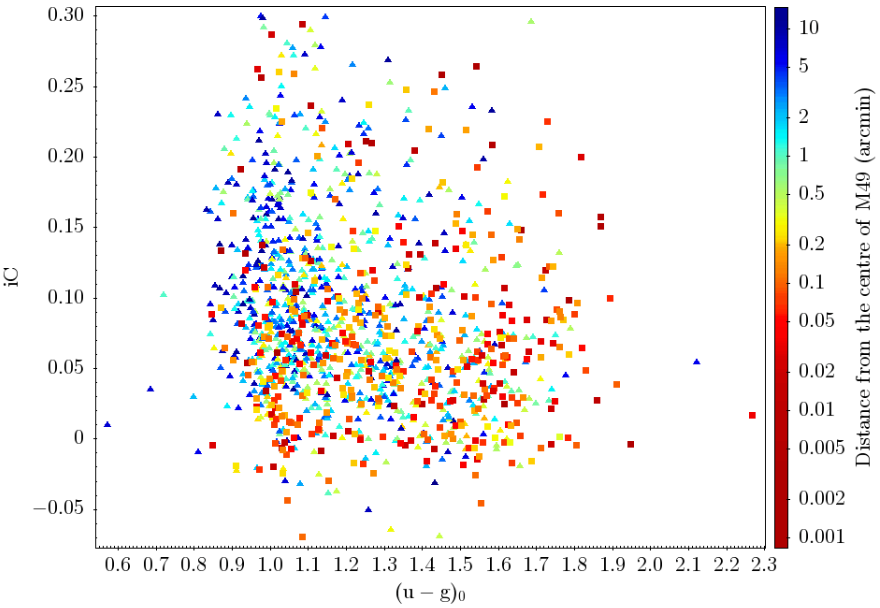

Figure 5.7 The figure shows the $(u\text{-}g_0)$ color of GCs around M49 as a function of their concentration index (iC) and color coded by the square of their radial distance from the center of M49 (in arcmins). The triangles are the GCs outward of 4' radii from the centre of the GCs and the filled squares are the inner GCs. The redder GCs are predominantly smaller in sizes and also closer to the centre of the galaxy.

Figure 5.8 shows the distribution of GCs around M49 (right panel) and around M84 and M86 (left panel) color coded with their respective iC values. It can be seen that the fraction of GCs with larger iC values are is higher at larger distance from the center of the host galaxy for all the three galaxies, while the GCs with smaller values cluster around the centre of the galaxy. This pattern is consistent with the what is known for the GCs in larger GC systems.

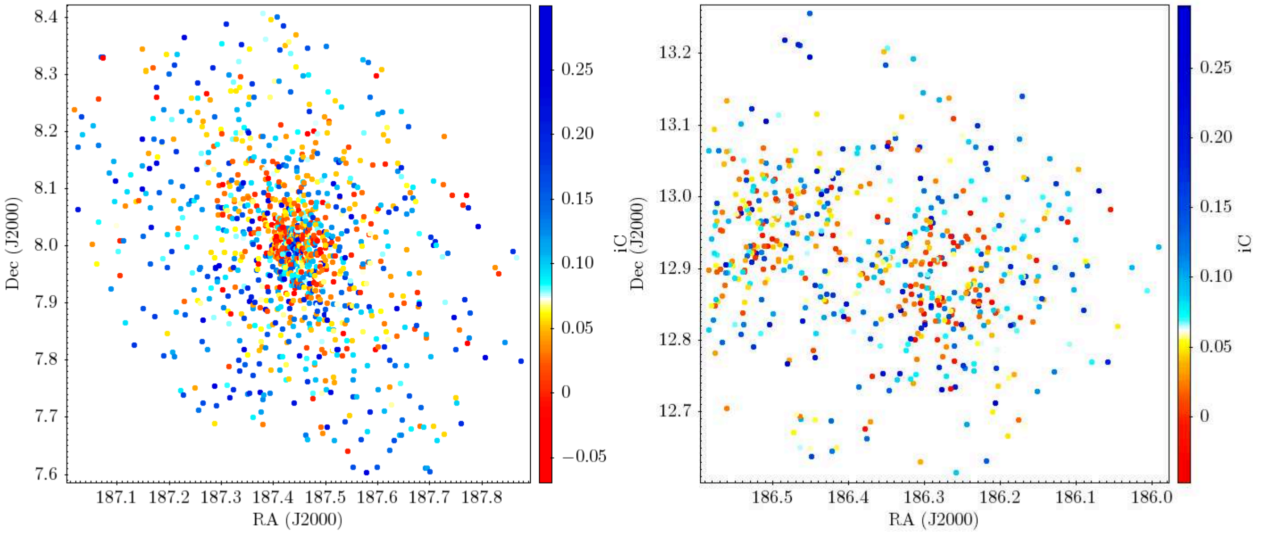

Figure 5.8 Concentration index (iC) for GCs in M49 (left panel) and M84 and M86 (right panel) as a function of their spatial position. The clusters with smaller iC values are found to be concentrated around galaxy centre, while the larger iC values are more scattered in the outskirt of galaxy. The lack of GCs in the centre of M84 and M86 is due to the presence of bright core of the galaxies.

5.2.2 GC system of NGC 4526 and NGC 4365

Next, we direct our discussion towards the GC population in e2 and e3 which belong to lenticular or S0 galaxy, NGC 4526 (Burstein, 1979; Samurović, 2017) and an elliptical galaxy, NGC 4365, respectively. The GCs in NGC 4526 are interesting because the morphology of the parent galaxy is slightly different from other groups, but seems very regular otherwise. NGC 4526 is an S0 galaxy which is believed to be the transition phase between a spiral galaxy and an elliptical galaxy.

If we talk about the distribution of GCs in NGC 4365, which is an early type galaxy, it seems that the distribution is skewed towards the red end and the blue population is scarce (right panel, figure 5.9). But NGC 4365 is very well known to have three distinct GC subgroups, which have an additional intermediate GC population apart from the usual blue and red ones. It has been confirmed based on kinematics studies as well that the GC subsystem of NGC 4365 is anything but uni-modal (Blom et al. 2012b, Blom et al. 2012a, Larsen et al. 2005). To be sure we are not misinterpreting the results we extended our e3 sample to include GC candidates from our extended GC catalog with lower SNR. The color distribution of the extended GC candidates shows a broader range on the color axis and it becomes evident that we are indeed missing the blue GC population of the galaxy if we only select the brightest objects. This trend is observed in all our GC samples. This comes as a consequence of selection effects in the Ks band. When we reject objects which are faint in near-IR, we essentially reject blue GCs and that gives an impression that the there is a lack of blue GCs in the galaxy.

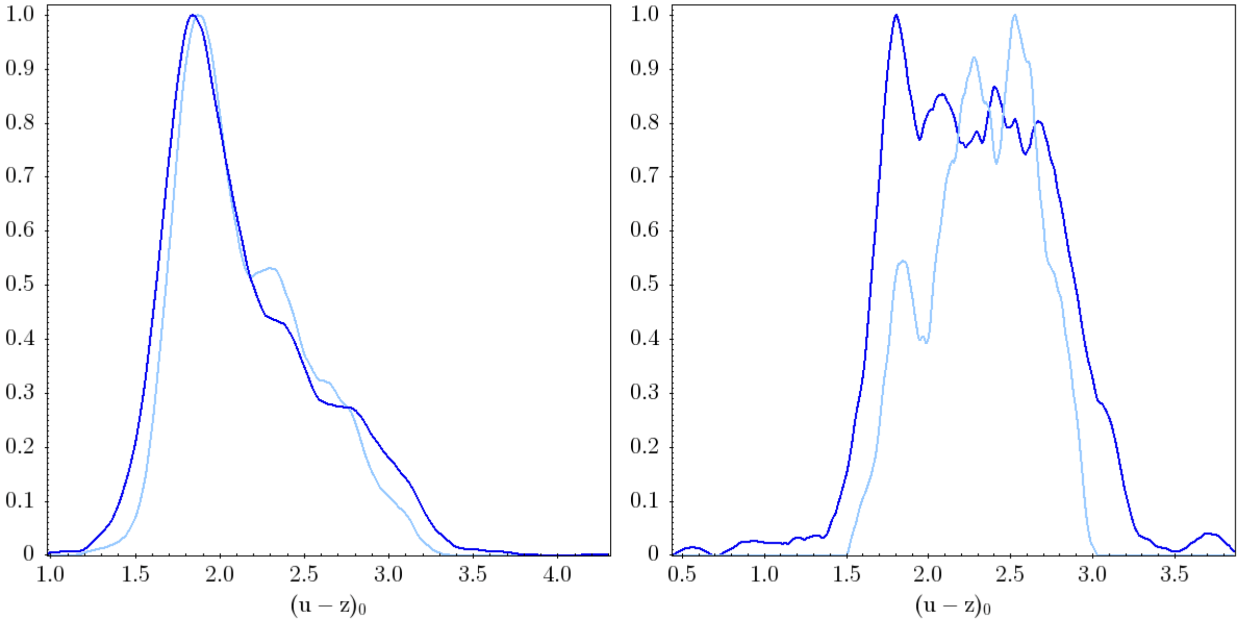

Figure 5.9 $(u\text{-}z)_0$ distribution of blue GCs in M49 (group e1) and GCs in NGC 4365 (group e3). The cyan curve shows the distribution of GCs with photometric errors smaller than 6 % and the blue curve shows the distribution of color for all the GCs. The selection criteria reject the blue GCs which are faint in near-IR.

5.2.3 Intra-cluster GCs

The presence of intra-cluster GCs (IGCs) in galaxy clusters has been proposed to be universal and the number of IGCs is associated with the mass of the parent galaxy cluster (West et al., 1995). Large elliptical galaxies in a cluster have a spectrum of S_N values that typically range from 3 to 20. Galaxies with a very high value of S_N hosts large number of GC per galaxy luminosity. It has been proposed that there can not be more than one galaxy with a high S_N in a cluster. The presence of IGCs is believed to be associated with the presence of a high S_N galaxy in the cluster. It is also theorized that all galaxies are born to have a normal value of S_N and have an intrinsic GC population. The galaxies that show a high S_N value at present epoch are the galaxies that are surrounded by an extended halo of IGCs. These galaxies are not special because of their morphology but they receive the advantage of being at the dynamical center of the galaxy cluster. Therefore the galaxies that reside at the center of the galaxy cluster are more likely to host large number of GCs than the galaxies which are farther out. The GCs in the halo of M87 in the Virgo cluster (Mould et al., 1987) and NGC 1399 (Grillmair et al., 1994) in the Fornax cluster are found to have high velocity dispersion which support the narrative.

Durrell et al. (2014) studied the GC distribution in the Virgo cluster and in their work they termed the GCs that lie outside 215 kpc from M87 as the IGCs. Ko et al. (2017) identified an IGC sample in a region including M87, M86 and M84 in the Virgo and studied their kinematics. They found that the IGCs also show bimodal color distribution with a majority of the clusters belonging to the blue part, and they tentatively trace their origin to dwarf galaxies. The red GCs were speculated to have been drawn from intermediate and high mass galaxies. They also found that the velocities of the GCs show a broad range with the peaks of radial velocity at $\mathrm{v}_r \sim 1026kms^{-1}$ and $36kms^{-1}$. The GC subsystem with higher v_r are located around the main body of the Virgo, while the GC system with smaller v_r values could be either in-falling or outgoing GCs that traces the in-falling galaxy trail of M84 and M86.

5.3 Color-color diagrams

With 6 photometric pass-bands (leaving out r which is available only in parts of the survey area), we can construct 15 color indices and 105 color-color diagrams. The availability of a wide range of photometric bands makes us well equipped with several possible combinations of different bands. After examining many of these, we select representative colors such that we sample the entire spectral range. Figure 5.10 shows the color-color diagrams for the galaxies in the P89 field. Figure 5.11 shows the color-color diagrams of inner and outer GCs of M49 (red and blue curves), combined GCs of M84 and M86 (cyan curves), and field GCs in P89 and P91 combined (orange curves). In both the figures each panel displays the maximum likelihood regression line fitted to the color distribution. The likelihood function that we adopt assumes the errors in color-color space are 2D Gaussians, with variances and a covariance computed for each cluster based on individual photometric measurements. The filled region around the fitted line is the 95% (2σ) confidence interval of the fitting based on 100 bootstrap recalculations of the fit. Panels placed symmetrically on either side of the diagonal correspond to the same color-combination, but with the two alternatives for the independent variable in the calculation of the errors. In the following when we mention shallow or steep relations, it will always refer to the bottom left half of the figure. The diagonal of the grid shows the probability density function (PDF) of colors plotted on the horizontal axis. The color distributions are smoothed using kernel density estimation (KDE) with a Gaussian kernel.

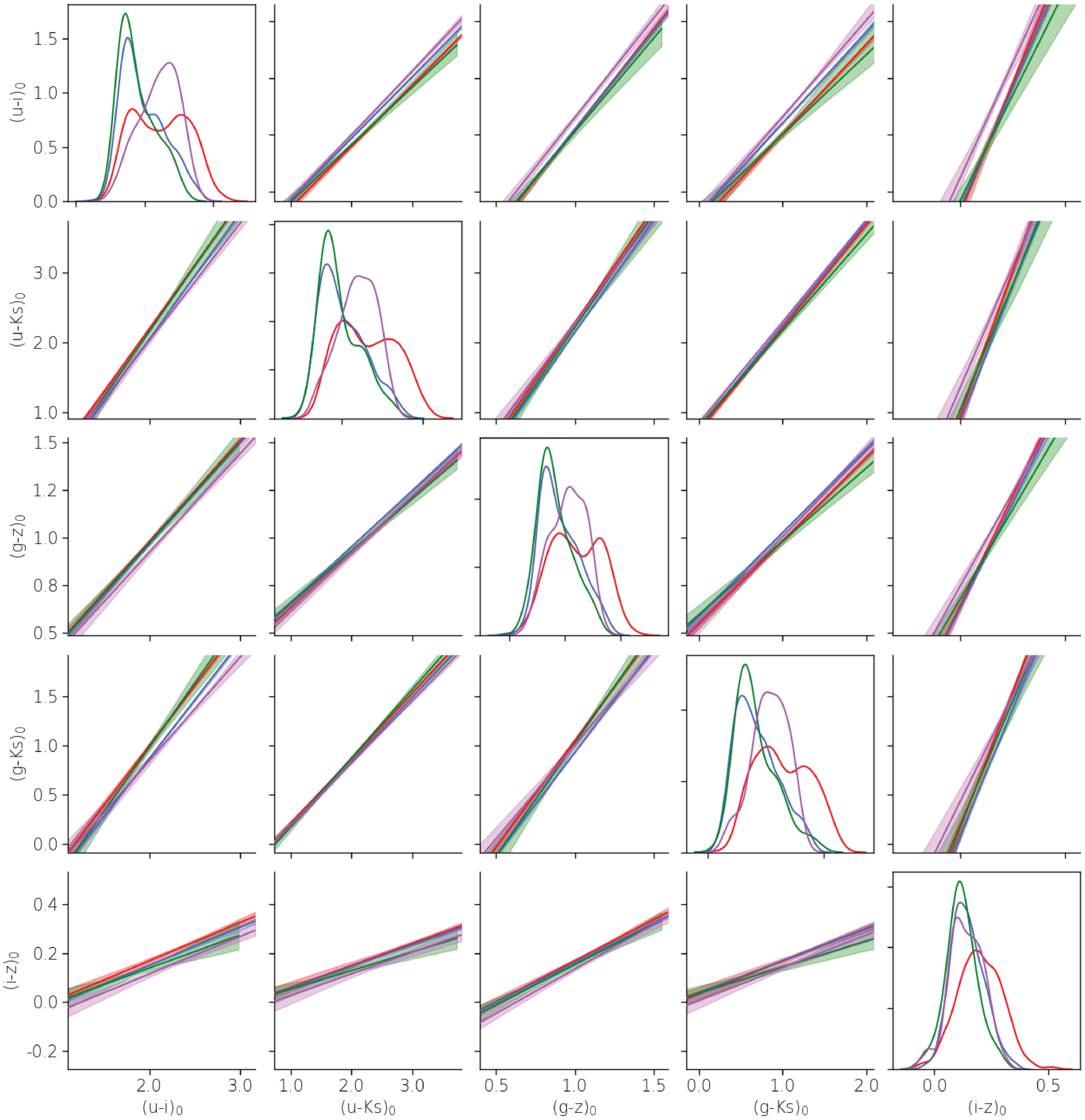

Figure 5.10 Each block in the plot shows the maximum likelihood regression line fitted to the color distribution of respective group from the groups of GCs that belong to galaxies in the P89 field. The color representing each group - e0:red, e1:blue, e2:green and e3:violet is same as in figure 4.13. The filled region along each line is 2-σ uncertainty evaluated using bootstrapping at each data point. The diagonal of shows the Kernel density estimation (kde) smoothed histogram of the respective colors on the horizontal axis.

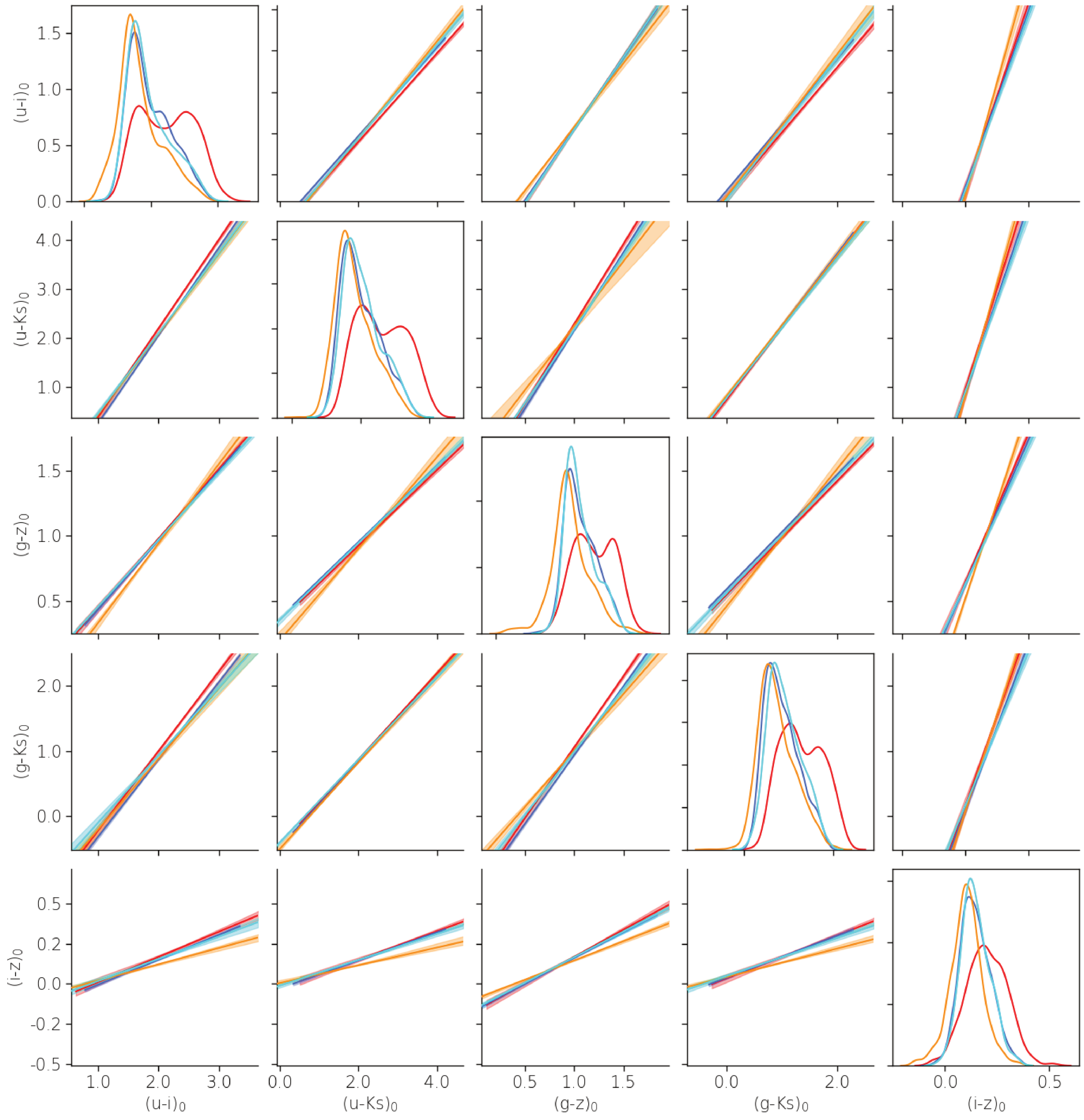

Figure 5.11 Each block in the plot shows the maximum likelihood regression line fitted to the color distribution of respective group from the groups of GCs that belong to the M49 (red and blue curves, group e0 and e1 respectively), GCs of M86 and M84 (cyan curve group e5) and field clusters (orange curve, combined e4 and e6 GCs). The filled region along each line is 2-σ uncertainty evaluated using bootstrapping at each data point. The diagonal of shows the Kernel density estimation (kde) smoothed histogram of the respective colors on the horizontal axis.

5.3.1 Influence of the environment on GC colors

In this section, we discuss the trends observed in the color-color diagrams of the different groups of clusters using colors from combinations of optical bands and the near IR bands of the objects. The various color-color trends observed amongst the different groups of GCs are observed to be similar on average but some color-color trends differ by more than 2σ and are worth examining further. The differences larger than 2σ are considered significant as they have less than 5% probability of being due to random sampling from intrinsically identical distribution.

In figure 5.10 we compare the color-color distribution of GCs in the galaxies in the P89 field. The best defined fits are for the inner and outer GCs of M49 (red and blue lines, respectively). In purely optical color combinations they lie within 2σ confidence intervals of each other, but in combinations involving both (u-i) and Ks they are separated very significantly. We also notice that at a given $(u\text{-}i)_0$, both $(u\text{-}Ks)_0$ and $(g\text{-}Ks)_0$ are redder for the more centrally located clusters.

When looking for most discrepant subsamples in figure 5.10, one observes that no single subset consistently disagrees with the others in all color-color diagrams. However, it is also notable that the samples associated with the edge-on S0 galaxy, NGC 4526 (e2, green) and with the elliptical galaxy NGC 4365 (e3, violet) often have distinct behaviors. For instance, there is a general offset between these samples in $(g\text{-}z)_0$ vs $(u\text{-}i)_0$, and a significant difference in slope in $(g\text{-}Ks)_0$ vs $(u\text{-}i)_0$; in other diagrams, the differences are only of the order of 1 or 2σ. We note that NGC 4365 is located at the edge of the Ks band images, where signal-to-noise is lower, but it is not on the edge of optical images.

When comparing M49 GCs with those of the other 2 galaxies in the field in Figure 5.10, we find that the color-color relations of the innermost M49 GCs (red lines) are often distinct with a high level of confidence from the relations for the elliptical galaxy NGC 4365 (violet lines). The relations for the outer M49 GCs (blue lines) lie closer to those of the NGC 4365. When comparing the color-color trends of GCs in M84 and M86 with the GCs of M49 and the field clusters in figure 5.11 we observe that the trends for GCs in M84 and M86 (cyan lines, e5 group) are closer to the blue GCs of M49 and thereby are also more similar those of the GCs around NGC 4365 (e3). The fit locations, when compared to those of inner M49 GCs, are essentially always in the same relative position (as e3 relative e0 in figure 5.10).

When searching for a subgroup that stands out we find that the color trends of field clusters are shallower than the color-color distributions of galaxy GCs in most bands.

The most prominent differences are seen when other colors are plotted against $(i\text{-}z)_0$. The two bands (i and z) are very close to each other on the spectral baseline and hence the range of the color is relatively smaller than other colors which enhances the differences between the different groups. Let's consider $(g\text{-}Ks)_0$ vs $(i\text{-}z)_0$ for instance. The slopes are steeper for the clusters that are closer to the galaxy and shallower for the clusters that belong to the field.

5.3.2 Comparison with M87 GC colors

M87 is another massive early type galaxy in the Virgo cluster that sits in relatively dynamically active of the cluster as compared to M49. A detailed study of the effect of environment on the colors of GCs around M87 was carried out by Powalka et al., 2016a. In this section we compare the trends as seen in our data with color trends of M87 GCs. We have adopted the color information as given in catalog provided by Powalka et al., 2016b. The optical colors for both the data sets are obtained from the Megacam imager on CFHT but the Ks bands belong to different systems. The one used by Powalka et al., 2016b is acquired from CFHT/WIRcam whereas the one in this work is from VISTA/VIRcam. Figure 5.13 shows the color-color diagram grid for GCs in M87. The various groups of GCs as described in the parent paper are A: GCs within 20kpc from core of M87, B: GCs in the annulus region with 20kpc $<$ r $<$ 200kpc, C: GCs beyond r = 200kpc and D: GCs associated with other galaxies in the field (M86, NGC 4435, NGC 4438 and NGC 4473) (see figure 5.12). The main result of the study was the environmental dependence of the color distributions of the GCs. The authors compared the *griz* colors of the four groups of GCs with each other and also with synthetic colors of 11 Milky Way GCs. They concluded that color - color trends seem to be a function of the environment in particular the trends in $(i\text{-}z)_0$ are prerogative of the red populations of the densest areas i.e. areas in and around massive galaxies.

A comparison of figure 5.13 with color trends of GCs in our survey area (figure 5.10 and 5.11) reveals that the relative trends seen among the different groups are similar for the GCs around M87 and the GCs in our study.

The field clusters around both, M87 and M49 the galaxies are bluer than other groups which is consistent as the intra-cluster GCs are known to have a predominantly blue GC population (Lee et al., 2010). The GCs in other smaller galaxies in the field are a mixed bag of objects and hence it is expected that they will not have a similar color-color trends.

5.3.3 Comparison with SSP tracks

In the previous section we discussed the color-color distribution of the GC groups that belong to different environments. One of the major consequences of these differences is their impact on stellar evolutionary models. GCs serve as the test objects for the SSP models, and in general these models do not consider the changes that could be introduced in the color-color

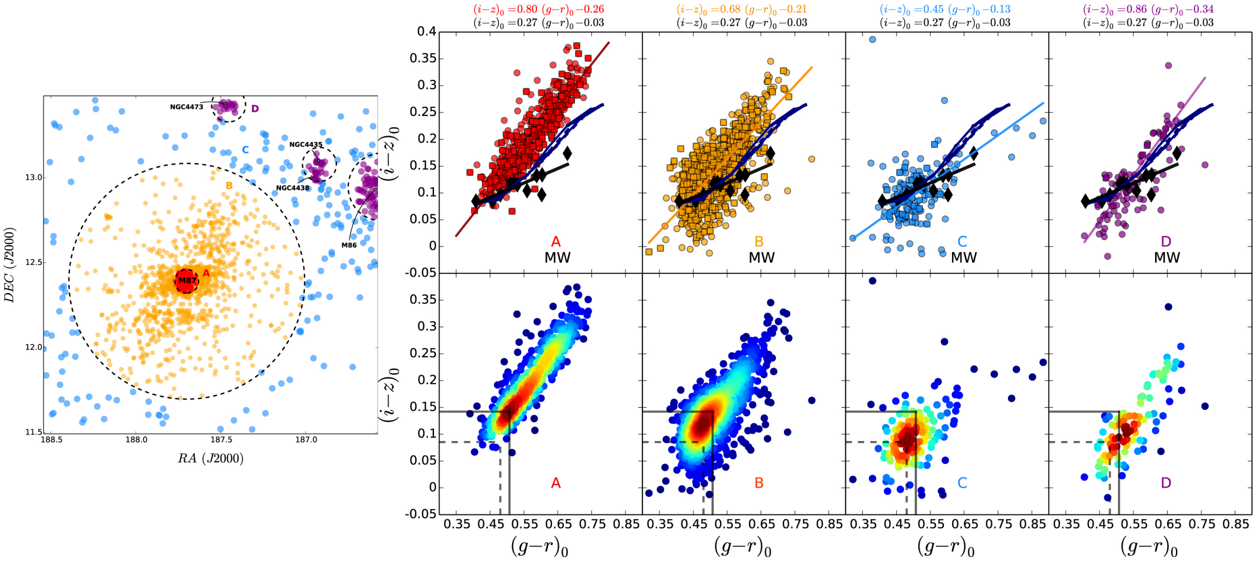

Figure 5.12 Classification of GCs in the region around M87. The left panel shows the distribution of the objects on the RA-Dec plane and their colors represent the group they are part of. The right panel shows *griz* color-color plot of each group as compared to the MW GCs (black diamonds). For more details on the plot see Powalka et al. (2016a).

distribution in specific environments. In figure 5.14 we compare the color-color distribution of GCs from this work and color-color distribution of GCs around M87 from Powalka et al., 2016b against PEGASE-HR SSP models (Le Borgne et al., 2004). The tracks correspond to ages from 5 to 15 Gyr and metallicity ranging from 10^{-4} to 0.05. The two sets of GCs shows similar level of agreement with the SSP models. The higher dispersion of inner M49 GCs as compared to the inner M87 GCs (leftmost panel, figure **??**) can come out as striking. In the GC sample selection near the core of M87, the selection criteria directly favor a less dispersed color-color distribution (Figure 8 in Powalka et al., 2016b) that gives rise to this visible difference in the distribution of the GCs around the core of the central galaxy. The relative position of the GCs in the second panel of figure 5.14 for M49 GCs (GCs in the outer region of M49, blue data points) and the GCs of M84 and M86 combined (cyan data points) seems to be shifted marginally upwards as compared to the SSP tracks in the corresponding panel in the M87 set. This offset between the GC colors and SSP tracks is also observed in the third and the fourth panel of the top row. In the bottom row this is also true for the GCs in the third panel but it is difficult to assess anything for the field clusters around M87 due to smaller sample size.

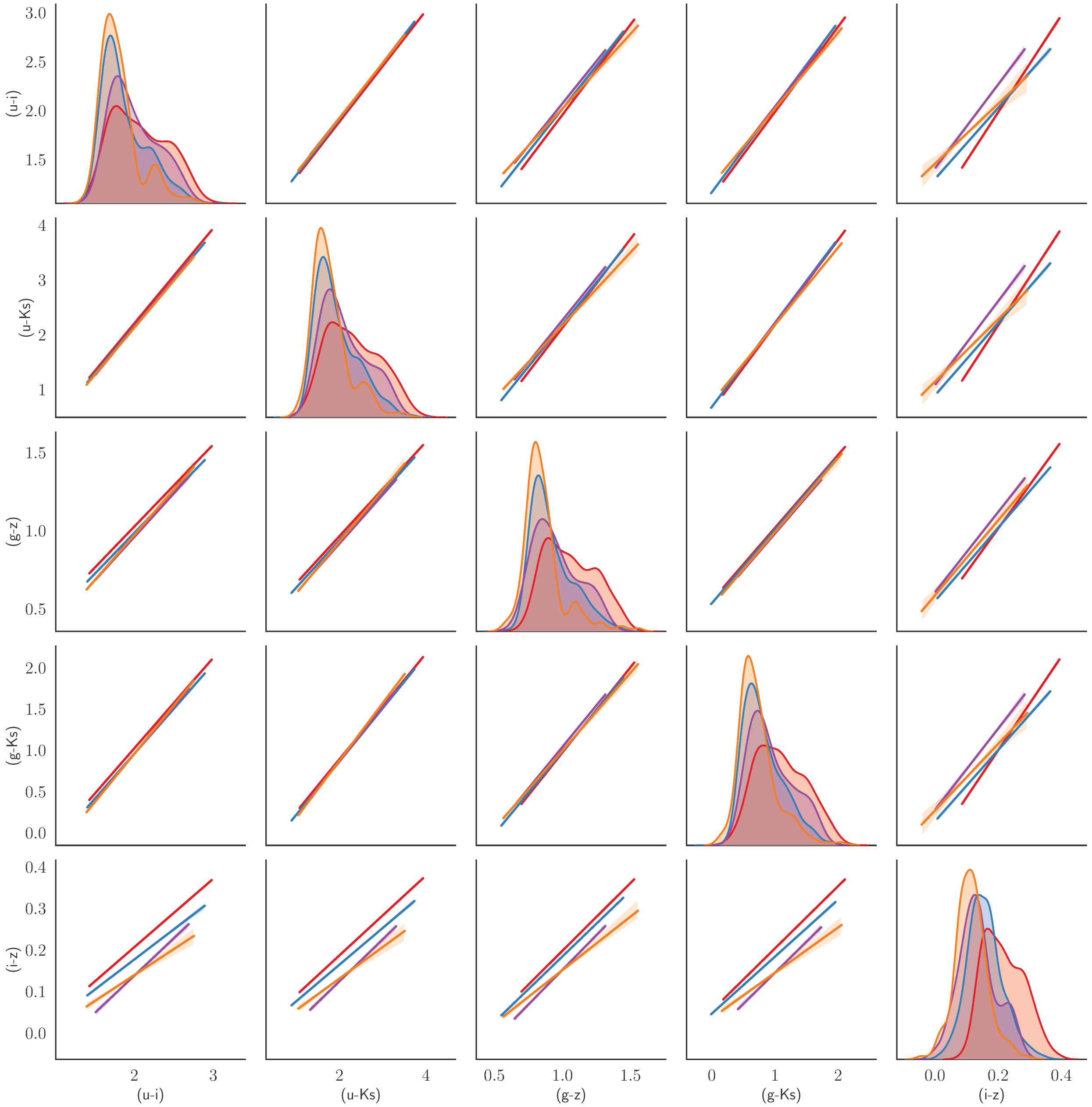

Figure 5.13 Each block in the plot shows the regression line fitted to the color distribution of respective group of GCs in the NGVS pilot field with M87 at its center. The various groups are described in Powalka et al. (2016a). The color representing each group - A:red, B:blue, C:orange and D:violet corresponds to groups A, B, C and D in the Powalka et al. (2016a) ans recalled in section 5.3.2. The filled region along each line is 1-σ uncertainty evaluated using bootstrapping. The diagonal of the figure shows the Kernel density estimation (kde) smoothed histogram of the respective colors on the horizontal axis.

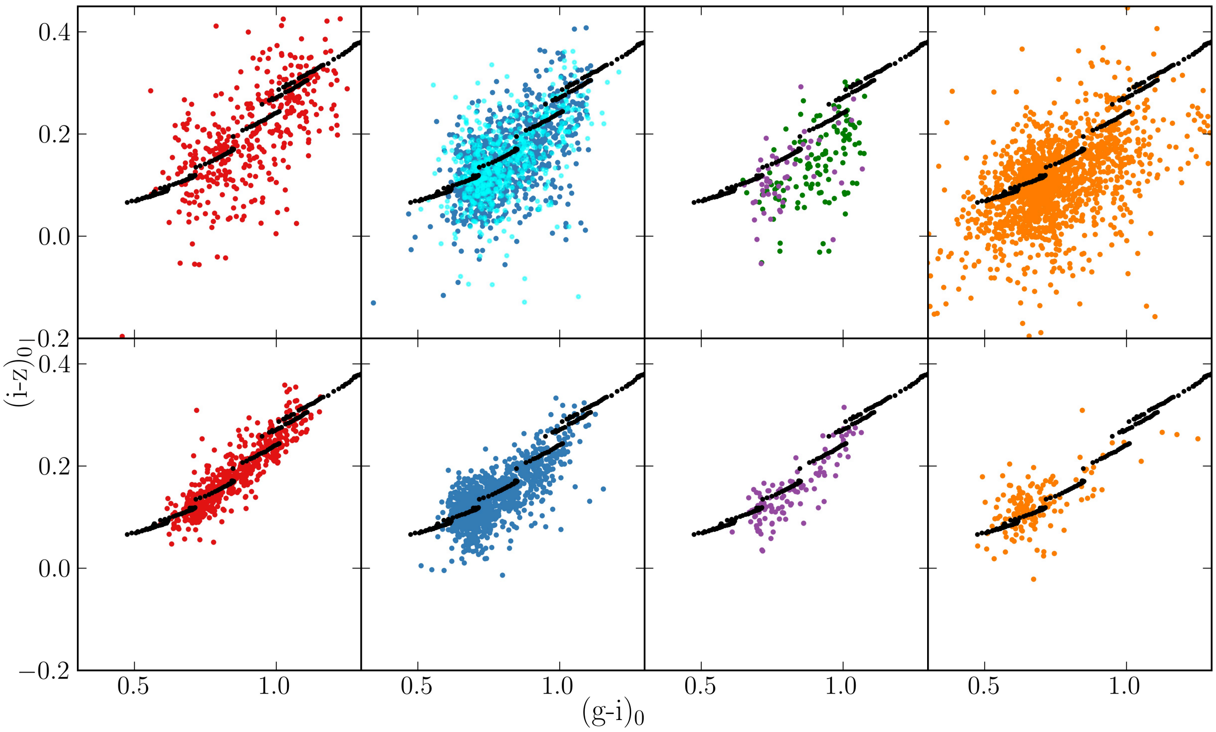

Figure 5.14 Comparing the *giz* color-color distribution of various GC groups around M49(top panel) and M87(bottom panel). The PEGASE SSP models corresponding to ages 5-15 Gyr and metallicity values ranging from the bluest models having Z = 0.0001 to th reddest models with Z = 0.05 are overlaid on the top of the GC color-color plot.

5.4 Colors and environment - Possible culprits

The differences in the color - color distributions of GCs belonging to different environments with the GCs around M87 are found to have no major disagreements. The differences between the color-color distribution in the GCs in our data set shows variation that are subtle but similar to what was found earlier in the GC system around M87 by Powalka et al., 2016a. These effects are more prominent when *i*,*z* or *Ks* bands are involved. This is also what Powalka et al., 2016a observed in their color-color trends. The environment seems to be an important catalyst in deriving the color relations of GCs. Apart from the age and metallicity of the GCs which are widely agreed causes of the color differences seen in GC systems of early-type galaxies, some other parameters should be considered to explain these more subtle differences. The possible reasons that could explain these differences could be related to surface chemistry of stars in these GCs which closely traces the chemistry of their environments. Another possible reason could be the initial mass function, which is also known to have been affected by the local conditions (Kroupa, 2001; Krumholz et al., 2011; Riaz et al., 2021). It can not be denied that the origin of these differences could be a combination of many factors. Unfortunately, any such effects will not be very strongly seen in photometry and the differences will be better resolved in the spectra of the GCs. Figure 5.15 shows the spectra of GCs generated using PEGASE-HR SSP models (Le Borgne et al., 2004). The figure shows the spectra of a typical metal poor GC (Z=0.0001) and a GC with super solar metallicity (Z=0.05) with the filter response curves for the filter used in this study (black curves) and the Euclid filters (grey dashed curves).

The role of environment in producing these differences is speculated but with the quality of available data the magnitude of these differences remain very small to provide a concrete explanation. To reproduce these effects in stellar population synthesis models we need isochrones that account for initial abundances considering scenarios that include the formation of multiple stellar populations and follow the evolution of abundances as theorized for the MSP scenario. Additionally, other processes that modify the surface abundances of stars like atomic diffusion and stellar winds also need to be integrated. These models also needs to extend to the near-IR regime.

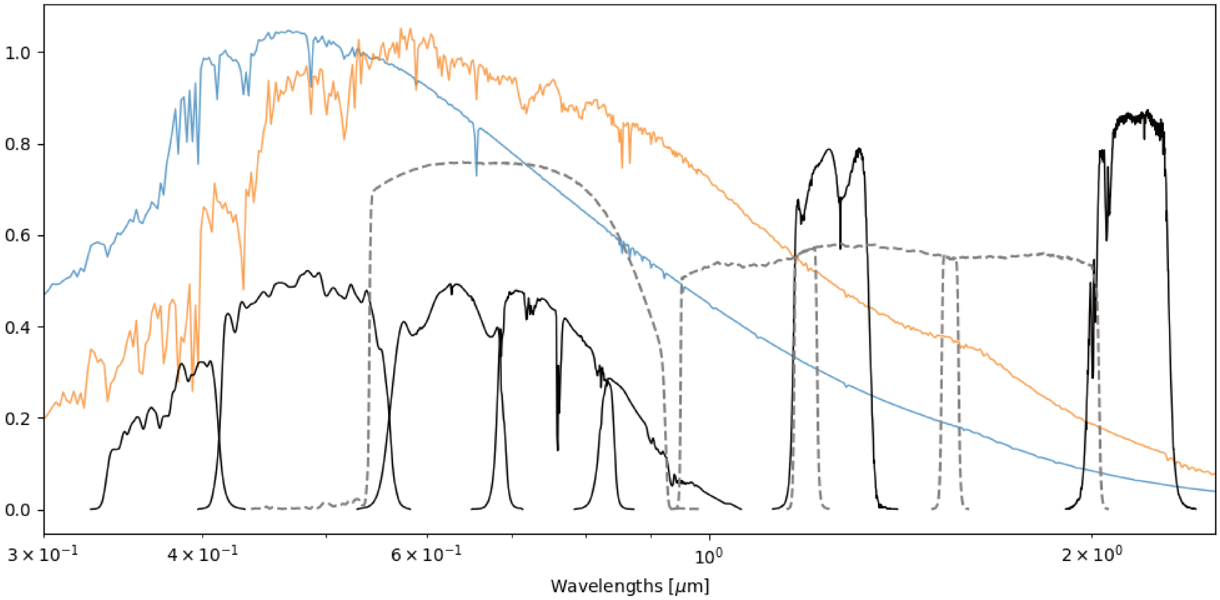

Figure 5.15 Normalized spectral energy distribution of GCs with low metallicity (Z=0.0001, blue spectra) and higher metallicity (super solar, Z=0.05, orange spectra). The black curves are filter response curves (in order from *left* to *right*): CFHT/MegaCam u, g, r, i, and z. Further towards left (near-IR regime) are VISTA/VIRCAM J and Ks. The dashed grey curves are Euclid visible, Y, J and H filter response curves.

CHAPTER SIX

SUMMARY AND CONCLUSION

"We are trapped in the amber of time. There is no why." - Kurt Vonnegut

Abstract

This chapter summarizes the thesis and discusses future work and upcoming surveys.

The work done in this thesis is a contribution to a broad community's efforts to understand globular clusters, both as individual entity and as tracers of the evolution of baryonic structure of the universe. Thanks to the impressive performance of the modern instruments, details that constrain the evolutionary models have become apparent in unprecedented ways. It has become possible to study the variation in surface chemical abundance of individual stars of a single cluster which will help in improving the predictive power of stellar evolutionary models. Hints of subtle differences from the spectral energy distribution of remote globular clusters in different environments have start to accumulate, and will require both confirmation and final interpretation, in a context where the co-existence of the multiple stellar populations inside a cluster has become a norm rather than the exception.

The high-performance instrumentation that has provided the empirical data on which this thesis is based comes with a counterpart: data volumes are gigantic, and the number of individual steps involved in the reduction, from large raw images to one-dimensional spectra or photometric catalogs is also very large. This thesis has used fully reduced spectra from the ESO/VLT/MUSE imaging spectrograph, but a large part of this work itself has been devoted to the reduciton of the wide-field near-infrared images of the ESO/VISTA/VIRCAM imager. A server with several CPU cores and 20 TB of data storage was made available for this work at Observatoire de Strasbourg, and another 10 TB of disk space was needed externally to save files generated in the intermediate steps and perform calculations.

In the first part of the thesis, we have discussed the inconsistencies between the different kinds of stellar libraries used in stellar population studies at large, by assessing the surface metallicity trends in the stars along the isochrones of the nearby Milky Way GC, NGC 6397. This work illustrates how globular clusters, which historically helped understanding the main phases of stellar evolution, now constrain very complex mixing processes that are thought to occur in stellar interiors. Some of these involve instabilities that lead to turbulent behaviours either locally or on large scales (convection); there is no detailed predictive physical theory for such mixing processes, and obtaining empirical constraints on their effects is essential, and not easy.

Indeed, this work has also emphasized to what extent the constraints may depend on the method used for extracting them from the observations. Stellar spectral libraries are a major ingredient of population synthesis models, and more effort is needed to construct or select libraries that suitably represent real stars. With empirical libraries, a main difficulty is to ascertain their own fundamental parameters and abundances : this requires the comparison with theoretical libraries, using methods such as the full-spectrum fitting that we carried out (or other methods, such as detailed studies of individual spectral lines for each element). In the empirical libraries ELODIE and MILES that we have explored, it is possible that the parameters of metal-poor stars might be biased. But we know from separate studies that the theoretical libraries are also imperfect. For instance, we followed the study of Lançon et al. (2021)[1] which showed that it remains difficult to reproduce the near-infrared energy distribution of stars with the models that best reproduce the absorption lines and molecular bands at optical wavelengths. The energy distributions set the relative contributions of stars of different types, or populations, to the light at optical and near-infrared wavelengths, and this has direct implications on our ability to interpret the optical and near-infrared absorption line strengths of the integrated light of remote stellar populations.

The second part of the thesis deals with the photometric characterization of extragalactic globular clusters, in particular in the near-infrared. It involved data reduction and analysis of 23 square degrees of near-IR data in and around M49 at the center of Virgo sub-cluster B and intra-cluster GCs in region between M87 and M49. We have described the extraction of sources and their flux measurement, followed by steps to calibrate the data. This data is cross-matched with optical data and the *uiKs* color-color information is used to select GCs in the field. We use certain selection criteria on the selected GC candidates to minimize contamination from stars and background galaxies. The selected GCs are classified into different groups based on their host environment and their color-color distributions are studied. These color-color distributions are compared amongst each group, the GCs around M87 and with the population synthesis models. After inspecting the relative trends we have come to conclude that there are differences in the color-color trends of the different groups of GCs. These trends are of small amplitude and are their origin is most likely linked to their environments.

---

[1] We performed an analysis of interpolation methods in the theoretical spectral library, which then helped selecting the method actually implemented for that article.

We speculate the possible causes that can give rise to the trends observed in the color-color distributions. The possible reasons include the variation in surface chemistry of stars in the clusters or initial mass function that could be a function of the environment. It is also a possibility that a combination of multiple factors can be responsible for the differences.

In order to better understand these trends we require stellar models that account for the abundance variation during and after the stellar population is born and the models that extend to near-IR. A number of groups are working on incorporating the complicated stellar evolution with multiple stellar populations to the evolutionary models and extending these to the infrared (Chantereau et al., 2015; Coelho et al., 2011; Sharina and Shimansky, 2020; Eitner et al., 2019), but there is still a shortage of models that go beyond 1 micron wavelength.

6.1 The importance of the Ks band

The importance of the Ks band data has been already demonstrated while discussing the diagnostic capability of the *uiKs* diagrams in separating the GCs efficiently from galaxies and stars. In addition to GCs, the *uiKs* diagram is also monumental in the selection of ultracompact dwarf (UCD) galaxies. To demonstrate this we take the example from Liu et al. (2020). In their work they have identified 600 UCD candidates in $\sim 100deg^2$ in the Virgo cluster using a combination of magnitudes, ellipticities, colors, surface brightnesses and half-light radii. However, the Ks band magnitude for the objects was adopted from UKIDSS and not all of the selected UCD candidates had Ks band photometry available. We cross-matched the UCD candidates from that archive catalog with our catalog to find 99 common objects. When we overlay these objects on the *uiKs* diagram we find that 32 objects out of 99 are most likely background galaxies (figure 6.1, cyan objects). Upon further investigation we find that these objects that stray away from the GC sequence either have no Ks band magnitude information in UKIDSS or have fainter Ks band magnitudes which means larger uncertainty.

This example portrays that the Ks band is advantageous in the study of mostly old compact stellar systems like UCDs in addition to GCs.

6.2 Upcoming surveys

We have demonstrated the role infrared data plays in the selection of compact stellar systems. The current understanding of these systems and their complicated relationship with their environments is not yet comprehensive. In particular, our ability to compare the color-color

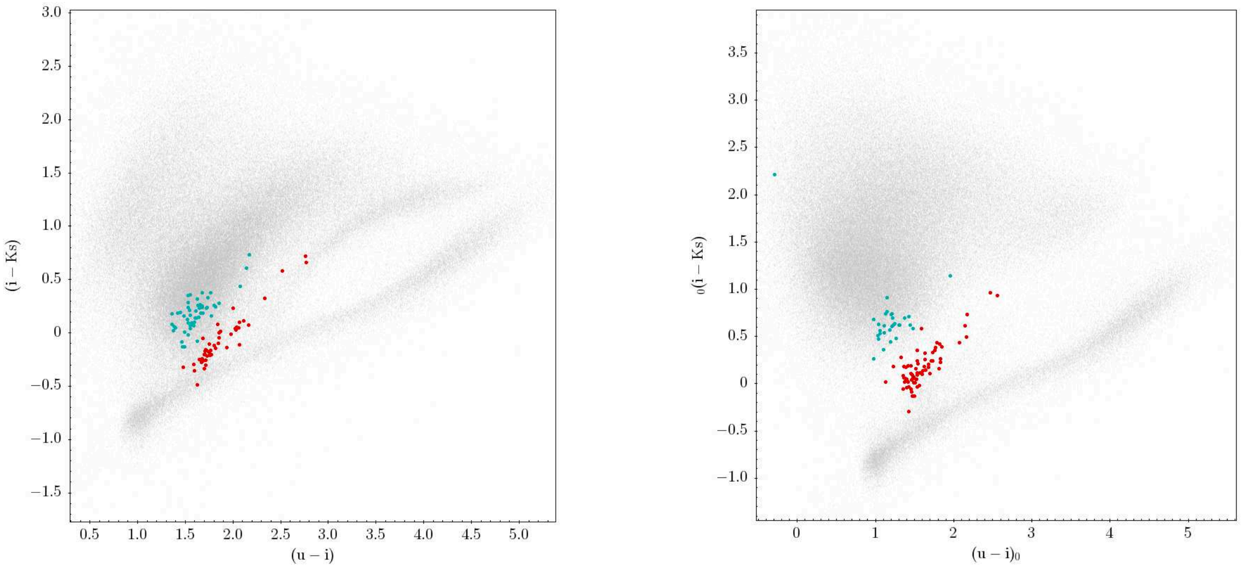

Figure 6.1 UCDs cross-matched with the catalog given by Liu et al. (2020) plotted on the top of *uiKs* diagram (*left panel*) and modified *uiKs* diagram (*right panel*). The cyan objects are likely background galaxies in their catalog.

relations of globular clusters in different ground-based surveys has been limited by systematic errors. In Chapter 4 we have shown that even within one large ground-based survey local calibration systematics lead to the need for a re-calibration of the colors (which in itself carries its own caveats). When colors are compared between different surveys, additional systematic uncertainties creep in via color transformations between photometric systems, that rely on either overlapping data sets or synthetic photometry (i.e. spectral libraries and an excellent knowledge of instrument transmissions). We have not attempted such comparisons, mainly because Mathieu Powalka, in his thesis manuscript in 2018, published attempts that showed that the results are inconclusive because of the systematic uncertainties. With the more ambitious photometric surveys and telescopes like Euclid (Scaramella et al., 2021) and the Nancy Grace Roman space telescope etc., the future of extra-galactic globular cluster science seems to improve. Although Euclid will provide data with photometric depth which is only marginally better than NGVS data, it will provide a more homogeneous data with a much broader coverage on the sky ($\sim 15\,000 deg^2$). Availability of uniform data over large area will minimize the efforts required in assessing the systematic uncertainties. In the next decade with the launch of Roman space telescope, which will provide pointed observations, but with a huge upgraded photometric depth which will allow us to explore GCs two to three magnitudes below the peak of the GCLF at the distance of Virgo. Such a sample will be useful in studying the survival/disruption processes of small objects, and any dependence on

Table 6.1 Upcoming Surveys and Telescopes [2]

Survey/Telescope	5σ detection limit	Resolution (FWHM)
UKIDSS Large Area Survey	20.8 AB (J) 20.1 AB (Ks)	$\sim 1acrsec$
VISTA	23.6 AB (J) 23.3 AB (Ks)	$\sim 0.7acrsec$
Euclid	24.5 AB (J)	$\sim 0.2acrsec$
The Nancy Grace Roman Space Telescope	28.0 AB (J) $\sim$ 1 hour 26.2 AB (Ks) $\sim$ 1 hour	$\sim 0.1acrsec$

the color properties on GC mass. Also Roman (or JWST) is needed to see the TOM of the GCLF at 100 Mpc. With that sort of depth, one can explore the GC populations of faint galaxies, which usually lack massive clusters; they may have GCLFs quite different from the ones in more massive galaxies.

---

[2] Information from -
UKIDSS - Lawrence et al. (2007)
VISTA - This work
Euclid - Scaramella et al. (2021)
The Nancy Grace Roman Space Telescope - Link to the page

APPENDICES

Appendix A

First Appendix

A.1 Color transformation from UKIDSS/WFCAM to VIRCAM.

A set of color transformations from the photometric system of the UKIDSS survey (camera WFCAM mounted on the UK Infrared Telescope UKIRT) to the VISTA/VIRCAM system, valid for Vega-based photometry, has been published by GF2018. It is based on the comparison between stellar photometry in reduced VIRCAM images that were calibrated against (transformed) 2MASS magnitudes, and the photometry of those stars in the UKIDSS point source catalog. We have performed an independent evaluation of the color-transformations using synthetic stellar photometry.

The system transmissions in the J and Ks bands are downloaded from the SVO filter services and synthetic star spectra are taken from the PHOENIX library of Husser et al., 2013. As in Powalka et al., 2016b, we have determined the range of atmospheric parameters of the stars present in our dataset based on the Besançon the model of the Milky Way (Robin et al., 2003), taking into account the magnitude limits of our data: at the blue end of the main stellar locus in color-color diagrams one finds mostly main sequence stars of the Galactic halo, while the stars at the blue end are mostly faint cool dwarfs of the local disk. The corresponding range of atmospheric parameters is given in Table A.1. We derived J and K band magnitudes of these stars in the VISTA and UKIDSS systems and then derived the color equation for each band with a linear least squares fit (Eqs. A.1, A.2).

$$Ks_V = K_W + 0.014^{\pm 0.002} \times (J-K)_W - 0.004 \tag{A.1}$$

$$J_V = J_W - 0.0026^{\pm 2.\,10^{-4}} \times (J-K)_W \tag{A.2}$$

The formal errors on the intercept are insignificant for both bands. The equations are valid for $(J-K)_W < 0.7$, a restriction adopted because the models become more uncertain at low effective temperatures ($0.7 < (J-K)_W < 1$) and the relations also deviate more from being linear at the red end (cf Fig. 11 of GF2018). For a typical $(J-K)_W$ of 0.5 mag, $(Ks_V - K_W)$ differs by 0.015 mag and $(J_V - J_W)$ by 0.017 mag depending on whether the above relations

Table A.1 Stellar properties along the NGVS line of sight

T_{eff}(K)	logg	[Fe/H]	[α/Fe]
3100	5	0.0	0.0
3600	5	-0.5	0.2
4000	5	-1	0.2
4500	5	-1.5	0.4
5000	4.5	-1.5	0.4
5500	4.5	-1.5	0.4
6000	4.5	-1.5	0.4
6400	4.5	-2	0.4

or those of GF2018 are used. This is fully consistent with typical uncertainties on absolute photometry and color transformations in the near-IR. For instance, GF2018 report that the two most recent version of the CASU pipeline (v1.3 and v1.5) have used slightly different relations to transform 2MASS magnitudes before using them to determine VIRCAM image zero points; the choice of one or the other led to systematic offsets of ∼0.01 magnitude in K_s and ∼0.02 magnitude in J. The final calibration in the present work is based on Eqs. A.1, A.2.

References

Agertz, Oscar, Romain Teyssier, and Ben Moore (Jan. 2011). "The formation of disc galaxies in a ΛCDM universe". In: 410.2, pp. 1391–1408. DOI: 10.1111/j.1365-2966.2010.17530.x. arXiv: 1004.0005 [astro-ph.CO].

Allard, F. and P. H. Hauschildt (May 1995). "Model atmospheres for M (sub)dwarf stars. 1: The base model grid". In: 445, pp. 433–450. DOI: 10.1086/175708. eprint: astro-ph/9601150.

Allende Prieto, C. et al. (Oct. 2018). "A collection of model stellar spectra for spectral types B to early-M". In: 618, A25, A25. DOI: 10.1051/0004-6361/201732484. arXiv: 1807.06049 [astro-ph.SR].

Anderson, J. et al. (June 2008). "The Acs Survey of Globular Clusters. V. Generating a Comprehensive Star Catalog for each Cluster". In: 135, pp. 2055–2073. DOI: 10.1088/0004-6256/135/6/2055. arXiv: 0804.2025.

Arentsen, A. et al. (July 2019). "Stellar atmospheric parameters for 754 spectra from the X-shooter Spectral Library". In: 627, A138, A138. DOI: 10.1051/0004-6361/201834273. arXiv: 1907.06391 [astro-ph.SR].

Armandroff, Taft E. (Feb. 1989). "The Properties of the Disk System of Globular Clusters". In: 97, p. 375. DOI: 10.1086/114988.

Ashman, Keith M. and Stephen E. Zepf (Jan. 1992). "The Formation of Globular Clusters in Merging and Interacting Galaxies". In: 384, p. 50. DOI: 10.1086/170850.

— (Jan. 1993). "Merging and Interacting Galaxies: Sites of Globular Cluster Formation". In: *The Globular Cluster-Galaxy Connection*. Ed. by Graeme H. Smith and Jean P. Brodie. Vol. 48. Astronomical Society of the Pacific Conference Series, p. 776.

— (1998). *Globular Cluster Systems*.

Bacon, R. et al. (Sept. 2014). "MUSE Commissioning". In: *The Messenger* 157, pp. 13–16.

Barmby, Pauline and John P. Huchra (Nov. 2001). "M31 Globular Clusters in the Hubble Space Telescope Archive. I. Cluster Detection and Completeness". In: 122.5, pp. 2458–2468. DOI: 10.1086/323457. arXiv: astro-ph/0107401 [astro-ph].

Bassino, Lilia P., Juan C. Muzzio, and Monica Rabolli (Aug. 1994). “Are Globular Clusters the Nuclei of Cannibalized Dwarf Galaxies?” In: 431, p. 634. DOI: 10.1086/174514.

Bastian, Nate and Carmela Lardo (Sept. 2018). “Multiple Stellar Populations in Globular Clusters”. In: 56, pp. 83–136. DOI: 10.1146/annurev-astro-081817-051839. arXiv: 1712.01286 `[astro-ph.SR]`.

Baumgardt, H. and S. Mieske (Dec. 2008). “High mass-to-light ratios of ultra-compact dwarf galaxies - evidence for dark matter?” In: 391.2, pp. 942–948. DOI: 10.1111/j.1365-2966.2008.13949.x. arXiv: 0809.2783 `[astro-ph]`.

Becker, Robert H., Richard L. White, and David J. Helfand (Sept. 1995). “The FIRST Survey: Faint Images of the Radio Sky at Twenty Centimeters”. In: 450, p. 559. DOI: 10.1086/176166.

Bekki, Kenji, Warrick J. Couch, and Michael J. Drinkwater (May 2001). “Galaxy Threshing and the Formation of Ultracompact Dwarf Galaxies”. In: 552.2, pp. L105–L108. DOI: 10.1086/320339. arXiv: astro-ph/0106402 `[astro-ph]`.

Bellazzini, M. et al. (Jan. 2015). “Kinematics of a globular cluster with an extended profile: NGC 5694”. In: 446.3, pp. 3130–3138. DOI: 10.1093/mnras/stu2303. arXiv: 1410.7929 `[astro-ph.SR]`.

Belokurov, V. et al. (Mar. 2007). “An Orphan in the “Field of Streams””. In: 658.1, pp. 337–344. DOI: 10.1086/511302. arXiv: astro-ph/0605705 `[astro-ph]`.

Bertelli Motta, C. et al. (July 2018). “The Gaia-ESO Survey: evidence of atomic diffusion in M67?” In: 478, pp. 425–438. DOI: 10.1093/mnras/sty1011. arXiv: 1804.06293 `[astro-ph.SR]`.

Bertin, E. (July 2006). “Automatic Astrometric and Photometric Calibration with SCAMP”. In: *Astronomical Data Analysis Software and Systems XV*. Ed. by C. Gabriel et al. Vol. 351. Astronomical Society of the Pacific Conference Series, p. 112.

Bertin, E. and S. Arnouts (June 1996). “SExtractor: Software for source extraction.” In: 117, pp. 393–404. DOI: 10.1051/aas:1996164.

Bertin, Emmanuel et al. (Jan. 2002). “The TERAPIX Pipeline”. In: *Astronomical Data Analysis Software and Systems XI*. Ed. by David A. Bohlender, Daniel Durand, and Thomas H. Handley. Vol. 281. Astronomical Society of the Pacific Conference Series, p. 228.

Bianchini, P., R. Ibata, and B. Famaey (Dec. 2019). “Exploring the Outskirts of Globular Clusters: The Peculiar Kinematics of NGC 3201”. In: 887.1, L12, p. L12. DOI: 10.3847/2041-8213/ab58d1. arXiv: 1912.02195 `[astro-ph.GA]`.

Bik, A. et al. (Jan. 2003). “Clusters in the inner spiral arms of M 51: The cluster IMF and the formation history”. In: 397, pp. 473–486. DOI: 10.1051/0004-6361:20021384. arXiv: astro-ph/0210594 [astro-ph].

Binggeli, B., A. Sandage, and G. A. Tammann (Sept. 1985). “Studies of the Virgo cluster. II. A catalog of 2096 galaxies in the Virgo cluster area.” In: 90, pp. 1681–1758. DOI: 10.1086/113874.

Blakeslee, John P., Michele Cantiello, and Eric W. Peng (Feb. 2010). “The Mass-Metallicity Relation of Globular Clusters in the Context of Nonlinear Color-Metallicty Relations”. In: 710.1, pp. 51–63. DOI: 10.1088/0004-637X/710/1/51. arXiv: 1001.0979 [astro-ph.CO].

Blom, Christina, Lee R. Spitler, and Duncan A. Forbes (Feb. 2012a). “Wide-field imaging of NGC 4365’s globular cluster system: the third subpopulation revisited”. In: 420.1, pp. 37–60. DOI: 10.1111/j.1365-2966.2011.19963.x. arXiv: 1110.1378 [astro-ph.CO].

Blom, Christina et al. (Nov. 2012b). “The SLUGGS survey: globular cluster system kinematics and substructure in NGC 4365”. In: 426.3, pp. 1959–1971. DOI: 10.1111/j.1365-2966.2012.21795.x. arXiv: 1207.6398 [astro-ph.CO].

Bonnell, Ian A., Matthew R. Bate, and Stephen G. Vine (Aug. 2003). “The hierarchical formation of a stellar cluster”. In: 343.2, pp. 413–418. DOI: 10.1046/j.1365-8711.2003.06687.x. arXiv: astro-ph/0305082 [astro-ph].

Bono, G. et al. (Jan. 2010). “On a New Near-Infrared Method to Estimate the Absolute Ages of Star Clusters: NGC 3201 as a First Test Case”. In: 708.2, pp. L74–L79. DOI: 10.1088/2041-8205/708/2/L74. arXiv: 0912.0824 [astro-ph.SR].

Boselli, A. et al. (Mar. 2010). “The Herschel Reference Survey”. In: 122.889, p. 261. DOI: 10.1086/651535. arXiv: 1001.5136 [astro-ph.CO].

Bressert, E. et al. (Nov. 2010). “The spatial distribution of star formation in the solar neighbourhood: do all stars form in dense clusters?” In: 409.1, pp. L54–L58. DOI: 10.1111/j.1745-3933.2010.00946.x. arXiv: 1009.1150 [astro-ph.SR].

Brodie, Jean P. and Jay Strader (Sept. 2006). “Extragalactic Globular Clusters and Galaxy Formation”. In: 44.1, pp. 193–267. DOI: 10.1146/annurev.astro.44.051905.092441. arXiv: astro-ph/0602601 [astro-ph].

Brodie, Jean P. et al. (Dec. 2011). “The Relationships among Compact Stellar Systems: A Fresh View of Ultracompact Dwarfs”. In: 142.6, 199, p. 199. DOI: 10.1088/0004-6256/142/6/199. arXiv: 1109.5696 [astro-ph.CO].

Bromm, Volker and Cathie J. Clarke (Feb. 2002). “The Formation of the First Globular Clusters in Dwarf Galaxies before the Epoch of Reionization”. In: 566.1, pp. L1–L4. DOI: 10.1086/339440. arXiv: astro-ph/0201066 [astro-ph].

Bruzual, G. and S. Charlot (Oct. 2003). “Stellar population synthesis at the resolution of 2003”. In: 344.4, pp. 1000–1028. DOI: 10.1046/j.1365-8711.2003.06897.x. arXiv: astro-ph/0309134 `[astro-ph]`.

Burstein, D. (Nov. 1979). “Structure and origin of S0 galaxies. I - Surface photometry of S0 galaxies”. In: 41, pp. 435–450. DOI: 10.1086/190625.

Caldwell, Nelson et al. (Feb. 2011). “Star Clusters in M31. II. Old Cluster Metallicities and Ages from Hectospec Data”. In: 141.2, 61, p. 61. DOI: 10.1088/0004-6256/141/2/61. arXiv: 1101.3779 `[astro-ph.GA]`.

Cantiello, Michele et al. (Apr. 2018). “The Next Generation Virgo Cluster Survey (NGVS). XVIII. Measurement and Calibration of Surface Brightness Fluctuation Distances for Bright Galaxies in Virgo (and Beyond)”. In: 856.2, 126, p. 126. DOI: 10.3847/1538-4357/aab043. arXiv: 1802.05526 `[astro-ph.GA]`.

Capetti, Alessandro et al. (Dec. 2009). “A Very Large Array Radio Survey of Early-Type Galaxies in the Virgo Cluster”. In: 138.6, pp. 1990–1997. DOI: 10.1088/0004-6256/138/6/1990. arXiv: 0910.4102 `[astro-ph.CO]`.

Cappellari, Michele et al. (May 2011). “The ATLAS^{3D} project - I. A volume-limited sample of 260 nearby early-type galaxies: science goals and selection criteria”. In: 413.2, pp. 813–836. DOI: 10.1111/j.1365-2966.2010.18174.x. arXiv: 1012.1551 `[astro-ph.CO]`.

Cardelli, Jason A., Geoffrey C. Clayton, and John S. Mathis (Oct. 1989). “The Relationship between Infrared, Optical, and Ultraviolet Extinction”. In: 345, p. 245. DOI: 10.1086/167900.

Carretta, E. et al. (Oct. 2009a). “Na-O anticorrelation and HB. VII. The chemical composition of first and second-generation stars in 15 globular clusters from GIRAFFE spectra”. In: 505.1, pp. 117–138. DOI: 10.1051/0004-6361/200912096. arXiv: 0909.2938 `[astro-ph.GA]`.

— (Oct. 2009b). “Na-O anticorrelation and HB. VII. The chemical composition of first and second-generation stars in 15 globular clusters from GIRAFFE spectra”. In: 505, pp. 117–138. DOI: 10.1051/0004-6361/200912096. arXiv: 0909.2938.

Carretta, E. et al. (Oct. 2009c). “Na-O anticorrelation and HB. VIII. Proton-capture elements and metallicities in 17 globular clusters from UVES spectra”. In: 505.1, pp. 139–155. DOI: 10.1051/0004-6361/200912097. arXiv: 0909.2941 `[astro-ph.GA]`.

— (Oct. 2009d). “Na-O anticorrelation and HB. VIII. Proton-capture elements and metallicities in 17 globular clusters from UVES spectra”. In: 505, pp. 139–155. DOI: 10.1051/0004-6361/200912097. arXiv: 0909.2941.

Carretta, Eugenio et al. (Apr. 2000). "Distances, Ages, and Epoch of Formation of Globular Clusters". In: 533.1, pp. 215–235. DOI: 10.1086/308629. arXiv: astro-ph/9902086 `[astro-ph]`.

Chantereau, W., C. Charbonnel, and T. Decressin (June 2015). "Evolution of long-lived globular cluster stars. I. Grid of stellar models with helium enhancement at [Fe/H] = -1.75". In: 578, A117, A117. DOI: 10.1051/0004-6361/201525929. arXiv: 1504.01878 `[astro-ph.SR]`.

Chapman, S. (May 1917a). "Convection and diffusion within giant stars". In: 77, p. 540. DOI: 10.1093/mnras/77.7.540.

— (May 1917b). "Convection and diffusion within giant stars". In: 77, p. 540. DOI: 10.1093/mnras/77.7.540.

Charbonnel, C. (Nov. 2016). "Multiple Stellar Populations and Their Evolution in Globular Clusters: A Nucleosynthesis Perspective". In: *EAS Publications Series*. Vol. 80-81. EAS Publications Series, pp. 177–226. DOI: 10.1051/eas/1680006. arXiv: 1611.08855 `[astro-ph.SR]`.

Ciambur, B. C. (Sept. 2015). "Beyond Ellipse(s): Accurately Modelling the Isophotal Structure of Galaxies with ISOFIT and CMODEL". In: 810.2, 120, p. 120. DOI: 10.1088/0004-637X/810/2/120. arXiv: 1507.02691 `[astro-ph.GA]`.

Coelho, P., S. M. Percival, and M. Salaris (June 2011). "Chemical Abundance Anticorrelations in Globular Cluster Stars: The Effect on Cluster Integrated Spectra". In: 734.1, 72, p. 72. DOI: 10.1088/0004-637X/734/1/72. arXiv: 1104.1618 `[astro-ph.GA]`.

Coelho, P. et al. (2005). "A library of high resolution synthetic stellar spectra from 300 nm to 1.8 μm with solar and α-enhanced composition". In: 443.2, pp. 735–746. DOI: 10.1051/0004-6361:20053511. arXiv: astro-ph/0505511 `[astro-ph]`.

Coelho, P. R. T. (May 2014). "A new library of theoretical stellar spectra with scaled-solar and α-enhanced mixtures". In: 440, pp. 1027–1043. DOI: 10.1093/mnras/stu365. arXiv: 1404.3243 `[astro-ph.SR]`.

Cohen, Judith G., J. P. Blakeslee, and P. Côté (Aug. 2003). "The Ages and Abundances of a Sample of Globular Clusters in M49 (NGC 4472)". In: 592.2, pp. 866–883. DOI: 10.1086/375865. arXiv: astro-ph/0304333 `[astro-ph]`.

Cole, David R. et al. (Oct. 2012). "The mass distribution of the Fornax dSph: constraints from its globular cluster distribution". In: 426.1, pp. 601–613. DOI: 10.1111/j.1365-2966.2012.21885.x. arXiv: 1205.6327 `[astro-ph.CO]`.

Condon, J. J. et al. (May 1998). "The NRAO VLA Sky Survey". In: 115.5, pp. 1693–1716. DOI: 10.1086/300337.

Cote, P. et al. (May 1999). “Globular Cluster Metallicity Distribution Functions: Multimodality as a Consequence of Intrinsic Processes and Capture”. In: *American Astronomical Society Meeting Abstracts #194*. Vol. 194. American Astronomical Society Meeting Abstracts, p. 40.16.

Côté, Patrick, Ronald O. Marzke, and Michael J. West (July 1998). “The Formation of Giant Elliptical Galaxies and Their Globular Cluster Systems”. In: 501.2, pp. 554–570. DOI: 10.1086/305838. arXiv: astro-ph/9804319 `[astro-ph]`.

Côté, Patrick et al. (July 2004). “The ACS Virgo Cluster Survey. I. Introduction to the Survey”. In: 153.1, pp. 223–242. DOI: 10.1086/421490. arXiv: astro-ph/0404138 `[astro-ph]`.

Côté, Patrick et al. (July 2006). “The ACS Virgo Cluster Survey. VIII. The Nuclei of Early-Type Galaxies”. In: 165.1, pp. 57–94. DOI: 10.1086/504042. arXiv: astro-ph/0603252 `[astro-ph]`.

Dabringhausen, J., M. Hilker, and P. Kroupa (May 2008). “From star clusters to dwarf galaxies: the properties of dynamically hot stellar systems”. In: 386.2, pp. 864–886. DOI: 10.1111/j.1365-2966.2008.13065.x. arXiv: 0802.0703 `[astro-ph]`.

Daddi, E. et al. (Dec. 2004). “A New Photometric Technique for the Joint Selection of Star-forming and Passive Galaxies at 1.4 <~z <~2.5”. In: 617.2, pp. 746–764. DOI: 10.1086/425569. arXiv: astro-ph/0409041 `[astro-ph]`.

Dale, James Edward (Aug. 2015). “The influence of feedback from massive stars on the formation and emergence of massive clusters”. In: *IAU General Assembly*. Vol. 29, p. 2254661.

Dalton, G. B. et al. (June 2006). “The VISTA infrared camera”. In: vol. 6269. Society of Photo-Optical Instrumentation Engineers (SPIE) Conference Series, p. 62690X. DOI: 10.1117/12.670018.

Davies, J. I. et al. (July 2010). “The Herschel Virgo Cluster Survey. I. Luminosity function”. In: 518, L48, p. L48. DOI: 10.1051/0004-6361/201014571. arXiv: 1005.3054 `[astro-ph.CO]`.

de Vaucouleurs, Gerard (Feb. 1953). “Evidence for a local super,galaxy”. In: 58, p. 30. DOI: 10.1086/106805.

— (July 1958). “Further evidence for a local super-cluster of galaxies: rotation and expansion”. In: 63, p. 253. DOI: 10.1086/107742.

Deal, M. et al. (Jan. 2020). “Chemical mixing in low mass stars. I. Rotation against atomic diffusion including radiative acceleration”. In: 633, A23, A23. DOI: 10.1051/0004-6361/201936666. arXiv: 1910.14335 `[astro-ph.SR]`.

Denissenkov, P. A. et al. (Apr. 2015). “The primordial and evolutionary abundance variations in globular-cluster stars: a problem with two unknowns”. In: 448.4, pp. 3314–3324. DOI: 10.1093/mnras/stv211. arXiv: 1409.1193 `[astro-ph.SR]`.

Dotter, A. et al. (May 2017). "The Influence of Atomic Diffusion on Stellar Ages and Chemical Tagging". In: 840, 99, p. 99. DOI: 10.3847/1538-4357/aa6d10. arXiv: 1704.03465 [astro-ph.SR].

Drinkwater, M. J. et al. (Dec. 2000). "Compact Stellar Systems in the Fornax Cluster: Supermassive Star Clusters or Extremely Compact Dwarf Galaxies?" In: 17.3, pp. 227–233. DOI: 10.1071/AS00034. arXiv: astro-ph/0002003 [astro-ph].

Drinkwater, M. J. et al. (May 2003). "A class of compact dwarf galaxies from disruptive processes in galaxy clusters". In: 423.6939, pp. 519–521. DOI: 10.1038/nature01666. arXiv: astro-ph/0306026 [astro-ph].

Drukier, G. A. et al. (Feb. 1998). "Global Kinematics of the Globular Cluster M15". In: 115.2, pp. 708–724. DOI: 10.1086/300231. arXiv: astro-ph/9711059 [astro-ph].

Durrell, Patrick R. et al. (Oct. 2014). "The Next Generation Virgo Cluster Survey. VIII. The Spatial Distribution of Globular Clusters in the Virgo Cluster". In: 794.2, 103, p. 103. DOI: 10.1088/0004-637X/794/2/103. arXiv: 1408.2821 [astro-ph.GA].

Eigenthaler, Paul et al. (Mar. 2018). "The Next Generation Fornax Survey (NGFS). II. The Central Dwarf Galaxy Population". In: 855.2, 142, p. 142. DOI: 10.3847/1538-4357/aaab60. arXiv: 1801.02633 [astro-ph.GA].

Eitner, P., M. Bergemann, and S. Larsen (July 2019). "NLTE modelling of integrated light spectra. Abundances of barium, magnesium, and manganese in a metal-poor globular cluster". In: 627, A40, A40. DOI: 10.1051/0004-6361/201935416. arXiv: 1904.11502 [astro-ph.SR].

Elmegreen, Bruce G. and Edith Falgarone (Nov. 1996). "A Fractal Origin for the Mass Spectrum of Interstellar Clouds". In: 471, p. 816. DOI: 10.1086/178009.

Evans, N. W. and M. I. Wilkinson (Aug. 2000). "The mass of the Andromeda galaxy". In: 316.4, pp. 929–942. DOI: 10.1046/j.1365-8711.2000.03645.x. arXiv: astro-ph/0004187 [astro-ph].

Fall, S. M. and M. J. Rees (Nov. 1985). "A theory for the origin of globular clusters." In: 298, pp. 18–26. DOI: 10.1086/163585.

Fellhauer, M. and P. Kroupa (May 2005). "A possible formation scenario for the heavyweight young cluster W3 in NGC 7252". In: *Starbursts: From 30 Doradus to Lyman Break Galaxies*. Ed. by R. de Grijs and R. M. González Delgado. Vol. 329. Astrophysics and Space Science Library, P18. arXiv: astro-ph/0411382 [astro-ph].

Fellhauer, Michael and Pavel Kroupa (Mar. 2002). "The formation of ultracompact dwarf galaxies". In: 330.3, pp. 642–650. DOI: 10.1046/j.1365-8711.2002.05087.x. arXiv: astro-ph/0110621 [astro-ph].

Ferrarese, Laura et al. (May 2012). "The Next Generation Virgo Cluster Survey (NGVS). I. Introduction to the Survey". In: 200.1, 4, p. 4. DOI: 10.1088/0067-0049/200/1/4.

Ferrarese, Laura et al. (June 2016). "The Next Generation Virgo Cluster Survey (NGVS). XIII. The Luminosity and Mass Function of Galaxies in the Core of the Virgo Cluster and the Contribution from Disrupted Satellites". In: 824.1, 10, p. 10. DOI: 10.3847/0004-637X/824/1/10. arXiv: 1604.06462 `[astro-ph.GA]`.

Ferrarese, Laura et al. (Feb. 2020). "The Next Generation Virgo Cluster Survey (NGVS). XIV. The Discovery of Low-mass Galaxies and a New Galaxy Catalog in the Core of the Virgo Cluster". In: 890.2, 128, p. 128. DOI: 10.3847/1538-4357/ab339f.

Fioc, M. and B. Rocca-Volmerange (Oct. 1997). "PEGASE: a UV to NIR spectral evolution model of galaxies. Application to the calibration of bright galaxy counts." In: 500, pp. 507–519. arXiv: astro-ph/9707017 `[astro-ph]`.

Fitzpatrick, Edward L. (Jan. 1999). "Correcting for the Effects of Interstellar Extinction". In: 111.755, pp. 63–75. DOI: 10.1086/316293. arXiv: astro-ph/9809387 `[astro-ph]`.

Forbes, Duncan (Nov. 1997). "Globular Clusters in Elliptical Galaxies: Constraints on Mergers". In: *arXiv e-prints*, astro-ph/9711165, astro–ph/9711165. arXiv: astro-ph/9711165 `[astro-ph]`.

Forbes, Duncan A. and Terry Bridges (May 2010). "Accreted versus in situ Milky Way globular clusters". In: 404.3, pp. 1203–1214. DOI: 10.1111/j.1365-2966.2010.16373.x. arXiv: 1001.4289 `[astro-ph.GA]`.

Forbes, Duncan A., Jean P. Brodie, and Carl J. Grillmair (May 1997). "On the Origin of Globular Clusters in Elliptical and cD Galaxies". In: 113, p. 1652. DOI: 10.1086/118382. arXiv: astro-ph/9702146 `[astro-ph]`.

Forbes, Duncan A. et al. (June 2000). "The elliptical galaxy formerly known as the Local Group: merging the globular cluster systems". In: 358, pp. 471–480. arXiv: astro-ph/0001477 `[astro-ph]`.

Forbes, Duncan A. et al. (Sept. 2015). "The SLUGGS survey: inferring the formation epochs of metal-poor and metal-rich globular clusters". In: 452.1, pp. 1045–1051. DOI: 10.1093/mnras/stv1312. arXiv: 1506.06820 `[astro-ph.GA]`.

Franchini, M. et al. (Aug. 2018). "Gaia-ESO Survey: INTRIGOSSA New Library of High-resolution Synthetic Spectra". In: 862, 146, p. 146. DOI: 10.3847/1538-4357/aaca3c. arXiv: 1806.08096 `[astro-ph.SR]`.

Fraunhofer, J. (1817). "" In: *Denkschriften der Münch. Akademie der Wissenschaften* 5, p. 193.

— (1821). "" In: *Denkschriften der Münch. Akademie der Wissenschaften* 8, p. 1.

Fukui, Y. et al. (Nov. 2009). "Molecular and Atomic Gas in the Large Magellanic Cloud. II. Three-dimensional Correlation Between CO and H I". In: 705.1, pp. 144–155. DOI: 10.1088/0004-637X/705/1/144. arXiv: 0909.0382 [astro-ph.GA].

Gallo, Elena et al. (June 2008). "AMUSE-Virgo. I. Supermassive Black Holes in Low-Mass Spheroids". In: 680.1, pp. 154–168. DOI: 10.1086/588012. arXiv: 0711.2073 [astro-ph].

Gallo, Elena et al. (May 2010). "AMUSE-Virgo. II. Down-sizing in Black Hole Accretion". In: 714.1, pp. 25–36. DOI: 10.1088/0004-637X/714/1/25. arXiv: 1002.3619 [astro-ph.HE].

Gao, X. et al. (Dec. 2018). "The GALAH survey: verifying abundance trends in the open cluster M67 using non-LTE modelling". In: 481, pp. 2666–2684. DOI: 10.1093/mnras/sty2414. arXiv: 1804.06394 [astro-ph.SR].

García-Berro, Enrique et al. (Nov. 2014). "The white dwarf cooling sequence of 47 Tucanae". In: 571, A56, A56. DOI: 10.1051/0004-6361/201424652. arXiv: 1410.0536 [astro-ph.GA].

Gebhardt, Karl and Markus Kissler-Patig (Oct. 1999). "Globular Cluster Systems. I. V-I Color Distributions". In: 118.4, pp. 1526–1541. DOI: 10.1086/301059. arXiv: astro-ph/9906499 [astro-ph].

Gnedin, Oleg Y. and José L. Prieto (2009). "Formation of Globular Clusters in Hierarchical Cosmology: ART and Science". In: *Globular Clusters - Guides to Galaxies*. Ed. by Tom Richtler and Søren Larsen, p. 323. DOI: 10.1007/978-3-540-76961-3_77.

Gómez, Gilberto C. and Enrique Vázquez-Semadeni (Aug. 2014). "Filaments in Simulations of Molecular Cloud Formation". In: 791.2, 124, p. 124. DOI: 10.1088/0004-637X/791/2/124. arXiv: 1308.6298 [astro-ph.GA].

Gómez, M. and T. Richtler (Feb. 2004). "The globular cluster system of <ASTROBJ>NGC 4374</ASTROBJ>". In: 415, pp. 499–508. DOI: 10.1051/0004-6361:20034610. arXiv: astro-ph/0311188 [astro-ph].

González-Fernández, C. et al. (Mar. 2018). "The VISTA ZYJHKs photometric system: calibration from 2MASS". In: 474.4, pp. 5459–5478. DOI: 10.1093/mnras/stx3073. arXiv: 1711.08805 [astro-ph.IM].

Gratton, R. G. et al. (Apr. 2001). "The O-Na and Mg-Al anticorrelations in turn-off and early subgiants in globular clusters". In: 369, pp. 87–98. DOI: 10.1051/0004-6361:20010144. eprint: astro-ph/0012457.

Gratton, Raffaele, Christopher Sneden, and Eugenio Carretta (Sept. 2004). "Abundance Variations Within Globular Clusters". In: 42.1, pp. 385–440. DOI: 10.1146/annurev.astro.42.053102.133945.

Gratton, Raffaele et al. (Nov. 2019). "What is a globular cluster? An observational perspective". In: 27.1, 8, p. 8. DOI: 10.1007/s00159-019-0119-3. arXiv: 1911.02835 [astro-ph.SR].

Gratton, Raffaele G., Eugenio Carretta, and Angela Bragaglia (Feb. 2012). “Multiple populations in globular clusters. Lessons learned from the Milky Way globular clusters”. In: 20, 50, p. 50. DOI: 10.1007/s00159-012-0050-3. arXiv: 1201.6526 `[astro-ph.SR]`.

Grillmair, Carl J. et al. (Feb. 1994). “The Velocity Dispersion of Globular Clusters in NGC 1399”. In: 422, p. L9. DOI: 10.1086/187199.

Gruen, D., S. Seitz, and G. M. Bernstein (Feb. 2014). “Implementation of Robust Image Artifact Removal in SWarp through Clipped Mean Stacking”. In: 126.936, p. 158. DOI: 10.1086/675080. arXiv: 1401.4169 `[astro-ph.IM]`.

Gruyters, P. et al. (July 2013). “Atomic diffusion and mixing in old stars. IV. Weak abundance trends in the globular cluster NGC 6752”. In: 555, A31, A31. DOI: 10.1051/0004-6361/201220821. arXiv: 1305.1774 `[astro-ph.SR]`.

Gruyters, P. et al. (May 2016). “Atomic diffusion and mixing in old stars. VI. The lithium content of M30”. In: 589, A61, A61. DOI: 10.1051/0004-6361/201527948. arXiv: 1603.01565 `[astro-ph.SR]`.

Hanes, D. A. (May 1977). “Evidence for the uniformity of globular cluster populations.” In: 179, pp. 331–337. DOI: 10.1093/mnras/179.3.331.

Hansen, B. M. S. et al. (Aug. 2013). “An age difference of two billion years between a metal-rich and a metal-poor globular cluster”. In: 500.7460, pp. 51–53. DOI: 10.1038/nature12334. arXiv: 1308.0032 `[astro-ph.SR]`.

Harris, W. E. and S. van den Bergh (Nov. 1981). “Globular clusters in galaxies beyond the local group. I. New cluster systems in selected northern ellipticals.” In: 86, pp. 1627–1642. DOI: 10.1086/113047.

Harris, William E. (Jan. 1991). “Globular cluster systems in galaxies beyond the Local Group.” In: 29, pp. 543–579. DOI: 10.1146/annurev.aa.29.090191.002551.

— (Oct. 1996). “A Catalog of Parameters for Globular Clusters in the Milky Way”. In: 112, p. 1487. DOI: 10.1086/118116.

— (Dec. 2010). “A New Catalog of Globular Clusters in the Milky Way”. In: *arXiv e-prints*, arXiv:1012.3224, arXiv:1012.3224. arXiv: 1012.3224 `[astro-ph.GA]`.

Hartke, J. et al. (July 2017). “The halo of M 49 and its environment as traced by planetary nebulae populations”. In: 603, A104, A104. DOI: 10.1051/0004-6361/201730463. arXiv: 1703.06146 `[astro-ph.GA]`.

Hertzsprung, E. (Jan. 1911). “Number 63. Zweiundzwanzigsten Bandes Erstes Stuck. Uber die verwendung photographischer effecktiver wellenlangen zur bestimmung von farbenaquivalenten”. In: *Publikationen des Astrophysikalischen Observatoriums zu Potsdam* 22, A1–A40.1.

Hilker, M., L. Infante, and T. Richtler (July 1999). “The central region of the Fornax cluster. III. Dwarf galaxies, globular clusters, and cD halo - are there interrelations?” In: 138, pp. 55–70. DOI: 10.1051/aas:1999495. arXiv: astro-ph/9905112 `[astro-ph]`.

Hollyhead, K. et al. (Feb. 2017). “Evidence for multiple populations in the intermediate-age cluster Lindsay 1 in the SMC”. In: 465.1, pp. L39–L43. DOI: 10.1093/mnrasl/slw179. arXiv: 1609.01302 `[astro-ph.GA]`.

Hudson, Michael J., Gretchen L. Harris, and William E. Harris (May 2014). “Dark Matter Halos in Galaxies and Globular Cluster Populations”. In: 787.1, L5, p. L5. DOI: 10.1088/2041-8205/787/1/L5. arXiv: 1404.1920 `[astro-ph.GA]`.

Hunter, Deidre A. et al. (Oct. 2003). “Cluster Mass Functions in the Large and Small Magellanic Clouds: Fading and Size-of-Sample Effects”. In: 126.4, pp. 1836–1848. DOI: 10.1086/378056. arXiv: astro-ph/0306528 `[astro-ph]`.

Husser et al. (May 2013). “A new extensive library of PHOENIX stellar atmospheres and synthetic spectra”. In: 553, A6, A6. DOI: 10.1051/0004-6361/201219058. arXiv: 1303.5632 `[astro-ph.SR]`.

Husser, T.-O. et al. (Apr. 2016). “MUSE crowded field 3D spectroscopy of over 12 000 stars in the globular cluster NGC 6397. I. The first comprehensive HRD of a globular cluster”. In: 588, A148, A148. DOI: 10.1051/0004-6361/201526949. arXiv: 1602.01649 `[astro-ph.SR]`.

Ibata, R. et al. (Feb. 2013). “Do globular clusters possess dark matter haloes? A case study in NGC 2419”. In: 428.4, pp. 3648–3659. DOI: 10.1093/mnras/sts302. arXiv: 1210.7787 `[astro-ph.CO]`.

Indebetouw, R. et al. (Feb. 2005). “The Wavelength Dependence of Interstellar Extinction from 1.25 to 8.0 μm Using GLIMPSE Data”. In: 619.2, pp. 931–938. DOI: 10.1086/426679. arXiv: astro-ph/0406403 `[astro-ph]`.

Irwin, Jimmy A. and Craig L. Sarazin (Nov. 1996). “X-Ray Evidence for the Interaction of the Giant Elliptical Galaxy NGC 4472 with Its Virgo Cluster Environment”. In: 471, p. 683. DOI: 10.1086/177998.

Jain, Rashi, S. Vig, and S. K. Ghosh (May 2019). “Investigation of the globular cluster NGC 2808 with the Ultra-Violet Imaging Telescope”. In: 485.2, pp. 2877–2888. DOI: 10.1093/mnras/stz544. arXiv: 1902.08371 `[astro-ph.SR]`.

Jain, Rashi et al. (Mar. 2020). “NGC 6397: The metallicity trend along the isochrone revisited”. In: 635, A161, A161. DOI: 10.1051/0004-6361/201936952. arXiv: 2002.07702 `[astro-ph.SR]`.

Jarvis, Matt J. et al. (Jan. 2013). “The VISTA Deep Extragalactic Observations (VIDEO) survey”. In: 428.2, pp. 1281–1295. DOI: 10.1093/mnras/sts118. arXiv: 1206.4263 `[astro-ph.CO]`.

Jensen, Joseph, Jeremy Mould, and Neill Reid (May 1988). "The Continuity of Cluster Formation in the Large Magellanic Cloud". In: 67, p. 77. DOI: 10.1086/191266.

Jordán, Andrés et al. (Dec. 2005). "The ACS Virgo Cluster Survey. X. Half-Light Radii of Globular Clusters in Early-Type Galaxies: Environmental Dependencies and a Standard Ruler for Distance Estimation". In: 634.2, pp. 1002–1019. DOI: 10.1086/497092. arXiv: astro-ph/0508219 `[astro-ph]`.

Jordán, Andrés et al. (Apr. 2007a). "The ACS Fornax Cluster Survey. I. Introduction to the Survey and Data Reduction Procedures". In: 169.2, pp. 213–224. DOI: 10.1086/512778. arXiv: astro-ph/0702320 `[astro-ph]`.

Jordán, Andrés et al. (July 2007b). "The ACS Virgo Cluster Survey. XII. The Luminosity Function of Globular Clusters in Early-Type Galaxies". In: 171.1, pp. 101–145. DOI: 10.1086/516840. arXiv: astro-ph/0702496 `[astro-ph]`.

Jordán, Andrés et al. (Jan. 2009). "The ACS Virgo Cluster Survey XVI. Selection Procedure and Catalogs of Globular Cluster Candidates". In: 180.1, pp. 54–66. DOI: 10.1088/0067-0049/180/1/54.

Jordán, Andrés et al. (Nov. 2015). "The ACS Fornax Cluster Survey. XI. Catalog of Globular Cluster Candidates". In: 221.1, 13, p. 13. DOI: 10.1088/0067-0049/221/1/13.

Jordi, C. et al. (Oct. 2016). "The Gaia Mission: Current Status and Spectroscopic Capabilities". In: *Multi-Object Spectroscopy in the Next Decade: Big Questions, Large Surveys, and Wide Fields*. Ed. by I. Skillen, M. Balcells, and S. Trager. Vol. 507. Astronomical Society of the Pacific Conference Series, p. 43.

Kamann, S., L. Wisotzki, and M. M. Roth (Jan. 2013). "Resolving stellar populations with crowded field 3D spectroscopy". In: 549, A71, A71. DOI: 10.1051/0004-6361/201220476. arXiv: 1211.0445 `[astro-ph.IM]`.

Kashibadze, Olga G., Igor D. Karachentsev, and Valentina E. Karachentseva (Mar. 2020). "Structure and kinematics of the Virgo cluster of galaxies". In: 635, A135, A135. DOI: 10.1051/0004-6361/201936172. arXiv: 2002.12820 `[astro-ph.GA]`.

Katz, Harley and Massimo Ricotti (Nov. 2014). "Clues on the missing sources of reionization from self-consistent modelling of Milky Way and dwarf galaxy globular clusters". In: 444.3, pp. 2377–2395. DOI: 10.1093/mnras/stu1489. arXiv: 1406.6055 `[astro-ph.GA]`.

Kharchenko, N. V. et al. (Oct. 2013). "Global survey of star clusters in the Milky Way. II. The catalogue of basic parameters". In: 558, A53, A53. DOI: 10.1051/0004-6361/201322302. arXiv: 1308.5822 `[astro-ph.GA]`.

King, Ivan (Oct. 1962). "The structure of star clusters. I. an empirical density law". In: 67, p. 471. DOI: 10.1086/108756.

King, Ivan R. (Feb. 1966). “The structure of star clusters. III. Some simple dynamical models”. In: 71, p. 64. DOI: 10.1086/109857.

Kinman, T. D. (Jan. 1959). “Globular clusters, III. An analysis of the cluster radial velocities”. In: 119, p. 559. DOI: 10.1093/mnras/119.5.559.

Klypin, Anatoly et al. (Oct. 2003). “Constrained Simulations of the Real Universe: The Local Supercluster”. In: 596.1, pp. 19–33. DOI: 10.1086/377574. arXiv: astro-ph/0107104 `[astro-ph]`.

Ko, Youkyung et al. (Feb. 2017). “To the Edge of M87 and Beyond: Spectroscopy of Intracluster Globular Clusters and Ultracompact Dwarfs in the Virgo Cluster”. In: 835.2, 212, p. 212. DOI: 10.3847/1538-4357/835/2/212. arXiv: 1612.04393 `[astro-ph.GA]`.

Koenig, X. P. et al. (Jan. 2012). “Wide-field Infrared Survey Explorer Observations of the Evolution of Massive Star-forming Regions”. In: 744.2, 130, p. 130. DOI: 10.1088/0004-637X/744/2/130.

Koleva, M. and A. Vazdekis (Feb. 2012). “Stellar population models in the UV. I. Characterisation of the New Generation Stellar Library”. In: 538, A143, A143. DOI: 10.1051/0004-6361/201118065. arXiv: 1111.5449 `[astro-ph.CO]`.

Koleva, M. et al. (July 2009). “ULySS: a full spectrum fitting package”. In: 501, pp. 1269–1279. DOI: 10.1051/0004-6361/200811467. arXiv: 0903.2979 `[astro-ph.IM]`.

Kormendy, John et al. (May 2009). “Structure and Formation of Elliptical and Spheroidal Galaxies”. In: 182.1, pp. 216–309. DOI: 10.1088/0067-0049/182/1/216. arXiv: 0810.1681 `[astro-ph]`.

Korn, A. J. et al. (Dec. 2007). “Atomic Diffusion and Mixing in Old Stars. I. Very Large Telescope FLAMES-UVES Observations of Stars in NGC 6397”. In: 671, pp. 402–419. DOI: 10.1086/523098. arXiv: 0709.0639.

Krause, Martin G. H. et al. (Mar. 2016). “Gas expulsion in massive star clusters?. Constraints from observations of young and gas-free objects”. In: 587, A53, A53. DOI: 10.1051/0004-6361/201526685. arXiv: 1512.04256 `[astro-ph.GA]`.

Krauss, Lawrence M. and Brian Chaboyer (Jan. 2003). “Age Estimates of Globular Clusters in the Milky Way: Constraints on Cosmology”. In: *Science* 299.5603, pp. 65–70. DOI: 10.1126/science.1075631.

Kroupa, Pavel (Apr. 2001). “On the variation of the initial mass function”. In: 322.2, pp. 231–246. DOI: 10.1046/j.1365-8711.2001.04022.x. arXiv: astro-ph/0009005 `[astro-ph]`.

Krumholz, M. R. et al. (Jan. 2014). “Star Cluster Formation and Feedback”. In: *Protostars and Planets VI*. Ed. by Henrik Beuther et al., p. 243. DOI: 10.2458/azu_uapress_9780816531240-ch011. arXiv: 1401.2473 `[astro-ph.GA]`.

Krumholz, Mark R., Richard I. Klein, and Christopher F. McKee (Oct. 2011). “Radiation-hydrodynamic Simulations of the Formation of Orion-like Star Clusters. I. Implications for the Origin of the Initial Mass Function”. In: 740.2, 74, p. 74. DOI: 10.1088/0004-637X/740/2/74. arXiv: 1104.2038 `[astro-ph.GA]`.

Kundu, A. and B. C. Whitmore (Dec. 1998). “WFPC2 Imaging of the Globular Cluster System of NGC 3115”. In: *American Astronomical Society Meeting Abstracts*. Vol. 193. American Astronomical Society Meeting Abstracts, p. 09.05.

Kundu, Arunav and Bradley C. Whitmore (June 2001). “New Insights from HST Studies of Globular Cluster Systems. I. Colors, Distances, and Specific Frequencies of 28 Elliptical Galaxies”. In: 121.6, pp. 2950–2973. DOI: 10.1086/321073. arXiv: astro-ph/0103021 `[astro-ph]`.

Kundu, Arunav et al. (Mar. 1999). “The Globular Cluster System in the Inner Region of M87”. In: 513.2, pp. 733–751. DOI: 10.1086/306865. arXiv: astro-ph/9812199 `[astro-ph]`.

La Barbera, F. et al. (Aug. 2013). “SPIDER VIII - constraints on the stellar initial mass function of early-type galaxies from a variety of spectral features”. In: 433.4, pp. 3017–3047. DOI: 10.1093/mnras/stt943. arXiv: 1305.2273 `[astro-ph.CO]`.

Laevens, Benjamin P. M. et al. (May 2014). “A New Distant Milky Way Globular Cluster in the Pan-STARRS1 3π Survey”. In: 786.1, L3, p. L3. DOI: 10.1088/2041-8205/786/1/L3. arXiv: 1403.6593 `[astro-ph.GA]`.

Lançon, A. et al. (May 2021). “A comparison between X-shooter spectra and PHOENIX models across the HR-diagram”. In: 649, A97, A97. DOI: 10.1051/0004-6361/202039371. arXiv: 2012.09129 `[astro-ph.SR]`.

Lane, Richard R. et al. (Aug. 2010). “Halo globular clusters observed with AAOmega: dark matter content, metallicity and tidal heating”. In: 406.4, pp. 2732–2742. DOI: 10.1111/j.1365-2966.2010.16874.x. arXiv: 1004.4696 `[astro-ph.GA]`.

Larsen, S. S., J. P. Brodie, and J. Strader (Nov. 2005). “Globular clusters in NGC 4365: new K-band imaging and a reassessment of the case for intermediate-age clusters”. In: 443.2, pp. 413–433. DOI: 10.1051/0004-6361:20053379. arXiv: astro-ph/0508181 `[astro-ph]`.

Larsen, S. S. et al. (Dec. 2001a). “Keck Spectroscopy and HST imaging of Globular Clusters in the Sombrero Galaxy”. In: *American Astronomical Society Meeting Abstracts*. Vol. 199. American Astronomical Society Meeting Abstracts, p. 52.04.

Larsen, Søren S. and Jean P. Brodie (Aug. 2003). “On the Size Difference between Red and Blue Globular Clusters”. In: 593.1, pp. 340–351. DOI: 10.1086/376503. arXiv: astro-ph/0304434 `[astro-ph]`.

Larsen, Søren S. et al. (June 2001b). “Properties of Globular Cluster Systems in Nearby Early-Type Galaxies”. In: 121.6, pp. 2974–2998. DOI: 10.1086/321081. arXiv: astro-ph/0102374 `[astro-ph]`.

Larsen, Søren S. et al. (Dec. 2014). “Nitrogen Abundances and Multiple Stellar Populations in the Globular Clusters of the Fornax dSph”. In: 797.1, 15, p. 15. DOI: 10.1088/0004-637X/797/1/15. arXiv: 1409.0541 `[astro-ph.GA]`.

Lawrence, A. et al. (Aug. 2007). “The UKIRT Infrared Deep Sky Survey (UKIDSS)”. In: 379.4, pp. 1599–1617. DOI: 10.1111/j.1365-2966.2007.12040.x. arXiv: astro-ph/0604426 `[astro-ph]`.

Le Borgne, D. et al. (Oct. 2004). “Evolutionary synthesis of galaxies at high spectral resolution with the code PEGASE-HR. Metallicity and age tracers”. In: 425, pp. 881–897. DOI: 10.1051/0004-6361:200400044. arXiv: astro-ph/0408419 `[astro-ph]`.

Leaman, Ryan, Don A VandenBerg, and J Trevor Mendel (2013). “The bifurcated age–metallicity relation of Milky Way globular clusters and its implications for the accretion history of the galaxy”. In: *Monthly Notices of the Royal Astronomical Society* 436.1, pp. 122–135.

Lee, Myung Gyoon, Hong Soo Park, and Ho Seong Hwang (Apr. 2010). “Detection of a Large-Scale Structure of Intracluster Globular Clusters in the Virgo Cluster”. In: *Science* 328.5976, p. 334. DOI: 10.1126/science.1186496. arXiv: 1003.2499 `[astro-ph.CO]`.

Lim, Sungsoon et al. (Aug. 2020). “The Next Generation Virgo Cluster Survey (NGVS). XXX. Ultra-diffuse Galaxies and Their Globular Cluster Systems”. In: 899.1, 69, p. 69. DOI: 10.3847/1538-4357/aba433. arXiv: 2007.10565 `[astro-ph.GA]`.

Lind, K. et al. (Nov. 2008). “Atomic diffusion and mixing in old stars. II. Observations of stars in the globular cluster NGC 6397 with VLT/FLAMES-GIRAFFE”. In: 490, pp. 777–786. DOI: 10.1051/0004-6361:200810051. arXiv: 0809.0317.

Lindegren, L. et al. (Nov. 2016). “Gaia Data Release 1. Astrometry: one billion positions, two million proper motions and parallaxes”. In: 595, A4, A4. DOI: 10.1051/0004-6361/201628714. arXiv: 1609.04303 `[astro-ph.GA]`.

Liu, Chengze et al. (Feb. 2011). “The ACS Fornax Cluster Survey. X. Color Gradients of Globular Cluster Systems in Early-type Galaxies”. In: 728.2, 116, p. 116. DOI: 10.1088/0004-637X/728/2/116. arXiv: 1012.2634 `[astro-ph.CO]`.

Liu, Chengze et al. (Oct. 2019a). “The properties of bright globular clusters, ultra-compact dwarfs and dwarf nuclei in the Virgo core: hints on origin of ultra-compact dwarf galaxies (UCDs)”. In: *Dwarf Galaxies: From the Deep Universe to the Present*. Ed. by Kristen B. W. McQuinn and Sabrina Stierwalt. Vol. 344, pp. 384–388. DOI: 10.1017/S1743921318006701.

Liu, Chengze et al. (Sept. 2020). “The Next Generation Virgo Cluster Survey. XXXIV. Ultracompact Dwarf Galaxies in the Virgo Cluster”. In: 250.1, 17, p. 17. DOI: 10.3847/1538-4365/abad91. arXiv: 2007.15275 [astro-ph.GA].

Liu, F. et al. (July 2019b). “Chemical (in)homogeneity and atomic diffusion in the open cluster M 67”. In: 627, A117, A117. DOI: 10.1051/0004-6361/201935306. arXiv: 1902.11008 [astro-ph.SR].

Liu, Yiqing et al. (Oct. 2016). “The ACS Fornax Cluster Survey. XII. Diffuse Star Clusters in Early-type Galaxies”. In: 830.2, 99, p. 99. DOI: 10.3847/0004-637X/830/2/99. arXiv: 1608.03185 [astro-ph.GA].

Liu, Yiqing et al. (Apr. 2019c). “The ACS Fornax Cluster Survey. III. Globular Cluster Specific Frequencies of Early-type Galaxies”. In: 875.2, 156, p. 156. DOI: 10.3847/1538-4357/ab12d9. arXiv: 1904.06909 [astro-ph.GA].

Lokhorst, Deborah et al. (Mar. 2016). “The Next Generation Virgo Cluster Survey. XIX. Tomography of Milky Way Substructures in the NGVS Footprint”. In: 819.2, 124, p. 124. DOI: 10.3847/0004-637X/819/2/124. arXiv: 1601.05385 [astro-ph.GA].

Longobardi, Alessia et al. (Sept. 2018). “The Next Generation Virgo Cluster Survey (NGVS). XXXI. The Kinematics of Intracluster Globular Clusters in the Core of the Virgo Cluster”. In: 864.1, 36, p. 36. DOI: 10.3847/1538-4357/aad3d2. arXiv: 1807.08750 [astro-ph.GA].

Lovisi, L. et al. (Aug. 2012). “Chemical and Kinematical Properties of Blue Straggler Stars and Horizontal Branch Stars in NGC 6397”. In: 754, 91, p. 91. DOI: 10.1088/0004-637X/754/2/91. arXiv: 1205.5561 [astro-ph.SR].

Mackey, A. D. and Sidney van den Bergh (June 2005). “The properties of Galactic globular cluster subsystems”. In: 360.2, pp. 631–645. DOI: 10.1111/j.1365-2966.2005.09080.x. arXiv: astro-ph/0504142 [astro-ph].

Mackey, A. D. et al. (Apr. 2019). “The outer halo globular cluster system of M31 - III. Relationship to the stellar halo”. In: 484.2, pp. 1756–1789. DOI: 10.1093/mnras/stz072. arXiv: 1810.10719 [astro-ph.GA].

Marín-Franch, Antonio et al. (Apr. 2009). “The ACS Survey of Galactic Globular Clusters. VII. Relative Ages”. In: 694.2, pp. 1498–1516. DOI: 10.1088/0004-637X/694/2/1498. arXiv: 0812.4541 [astro-ph].

Martins, L. P. et al. (Aug. 2014). “ALICCE: Atomic Lines Calibration using the Cross-Entropy Algorithm”. In: 442, pp. 1294–1302. DOI: 10.1093/mnras/stu894. arXiv: 1405.1055 [astro-ph.SR].

Martins, L. P. et al. (Apr. 2019). “Testing stellar population fitting ingredients with Globular Clusters I: Stellar libraries”. In: 484, pp. 2388–2402. DOI: 10.1093/mnras/stz126. arXiv: 1902.00420 [astro-ph.SR].

McCracken, H. J. et al. (Aug. 2012). “UltraVISTA: a new ultra-deep near-infrared survey in COSMOS”. In: 544, A156, A156. DOI: 10.1051/0004-6361/201219507. arXiv: 1204.6586 [astro-ph.CO].

McLaughlin, Dean E. (Feb. 1999). “Evidence in Virgo for the Universal Dark Matter Halo”. In: 512.1, pp. L9–L12. DOI: 10.1086/311860. arXiv: astro-ph/9812242 [astro-ph].

McLaughlin, Dean E. and Ralph E. Pudritz (Dec. 1994). “Modelling the Distribution of Globular Cluster Masses”. In: *American Astronomical Society Meeting Abstracts*. Vol. 185. American Astronomical Society Meeting Abstracts, p. 52.10.

Mei, Simona et al. (Jan. 2007). “The ACS Virgo Cluster Survey. XIII. SBF Distance Catalog and the Three-dimensional Structure of the Virgo Cluster”. In: 655.1, pp. 144–162. DOI: 10.1086/509598. arXiv: astro-ph/0702510 [astro-ph].

Meylan, G. and D. C. Heggie (Jan. 1997). “Internal dynamics of globular clusters”. In: 8, pp. 1–143. DOI: 10.1007/s001590050008. arXiv: astro-ph/9610076 [astro-ph].

Mieske, S. (June 2006). “The transition between UCDs and GCs in Fornax”. In: *Revista Mexicana de Astronomia y Astrofisica Conference Series*. Vol. 26. Revista Mexicana de Astronomia y Astrofisica Conference Series, p. 194.

Mieske, S., M. Hilker, and L. Infante (Mar. 2002). “Ultra compact objects in the Fornax cluster of galaxies: Globular clusters or dwarf galaxies?” In: 383, pp. 823–837. DOI: 10.1051/0004-6361:20011833. arXiv: astro-ph/0201011 [astro-ph].

Mighell, Kenneth J., Ata Sarajedini, and Rica S. French (Nov. 1998). “WFPC2 Observations of Star Clusters in the Magellanic Clouds. II. The Oldest Star Clusters in the Small Magellanic Cloud”. In: 116.5, pp. 2395–2414. DOI: 10.1086/300591. arXiv: astro-ph/9808091 [astro-ph].

Milone, A. P. et al. (July 2015). “The Hubble Space Telescope UV Legacy Survey of Galactic Globular Clusters. III. A Quintuple Stellar Population in NGC 2808”. In: 808.1, 51, p. 51. DOI: 10.1088/0004-637X/808/1/51. arXiv: 1505.05934 [astro-ph.SR].

Milone, A. P. et al. (Jan. 2017). “The Hubble Space Telescope UV Legacy Survey of Galactic globular clusters - IX. The Atlas of multiple stellar populations”. In: 464.3, pp. 3636–3656. DOI: 10.1093/mnras/stw2531. arXiv: 1610.00451 [astro-ph.SR].

Milosavljević, Miloš (Apr. 2004). “On the Origin of Nuclear Star Clusters in Late-Type Spiral Galaxies”. In: 605.1, pp. L13–L16. DOI: 10.1086/420696. arXiv: astro-ph/0310574 [astro-ph].

Minniti, D. et al. (July 2010). “VISTA Variables in the Via Lactea (VVV): The public ESO near-IR variability survey of the Milky Way”. In: 15.5, pp. 433–443. DOI: 10.1016/j.newast.2009.12.002. arXiv: 0912.1056 [astro-ph.GA].

Miville-Deschênes, Marc-Antoine, Norman Murray, and Eve J. Lee (Jan. 2017). “Physical Properties of Molecular Clouds for the Entire Milky Way Disk”. In: 834.1, 57, p. 57. DOI: 10.3847/1538-4357/834/1/57. arXiv: 1610.05918 [astro-ph.GA].

Mould, J. R., J. B. Oke, and J. M. Nemec (Jan. 1987). “Spectroscopy of the Globular Clusters in M87”. In: 93, p. 53. DOI: 10.1086/114289.

Muñoz, Roberto P. et al. (Jan. 2014). “The Next Generation Virgo Cluster Survey-Infrared (NGVS-IR). I. A New Near-Ultraviolet, Optical, and Near-Infrared Globular Cluster Selection Tool”. In: 210.1, 4, p. 4. DOI: 10.1088/0067-0049/210/1/4. arXiv: 1311.0873 [astro-ph.CO].

Mucciarelli, Alessio et al. (Apr. 2009). “Looking Outside the Galaxy: The Discovery of Chemical Anomalies in Three Old Large Magellanic Cloud Clusters”. In: 695.2, pp. L134–L139. DOI: 10.1088/0004-637X/695/2/L134. arXiv: 0902.4778 [astro-ph.SR].

Murray, Norman (Apr. 2010). “Stellar Feedback and Galaxy Formation”. In: *From Stars to Galaxies: Connecting our Understanding of Star and Galaxy Formation*, p. 133.

Neumayer, Nadine (Nov. 2012). “Nuclear Star Clusters - Structure and Stellar Populations”. In: *arXiv e-prints*, arXiv:1211.1795, arXiv:1211.1795. arXiv: 1211.1795 [astro-ph.CO].

Neumayer, Nadine, Anil Seth, and Torsten Böker (July 2020). “Nuclear star clusters”. In: 28.1, 4, p. 4. DOI: 10.1007/s00159-020-00125-0. arXiv: 2001.03626 [astro-ph.GA].

Nordlander, T. et al. (July 2012a). “Atomic Diffusion and Mixing in Old Stars. III. Analysis of NGC 6397 Stars under New Constraints”. In: 753.1, 48, p. 48. DOI: 10.1088/0004-637X/753/1/48. arXiv: 1204.5600 [astro-ph.SR].

— (July 2012b). “Atomic Diffusion and Mixing in Old Stars. III. Analysis of NGC 6397 Stars under New Constraints”. In: 753, 48, p. 48. DOI: 10.1088/0004-637X/753/1/48. arXiv: 1204.5600 [astro-ph.SR].

Norris, Mark A. and Sheila J. Kannappan (June 2011). “The ubiquity and dual nature of ultra-compact dwarfs”. In: 414.1, pp. 739–758. DOI: 10.1111/j.1365-2966.2011.18440.x. arXiv: 1102.0001 [astro-ph.CO].

Oliveira, R. A. P. et al. (Mar. 2020). “The Hubble Space Telescope UV Legacy Survey of Galactic Globular Clusters. XX. Ages of Single and Multiple Stellar Populations in Seven Bulge Globular Clusters”. In: 891.1, 37, p. 37. DOI: 10.3847/1538-4357/ab6f76. arXiv: 2001.08611 [astro-ph.GA].

Ordenes-Briceño, Yasna et al. (June 2018). “The Next Generation Fornax Survey (NGFS). IV. Mass and Age Bimodality of Nuclear Clusters in the Fornax Core Region”. In: 860.1, 4, p. 4. DOI: 10.3847/1538-4357/aac1b8. arXiv: 1805.00491 [astro-ph.GA].

Orkney, M. D. A. et al. (Sept. 2019). "Globular clusters as probes of dark matter cusp-core transformations". In: 488.3, pp. 2977–2988. DOI: 10.1093/mnras/stz1625. arXiv: 1906.04759 `[astro-ph.GA]`.

Ostrov, Pablo, Doug Geisler, and Juan C. Forte (May 1993). "The Metallicity Gradient and Distribution Function of Globular Clusters Around NGC 1399". In: 105, p. 1762. DOI: 10.1086/116553.

Padmanabhan, Nikhil et al. (Feb. 2008). "An Improved Photometric Calibration of the Sloan Digital Sky Survey Imaging Data". In: 674.2, pp. 1217–1233. DOI: 10.1086/524677. arXiv: astro-ph/0703454 `[astro-ph]`.

Patterson, Richard J. and Trinh X. Thuan (Dec. 1992). "UGC 7636 and NGC 4472: Tidal Interaction between a Stripped Dwarf Irregular and a Giant Elliptical Galaxy". In: 400, p. L55. DOI: 10.1086/186648.

Peebles, P. J. E. and R. H. Dicke (Dec. 1968). "Origin of the Globular Star Clusters". In: 154, p. 891. DOI: 10.1086/149811.

Peng, Eric et al. (Feb. 2008). *The Dark Matter Content of Early-Type Galaxies in the ACS Virgo Cluster Survey*. NOAO Proposal.

Peng, Eric W. et al. (Mar. 2006). "The ACS Virgo Cluster Survey. IX. The Color Distributions of Globular Cluster Systems in Early-Type Galaxies". In: 639.1, pp. 95–119. DOI: 10.1086/498210. arXiv: astro-ph/0509654 `[astro-ph]`.

Phillipps, S. et al. (Oct. 2001). "Ultracompact Dwarf Galaxies in the Fornax Cluster". In: 560.1, pp. 201–206. DOI: 10.1086/322517. arXiv: astro-ph/0106377 `[astro-ph]`.

Piotto, G. et al. (May 2007). "A Triple Main Sequence in the Globular Cluster NGC 2808". In: 661.1, pp. L53–L56. DOI: 10.1086/518503. arXiv: astro-ph/0703767 `[astro-ph]`.

Piotto, G. et al. (Mar. 2015). "The Hubble Space Telescope UV Legacy Survey of Galactic Globular Clusters. I. Overview of the Project and Detection of Multiple Stellar Populations". In: 149.3, 91, p. 91. DOI: 10.1088/0004-6256/149/3/91. arXiv: 1410.4564 `[astro-ph.SR]`.

Powalka, Mathieu et al. (Sept. 2016a). "New Constraints on a Complex Relation between Globular Cluster Colors and Environment". In: 829.1, L5, p. L5. DOI: 10.3847/2041-8205/829/1/L5. arXiv: 1608.08628 `[astro-ph.GA]`.

Powalka, Mathieu et al. (Nov. 2016b). "The Next Generation Virgo Cluster Survey (NGVS). XXV. Fiducial Panchromatic Colors of Virgo Core Globular Clusters and Their Comparison to Model Predictions". In: 227.1, 12, p. 12. DOI: 10.3847/0067-0049/227/1/12. arXiv: 1608.04742 `[astro-ph.GA]`.

Powalka, Mathieu et al. (Mar. 2018). “The Next Generation Virgo Cluster Survey (NGVS). XXXII. A Search for Globular Cluster Substructures in the Virgo Galaxy Cluster Core”. In: 856.1, 84, p. 84. DOI: 10.3847/1538-4357/aaae63. arXiv: 1802.06814 `[astro-ph.GA]`.

Prantzos, N. and C. Charbonnel (Oct. 2006). “On the self-enrichment scenario of galactic globular clusters: constraints on the IMF”. In: 458.1, pp. 135–149. DOI: 10.1051/0004-6361:20065374. arXiv: astro-ph/0606112 `[astro-ph]`.

Press, William H. and Paul Schechter (Feb. 1974). “Formation of Galaxies and Clusters of Galaxies by Self-Similar Gravitational Condensation”. In: 187, pp. 425–438. DOI: 10.1086/152650.

Prugniel, P. and C. Soubiran (Apr. 2001). “A database of high and medium-resolution stellar spectra”. In: 369, pp. 1048–1057. DOI: 10.1051/0004-6361:20010163. eprint: astro-ph/0101378.

Prugniel, P., I. Vauglin, and M. Koleva (July 2011). “The atmospheric parameters and spectral interpolator for the MILES stars”. In: 531, A165, A165. DOI: 10.1051/0004-6361/201116769. arXiv: 1104.4952.

Puget, Pascal et al. (Sept. 2004). “WIRCam: the infrared wide-field camera for the Canada-France-Hawaii Telescope”. In: ed. by Alan F. M. Moorwood and Masanori Iye. Vol. 5492. Society of Photo-Optical Instrumentation Engineers (SPIE) Conference Series, pp. 978–987. DOI: 10.1117/12.551097.

Rejkuba, M. (Sept. 2012). “Globular cluster luminosity function as distance indicator”. In: 341.1, pp. 195–206. DOI: 10.1007/s10509-012-0986-9. arXiv: 1201.3936 `[astro-ph.CO]`.

Renaud, Florent (Apr. 2018). “Star clusters in evolving galaxies”. In: 81, pp. 1–38. DOI: 10.1016/j.newar.2018.03.001. arXiv: 1801.04278 `[astro-ph.GA]`.

Renaud, Florent, Oscar Agertz, and Mark Gieles (Mar. 2017). “The origin of the Milky Way globular clusters”. In: 465.3, pp. 3622–3636. DOI: 10.1093/mnras/stw2969. arXiv: 1610.03101 `[astro-ph.GA]`.

Renzini, A. et al. (Dec. 2015). “The Hubble Space Telescope UV Legacy Survey of Galactic Globular Clusters - V. Constraints on formation scenarios”. In: 454.4, pp. 4197–4207. DOI: 10.1093/mnras/stv2268. arXiv: 1510.01468 `[astro-ph.GA]`.

Renzini, Alvio (Sept. 2006). “Stellar Population Diagnostics of Elliptical Galaxy Formation”. In: 44.1, pp. 141–192. DOI: 10.1146/annurev.astro.44.051905.092450. arXiv: astro-ph/0603479 `[astro-ph]`.

— (Jan. 2013). “Rethinking globular clusters formation”. In: 84, p. 162. arXiv: 1302.0329 `[astro-ph.GA]`.

Rhode, Katherine L. and Stephen E. Zepf (Jan. 2004). “The Globular Cluster Systems of the Early-Type Galaxies NGC 3379, NGC 4406, and NGC 4594 and Implications for Galaxy

Formation". In: 127.1, pp. 302–317. DOI: 10.1086/380616. arXiv: astro-ph/0310277 [astro-ph].

Riaz, Rafeel et al. (Jan. 2021). "Stellar initial mass function over a range of redshifts". In: *Astronomische Nachrichten* 342.1-2, pp. 157–163. DOI: 10.1002/asna.202113897. arXiv: 2010.07692 [astro-ph.GA].

Richard, O. et al. (Apr. 2002). "Models of Metal-poor Stars with Gravitational Settling and Radiative Accelerations. I. Evolution and Abundance Anomalies". In: 568.2, pp. 979–997. DOI: 10.1086/338952.

Richtler, Tom (2003). "The Globular Cluster Luminosity Function: New Progress in Understanding an Old Distance Indicator". In: *Stellar Candles for the Extragalactic Distance Scale*. Ed. by D. Alloin and W. Gieren. Vol. 635, pp. 281–305. DOI: 10.1007/978-3-540-39882-0_15.

Robin, A. C. et al. (Oct. 2003). "A synthetic view on structure and evolution of the Milky Way". In: 409, pp. 523–540. DOI: 10.1051/0004-6361:20031117.

Roediger, Joel C. et al. (Feb. 2017). "The Next Generation Virgo Cluster Survey (NGVS). XXIV. The Red Sequence to ~10^6 L $_\odot$ and Comparisons with Galaxy Formation Models". In: 836.1, 120, p. 120. DOI: 10.3847/1538-4357/836/1/120. arXiv: 1610.09377 [astro-ph.GA].

Romanowsky, Aaron J. (2009). "Kinematics of Globular Cluster Systems". In: *Globular Clusters - Guides to Galaxies*. Ed. by Tom Richtler and Søren Larsen, p. 433. DOI: 10.1007/978-3-540-76961-3_102.

Rosolowsky, Erik et al. (June 2007). "High-Resolution Molecular Gas Maps of M33". In: 661.2, pp. 830–844. DOI: 10.1086/516621. arXiv: astro-ph/0703006 [astro-ph].

Rosolowsky, Erik W. (Jan. 2007). "Understanding starbursts through giant molecular clouds in high density environments". In: *Triggered Star Formation in a Turbulent ISM*. Ed. by Bruce G. Elmegreen and Jan Palous. Vol. 237, pp. 208–211. DOI: 10.1017/S1743921307001482.

Russell, H. N. (Aug. 1913). ""Giant" and "dwarf" stars". In: *The Observatory* 36, pp. 324–329.

Russell, Henry Norris (May 1914). "Relations Between the Spectra and Other Characteristics of the Stars". In: *Popular Astronomy* 22, pp. 275–294.

Samurović, S. (Dec. 2017). "Dynamical Models of the Two Lenticular Galaxies: NGC 1023 and NGC 4526". In: *Serbian Astronomical Journal* 195, pp. 9–21. DOI: 10.2298/SAJ170330006S.

Sánchez-Blázquez, P. et al. (Sept. 2006). "Medium-resolution Isaac Newton Telescope library of empirical spectra". In: 371, pp. 703–718. DOI: 10.1111/j.1365-2966.2006.10699.x. eprint: astro-ph/0607009.

Sánchez-Janssen, R. et al. (June 2019a). “How nucleation and luminosity shape faint dwarf galaxies”. In: 486.1, pp. L1–L5. DOI: 10.1093/mnrasl/slz008. arXiv: 1901.04509 [astro-ph.GA].

Sánchez-Janssen, Rubén et al. (June 2019b). “The Next Generation Virgo Cluster Survey. XXIII. Fundamentals of Nuclear Star Clusters over Seven Decades in Galaxy Mass”. In: 878.1, 18, p. 18. DOI: 10.3847/1538-4357/aaf4fd. arXiv: 1812.01019 [astro-ph.GA].

Scaramella, R. et al. (Aug. 2021). “Euclid preparation: I. The Euclid Wide Survey”. In: *arXiv e-prints*, arXiv:2108.01201, arXiv:2108.01201. arXiv: 2108.01201 [astro-ph.CO].

Scarpa, R. et al. (Jan. 2007). “Using globular clusters to test gravity in the weak acceleration regime: NGC 7099”. In: 462.1, pp. L9–L12. DOI: 10.1051/0004-6361:20066182. arXiv: astro-ph/0611504 [astro-ph].

Schlegel, David J., Douglas P. Finkbeiner, and Marc Davis (June 1998). “Maps of Dust Infrared Emission for Use in Estimation of Reddening and Cosmic Microwave Background Radiation Foregrounds”. In: 500.2, pp. 525–553. DOI: 10.1086/305772. arXiv: astro-ph/9710327 [astro-ph].

Schuberth, Y. et al. (Apr. 2010). “The globular cluster system of NGC 1399. V. dynamics of the cluster system out to 80 kpc”. In: 513, A52, A52. DOI: 10.1051/0004-6361/200912482. arXiv: 0911.0420 [astro-ph.CO].

Schweizer, Francois (Jan. 1987). “Star Formation in Colliding and Merging Galaxies”. In: *Nearly Normal Galaxies. From the Planck Time to the Present*. Ed. by Sandra M. Faber, p. 18.

Secker, Jeff (Oct. 1992). “A statistical investigation into the shape of the globular cluster luminosity distribution.” In: 104, pp. 1472–1481. DOI: 10.1086/116332.

Semenov, Vadim A., Andrey V. Kravtsov, and Nickolay Y. Gnedin (Aug. 2017). “The Physical Origin of Long Gas Depletion Times in Galaxies”. In: 845.2, 133, p. 133. DOI: 10.3847/1538-4357/aa8096. arXiv: 1704.04239 [astro-ph.GA].

Seth, Anil C. et al. (Dec. 2006). “Clues to Nuclear Star Cluster Formation from Edge-on Spirals”. In: 132.6, pp. 2539–2555. DOI: 10.1086/508994. arXiv: astro-ph/0609302 [astro-ph].

Sharina, M. and V. Shimansky (Dec. 2020). “On the Influence of Multiple Stellar Populations in Globular Clusters on Their Medium-Resolution Integrated-Light Spectra”. In: *Ground-Based Astronomy in Russia. 21st Century*. Ed. by I. I. Romanyuk et al., pp. 267–270. DOI: 10.26119/978-5-6045062-0-2_2020_267. arXiv: 2012.09044 [astro-ph.GA].

Sharma, K., P. Prugniel, and H. P. Singh (Jan. 2016). “New atmospheric parameters and spectral interpolator for the MILES cool stars”. In: 585, A64, A64. DOI: 10.1051/0004-6361/201526111. arXiv: 1512.04882 [astro-ph.SR].

Shima, Kazuhiro, Elizabeth J. Tasker, and Asao Habe (May 2017). “Does feedback help or hinder star formation? The effect of photoionization on star formation in giant molecular clouds”. In: 467.1, pp. 512–523. DOI: 10.1093/mnras/stw3279. arXiv: 1612.06381 [astro-ph.GA].

Skrutskie, M. F. et al. (Feb. 2006). “The Two Micron All Sky Survey (2MASS)”. In: 131.2, pp. 1163–1183. DOI: 10.1086/498708.

Souto, D. et al. (Apr. 2018). “Chemical Abundances of Main-sequence, Turnoff, Subgiant, and Red Giant Stars from APOGEE Spectra. I. Signatures of Diffusion in the Open Cluster M67”. In: 857, 14, p. 14. DOI: 10.3847/1538-4357/aab612. arXiv: 1803.04461 [astro-ph.SR].

Sutherland, Will et al. (Mar. 2015). “The Visible and Infrared Survey Telescope for Astronomy (VISTA): Design, technical overview, and performance”. In: 575, A25, A25. DOI: 10.1051/0004-6361/201424973. arXiv: 1409.4780 [astro-ph.IM].

Taylor, Matthew A. et al. (Aug. 2017). “The Survey of Centaurus A’s Baryonic Structures (SCABS) - II. The extended globular cluster system of NGC 5128 and its nearby environment”. In: 469.3, pp. 3444–3467. DOI: 10.1093/mnras/stx1021. arXiv: 1608.07288 [astro-ph.GA].

Tonini, Chiara (Jan. 2013). “The Metallicity Bimodality of Globular Cluster Systems: A Test of Galaxy Assembly and of the Evolution of the Galaxy Mass-Metallicity Relation”. In: 762.1, 39, p. 39. DOI: 10.1088/0004-637X/762/1/39. arXiv: 1211.1434 [astro-ph.CO].

Trager, S. C. et al. (Apr. 2000). “The Stellar Population Histories of Local Early-Type Galaxies. I. Population Parameters”. In: 119.4, pp. 1645–1676. DOI: 10.1086/301299. arXiv: astro-ph/0001072 [astro-ph].

Tremaine, S. D., J. P. Ostriker, and Jr. Spitzer L. (Mar. 1975). “The formation of the nuclei of galaxies. I. M31.” In: 196, pp. 407–411. DOI: 10.1086/153422.

Tully, R. B. (June 1982). “The Local Supercluster”. In: 257, pp. 389–422. DOI: 10.1086/159999.

van den Bergh, S. (Jan. 1975). “Stellar populations in galaxies.” In: 13, pp. 217–255. DOI: 10.1146/annurev.aa.13.090175.001245.

— (Aug. 1985). “The age of the universe”. In: 79, pp. 153–159.

van den Bergh, Sidney, Christopher Morbey, and John Pazder (July 1991). “Diameters of Galactic Globular Clusters”. In: 375, p. 594. DOI: 10.1086/170220.

VandenBerg, D. A. et al. (May 2002a). “Models of Metal-poor Stars with Gravitational Settling and Radiative Accelerations. II. The Age of the Oldest Stars”. In: 571, pp. 487–500. DOI: 10.1086/339895.

Vandenberg, Don (July 2003). *Parallaxes of Extreme Halo Subgiants: Calibrating Globular Cluster Distances and the Ages of the Oldest Stars*. HST Proposal.

VandenBerg, Don A. et al. (May 2002b). "Models of Metal-poor Stars with Gravitational Settling and Radiative Accelerations. II. The Age of the Oldest Stars". In: 571.1, pp. 487–500. DOI: 10.1086/339895.

Vázquez-Semadeni, Enrique et al. (Dec. 2019). "Global hierarchical collapse in molecular clouds. Towards a comprehensive scenario". In: 490.3, pp. 3061–3097. DOI: 10.1093/mnras/stz2736. arXiv: 1903.11247 `[astro-ph.GA]`.

Villegas, Daniela et al. (July 2010). "The ACS Fornax Cluster Survey. VIII. The Luminosity Function of Globular Clusters in Virgo and Fornax Early-type Galaxies and Its Use as a Distance Indicator". In: 717.2, pp. 603–616. DOI: 10.1088/0004-637X/717/2/603. arXiv: 1004.2883 `[astro-ph.CO]`.

Wang, Qiushi et al. (June 2013). "The ACS Virgo Cluster Survey. XVII. The Spatial Alignment of Globular Cluster Systems with Early-type Host Galaxies". In: 769.2, 145, p. 145. DOI: 10.1088/0004-637X/769/2/145. arXiv: 1304.0824 `[astro-ph.GA]`.

Watkins, Laura L., N. Wyn Evans, and Jin H. An (July 2010). "The masses of the Milky Way and Andromeda galaxies". In: 406.1, pp. 264–278. DOI: 10.1111/j.1365-2966.2010.16708.x. arXiv: 1002.4565 `[astro-ph.GA]`.

West, Michael J. et al. (Nov. 1995). "Intracluster Globular Clusters". In: 453, p. L77. DOI: 10.1086/309748. arXiv: astro-ph/9508141 `[astro-ph]`.

White, Richard L. et al. (Feb. 1997). "A Catalog of 1.4 GHz Radio Sources from the FIRST Survey". In: 475.2, pp. 479–493. DOI: 10.1086/303564.

Whitmore, Bradley C. et al. (Oct. 1999). "The Luminosity Function of Young Star Clusters in "the Antennae" Galaxies (NGC 4038-4039)". In: 118.4, pp. 1551–1576. DOI: 10.1086/301041. arXiv: astro-ph/9907430 `[astro-ph]`.

Worthey, Guy (Nov. 1994). "Comprehensive Stellar Population Models and the Disentanglement of Age and Metallicity Effects". In: 95, p. 107. DOI: 10.1086/192096.

Wu, Y. et al. (Jan. 2011). "Coudé-feed stellar spectral library - atmospheric parameters". In: 525, A71, A71. DOI: 10.1051/0004-6361/201015014. arXiv: 1009.1491 `[astro-ph.SR]`.

Yoon et al. (June 2006a). "On the Origin of Bimodal Color Distribution of Globular Clusters in Early-type Galaxies". In: *American Astronomical Society Meeting Abstracts #207*. Vol. 207. American Astronomical Society Meeting Abstracts, p. 128.22.

Yoon, Suk-Jin, Sukyoung Ken Yi, and Young-Wook Lee (Feb. 2006b). "Explaining the Color Distributions of Globular Cluster Systems in Elliptical Galaxies". In: *Science* 311.5764, pp. 1129–1132. DOI: 10.1126/science.1122294. arXiv: astro-ph/0601526 `[astro-ph]`.

York, Donald G. et al. (Sept. 2000). “The Sloan Digital Sky Survey: Technical Summary”. In: 120.3, pp. 1579–1587. DOI: 10.1086/301513. arXiv: astro-ph/0006396 [astro-ph].

Zaritsky, Dennis et al. (Feb. 2015). “Globular Cluster Populations: First Results from S^4G Early-type Galaxies”. In: 799.2, 159, p. 159. DOI: 10.1088/0004-637X/799/2/159. arXiv: 1411.4615 [astro-ph.GA].

Zepf, Stephen E. and Keith M. Ashman (Jan. 1993). “Globular cluster systems as clues to galaxy evolution”. In: *Evolution of Galaxies and their Environment*. Ed. by J. M. Shull and H. A. Thronson, pp. 48–49.

Zhang, Q. and S. M. Fall (Dec. 1999). “The Mass Function of Young Star Clusters in the “Antennae” Galaxies”. In: *American Astronomical Society Meeting Abstracts*. Vol. 195. American Astronomical Society Meeting Abstracts, p. 47.15.

Zinn, R. (Nov. 1978). “The metal abundance range in the Draco dwarf galaxy.” In: 225, pp. 790–803. DOI: 10.1086/156544.

— (June 1985). “The Globular Cluster System of the Galaxy. IV. The Halo and Disk Subsystems”. In: 293, p. 424. DOI: 10.1086/163249.

Zinn, Robert (Jan. 1993). “The Galactic Halo Cluster Systems: Evidence for Accretion”. In: *The Globular Cluster-Galaxy Connection*. Ed. by Graeme H. Smith and Jean P. Brodie. Vol. 48. Astronomical Society of the Pacific Conference Series, p. 38.

UNIVERSITÉ DE STRASBOURG

Observatoire astronomique
de Strasbourg

Rashi JAIN

Stellar populations in Globular Clusters

Constraints on stellar physics and Subtle Relationships between color and environment

Résumé

Les amas globulaires sont omniprésents dans les galaxies de toutes morphologies et de tous âges. Leurs propriétés sont étroitement liées à celles de leurs galaxies hôtes et de leurs environnements. L'étude des GCs résolus de la Voie Lactée est monumentale dans notre compréhension de la physique stellaire. Nous avons utilisé les données spectroscopiques des étoiles d'un GC de la Voie lactée pour comparer les performances des bibliothèques stellaires théoriques et empiriques dans le régime pauvre en métaux. Ces bibliothèques sont utilisées pour estimer les paramètres atmosphériques des étoiles de notre jeu de données et montrent l'effet de la diffusion atomique dans les étoiles sur le gradient de métallicité le long de la branche géante. Dans ce travail, nous avons mis en évidence les lacunes qui existent entre les bibliothèques stellaires utilisées.

Dans la deuxième partie de la thèse, nous nous sommes concentrés sur l'étude des couleurs des GCs autour de la galaxie de type précoce dans l'amas de la Vierge, M49, et des GCs dans la région intra-amas. Nous avons utilisé des données photométriques dans un champ de ∼23 degrés carrés dans six bandes proches de l'UV, de l'optique et de l'IR pour étudier les différentes propriétés de couleur des GCs dans le champ mentionné ci-dessus. Nous avons classé les populations de GCs en fonction de leur environnement et caractérisé les distributions de couleur et de couleur des GCs. Ce travail met en évidence la dépendance de la distribution des couleurs des GCs par rapport à leur environnement local. Les effets photométriques sont faibles et doivent être suivis de plus près pour mieux comprendre leur origine. Ceci peut être réalisé avec une photométrie plus profonde et plus précise, ce qui est attendu dans un futur proche par les études de zones lagunes comme Euclid et LSST.

Mots-clés : Amas globulaires ; bibliothèques stellaires ; photométrie ; galaxies massives

Résumé en Anglais

Globular clusters are ubiquitously found in galaxies of all morphologies and ages. Their properties are closely tied to the properties of their host galaxies and their environments. The study of resolved Milky Way GCs is monumental in our understanding of stellar physics. We have used the spectroscopic data for the stars of a GC in the Milky Way to compare the performances of theoretical and empirical stellar libraries in the metal-poor regime. These libraries are used to estimate the atmospheric parameters for the stars in our dataset and show the effect of atomic diffusion in stars on the metallicity gradient along the giant branch. In this work, we have highlighted the gaps that exist between the stellar libraries used.

In the second part of the thesis, we have focussed on the study of colors of GCs around the early-type galaxy in the Virgo cluster, M49, and GCs in the intracluster region. We have used photometric data in a field of ∼23 square degrees in six near-UV, optical and near-IR bands to study various color-color properties of the GCs in the aforementioned field. We have classified the GC populations according to their environment and characterized the color-color distributions of the GCs. This work highlights the dependence of the color-color distribution of the GCs on their local environment. The photometric effects are small and need to be followed up further for a better understanding of their origin. This can be achieved with deeper and more precise photometry which is expected from the large area surveys like Euclid and LSST in the near future.

Keywords: Globular clusters; stellar libraries; photometry; massive galaxies